SYNTHESIS, CHARACTERIZATION AND INVESTIGATION OF METAL-METAL BONDED DIRHODIUM COMPLEXES

A Dissertation

by

ZHANYONG LI

Submitted to the Office of Graduate and Professional Studies of
Texas A&M University
in partial fulfillment of the requirements for the degree of

DOCTOR OF PHILOSOPHY

Chair of Committee,	Kim R. Dunbar
Committee Members,	Timothy Hughbanks
	Marcetta Darensbourg
	James Sacchettini
Head of Department,	David Russell

August 2014

Major Subject: Chemistry

ABSTRACT

This dissertation focuses on the design and tailoring of dirhodium complexes and the investigation of their structural, spectroscopic and theoretical properties. The variation of the ligands occupying the equatorial (eq) positions results in appreciable changes in the structure and the electronic properties, which renders them suitable for different applications.

The coordination of methyl isocyanide ligands to dirhodium centers bridged by electron-rich formamidinate or orthometalated phosphine ligands led to a family of unprecedented dirhodium complexes of general formula *cis*-$[Rh_2(\mu\text{-}L)_2(CNCH_3)_6]^{2+}$ (L = bridging ligand). These complexes exhibit unusually long Rh-Rh bond distances and short Rh-C (CH_3NC) contacts and exhibit the unexpected bonding situation in which the $Rh_2(\pi^*)$ levels lie lower in energy than the $Rh_2(\sigma)$ orbitals.

Reactions between *cis*-$[Rh_2(Form)_2(CH_3CN)_6]^{2+}$ (Form = formamidinate) and the electron accepting chelating diimine ligands dpq = dipyrido[3,2-f:2',3'-h]-quinoxaline, dppz = dipyrido[3,2-a:2',3'-c]phenazine and dppn = benzo[i]dipyrido[3,2-a:2',3'-h]quinoxaline produce complexes of the general type *cis*-$[Rh_2(Form)_2(N\text{-}N)_2]^{2+}$ with intriguing photophysical properties. The lowest energy absorption in their electronic absorption spectra is a Ligand-to-Ligand Charger-Transfer (LL'CT) transition which leads to interesting excited state reactivity patterns, most notably water reduction to produce hydrogen.

Three 6-R-hydroxyl-pyridine ligand with different substituents (R= $-CH_3$, -F, -Cl) was selected as a bridging ligand for the series of partial paddlewheel complexes *cis*-

$[Rh_2(\mu\text{-}L)_2(CH_3CN)_6]^{2+}$. The goal was to probe the effect of the bridging ligand substituents on the lability of the eq CH_3CN ligands. It was shown the substitution rate of the eq CH_3CN ligands is intimately correlated to the electronic characteristics of the bridging ligands with decreased lability occurring in the order of $-F < -Cl < -CH_3$, in accord with the stronger *trans* effect exerted by the more electron donating ligands.

Additional efforts to tune the electronic properties of dirhodium complexes with chelating diimine ligands include the search for new bridging ligands, *e.g.* $[Ph_2P(C_6H_4)]^-$. Density Functional Theory (DFT) and Time Dependent (TD) DFT calculations on the synthesized *cis*-$[Rh_2[Ph_2P(C_6H_4)]_2(N\text{-}N)_2]^{2+}$ (N-N = dpq, dppz, and dppn) complexes indicate that they exhibit very different electronic structures as compared to the dirhodium complexes with formamidinate bridging ligands.

Finally, additional studies were directed at the synthesis of ligands with hydrophilic functional groups to improve the water solubility of the complexes in order to enhance their activity as photodynamic anticancer therapy agents and water reduction photocatalysts.

ACKNOWLEDGEMENTS

The dissertation presented here would not have been possible without the guidance from Prof. Kim R. Dunbar. She is a great chemist, mentor and I appreciate all of the efforts she put into my education and development as a scientist. I also would like to thank other important members of the research team, namely our talented and dedicated collaborators, Prof. Claudia Turro, Dr. Scott Burya and Dr. Nicholas Leed from The Ohio State University.

The five years spent in the Dunbar group at Texas A&M University was a great experience. I appreciate the deep friendships I have forged with past and current group members. I would like to give my sincerest thanks to them including Dr. Helen Chifotides, Dr. Ming Fang, Dr. Ian Giles, Dr. Dawid Pinkowicz, Dr. Mohamed Saber, Dr. Heather Southerland, Dr. Zhao-xi Wang, Dr. Yuan-zhu Zhang, Dr. Zhongyue Zhang, Dr. Hanhua Zhao as well as Francisco Birk, Andrew Brown, Amanda David, Jill Frank, David Kempe, Sarah Lane, Jarett Martin, Bruno Pena, Sayan Saha, Codi Sanders, Toby Woods and Xuan Zhang.

I would also like to thank my parents and sister for their unconditional love and my friends for all the encouragement that I have received from them over the years.

TABLE OF CONTENTS

Page

Page

LIST OF FIGURES

FIGURE Page

FIGURE Page

FIGURE Page

FIGURE Page

FIGURE Page

FIGURE Page

LIST OF TABLES

TABLE Page

TABLE Page

TABLE Page

CHAPTER I

INTRODUCTION

Dirhodium complexes play important roles in various areas of chemical research due to the ease with which their properties can be tuned through rational ligand design. They have been widely used in many different applications such as carbene transfer reaction catalysts, [1,2] anticancer [3-7] and photodynamic therapy agents, [8-10] building blocks for supramolecular arrays, [11,12] photocatalysts for H_2O reduction, [13-17] chromogenic or fluorescence-based sensors for small gaseous molecules such as NO [18] and CO [19,20] as well as many others.[21] The most common dirhodium complexes in the literature are those bridged by four carboxylate ligands in the equatorial (eq) positions with two labile ligands occupying the axial (ax) positions as shown in Figure 1.1. Other important bridging ligands include formamidinates, triazenides and acetamides as well as orthometalated phosphines.[21] One fundamental aspect of the investigation of these dirhodium complexes is the effect of the co-ligands on their electronic structures. Without the perturbation of the ligand field, the d^7-d^7 dirhodium(II,II) center core generally adopts the electronic structure $\sigma^2\pi^4\delta^2\delta^{*2}\pi^{*4}\sigma^0$, which results in a bond order of 1 (Figure 1.2).[21] Upon coordination of bridging ligands, such as the carboxylate groups, the interactions between the $Rh_2(\delta^*)$ orbitals with the $p\pi$ lone pairs on the O atoms results in a destabilization of the $Rh_2(\delta^*)$ orbital. Therefore, the electronic configuration pertaining to the dimetal centers changes to $\sigma^2\pi^4\delta^2\ \pi^{*4}\delta^{*2}\sigma^0$.[22] In the electronic absorption spectra of $Rh_2(\mu\text{-OCCR})_4\bullet 2L$ (L = CH_3CN, CH_3OH, pyridine, PPh_3), the lowest energy absorption band originates from the $Rh_2(\pi^*)$ to the $Rh_2(\sigma^*)$ orbital

transitions as predicted by many different levels of calculations: this transition is responsible for the wide variety of colors observed for dirhodium paddlewheel complexes. The ax ligands, which are usually kinetically labile, only affect the σ type orbitals.[21] On the other hand, the eq ligands, which are generally more stable as compared to the ax ligands, influence both the π and δ types of orbitals. Generally, the eq ligands are more influential in determining the chemical properties of the complexes. For example, dirhodium complexes with chiral carboxylate groups in the eq positions are demonstrated to be effective for catalyzing the formation of chiral organic molecules.[1,2] Another good example is that the replacement of the four eq carboxylate groups with more electron-rich formamidinate groups, *e.g.* $Rh_2(DTolF)_4$, $Rh_2(F\text{-}form)_4$, renders them excellent reducing agents in their excited states and thus useful for the decomposition of harmful organic pollutants in the environment.[23]

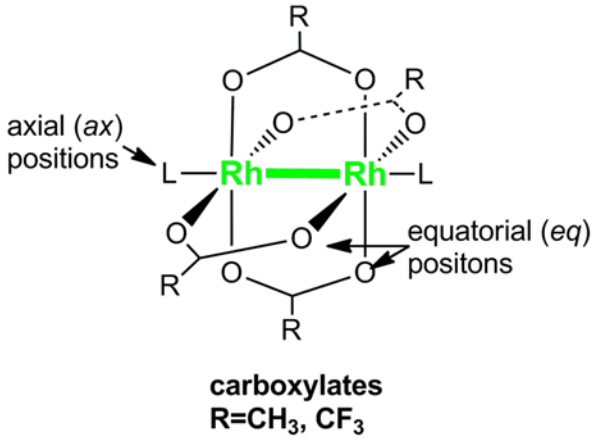

Figure 1.1 Structural representation of dirhodium tetracarboxylate complexes.

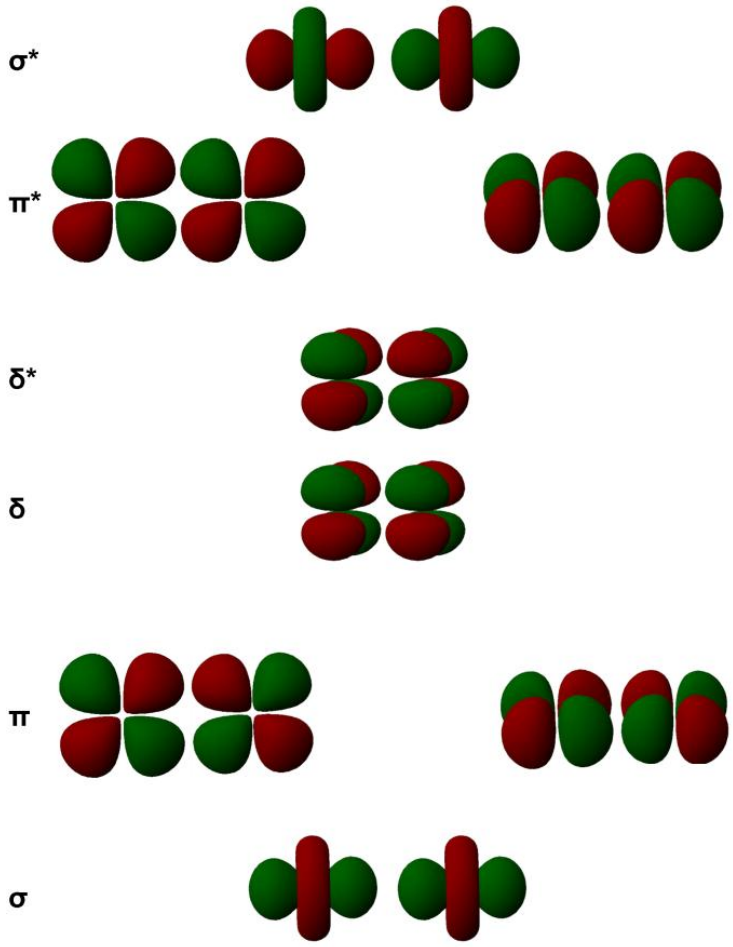

Figure 1.2 Depictions of the d orbital overlap for metal-metal bonded units.

In the Dunbar research group, we have long been interested in the design and synthesis of partial paddlewheel dirhodium complexes featuring two *cis*-oriented bridging groups in the eq positions with the remaining sites being occupied by either monodentate or diimine ligands as shown in Figure 1.3. The exploration of their applications as photodynamic therapy (PDT) agents for cancer treatment and photocatalysts for H_2O reduction are important aspects of our research in this area.

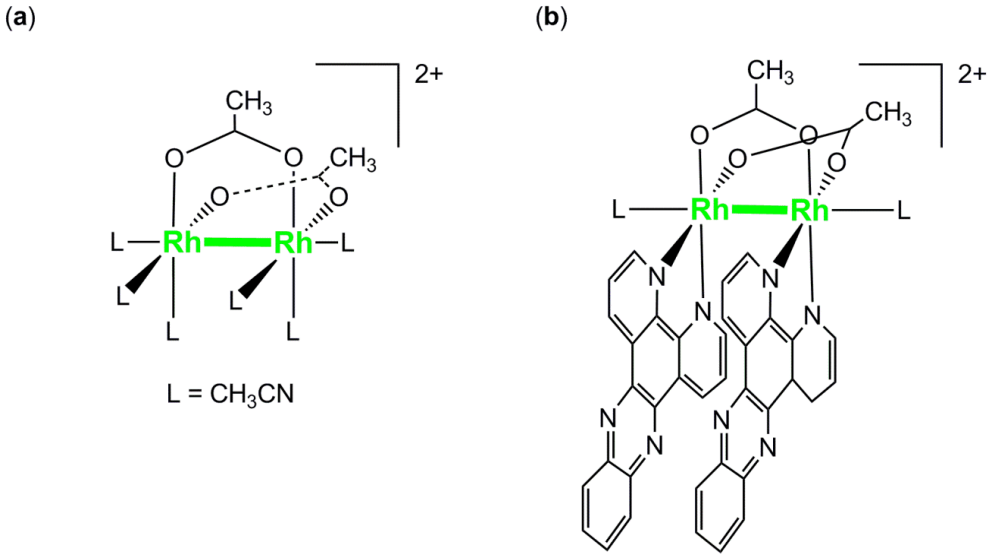

Figure 1.3 Structural representation of two types of partial paddlewheel complexes.

Photodynamic therapy

Photodynamic therapy is a rapidly evolving approach for the treatment of cancer and pre-cancerous conditions.[24] Typically, the administration of photosensitizers (PS) is followed by selectively irradiating the affected area with low intensity light (preferably ~

600-850 nm). Reactive oxygen species (ROS) such as singlet oxygen, $^1O_2$, are generated through an energy transfer process (Figure 1.4).[25-27] Subsequently, these cytotoxic ROS oxidize various biomolecules including proteins, nucleic acids and lipids.[28] These reactions eventually lead to cell death in the tumors while only inducing a low level of systematic cytotoxicity towards normal tissues.[29-33]

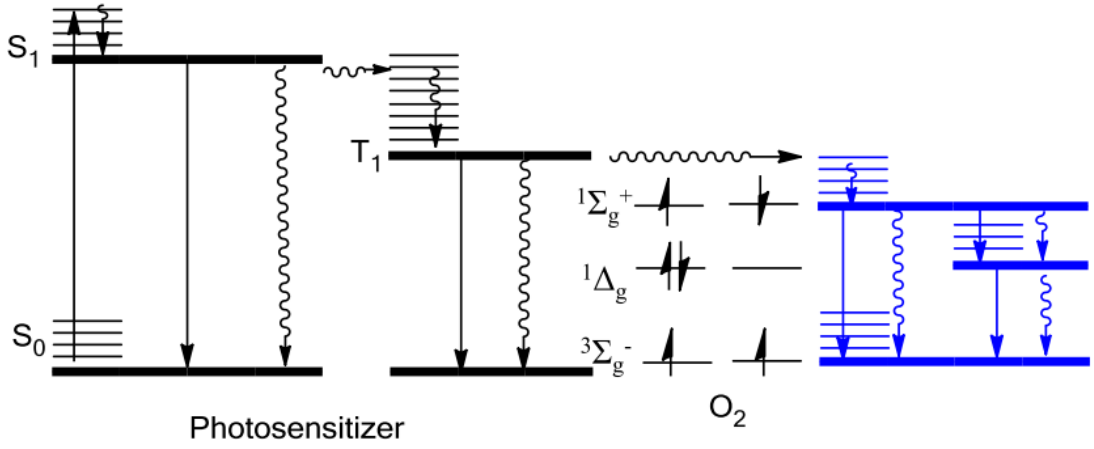

Figure 1.4 Relaxation pathways for the excited photosensitizer, with the display of the $^1O_2$ generation through an energy transfer process.

Successful candidates as photosensitizers in PDT treatment should conform to the following criteria: Firstly, it is preferable for them to be activated by red or near infrared light, for the purpose of deeper tissue penetration as well as producing less damage to the surrounding normal tissues. Secondly, they should be soluble in aqueous solution for easy administration. Thirdly, they should be chemically stable and have very low systemic cytotoxicity in the dark.

Most $^1O_2$ sensitizing agents are organic molecules such as those depicted in Figure 1.5,[34] but some transition metal complexes are also very efficient photosensitizers for the generation of $^1O_2$ especially Ru(II)[35,36], Os(II)[37], Ir(III)[38,39], Re(I) [40,41]compounds. In particular, various Ru(II) diimine complexes exhibit very strong absorptions in the visible region and can generate $^1O_2$ in aerated solutions through a long-lived metal-to-ligand charge-transfer (MLCT) process with relatively high quantum yields upon light irradiation.[42] In addition to the sensitization of $^1O_2$, the quenching of the excited states of transition metal complexes can be triggered by an electron transfer process (redox event). During this period, the *in situ* generated products are shown to capable of binding to or oxidizing biomolecules[43] which provides an advantage for transition metal complexes as effective PDT agents against hypoxic tumors, since their anticancer activity is independent of O_2.

Initially, the Turro group explored the photochemistry of $Rh_2(\mu\text{-}O_2CCH_3)_4\bullet 2L$ (L: alcohol, PPh_3, pyridine, THF, H_2O).[44] These complexes exhibit long-lived excited states (τ = 3.5-5.0 μs) that can be accessed by visible light irradiation (500-700 nm). Moreover, the bis-aqua species $Rh_2(\mu\text{-}O_2CCH_3)_4\bullet 2H_2O$ is able to bind to and photocleave DNA ($K_b = 4.6x10^2\ M^{-1}$) in the presence of electron acceptors such as 3-cyano-1-methylpyridinium tetrafluoroborate in its excited state due to the generation of the mixed valence cation $[Rh_2(\mu\text{-}O_2CCH_3)_4]^+$.

Follow-up studies by us involved the incorporation of electron accepting diimine ligands directly into the scaffold of the dirhodium core; these include dpq (dipyrido[3,2-

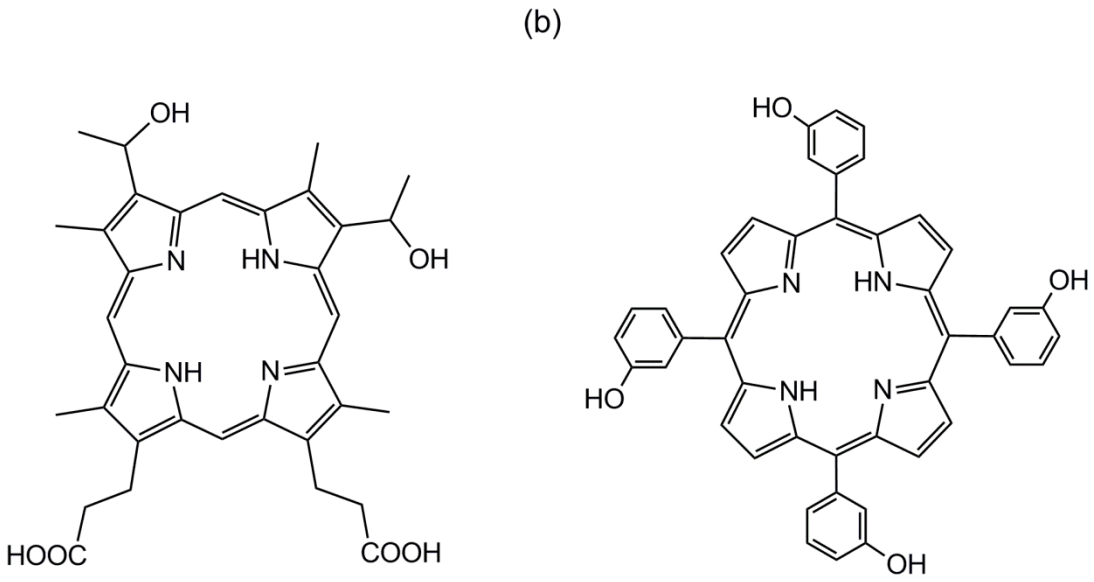

Figure 1.5 Chemical structures of commonly used organic photosensitizers for the generation of $^1O_2$.

f:2',3'-h]-quinoxaline), dppz (dipyrido[3,2-a:2',3'-c]phenazine) and dppn ((benzo[i]dipyrido[3,2-a:2',3'-h] quinoxaline) ligands. For example, the compounds *cis*-$[Rh_2(\mu\text{-}O_2CCH_3)_2(dppz)(\eta^1\text{-}O_2CCH_3)(CH_3OH)]^+$ and *cis*-$[Rh_2(\mu\text{-}O_2CCH_3)_2(dppz)_2]^{2+}$ cause direct pUC18 plasmid cleavage *in vitro* upon the irradiation with visible light (λ_{irr} > 395 nm, 15 min), resulting in the formation of nicked circular DNA (Figure 1.6).[45-47] One advantage afforded by the aforementioned complexes as compared to the commonly used organic photosensitizers is that the photocleavage of DNA occurs in the absence of O_2. In addition, cell studies showed a 3.4-fold increase of the cytotoxicity for *cis*-$[Rh_2(\mu\text{-}O_2CCH_3)_2(dppz)_2]^{2+}$ towards human skin cells (Hs-27) upon irradiation (with 400-700 nm light for 30 min). Moreover, the series of dirhodium-dppn complexes, *e.g. cis*-$[Rh_2(\mu\text{-}O_2CCH_3)_2(dppz)(dppn)]^{2+}$ and *cis*-$[Rh_2(\mu\text{-}O_2CCH_3)_2(dppn)_2]^{2+}$ were reported to

exhibit a 21- and 24- fold increase of cytotoxicity towards Hs-27 human skin fibroblasts upon irradiation with visible light (λ_{irr} > 375 nm, 30 min) respectively as compared to their activities in the dark.[48]

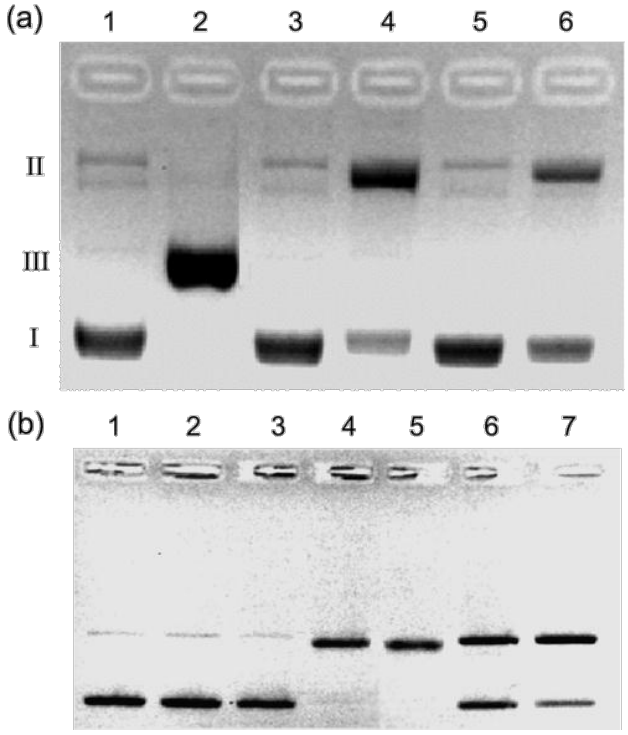

Figure 1.6 Ethidium bromide stained agarose gels (2%) of 100 μM pUC18 plasmid in the presence of 20 μM *cis*-$[Rh_2(\mu\text{-}O_2CCH_3)_2(dppz)_2]^{2+}$ in 5 mM Tris, 50 mM NaCl (pH = 7.5) buffer solution irradiated with λ_{irr} > 395 nm light: (a) lane 1, plasmid only, dark; lane 2, plasmid + SmaI; lane 3, plasmid + **1**, dark; lane 4, plasmid + **1**, irr 15 min; lane 5, plasmid + compound, dark; lane 6, plasmid + compound, irr for 15 min; (b) lane 1, plasmid only, dark; lane 2, plasmid only, irr for 20 min; lane 3, plasmid + compound, dark; lane 4, plasmid + compound, irr for 20 min, air; lane 5, plasmid + compound, irr for 20 min, 50% D_2O; lane 6, plasmid + compound, irr for 20 min, under N_2 ; lane 7, plasmid + compound, irr for 20 min, freeze-pump-thaw.

Another important partial paddlewheel dirhodium (II,II) complex with excellent potential as a PDT agent is depicted in Figure 1.3a, namely *cis*-$[Rh_2(\mu\text{-}O_2CCH_3)_2(CH_3CN)_6][BF_4]_2$.[8] Irradiation of this compound with visible light (400-700 nm) for 30 minutes induced cell damage towards the Hs-27 human skin cells with LC_{50} values decreasing from 410 ± 9 to 12 ± 2μM. The 34-fold increase of toxicity upon irradiation is attributed to the generation of the photoactive species *cis*-$[Rh_2(\mu\text{-}O_2CCH_3)_2(CH_3CN)_2(H_2O)_4]^{2+}$, which binds to double-stranded DNA (ds-DNA) as evidenced by the gel mobility studies shown in Figure 1.7. The generation of this active species occurs via a one-photon process, leading to the initial photosubstitution of one eq CH_3CN ligand, followed by the loss of a second eq CH_3CN ligand bound to the same metal center in a dark reaction.[9] Time-dependent Density Functional Theory (TD-DFT) calculations for three different isomers of *cis*-$[Rh_2(\mu\text{-}O_2CCH_3)_2(CH_3CN)_2(H_2O)_4]^{2+}$ were performed, indicating the charge-transfer process in the excited states involving placing electron density onto the σ* molecular orbital between Rh and the eq CH_3CN ligands. This explains the facile dissociation of two eq CH_3CN ligands upon irradiation. The quantum yield for this exchange process is also dependent on the power of the light used during the photolysis experiment, which is characteristic of the excited states of transition metal complexes. Of even greater interest, the increase of cytotoxicity is also independent of O_2.

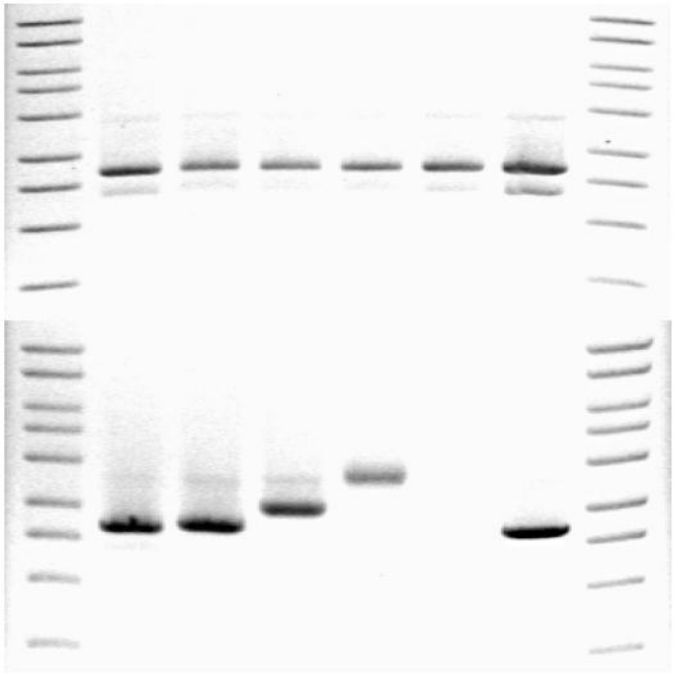

Figure 1.7 Imaged ethidium bromide stained agarose gel of 50 μM linearized pUC18 plasmid (10 mM phosphate, pH = 7.5) in the presence of various concentrations of *cis*-$[Rh_2(\mu\text{-}O_2CCH_3)_2(CH_3CN)_6][BF_4]_2$ (a) irradiated ($\lambda > 455$ nm) and (b) incubated in the dark at 25 °C for 20 min; lanes 1 and 8: DNA molecular weight standard (1kb, Sigma); lanes 2 and 7: linearized plasmid alone; lanes 3-6: [DNA bp]/[complex]) 100, 20, 10, 5.

Photocatalysis for H_2O reduction

The environmental issues and impending energy crisis arising from the rapid consumption of traditional fossil fuels has led to an upsurgence in research aimed at developing clean and renewable energy resources.[49] Utilization of abundant sunlight is an attractive alternative solution to these problems but one major challenge lies in its storage for further use.[50-51] One simple and effective way is to convert it into chemical bonds, such as the photocatalytic reduction of H_2O to produce H_2 as a clean fuel. Nature provides elegant catalytic systems for this purpose in the form of hydrogenases whose active sites are composed of dinuclear thiolate bridged nickel and/or iron complexes with ancillary CO and CN^- ligands.[52] Their instability under ambient conditions[53, 54] requires further development using more stable coordination complexes.

The photocatalytic systems for H_2O reduction studied to date are typically composed of multiple parts: a photosensitizer to harvest photons, a sacrificial electron donor to provide the electron source, the photocatalyst, and a redox-active electron mediator couple to effect electron transfer between the photosensitizer and the photocatalyst under most conditions.[55] The commonly used photosensitizers include complexes of Ru(II),[56] Pt(II),[57, 58] Re(I),[59,60] Ir(III)[61] as well as some newly reported Cu(I) complexes.[62] The catalysts used with these sensitizers are generally based on Co(II),[63] Ni(II),[64] Mo(III),[65] and Fe(II).[66] These systems, however, require further improvement since the additional charge-transfer step between the photosensitizer and the catalysts reduces the efficiency of the H^+ reduction process.

Two different strategies have been developed to address this issue. The first one is the incorporation of the photosensitizer directly into the water reduction catalyst. One typical example in this category is the tethering of a Ir(III) photosensitizer to the cobaloxime catalyst (Figure 1.8), leading to a turnover number (TON) of 210 after 15 h irradiation (TOF = 42 h^{-1}) for the catalytic system (600 equivalents of Et_3N as sacrificial electron donor and 600 equivalents of Et_3NH^+ as the proton source).[67] This result represents a better performance as compared to a TON of 160 under the same conditions for the multicomponent system.

Another strategy is to design transition metal complexes that can act as both a photosensitizer and a H^+ reduction catalyst, such as $LRh(0)_2(dfpma)_3L$ or the mixed-valence compound $LRh(0)Rh(II)(dfpma)_3X_2$ (Figure 1.9a) (dfpma = $MeN(PF_2)_2$, L = CO, PR_3, CNR, X = Cl, Br) studied by Nocera and coworkers.[68-70] Important progress has been made by the same group of researchers, including the design of complexes with more oxidizing dimetal centers, such as the homobimetallic bioctahedral d^7–d^7 complex $Pt_2(III,III)(tfepma)_2Cl_6$ (tfepma = $MeN[P(OCH_2CF_3)_2]_2$) (Figure 1.9b) which photoeliminates Cl_2 in the excited state. The quantum yield for the bis-platinum complex reaches 38% as compared to a quantum yield of < 1% for the aforementioned dirhodium complexes.[71]

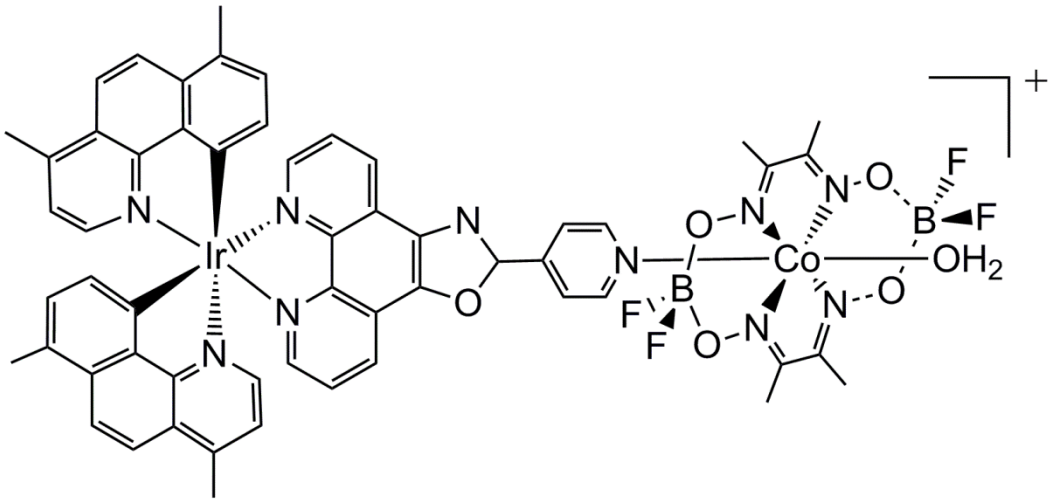

Figure 1.8 Chemical structure of the assembly of an Ir(III) photosensitizer with the Co(II) catalyst.

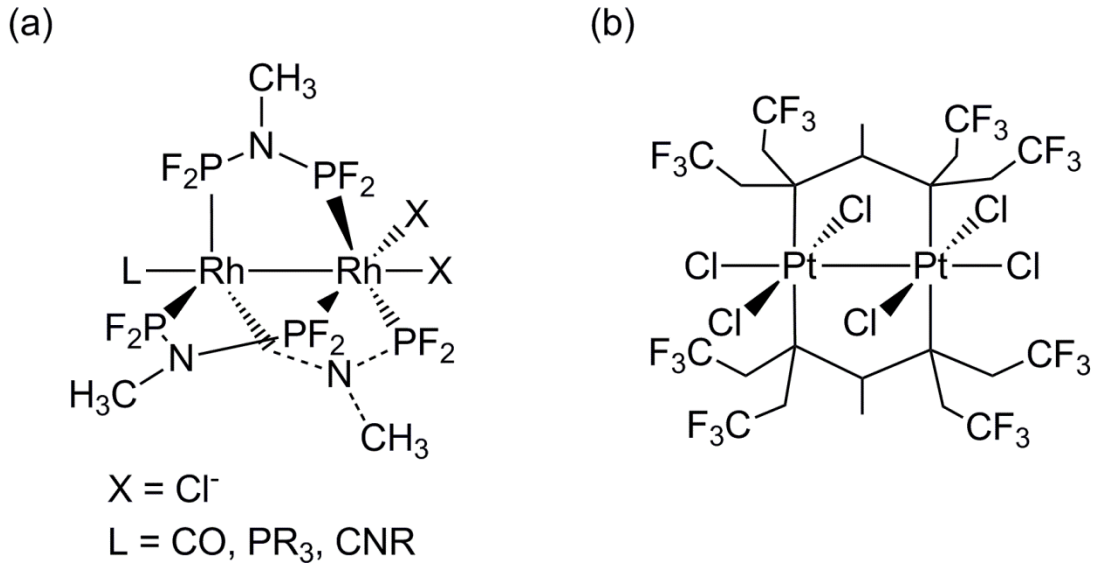

Figure 1.9 Structures of Rh and Pt catalysts for H_2 generation.

CHAPTER II

COMPREHENSIVE INVESTIGATION OF A FAMILY OF UNUSUAL PARTIAL PADDLEWHEEL DIRHODIUM ISOCYANIDE COMPLEXES*

Introduction

Dirhodium complexes are important members of the large family of metal-metal bonded compounds. One central issue for research pertaining to dirhodium complexes is the modification of the equatorial ligands to tune properties. For example, *cis*-$[Rh_2(DTolF)_2(O_2CCF_3)_2]\bullet 2H_2O$ ($[DTolF]^-$ = p-ditolylformamidinate) exhibits comparable anticancer activity to the widely used chemotherapy drug cisplatin but with reduced toxicities,[72] and dirhodium complexes with orthometalated phosphines and other N,O-donor type bridging groups are excellent catalysts for enantioselective C-H insertion reactions of α-diazo compounds via metallocarbene intermediates.[1,2,73] In a similar vein, the progressive replacement of the acetate groups by the more electron-rich acetamidate ligands in the series of $Rh_2(O_2CCH_3)_{4-n}(HNCOCH_3)_n$ (n = 1-4) increases the electron density on the dirhodium core and thus raises the energy of the HOMO orbital rendering the substituted derivatives better electron donors than $Rh_2(O_2CCH_3)_4$.[74,75] In fact, $Rh_2(HNCOCH_3)_4$, $Rh_2(DPhF)_4$ [76] (DPhF: N,N'-diphenylformamidinate) and $Rh_2(DTolF)_4$ form stable complexes with CO at room temperature,[77] as compared to $Rh_2(O_2CCH_3)_4(CO)_2$ which can be isolated only at low temperatures.[22] Of special interest in this vein is that a dirhodium compound with two orthometalated phosphine

*Reprinted with permission from "Unprecedented partial paddlewheel dirhodium methyl isocyanide compounds with unusual structural and electronic properties: a comprehensive experimental and theoretical study" by Zhanyong Li, Helen T. Chifotides, and Kim R. Dunbar, 2013. Chem. Sci., 4, 4470-4485, Copyright [2013] by The Royal Society of Chemistry (RSC). http://pubs.rsc.org/en/content/articlelanding/2013/sc/c3sc51641e#!divCitation

groups has been recently applied as a sensitive and selective chromogenic CO sensor.[19,20] These phosphine ligands render the dirhodium unit more electron-rich, leading to enhanced π-backbonding to the CO ligand.[78-80]

Of specific relevance to the present study is the use of isocyanide ligands in transition metal chemistry.[81] Reports of Rh_2(II,II) metal-metal bonded isocyanide complexes are quite scarce,[82,83] however, due to the ease of reduction to Rh(I) species, and, in the case of other metal-metal bonded dimetallic cores such as Cr_2(II,II), Mo_2(II,II), W_2(II,II) and Re_2(III,III), cleavage of the dimetal unit has been found to be facile.[84-88] Pioneering studies by Gray *et al*. in the late 1970s led to an exciting discovery involving dirhodium isocyanide compounds, *viz.*, oxidative addition of halogens to the Rh(I) isocyanide precursors $Rh_2[CN(CH_2)_3NC]_4^{2+}$ [89] and $[Rh_2(TMB)_4]^{2+}$, upon irradiation at 550 nm in strongly acidic HCl solutions, to form H_2 and the dirhodium(II,II) containing salts $[Rh_2[CN(CH_2)_3NC]_4Cl_2]Cl_2$ [90] and $[Rh_2(TMB)_4Cl_2][PF_6]_2$ (TMB = 2,5-di-isocyano-2,5-dimethylhexane) [91], respectively. More recently, Nocera and coworkers have made important progress in developing dirhodium-based photocatalysts bearing isocyanide ligands.[15-17] From the mechanistic studies, they found that L-Rh(0)-Rh(II)-X_2 or L-Rh(0)-Rh(0)-L complexes (L = CO, PR_3, CNR; X= Br, Cl) lead to Rh(II)-Rh(II) species, which are responsible for the photocatalytic production of H_2 or the reduction of O_2 in HX solutions.

The promising chemistry that has been reported over the years with a handful of Rh_2(II,II) isocyanide complexes with halogens in the axial positions notwithstanding,[92-100] this chemistry, especially with monodentate isocyanide ligands, remains relatively unexplored due to the challenge of preventing reduction to Rh(I) mononuclear products. In this chapter several members of an entirely new type of metal-metal bonded complex (**5**-**8**) are described which feature two *cis* strong σ-donating bridging groups *p*-ditolylformamidinate (a), *p*-difluorophenylformamidinate (b), *p*-ditolyltriazenide (c) or orthometalated phosphine (d) and methyl isocyanide ligands in the axial and the other four equatorial positions (Scheme 2.1). The isocyanide series of dirhodium complexes **5**-**8** (Scheme 2.1, L = CH_3NC) and the corresponding acetonitrile analogs **1**-**4** (Scheme 2.1, L = CH_3CN), which are synthetic precursors for the methyl isocyanide derivatives, were fully characterized by X-ray crystallography, ^1H, ^{31}P NMR, electronic and infrared spectroscopies as well as electrochemical studies. Noteworthy structural and spectroscopic features of **5**-**8** were probed in a comprehensive fashion as compared to **1**-**4**. In particular, compound **8** (Scheme 2.1, L = CH_3NC) exhibits nearly the same ax and eq Rh-C (CH_3NC) distances, which, to our knowledge, is unprecedented for dirhodium compounds. The experimental data for **1**-**8** were corroborated by DFT and TD-DFT calculations, which also unearthed notable findings that are detailed herein.

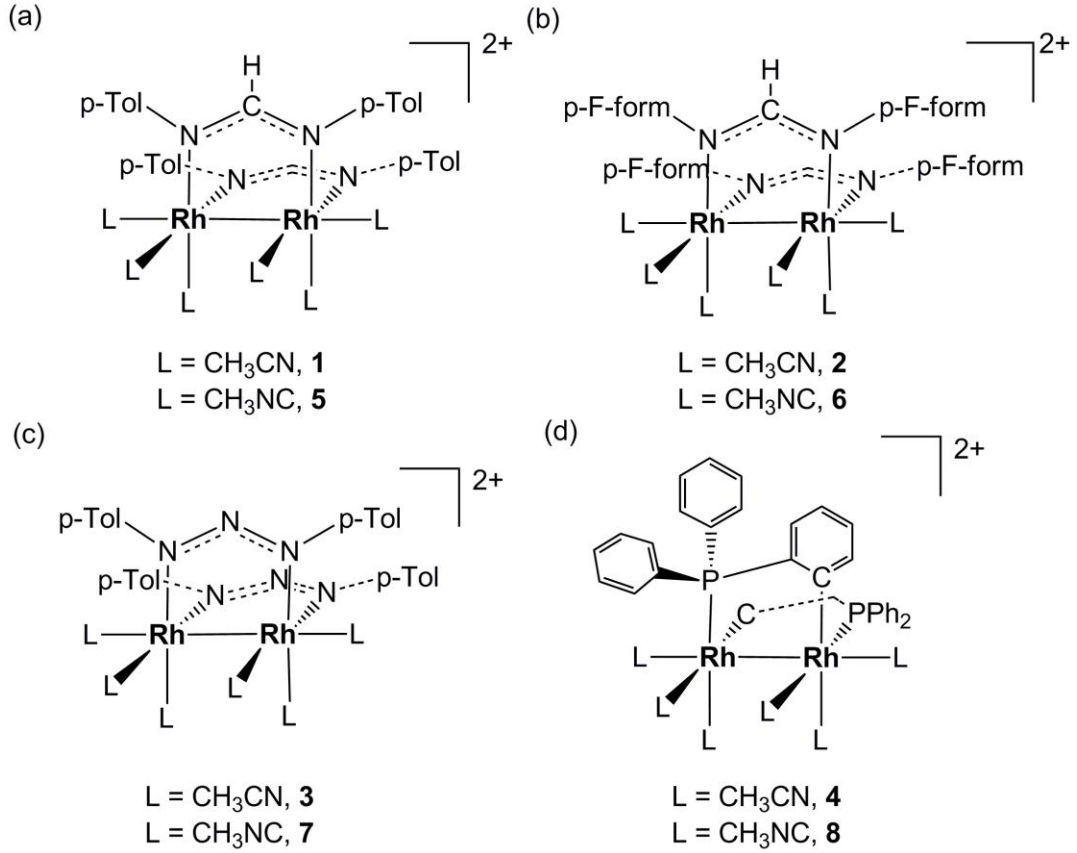

Scheme 2.1 Structural representation of partial paddlewheel dirhodium (II,II) compounds with the bridging groups (a) *p*-ditolylformamidinate (**1**, **5**), (b) *p*-difluorophenylformamidinate (**2**, **6**), (c) *p*-ditolyltriazenide (**3**, **7**) and (d) orthometalated phosphine (**4**, **8**).

Experimental section

Starting materials

The precursor $[RhCl(COD)]_2$ (COD: cycloocta-1,5-diene) was purchased from Pressure Chemicals whereas $[FeCp_2][BF_4]$ and $[RhCl(CO)_2]_2$ were purchased from Sigma-Aldrich; all reagents were used as received. Methyl isocyanide [101], [Rh(F-form)(COD)]$_2$,[102] and $[Rh(NNN)(CO)_2]_2$ and NNNH (ditolyltriazene)[103] were prepared by slightly modified published procedures. The compounds *cis*-$[Rh_2(DTolF)_2(CH_3CN)_6][BF_4]_2$ [104](**1**) and *cis*-$[Rh_2[Ph_2P(C_6H_4)]_2(CH_3CN)_6][BF_4]_2$[105] (**4**) were synthesized according to published methods. The acetonitrile solvent was pre-dried over 3 Å molecular sieves and distilled under N_2 whereas dichloromethane was pre-dried over 4 Å molecular sieves and distilled over P_2O_5 under N_2. All manipulations were conducted using standard Schlenk-line techniques unless otherwise stated. The work-up and isolation of the products, however, were conducted in air.

Preparation of *cis*-$[Rh_2(F\text{-}form)_2(CH_3CN)_6][BF_4]_2$ (**2**). A quantity of [Rh(F-form)(COD)]$_2$ (120 mg, 0.14 mmol) was added to 30 mL of CH_2Cl_2:CH_3CN (1:1 v/v) and the red/orange solution was stirred until the solid was fully dissolved. Subsequently $AgBF_4$ (106 mg, 0.55 mmol) was added to the solution which led to a gradual color change to green. The reaction solution was stirred in the dark at room temperature for 24 h and then filtered through Celite® to remove finely divided silver particles. The filtrate was evaporated to dryness and redissolved in 10 mL of CH_3CN (red solution). The addition of diethyl ether (40 mL) induced precipitation of the desired product. Yield: 75% (112 mg, 0.10 mmol). Anal. Calcd for $C_{38}H_{36}N_{10}B_2F_{12}Rh_2 \cdot 3CH_2Cl_2$: C, 36.64; N,

10.43; H, 3.15 %. Found: C, 36.67; N, 10.33; H, 3.11%. ^{1}H NMR (CD_3CN-d_3), δ (ppm): 2.53 (s, eq CH_3CN), 7.05 (m, p-difluorophenyl), 7.49 (t, NCHN, $^{3}J_{Rh-H}$ = 4 Hz).

Preparation of *cis*-$[Rh_2(NNN)_2(CH_3CN)_6][BF_4]_2$ (3). Samples of $[RhCl(CO)_2]_2$ (50 mg, 0.13 mmol) and 58 mg (0.26 mmol) of NNNH were added to dry CH_2Cl_2 (25 mL). After dissolution of the two reactants, NEt_3 (45 μL, 0.32 mmol) was added to the solution which was accompanied by an instantaneous color change from yellow to red. The reaction solution was stirred under N_2 for 20 minutes and evaporated to dryness. The product $[Rh(NNN)(CO)_2]_2$ was extracted with hexanes (3 x 10 mL). The three extracts of hexanes were combined, reduced to dryness and re-dissolved in dry CH_3CN (30 mL). To this solution was added $[FeCp_2][BF_4]$ (70 mg, 0.26 mmol) and the mixture was refluxed for 48 h. The solution was filtered and concentrated to 5 mL and diethyl ether was added to precipitate the product. Yield: 81 mg, 60%. X-ray quality crystals were obtained by slow diffusion of diethyl ether into an acetonitrile solution of the product. Anal. Calcd for $C_{40}H_{46}N_{12}B_2F_8Rh_2 \bullet 5CH_2Cl_2 \bullet H_2O$: C, 35.60; N, 11.08; H, 3.85%. Found: C, 35.71; N, 11.07; H, 3.91 %. ^{1}H NMR in (CD_3CN-d_3), δ (ppm): 2.31 (s, CH_3, tolyl), 2.52 (s, eq CH_3CN), 7.11 (m, tolyl-triazenide).

Preparation of *cis*-$[Rh_2(DTolF)_2(CNCH_3)_6][BF_4]_2$ (5). Methyl isocyanide (39 μL, 0.75 mmol) was added to a reddish/brown slurry of *cis*-$[Rh_2(DTolF)_2(CH_3CN)_6][BF_4]_2$ (80 mg, 0.075 mmol) in CH_3CN (10 mL) which led to a color change to yellow. The solution was stirred under N_2 for 8 h, concentrated to 5 mL and then treated with an excess of diethyl ether to induce precipitation of the product. The filtered solid was washed with diethyl ether (3 x 5 mL) and dried overnight under vacuum. Yield 83% (66 mg, 0.062

mmol). X-ray quality crystals were obtained by slow diffusion of diethyl ether into a solution of the product in acetonitrile. Anal. Calcd for $C_{42}H_{48}N_{10}B_2F_8Rh_2$•$CH_3CN$•$CH_2Cl_2$: C, 45.07; N, 12.86; H, 4.46 %. Found: C, 45.11; N, 12.75; H, 4.26 %. ^{1}H NMR (CD_3CN-d_3) δ (ppm): 2.28 (s, tolyl CH_3), 2.60 (s, ax CH_3NC), 3.67 (s, eq CH_3NC), 7.02 (m, tolyl), 7.86 (t, $^3J_{Rh-H}$ = 3 Hz, NCHN). ESI-MS: *m/z*: 408.02 for $[Rh_2(DTolF)_2(CNCH_3)_3]^{2+}$.

Preparation of *cis*-[Rh$_2$(F-form)$_2$(CNCH$_3$)$_6$][BF$_4$]$_2$ (6). Methyl isocyanide (48 μL, 0.92 mmol) was added to a reddish/brown slurry of *cis*-$[Rh_2(F\text{-form})_2(CH_3CN)_6][BF_4]_2$ (100 mg, 0.092 mmol) in CH_3CN (10 mL) which led to the instantaneous formation of a yellow solution which was stirred under N_2 for 12 h to complete the reaction and then concentrated to 5 mL. An excess volume of diethyl ether was added to the solution to induce precipitation of **6**. The resulting solid was washed with diethyl ether (3 x 5 mL) and dried overnight under vacuum to afford the product. Yield 81% (81 mg, 0.074 mmol). X-ray quality crystals were obtained by slow diffusion of diethyl ether into a solution of the product in acetonitrile. Anal. Calcd for $C_{38}H_{36}N_{10}B_2F_{12}Rh_2$•$2H_2O$: C, 40.56; N, 12.46; H, 3.59 %. Found: C, 40.60; N, 12.06; H, 3.19 %. ^{1}H NMR (CD_3CN-d_3) δ (ppm): 2.74 (s, ax CH_3NC), 3.68 (s, eq CH_3NC), 7.04 (m, p-difluorophenyl), 7.84 (t, $^3J_{Rh-H}$ = 3 Hz, NCHN). ESI-MS: 436.54 for $[Rh_2(F\text{-form})_2(CNCH_3)_4]^{2+}$.

Preparation of *cis*-[Rh$_2$(NNN)$_2$(CNCH$_3$)$_6$][BF$_4$]$_2$ (7). The addition of methyl isocyanide (38 μL, 0.73 mmol) to a reddish/brown slurry of *cis*-$[Rh_2(NNN)_2(CH_3CN)_6][BF_4]_2$ (78 mg, 0.073 mmol) in CH_3CN (10 mL) led to an immediate color change to yellow. The solution was stirred under N_2 for 12 h and

concentrated to 5 mL. Excess diethyl ether was added to the solution to induce precipitation of the product which was collected, washed with diethyl ether (3 x 5 mL) and dried overnight under vacuum to afford **7**. Yield 85% **(**66 mg, 0.061 mmol). X-ray quality crystals were obtained by slow diffusion of diethyl ether into a solution of the product in acetonitrile. Anal. Calcd for $C_{46}H_{55}B_2F_8N_{15}Rh_2 \cdot 6CH_2Cl_2$: C, 36.56; N 12.31; H, 3.96 %. Found: C, 36.34; N, 12.44; H, 4.13 %. ^{1}H NMR (CD_3CN-d_3) δ (ppm): 2.31 (s, tolyl CH_3), 2.73 (s, ax CH_3NC), 3.66 (s, eq CH_3NC), 7.10 (m, tolyl-triazenide). ESI-MS: $[Rh_2(NNN)_2(CNCH_3)_3]^{2+}$, 408.02.

Preparation of *cis*-$[Rh_2[Ph_2P(C_6H_4)]_2(CNCH_3)_6][BF_4]_2$ (8). Methyl isocyanide (45 μL, 0.86 mmol) was added to a solution of *cis*-$[Rh_2[Ph_2P(C_6H_4)]_2(CH_3CN)_6][BF_4]_2$ (85 mg, 0.074 mmol) in CH_3CN (5 mL) which led to a color change from reddish-yellow to light yellow. The reaction mixture was stirred for 30 min under N_2 and treated with diethyl ether which led to precipitation of the desired product Yield 88 % (75 mg, 0.65 mmol). X-ray quality crystals were obtained by slow diffusion of diethyl ether into an acetonitrile solution of the product in the dark. $C_{48}H_{46}N_6B_2F_8P_2Rh_2 \cdot 2H_2O$: C, 48.64; N 7.10; H, 4.26 %. Found: C, 48.78; N, 7.22; H, 4.07 %. ^{1}H NMR (CD_3CN-d_3) δ (ppm): 2.50 (s, ax CH_3NC), 3.27 (s, eq CH_3NC, *trans* to C), 3.48 (s, eq CH_3NC, *trans* to P), 6.70-7.70 ppm (m, $Ph_2P(C_6H_4)$). ^{31}P NMR (CD_3CN-d_3) δ (ppm): 20.94 ($^1J_{Rh\text{-}P}$=101.5 Hz). ESI-MS: $\{[Rh_2[Ph_2P(C_6H_4)]_2(CNCH_3)_6][BF_4]\}^+$ 1061.16; $\{[Rh_2[Ph_2P(C_6H_4)]_2(CNCH_3)_5][BF_4]\}^+$ 1020.13; $\{[Rh_2[Ph_2P(C_6H_4)]_2(CNCH_3)_5][BF_4]\}^+$ 979.11.

Instrumentation

The ^{1}H NMR spectra were collected on a 300 MHz Varian spectrometer and the chemical shifts were referenced relative to the residual proton impurities of the deuterated solvent (CD_3CN, d_3). Electronic absorption spectra were obtained on a Shimadzu UV-1601PC spectrophotometer. Infrared spectra were recorded as Nujol mulls between KBr plates with a Nicolet Nexus 470 FT-IR spectrometer. Elemental analyses were performed by Atlantic Microlab, Inc. Electrospray mass spectral data were obtained in the Laboratory for Biological Mass Spectrometry at Texas A&M University using a PE Sciex (Concord, Ontario, Canada) API Qstar Pulsar with an Ionwerks time-to-digital converter, TDCx4, for data recording. Electrochemical data were collected using a CH Instruments analyzer in dry CH_3CN. The working electrode was a BAS Pt disk electrode, the reference electrode was Ag/AgCl, and the counter electrode was a Pt wire. X-ray data sets for **2**, **3**, **5**-**8** were collected on a Bruker CCD APEX diffractometer with graphite monochromated Mo Kα radiation (λ = 0.71073 Å).

Methods

Cyclic voltammetric measurements were performed at 298 K in CH_3CN with 0.1 M tetra-*n*-butylammonium hexafluorophosphate ([n-Bu_4N][PF_6]) as the supporting electrolyte. The $E_{1/2}$ values were referenced to the Ag/AgCl electrode without correction for the junction potentials [$E_{1/2} = (E_{p,a} + E_{p,c})/2$]. The $FeCp_2/[FeCp_2]^+$ couple is located at $E_{1/2}$ = + 0.45 V in CH_3CN at the same conditions used for the compounds.

The molecular and electronic structure calculations were performed by Density Functional Theory (DFT) methods using the Gaussian09 (G09) program package.[106] The

MPW1PW91 correlation and exchange functionals[107-109] were used with the Stuttgart RSC 1997 Electron Core Potential (ECP)[110] basis set for the Rh atoms and the 6-31G (d') basis set for the C, N, F, H atoms.[111,112] Geometric parameters were taken from the crystal structures without the $[BF_4]^-$ anions, and were used as the starting point for the simulations, followed by frequency calculations to evaluate the full optimization. Time-Dependent Density Functional Theory (TD-DFT)[113-119] calculations were conducted in the gas phase as well as using the polarized continuum model (PCM) with CH_3CN as the solvent,[120,121] based on the optimized singlet ground state geometry. The first twenty lowest singlet-to-singlet excitations were included for both the gas phase and solvation models in the singlet state calculations. The molecular orbitals were plotted with the graphic software 'agui' [122] with an iso-value = 0.04. Detailed analysis of the compositions of the orbitals was obtained through the Chemissian program http://www.chemissian.com.

A hemisphere of crystallographic data was collected by a combination of four sets of exposure. Each set had a different φ angle for the crystals, and each exposure covered 0.3° in ω. The exposure time for **5-8** was 10 s whereas for **2**, **3**, it was 20 s. Crystal decay was monitored by analyzing duplicate reflections and was found to be less than 1%, therefore no decay correction was applied. The frames were integrated with the Bruker AXS SAINT Software package,[123] and the data were corrected for absorption using the SADABS program in the same software package.[124] The structures were solved by direct methods and refined by using X-SEED,[125-127] a graphical interface to the SHELX97 suite

of programs.[128] In the final cycles of the refinement, all atoms except for hydrogen were refined anisotropically.

Results

Synthesis

Compounds **1**-**3** were prepared by oxidation of Rh(I) starting materials; **1** and **2** were synthesized by similar procedures whereas [Rh(F-form)(COD)]$_2$, which is a precursor to **2**, was synthesized according to a method similar to [Rh(DTolF)(COD)]$_2$. Subsequently, [Rh(F-form)(COD)]$_2$ was reacted with an excess of $AgBF_4$ to afford **2** (Eq. 2.1):

$$[Rh(F\text{-}form)(COD)]_2 \xrightarrow[CH_2Cl_2/CH_3CN,\ r.t.]{AgBF_4} \underset{\mathbf{2}}{cis\text{-}[Rh_2(F\text{-}form)_2(CH_3CN)_6][BF_4]_2} \qquad \text{Eq. 2.1}$$

The compound [Rh(NNN)(CO)$_2$]$_2$, which is a precursor to **3**, was prepared by a slightly modified published procedure. As shown in Eq. 2.2, a slight excess of [FeCp$_2$][BF$_4$] was used to oxidize Rh(I) to Rh(II) to afford **3** and ferrocene, which was removed by excess amount of diethyl ether.

$$[Rh(NNN)(CO)_2]_2 \xrightarrow[CH_3CN]{[Fe(Cp)_2][BF_4]} \underset{\mathbf{3}}{cis\text{-}[Rh_2(NNN)_2(CH_3CN)_6][BF_4]_2} \qquad \text{Eq. 2.2}$$

The corresponding methyl isocyanide analogs **5**-**8** were prepared by substitution of the monodentate acetonitrile ligands with methyl isocyanide in **1**-**4**. An excess of CH_3NC was used during the syntheses of the methyl isocyanide analogs **5**-**8**. The general synthetic route for **5**-**7** is depicted in Eq. 2.3:

$$cis\text{-}[Rh_2(N\text{-}N)_2(CH_3CN)_6][BF_4]_2 \xrightarrow[CH_3CN,\ r.t.]{10\ equ.\ CH_3NC} cis\text{-}[Rh_2(N\text{-}N)_2(CNCH_3)_6][BF_4]_2 \qquad \text{Eq. 2.3}$$

A characteristic color change occurs from reddish/brown to light yellow upon addition of methyl isocyanide to solutions of **1**-**3** to afford **5**-**7**, respectively. Unlike compounds **5**-**7**, prolonged stirring of **8** in CH_3CN leads to product decomposition as evidenced by ^{1}H-NMR spectroscopy (*vide infra*) therefore **8** was prepared by stirring **4** under N_2 for 30 min only, in the presence of CH_3NC.

X-ray crystallographic studies

The crystal parameters and information pertaining to the data collection and refinement for **2**, **3** and **5**-**8** are summarized in Table 2.1.

***cis*-$[Rh_2(F\text{-}form)_2(CH_3CN)_6)][BF_4]_2 \bullet Et_2O$ (2•Et_2O), (2).** A thermal ellipsoid plot of the cationic unit in **2** is shown in Figure 2.1. The dirhodium unit is bridged by two $[F\text{-}form]^-$ ligands in a *cis* arrangement with six CH_3CN ligands occupying the remaining Rh(II) coordination sites. The Rh-Rh bond distance is 2.571(1) Å which is comparable to **1** and the compounds *cis*-$[Rh_2(DTolF)_2(bpy)(CH_3CN)_3][BF_4]_2$ and *cis*-$[Rh_2(DTolF)_2(bpy)_2(CH_3CN)][BF_4]_2$.[129] The Rh-N $[F\text{-}form]^-$ and Rh-N (eq CH_3CN) distances are in the ranges 2.024(4)-2.052(5) and 2.032(5)-2.043(5) Å, respectively. The previous distances are similar to **1** but longer than the corresponding distances in *cis*-$[Rh_2(O_2CCH_3)_2(CH_3CN)_6][BF_4]_2$.[130] As in the case of **1** and *cis*-$[Ir_2(DTolF)_2(CH_3CN)_6][BF_4]_2$,[131] a splaying of the four eq CH_3CN ligands occurs. The $[F\text{-}form]^-$ groups are twisted by 18.0(2)° from the eclipsed conformation and the eq CH_3CN groups are twisted by 22.8(2)° due to the steric constraints imposed by the bridging ligands.

Table 2.1 Crystal and structural refinement data for **2**•Et_2O, **3**, **5-8**.

	2•Et_2O	**3**	**5**
Formula	$C_{42}H_{46}N_{10}F_{12}B_2ORh_2$	$C_{40}H_{46}N_{12}B_2F_8Rh_2$	$C_{42}H_{48}N_{10}B_2F_8Rh_2$
Formula weight	1162.31	1074.30	1072.33
Temperature/ K	110(2)	110(2)	110(2)
Crystal system	Monoclinic	Orthorhombic	Orthorhombic
Space group	$P2_1/c$	Pbca	Pbca
a, b, c/ Å	11.042(2), 32.589(7), 14.243(3)	14.135(3), 21.331(4), 31.170(6)	14.338(3), 21.619(4), 31.136(6)
α, β, γ/ º	90, 100.66(3), 90	90, 90, 90	90, 90, 90
V/ Å^3	5036.5(17)	9399(3)	9651(3)
Crystal description, color	red plate	red block	yellow plate
Crystal size/ mm^3	0.04 x 0.08 x 0.10	0.08 x 0.10 x 0.13	0.02 x 0.06 x 0.25
Z	4	8	8
$D_{calc.}$/g/cm^3	1.5314	1.5183	1.4758
2θ range for data collection/º	53.62	41.63	57.24
Diffraction limits (h, k, l)	$-13 \le h \le 13$ $-41 \le k \le 41$ $-17 \le l \le 17$	$-14 \le h \le 14$ $-21 \le k \le 21$ $-31 \le l \le 31$	$-18 \le h \le 19$ $-29 \le k \le 28$ $-41 \le l \le 39$
Reflections measured	54314	57506	105468
Independent reflections	R(int) = 0.0635	R(int) = 0.0248	R(int) = 0.0301
Completeness to θ max/%	99.3	99.9	95.4
Data/restraints/parameters	10690/0/630	4201 /12/588	11808/0/587
R_1,[a] wR_2[b] [$I > 2\sigma(I)$]	R = 0.0587, wR = 0.1314	R = 0.059, wR = 0.1570	R = 0.0262, wR = 0.0590
R_1,[a] wR_2[b] (all data)	R = 0.0852, wR = 0.1435	R = 0.0677, wR = 0.1719	R = 0.0374, wR = 0.0660
Goodness-of-fit parameter (all data)[c](F^2)	1.052	1.193	1.059
Largest diff. peak and hole/ e.Å^{-3}	0.91/-0.93	0.88/-0.65	0.83/-0.62

Table 2.1 Continued

	6•Et_2O	**7**	**8**
Formula	$C_{42}H_{46}N_{10}F_{12}B_2ORh_2$	$C_{40}H_{46}N_{12}B_2F_8Rh_2$	$C_{96}H_{92}N_{12}P_4B_4F_{16}Rh_4$
Formula weight	1162.31	1074.30	2296.60
Temperature/ K	110(2)	110(2)	110(2)
Crystal system	Monoclinic	Orthorhombic	Monoclinic
Space group	$P2_1/c$	$Pbca$	$P2_1/c$
a, b, c/ Å	11.110(2), 31.777(6), 14.195(3)	14.126(3), 21.399(4), 31.434(6)	22.272(4), 22.161(4), 22.409(4)
α, β, γ/ °	90, 101.13(3), 90	90, 90, 90	90, 119.43(3), 90
V/ Å^3	4917.3(17)	9502(3)	9633(3)
Crystal description, color	Yellow block	Yellow plate	Yellow block
Crystal size/ mm^3	0.05 x 0.10 x 0.11	0.13 x 0.10 x 0.03	0.16 x 0.12 x 0.11
Z	4	8	4
$D_{calc.}$/ g/cm^3	1.5698	1.5017	1.5833
2θ range for data collection/°	50.02	49.46	54.64
Diffraction limits (h, k, l)	$-13 \le h \le 13$ $-37 \le k \le 37$ $-16 \le l \le 16$	$-16 \le h \le 16$ $-25 \le k \le 25$ $-36 \le l \le 36$	$-28 \le h \le 28$ $-28 \le k \le 28$ $-28 \le l \le 28$
Reflections measured	44350	83459	107654
Independent reflections	R(int) = 0.0359	R(int) = 0.0885	R(int) = 0.0443
Completeness to θ max/%	100	100	99.5
Data/restraints/parameters	8664/ 0/630	8110/0/587	21603/0/1256
R_1,[a] wR_2[b] [$I > 2\sigma(I)$]	R = 0.0374, wR = 0.0914	R = 0.0443, wR = 0.1010	R = 0.0328, wR = 0.0899
R_1,[a] wR_2[b] (all data)	R = 0.0480, wR = 0.0981	R = 0.0680, wR = 0.1133	R = 0.0459, wR = 0.0978
Goodness-of-fit parameter (all data)[c]	1.038	1.019	1.060
Largest diff. peak and hole/ e.Å^{-3}	1.08/-0.66	1.08/-1.09	0.62/-0.78

[a] $R = \sum \big| |F_o| - |F_c| \big| / \sum |F_o|$. [b] $wR = \{\sum[w(F_o^2 - F_c^2)^2] / \sum w(F_o^2)^2]\}^{1/2}$. [c] Goodness-of-fit = $\{\sum[w(F_o^2 - F_c^2)^2]/(n-p)\}^{1/2}$, where n is the number of reflections and p is the total number of parameters refined.

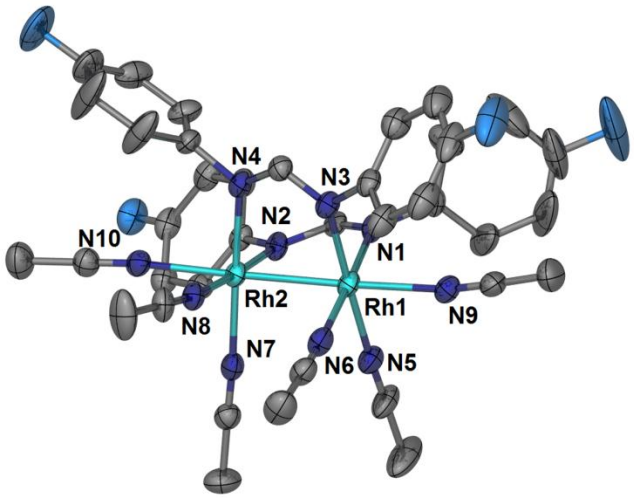

Figure 2.1 Thermal ellipsoid plot for the cationic unit in **2** at the 50% probability level.

***cis*-[Rh$_2$(NNN)$_2$(CH$_3$CN)$_6$][BF$_4$]$_2$, (3).** The cationic unit in **3** is shown in Figure 2.2. The Rh-Rh bond distance is 2.5135(9) Å, which is slightly shorter than the Rh-Rh distance in *cis*-[Rh$_2$(NNN)$_2$(CH$_3$CN)$_3$(bpy)][PF$_6$]$_2$ (2.534(2) Å).[132] The Rh-N (eq CH$_3$CN) bond distances are in the range 1.996(7)-2.024(6) Å and are comparable to the corresponding distances in **1**, **2** and *cis*-[Rh$_2$(NNN)$_2$(CH$_3$CN)$_3$(bpy)][PF$_6$]$_2$. The Rh-N ([NNN]$^-$) bond distances are in the range 2.011(6)-2.024(6) Å, and are slightly shorter than the corresponding ones in **1**, **2** and Rh-N (N *trans* to eq bpy in [NNN]$^-$) and comparable to the Rh-N ([NNN]$^-$, *trans* to eq CH$_3$CN) in *cis*-[Rh$_2$(NNN)$_2$(CH$_3$CN)$_3$(bpy)][PF$_6$]$_2$. The eq CH$_3$CN groups and the bridging ligands ([NNN]$^-$) are twisted by ~23.0° and ~20.3°, respectively, from the eclipsed configuration.

***cis*-[Rh$_2$(DTolF)$_2$(CNCH$_3$)$_6$][BF$_4$]$_2$, (5).** Compound **5** crystallizes in the space group *P*bca. The cationic unit is shown in Figure 2.3. The coordination sphere of the Rh(II)

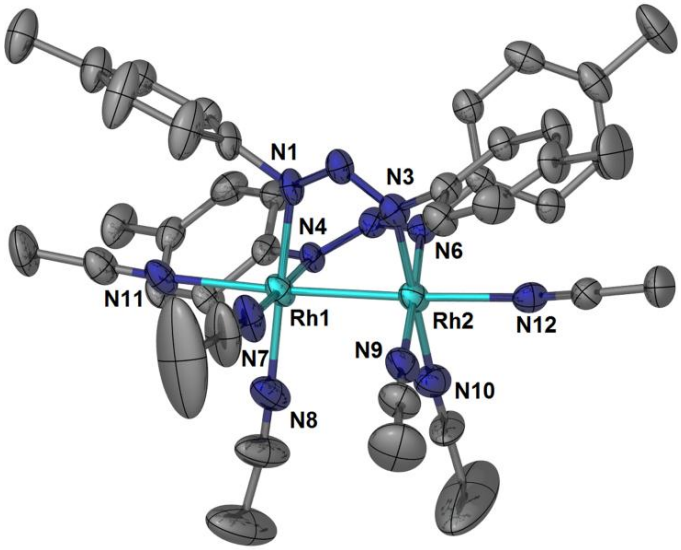

Figure 2.2 Thermal ellipsoid plot for the cationic unit in **3** at the 50% probability level.

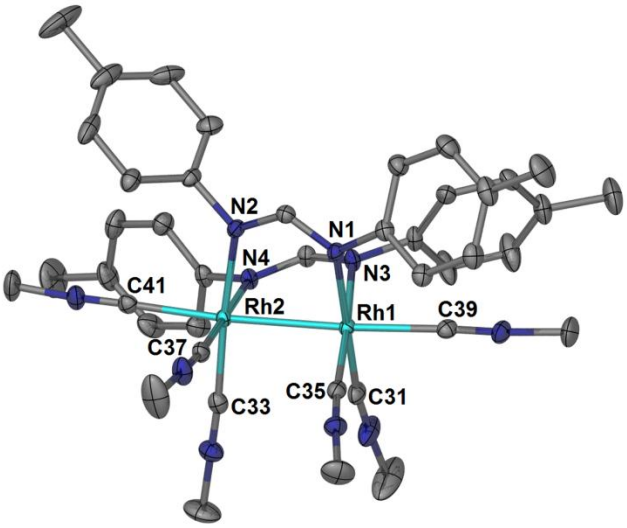

Figure 2.3 Thermal ellipsoid plot for the cationic unit in **5** at the 50% probability level.

atoms is similar to those in **1**-**3**, but with all the CH_3CN ligands being substituted by CH_3NC. The Rh-Rh distance is 2.6262(4) Å, *i.e.*, slightly longer than the corresponding distances in **1**-**3** and much shorter than in $[Rh_2(p\text{-}CNC_6H_4CH_3)_8I_2][PF_6]_2$[95] and $[Rh_2[CN(CH_2)_3NC]_4Cl_2]C1_2{\bullet}8H_2O$[89], for which the Rh-Rh distances are 2.785(2) and 2.837(1) Å, respectively. The bond distances Rh-C (ax CH_3NC) in **5** (2.099(2) and 2.080(2) Å) are longer than the corresponding distance in $Rh_2(DPhF)_4(CNC_6H_5)$[82] (1.991(4) Å) and shorter than in $Rh_2(O_2CCH_3)_4{\bullet}2CNC_6H_4R$ {R = $(CH_3)_2N$, H, CF_3} wherein the Rh-C (ax) distances are 2.148(4), 2.133(3), 2.122(3) Å,[133] respectively. The Rh-C (eq CH_3NC) distances are in the range 1.935(2)-1.949(2) Å, and are comparable to the corresponding distances in $[\{Rh_2(\mu\text{-}pz)_2(I)(CN^tBu)_4\}_2(\eta\text{-}I)][CF_3SO_3]$ {Rh-C (eq CN^tBu) ~ 1.896(11)-1.958(12) Å}.[97] The Rh-N ($[DTolF]^-$) bond distances range from 2.078(2) to 2.094(2) Å, and are thus longer than the corresponding ones in **1**. The dihedral angles C31-Rh1-Rh2-C33 and C35-Rh1-Rh2-C37 are 20.99(8)° and 20.48(8)°, respectively. Additionally, the angles N1-Rh1-Rh2-N2 and N3-Rh1-Rh2-N4 are 17.79(6)° and 17.97(6)°, respectively, following a similar trend as observed for **1**-**3**.

***cis*-$[Rh_2(F\text{-}form)_2(CNCH_3)_6][BF_4]_2$, (6).** Compound **6** crystallizes in the same space group as **2**, namely $P2_1/c$. The structure of the cationic unit in **6** is similar to **2** (Figure 2.4). The Rh-Rh bond distance is 2.6105(9) Å, which is ~ 0.04 Å longer than the corresponding distance in **2**. The Rh-C (ax) bond distances are 2.074(4), 2.133(4) Å, and the Rh-C(eq) bond distances are in the range 1.937(5)-1.953(4) Å, which is similar to the range in **5**. The Rh-N ($[F\text{-}form]^-$) bond distances range from 2.079(3) to 2.098(3) Å and are longer than the corresponding distances in **2.** The CH_3NC groups and the bridging

[F-form]$^-$ ligands are twisted from the eclipsed geometry by 21.6(2)°, 23.5(2)° and 18.1(1)°, 17.2(1)°, respectively.

***cis*-[Rh$_2$(NNN)$_2$(CNCH$_3$)$_6$][BF$_4$]$_2$, (7).** As in the case of **3**, complex **7** crystallizes in the space group *P*bca. The thermal ellipsoid plot of the cationic unit is shown in Figure 2.5. The Rh-Rh bond distance is 2.5852(6) Å which is ~ 0.07 Å longer than that in **3**, following a similar trend as observed for **1** *vs.* **5** and **2** *vs.* **6**. The Rh-C (The Rh-C (ax CH_3NC 2.089(4) and 2.093(4) Å), and Rh-C (eq CH_3NC 1.940(5)-1.950(5) Å) are in a similar range as the corresponding distances in **5** and **6**. The Rh-N [NNN]$^-$ bond distances range from 2.070(3) to 2.089(3) Å, which is ~0.06 Å longer than the corresponding Rh-N distances in **3**. The four eq CH_3NC ligands are twisted by 21.8(2)° and 21.0(2)° and the two [NNN]$^-$ ligands by 18.9(1)° and 19.8(1)° from the eclipsed conformation.

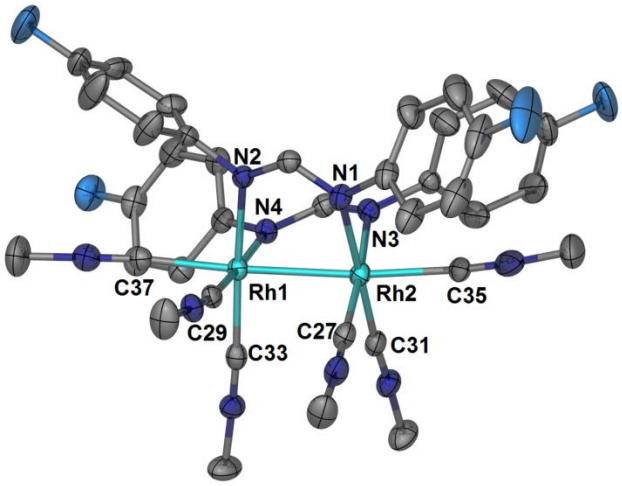

Figure 2.4 Thermal ellipsoid plot for the cationic unit in **6** at the 50% probability level.

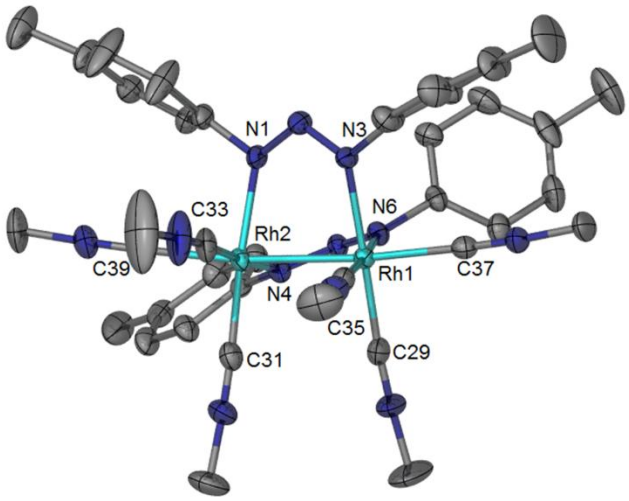

Figure 2.5 Thermal ellipsoid plot for the cationic unit in **7** at the 50% probability level.

***cis*-[Rh_2[$Ph_2P(C_6H_4)$]$_2$($CNCH_3$)$_6$][BF_4]$_2$, (8).** Compound **8** crystallizes in the centrosymmetric monoclinic space group $P2_1/c$ with two independent dimetal complexes in one asymmetric unit and two isomers **8**-*R* and **8**-*S*, as was found for compound **4**. The cationic units of the two isomers **8**-*R* and **8**-*S* are shown in Figure 2.6. As is the case of **4**, both the *R* and *S* isomers in **8** exhibit similar structural parameters. The Rh-Rh bond distances in **8**-*S* and **8**-*R* are 2.7682(6) and 2.766(1) Å, respectively, *i.e.*, longer than the corresponding distances in **4** (2.655(1) and 2.656(1) Å) and **5**-**7**.

It is important to note that, to our initial surprise, **8** exhibits very similar distances for the ax and eq Rh-C bonds (with $CNCH_3$) which is unprecedented for dirhodium compounds. The Rh-C (ax CH_3NC) bond lengths are 2.023(4), 2.037(4) Å for **8**-*S* and 2.033(3), 2.040(2) Å for **8**-*R*, *i.e.*, by ~ 0.07 Å shorter than the corresponding distances in **5**-**7**. For both isomers of **8**, the Rh-C (eq CH_3NC) distances are in the range 2.00-2.02

Å. The Rh-P bond lengths for both isomers of **8** are ~ 2.30 Å, *i.e.*, by ~ 0.10 Å longer than the corresponding distances in *cis*-$[Rh_2[Ph_2P(C_6H_4)]_2(O_2CCH_3)_2]\bullet 2CH_3CO_2H$ and *cis*-$[Rh_2(O_2CCH_3)_2[Ph_2P(C_6H_4)]_2]\bullet 2C_5H_5N$ [134], and by ~ 0.05 Å longer than those in **4**.[105] The Rh-C (bridging phosphine) bond lengths in **8** are ~ 2.07 Å, *i.e.*, by 0.07 Å longer than the corresponding distances in the orthometalated compounds *cis*-$[Rh_2[Ph_2P(C_6H_4)]_2(O_2CCH_3)_2]\bullet 2CH_3CO_2H$, *cis*-$[Rh_2(O_2CCH_3)_2[Ph_2P(C_6H_4)]_2]\bullet 2C_5H_5N$ and **4**. The CH_3NC groups in **8**-*S* are considerably twisted from an eclipsed conformation by -35.9(1)° and -29.4(1)°, which are similar to the analogous ones for CH_3CN in **4.** The corresponding dihedral angles for the CH_3NC groups in **8**-*R* are 30.7(1)° and 31.8(1)°. Considerably smaller distortions are found for the bridging phosphine groups, with dihedral angles -21.29(8)° and -20.47(8)° in **8**-*S*. Likewise, for **8**-*R*, they are 21.08(8)° and 21.19(8)°. These distortions are similar to those encountered in **4**, but larger than the angles in *cis*-$[Rh_2[Ph_2P(C_6H_4)]_2(O_2CCH_3)_2]\bullet 2CH_3CO_2H$, wherein the acetate bridging groups are twisted by ~12.22° from the eclipsed conformation.

The detailed bond distances, and dihedral angles for complexes **2**, **3** and **5**-**8** are all complied in Table 2.2

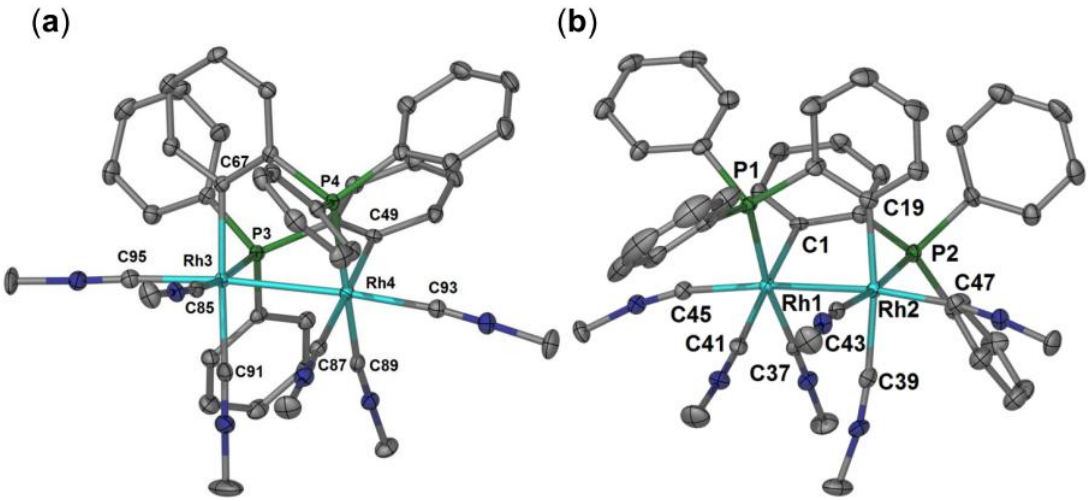

Figure 2.6 Thermal ellipsoid plot for the cationic unit of **8**-*R*, **8**-*S* at the 50% probability level.

Table 2.2 Important bond distances and dihedral angles in compounds **2-3**, **5-8**.

2		**3**	
Bond distances	Å	Bond distances	Å
Rh1-Rh2	2.571(1)	Rh2-Rh1	2.5135(9)
Rh1-N9	2.251(4)	Rh2-N12	2.202(7)
Rh1-N1	2.038(5)	Rh2-N3	2.017(6)
Rh1-N3	2.052(5)	Rh2-N6	2.011(6)
Rh1-N5	2.032(5)	Rh2-N10	1.996(7)
Rh1-N6	2.040(5)	Rh2-N9	2.024(6)
Rh2-N2	2.046(5)	Rh1-N4	2.023(6)
Rh2-N4	2.024(4)	Rh1-N11	2.225(7)
Rh2-N8	2.034(5)	Rh1-N1	2.024(6)
Rh2-N7	2.043(5)	Rh1-N7	2.007(8)
Rh2-N10	2.195(4)	Rh1-N8	2.004(6)
Dihedral angles	°	Dihedral angles	°
N5-Rh1-Rh2-N7	22.8(2)	N3-Rh2-Rh1-N1	20.2(2)
N1-Rh1-Rh2-N2	18.0(2)	N6-Rh2-Rh1-N4	20.6(2)
N6-Rh1-Rh2-N8	22.8(2)	N10-Rh2-Rh1-N8	23.0(3)
N3-Rh1-Rh2-N4	18.0(2)	N9-Rh2-Rh1-N7	22.7(3)
5		**6**	
Bond distances	Å	Bond distances	Å
Rh1-Rh2	2.6262(4)	Rh1-Rh2	2.6105(9)
Rh1-N1	2.093(2)	Rh1-N2	2.081(3)
Rh2-N2	2.078(2)	Rh2-N1	2.097(3)
Rh1-N3	2.094(2)	Rh1-N4	2.094(3)
Rh2-N4	2.081(2)	Rh2-N3	2.080(3)
Rh1-C39	2.099(2)	Rh1-C29	1.947(3)
Rh2-C41	2.080(2)	Rh2-C27	1.951(4)
Rh1-C31	1.935(2)	Rh1-C33	1.954(4)
Rh2-C33	1.948(2)	Rh2-C31	1.937(4)
Rh1-C35	1.949(2)	Rh1-C37	2.074(4)
Rh2-C37	1.939(2)	Rh2-C35	2.134(4)
Dihedral angles	°	Dihedral angles	°
C31-Rh1-Rh2-C33	20.99(8)	C33-Rh1-Rh2-C31	21.6(2)
C35-Rh1-Rh2-C37	20.48(8)	C29-Rh1-Rh2-C27	23.5(2)
N1-Rh1-Rh2-N2	17.79(6)	N2-Rh1-Rh2-N1	18.1(1)
N3-Rh1-Rh2-N4	17.97(6)	N4-Rh1-Rh2-N3	17.2(1)

Table 2.2 Continued

7		**8-S**	
Bond distances	Å	Bond distances	Å
Rh1-Rh2	2.5860(6)	Rh1-Rh2	2.7682(6)
Rh1-N3	2.068(4)	Rh1-P1	2.2929(9)
Rh1-N6	2.077(4)	Rh1-C45	2.023(4)
Rh1-C37	2.097(5)	Rh1-C37	2.007(2)
Rh1-C35	1.949(5)	Rh1-C41	2.000(3)
Rh1-C29	1.939(5)	Rh1-C1	2.078(2)
Rh2-N4	2.088(4)	Rh2-P2	2.3077(9)
Rh2-N1	2.091(4)	Rh2-C43	2.009(2)
Rh2-C39	2.094(5)	Rh2-C19	2.090(3)
Rh2-C31	1.949(5)	Rh2-C47	2.037(4)
Rh2-C33	1.946(5)	Rh2-C39	2.026(3)
Dihedral angles	°	Dihedral angles	°
N3-Rh1-Rh2-N1	18.9(2)	C41-Rh1-Rh2-C43	-29.4(1)
N6-Rh1-Rh2-N4	19.8(2)	C37-Rh1-Rh2-C39	-35.9(1)
C35-Rh1-Rh2-C33	21.7(2)	P1-Rh1-Rh2-C19	-21.29(8)
C29-Rh1-Rh2-C31	21.1(2)	C1-Rh1-Rh2-P2	-20.47(8)

NMR spectroscopic studies

In the ^{1}H NMR spectrum of **2**, the characteristic triplet resonance, attributed to the bridging head H atoms on the [F-form]$^{-}$ ligands, appears at 7.49 ppm (Figure 2.7a), with the coupling constant to the Rh(II) centers being 3 Hz, similar to that in **1**. The multiplet at 7.05 ppm results from the protons on the phenyl ring of the [F-form]$^{-}$ ligands. The resonance at δ = 2.53 ppm corresponds to the protons of the eq CH_3CN ligands but the ratio of the integration between this resonance and the one at δ = 7.49 ppm (bridging head H) is less than 6 after the dissolution of **2** in CD_3CN for only 10 min, indicating the fast exchange of eq CH_3CN ligands with the CD_3CN solvent molecules (Figure 2.7a). The spectrum obtained after dissolving **2** in CD_3CN for 6 hours shows the total disappearance of this resonance, confirming the fast exchange process of the eq CH_3CN ligands. For compound **3**, the multiplet at δ = 7.11 ppm corresponds to the H nucleus on the phenyl ring of the bridging [NNN]$^{-}$ ligands. The resonances at δ = 2.52 ppm and δ = 2.31 ppm is attributed to the eq CH_3CN ligands and $-CH_3$ groups on the [NNN]$^{-}$ ligands respectively. The ratio of the integration of those two resonances is less than 1 after 10 min dissolution, indicating the lability of the eq CH_3CN ligands in the CD_3CN solution, same as **2**. This is also confirmed by the disappearance of the resonance at δ = 2.52 ppm after 24 h dissolution in the dark.

For compounds **5** and **6**, the triplet of the bridge-head H nuclei appear at δ = 7.87 and δ = 7.84 ppm respectively, downfield shifted compared to those of **1** and **2** with the same coupling constant to the two Rh(II) centers. The singlets at 3.67, 2.61 ppm in **5**, 3.68,

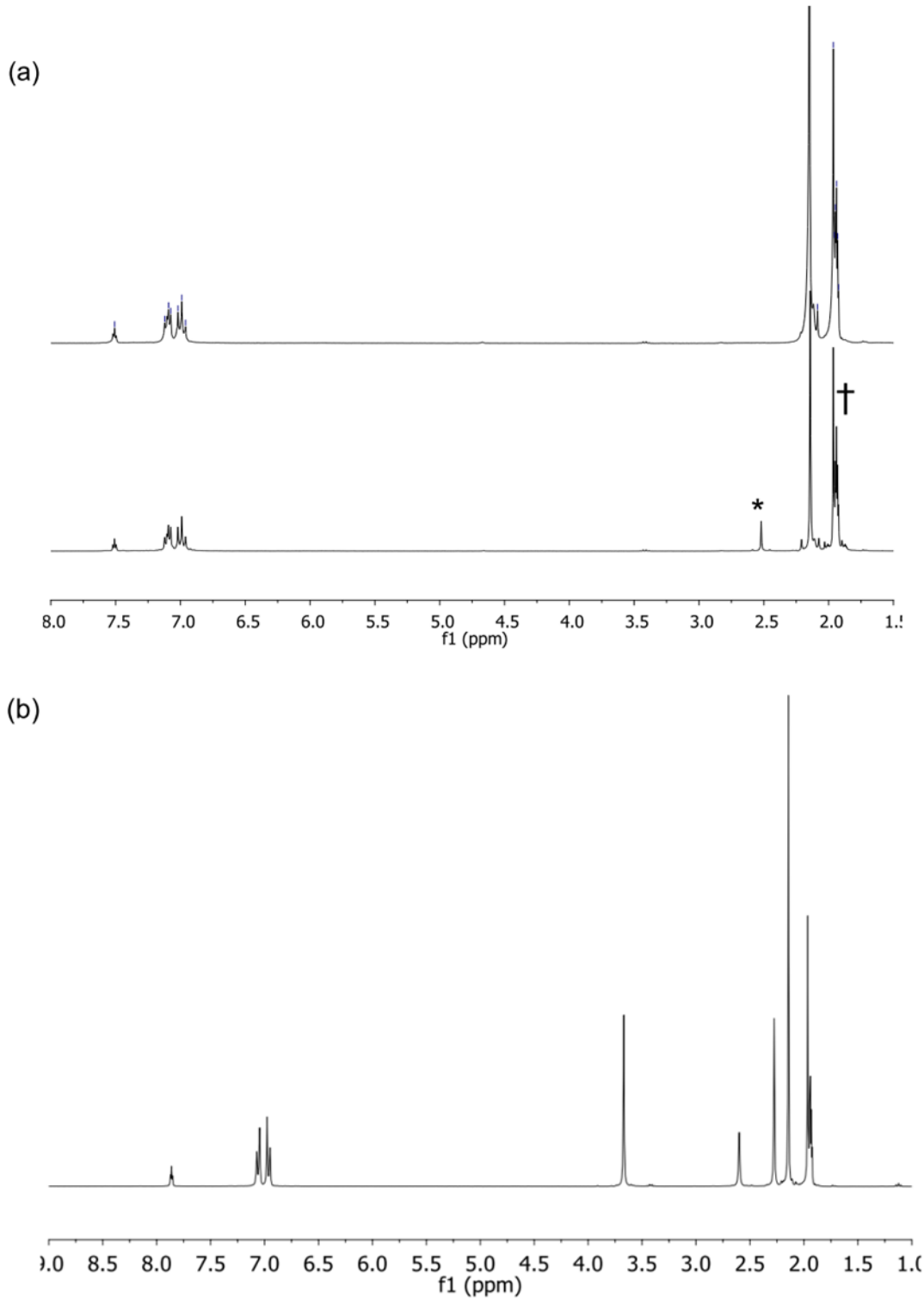

Figure 2.7 (a) ^{1}H NMR spectra change of compound **2** after dissolving in CD_3CN for 6 h (b) ^{1}H NMR spectrum of compound **5** after dissolution in CD_3CN for 1 week.

2.74 ppm in **6**, 3.66, 2.73 ppm in **7** correspond to the eq CH_3NC and ax CH_3NC ligands with integration ratios of 2:1. No exchange of the CH_3NC ligands with CD_3CN in **5-7** (Figure 2.7b for **5**) for one week indicates the stronger interaction of those CH_3NC with the dimetal core in those compounds.

The X-ray crystallographic data for the orthometalated compounds **4** and **8** revealed racemic mixtures of the *R* and *S* isomers; the Rh centers are supported by two *cis* $[Ph_2P(C_6H_4)]^-$ groups in a head-to-tail orientation. As evidenced by the ^{1}H-NMR spectra, both isomers exhibit the same chemical shifts due to fast rotation of the molecules in solution. The presence of only one resonance for CH_3CN in the ^{1}H NMR spectrum of **4**, within 10 min of dissolution, indicates fast exchange of the eq CH_3CN ligands with the CD_3CN solvent due to the strong σ-donating ability of the bridging phosphine ligands. In contrast, due to the decreased lability of CH_3NC, as compared to CH_3CN, and the asymmetry of the bridging ligands, the ^{1}H NMR spectrum of **8** displays three CH_3NC resonances at δ 3.48, 3.27 and 2.50 ppm, in a 1:1:1 ratio (Figure 2.8a), which correspond to eq CH_3NC *trans* to the P and C atoms as well as the ax CH_3NC groups, respectively. A monitoring of **8** with ^{1}H NMR spectroscopy in CD_3CN, however, revealed slow decomposition as indicated by the disappearance of the three aforementioned CH_3NC resonances at the same rate and the concomitant appearance of a new resonance at δ 3.38 ppm in the ^{1}H NMR spectra (Figure 2.8a). The $^{31}P\{^1H\}$ NMR spectrum of **8** exhibits a doublet at δ ~ 21 ppm ($^1J_{Rh\text{-}P}$ = 101.5 Hz) with the characteristic ^{102}Rh-^{31}P coupling;[135] the doublet decreases in intensity and after 12 h, new resonances appear in the spectrum, and increase in intensity with time (Figure 2.8b; spectra at 12 h and 4 days). The

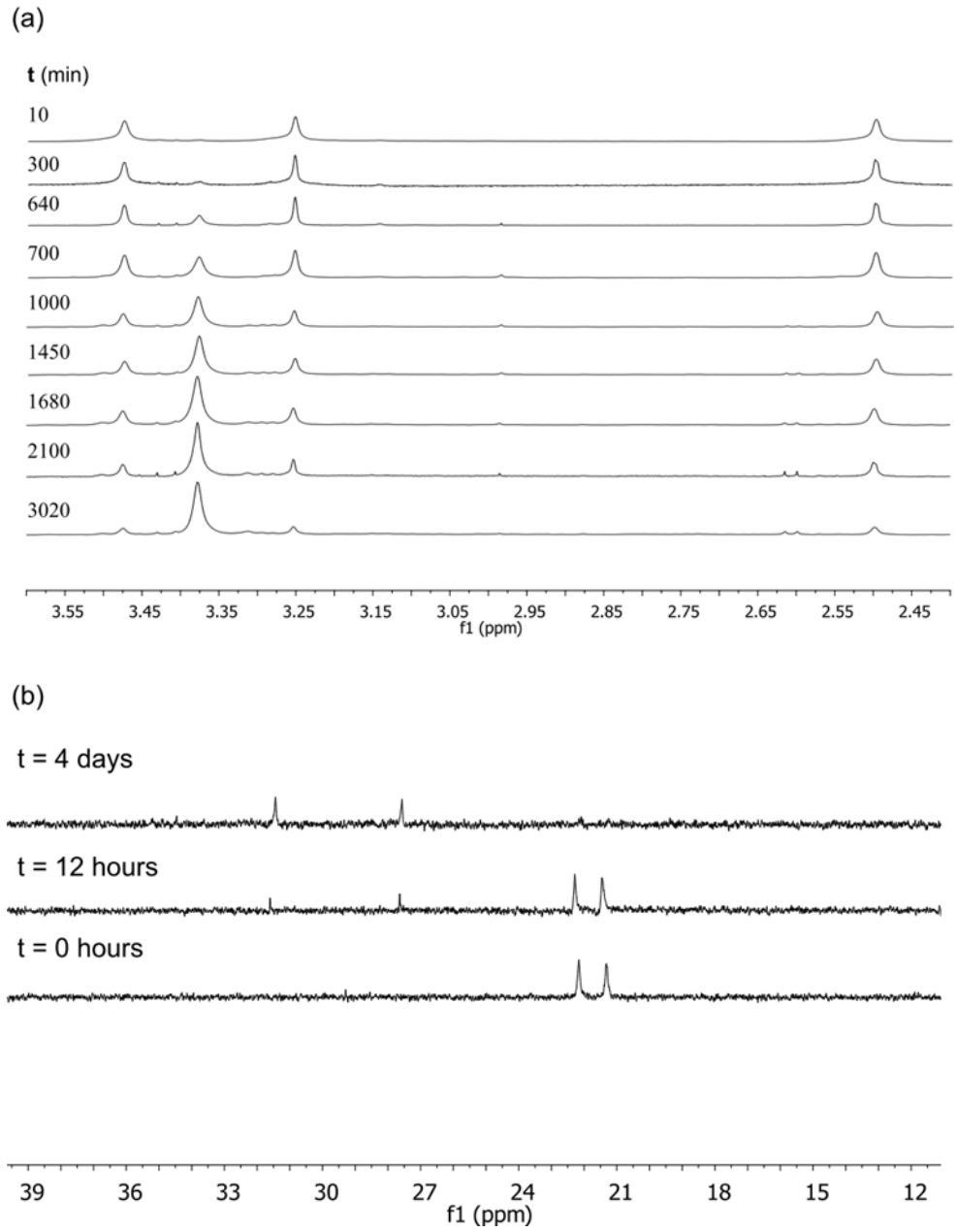

Figure 2.8 (a)^{1}H NMR and (b) ^{31}P NMR spectra of compound **8** after dissolution in CD_3CN.

instability of **8** in solution as a function of time, indicated by the NMR data, is also corroborated by the fragmentation pattern of **8** in the MS studies. On the contrary, the ESI-MS data for **2-7** show the main peaks corresponding to the parent species with a 2^+ charge and the appropriate isotopic distributions. Sequential loss of the monodentate ligands, either CH_3CN or CH_3NC, is observed in the ESI-MS of **2-7**.

In the ESI-MS spectra of **2-3**, **5-7**, all the main peaks are correspondent to the 2^+ charge with the appropriate isotope distributions, assigned to be the cationic part of the compounds respectively. Moreover, sequential loss of the monodentate ligands, either CH_3CN or CH_3NC, are observed in the ESI-MS spectra of those compounds. In the ESI spectrum of **8** in CH_3CN, different small fragments of the molecule are observed, with the assignments as follows: $[Rh_2\{Ph_2P(C_6H_4)\}_2]^{2+}$, 366.00; $[Rh_2\{Ph_2P(C_6H_4)\}_2(CNCH_3)]^{2+}$, 384.51; $[Rh_2\{Ph_2P(C_6H_4)\}_2(CNCH_3)_2]^{2+}$, 405.00; $[Rh_2\{Ph_2P(C_6H_4)\}_2(CNCH_3)_3]^{2+}$, 425.51; $[Rh_2\{Ph_2P(C_6H_4)\}_2(CNCH_3)_4]^{2+}$, 446.03; $[Rh_2\{Ph_2P(C_6H_4)\}_2(CNCH_3)_5]^{2+}$, 466.56; $[Rh\{Ph_2P(C_6H_4)\}_2]+H^+$, 625.07; $[Rh\{Ph_2P(C_6H_4)\}_2(CNCH_3)]+H^+$, 666.09; $[Rh\{Ph_2P(C_6H_4)\}_2(CNCH_3)_2]+H^+$, 707.13; $[Rh_2\{PPh_2P(C_6H_4)\}_2(CNCH_3)_3](BF_4)^+$, 938.08; $[Rh_2\{Ph_2P(C_6H_4)\}_2(CNCH_3)_4](BF_4)^+$, 979.11; $[Rh_2\{Ph_2P(C_6H_4)\}_2(CNCH_3)_5](BF_4)^+$, 1020.13; $[Rh_2\{Ph_2P(C_6H_4)\}_2(CNCH_3)_6](BF_4)^+$, 1061.16. These data reveal the instability of the compound, in accord with the NMR studies. The identity of the decomposition product has not been determined as of yet, but it is postulated to be the product caused by the cleavage of the Rh-Rh bond.

Electronic absorption spectral studies

The electronic absorption data for **1**-**8** measured in CH_3CN are summarized in Table 2.3 and selected spectra in the range 200-600 nm are depicted in Figure 2.9.

Given that compounds **1**, **2** and **5**, **6** are structurally analogous, it is not surprising that similar electronic absorption features are observed in each case. Compounds **1**-**2** (Figure 2.9a**)** and **5**-**6** exhibit characteristic intense bands at λ ~ 260 nm, which are ascribed to metal-centered transitions involving contributions from the orbitals of both the bridging and monodentate ligands. In **1**-**3** (Figure 2.9a, c), there is a shoulder of moderate intensity at λ ~ 320 nm (ε ~ 8.0 x 10^3 M^{-1} cm^{-1}) in addition to the intense absorption at λ = 258 nm (Figure 2.9a, c). It is notable that two weak but obvious shoulders appear at λ = 420 and 515 nm (ε ~10^3 and 500 $M^{-1}cm^{-1}$, respectively); these maxima display significant hypsochromic shifts as compared to the lowest energy bands of the series Rh_2(R-DPhF)$_4$ (R = OCH_3, Cl), which occur at λ > 800 nm and are attributed to the $Rh_2(\pi^*)\rightarrow Rh_2(\sigma^*)$ transitions.[136, 137] The aforementioned band shifts indicates the differences in the electronic structures of the partial paddlewheel Rh_2(II,II) compounds **1**-**3** after substituting two *cis*-formamidinate bridging ligands with four monodentate CH_3CN groups. Furthermore, the substitution of CH_3CN with CH_3NC in the series **5**-**7** results in a shift of the lowest energy bands to higher energies (λ ~ 420 nm) with no apparent absorptions at λ > 500 nm (Figure 2.9b, c). The electronic absorption spectrum of **3** is similar to those of **1** and **2**, presumably due to the similarity of the interactions between Rh_2(II,II) with the $[NNN]^-$ and $[DTolF]^-$ bridging ligands. The intense absorption maximum at λ = 250 nm is of the same character as that in **1** and **2** at ~260

Table 2.3 Electronic absorption data for compounds **1**-**8** in CH_3CN.

Compound	λ_{max} (ε x 10^3) (nm, $M^{-1}cm^{-1}$)
1	258 (55), ~321 (8.8), ~425 (1.05), ~521 (0.45)
2	254 (47.5), ~312 (7.4), ~416 (0.85), ~510 (0.4)
3	244 (19.28), 285 (13.9), ~ 463 (0.8), ~ 534 (0.2)
4	206 (67), ~ 246 (23), 286 (19.3), ~ 355 (1.5), 478 (0.57)
5	267 (46.6), ~313 (10.9), ~345 (5), ~392 (1.2), ~425 (0.76)
6	259 (40.9), ~ 318 (11), ~ 340 (4.4), ~ 388 (1.9), ~ 420 (0.8)
7	232 (18.3), 284 (11), 389 (1.4), ~450 (0.3)
8	204 (120), 273 (14), ~290 (11), 362 (10)

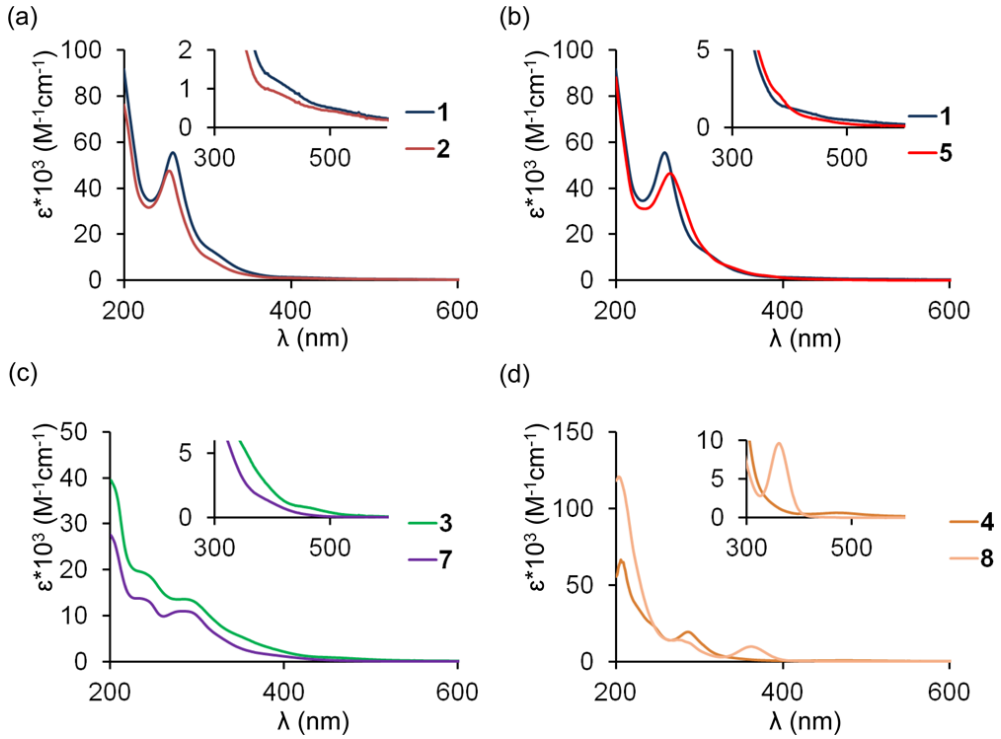

Figure 2.9 Overlay of the electronic spectra for (a) **1** and **2**, (b) **1** and **5**, (c) **3** and **7**, and (d) **4** and **8**.

nm, whereas the transition at λ = 285 nm is tentatively assigned to the intramolecular $^1\pi\pi^*$ transition of the $[NNN]^-$ ligands in **3** because it is also present, albeit slightly shifted, in the electronic spectrum of the free ligand as well as **7**. A distinct feature in the electronic spectrum of **4** is the weak but apparent absorption at λ = 478 nm ($\varepsilon \sim 570$ $M^{-1}cm^{-1}$) as opposed to **8**, which exhibits a moderately strong absorption at λ = 362 nm ($\varepsilon \sim 9700$ $M^{-1}cm^{-1}$) (Figure 2.9d). This difference in the spectra of **4** and **8** reflects the drastic changes in their electronic configurations upon substitution of CH_3CN for CH_3NC ligands.

Computational studies

DFT calculations were performed on the cationic units of **1**-**8** in an attempt to gain further insight into their structural, electrochemical and electronic absorption properties. The structural parameters of the optimized metal complexes closely resemble those experimentally found by X-ray crystallography. In **1**-**3**, the Rh-Rh bond distances in the cationic units are ~ 0.09 Å shorter than the distances in **5**-**7**. Moreover, a significant decrease of the Rh-L bond distances (L monodentate ligand, L: CH_3CN in **1**-**3**, L: CH_3NC in **5**-**7**) was also successfully predicted by the calculations for the pairs **1**/**5**, **2/6,** **3**/**7**. The Rh-Rh bond distance in the optimized cationic unit of **4** is comparable to the crystal structure, whereas in **8**, it is ~ 0.05 Å longer than the experimentally value. In **4**, slightly longer Rh-N bond distances (eq CH_3CN, *trans* to C) than the Rh-N bond distances (eq CH_3CN *trans* to P) were also successfully predicted, indicating the stronger *trans* influence imposed by the Rh-C bond. For **8**, the Rh-C (ax $CNCH_3$) and Rh-C (eq $CNCH_3$) bond distances are very similar, in agreement with the X-ray diffraction data.

The calculated dihedral angles ω in **1**-**8**, defined by the eq ligands and the two Rh centers, are slightly higher than those in the crystal structures but within a similar range. In general, the good agreement of the bond distances and angles with the X-ray data indicates that the level of theory and the basis sets that were used are reliable.

DFT calculations for CH_3CN and CH_3NC were also conducted to illustrate the different electronic properties of the ligands. From the MO diagrams depicted in Figure 2.10, the HOMO of CH_3NC between the C and N atoms has σ* character with the electron density mainly localized on the terminal C atom, whereas the HOMO of CH_3CN is mainly the π bonding orbital between the C and N atoms. Moreover, the HOMO of CH_3NC lies higher than that of CH_3CN (the HOMO and HOMO-1 for CH_3CN are degenerate). These features explain the better σ-donating ability of CH_3NC as compared to CH_3CN. The LUMO+1 and LUMO+2 levels for both ligands are sets of degenerate π* orbitals, lying at ~ 0.12 eV and ~ 0.56 eV for CH_3NC and CH_3CN, respectively, in accord with the improved π-accepting ability of CH_3NC. The aforementioned factors also affect the Rh-Rh bond lengths of compounds **5**-**8** in an interdependent fashion (*vide infra*).

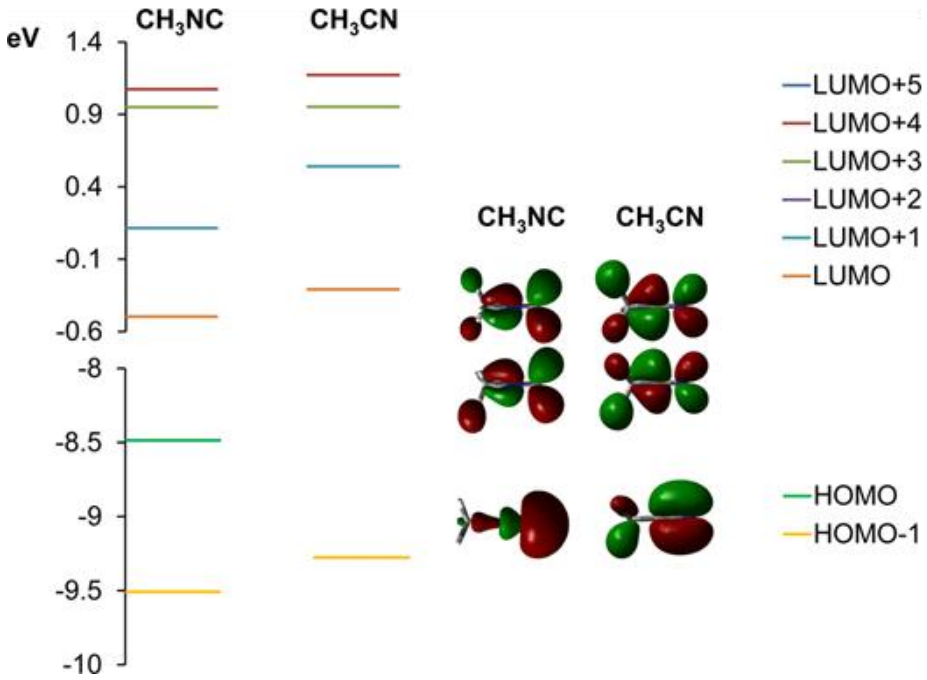

Figure 2.10 MO diagrams for the ligands CH_3CN and CH_3NC with graphical representations of the HOMO, LUMO+1, LUMO+2 (iso-value 0.04); the HOMO and HOMO-1 for CH_3CN are degenerate.

Bonding in the dirhodium unit

It is widely accepted that without perturbation from the ligand field, the electronic configuration of the Rh_2(II,II) dimetallic core is $\sigma^2\pi^4\delta^2\delta^{*2}\pi^{*4}\sigma^{*0}$, resulting in a bond order of one.[21] Upon coordination of the four $[DTolF]^-$ ligands, however, the dirhodium unit adopts the electronic configuration $\sigma^2\pi^4\delta^2\pi^{*4}\delta^{*2}\pi^{*0}$ as the $Rh_2(\delta^*)$ orbital is destabilized due to the antibonding interaction with the pπ lone pairs of the bridging $[DTolF]^-$ groups.[136] It is notable that in the two sets of dirhodium compounds **1**, **2** and **5**, **6** with monodentate acetonitrile and methyl isocyanide ligands, respectively, however, unusual configurations of the molecular orbitals arise; these differences entail lowering of the $Rh_2(\delta^*)$ below the $Rh_2(\delta)$ and considerable elevation of the $Rh_2(\sigma)$ orbitals (for

example, $Rh_2(\delta)$ lies ~ 0.98 and 1.02 eV higher in energy as compared to $Rh_2(\delta^*)$ in **1** and **2**, respectively; Table 2.4, Figure 2.11 for **1** and **5**; Table 2.5, Figure 2.12 for **2** and **6**). The substitution of two *cis*-$[DTolF]^-$ by four eq CH_3CN in $Rh_2(DTolF)_4$ and the presence of two ax CH_3CN ligands lead to stabilization of the $Rh_2(\delta^*)$ as compared to $Rh_2(\delta)$ in **1**. This is attributed to the combined effects of two factors: the presence of only two bridging ligands in **1** induces a staggered configuration with $\omega \sim 20^o$ and a subsequent reduced overlap between the two d_{xy} orbitals of the two Rh(II) centers, which are responsible for the formation of the $Rh_2(\delta)$ and $Rh_2(\delta^*)$ bonds. Furthermore, there are interactions of the $Rh_2(\delta^*)$ with the low lying π^* orbitals of the eq monodentate CH_3CN ligands as well as the $p\pi$ lone pairs of the formamidinate groups which further stabilize the $Rh_2(\delta^*)$ (Figure 2.13) and slightly destabilize the $p\pi$ lone pair, thus rendering it the HOMO in **1** (it has 27% $Rh_2(\delta^*)$ and 71% $[DTolF]^-$ contributions; Table 2.4).

In contrast to **1** and **2**, the $Rh_2(\delta^*)$ orbital in **3** is slightly higher in energy as compared to $Rh_2(\delta)$ (Table 2.6), which is not surprising as the graphic representation of its $Rh_2(\delta^*)$ indicates negligible participation of the low-lying π^* orbitals of the CH_3CN ligands. For similar reasons (Figure 2.13), the $Rh_2(\delta^*)$ orbitals are lower in energy as compared to $Rh_2(\delta)$ in **5**-**7**. Both orbitals $Rh_2(\pi)$ and $Rh_2(\pi^*)$, however, are stabilized as compared to their anologs **1**-**3**, since their interactions with the low lying empty π^* orbitals of the CH_3NC ligands are stronger due to the better π-accepting ability of CH_3NC.

Table 2.4 Bond character of orbitals, energy levels (eV) and orbital compositions (%) for the dirhodium units of **1** and **5**.

	1		**5**	
	Energy (eV)	Orbital Composition	Energy (eV)	Orbital Composition
δ*	-8.85	43 (DTolF) 42 Rh 15 (eq CH_3CN)	-9.05	51 Rh 24 (eq CH_3NC) 22 (DTolF)
π	-8.49	72 Rh 18 (DTolF) 5 (eq CH_3CN)	-8.88	58 Rh 19 (DTolF) 12 (eq CH_3NC) 11 (ax CH_3NC)
π	-8.30	80 Rh 9 (eq CH_3CN) 8 (DTolF)	-8.73	63 Rh 19 (eq CH_3NC) 12 (DTolF) 7 (ax CH_3NC)
δ	-7.83	79 Rh 13 (DTolF) 8 (eq CH_3CN)	-8.46	71 Rh 16 (eq CH_3NC) 12 (DTolF)
π*	-7.28	78 Rh 11 (DTolF) 9 (ax CH_3CN)	-8.10	81 Rh 9 (eq CH_3NC) 7 (ax CH_3NC)
π*	-7.25	88 Rh 5 (DTolF)	-8.08	83 Rh 8 (eq CH_3NC) 6 (ax CH_3NC)
σ	-7.21	78 Rh 13 (ax CH_3CN)	-6.76	51 Rh 26 (ax CH_3NC) 14 (DTolF) 9 (eq CH_3NC)
HOMO[a]	-5.75	71 (DTolF) 27 Rh	-5.97	80 (DTolF) 15 Rh
σ*	-2.11	66 Rh 12 (DTolF) 16 (ax CH_3CN) 6 (eq CH_3CN)	-1.84	63 Rh 13 (DTolF) 14 (ax CH_3NC) 10 (eq CH_3NC)

[a]Not a dirhodium-based orbital.

Table 2.5 Bond character of orbitals, energy levels (eV) and orbital compositions (%) for the dirhodium units of **2** and **6**.

	2		**6**	
	Energy (eV)	Orbital Composition	Energy (eV)	Orbital Composition
δ*	-8.90	46 (Rh) 37 (F-form) 17 (eq CH_3CN)	-9.15	50 (Rh) 26 (eq CH_3NC) 21 (F-form)
π	-8.58	71 (Rh) 18 (F-form) 6 (eq CH_3CN) 5 (ax CH_3CN)	-8.98	62 (Rh) 15 (F-form) 12 (eq CH_3NC) 11 (ax CH_3NC)
π	-8.33	79 (Rh) 10 (eq CH_3CN) 7 (F-form)	-8.81	64 (Rh) 19 (eq CH_3NC) 10 (F-form) 7 (ax CH_3NC)
δ	-7.88	77 (Rh) 14 (F-form) 10 (eq CH_3CN)	-8.54	72 (Rh) 17 (eq CH_3NC) 11 (F-form)
π*	-7.39	67 (Rh) 18 (F-form) 12 (ax CH_3CN)	-8.17	80 (Rh) 9 (eq CH_3NC) 6 (ax CH_3NC)
π*	-7.30	87 (Rh)	-8.15	84 (Rh) 8 (eq CH_3NC) 6 (ax CH_3NC)
σ	-7.23	72 (Rh) 15 (F-form) 9 (ax CH_3CN)	-6.85	52 (Rh) 26 (ax CH_3NC) 13 (F-form) 9 (eq CH_3NC)
HOMO[a]	-5.91	69 (F-form) 29 (Rh)	-6.11	80 (F-form) 15 (Rh)
σ*	-2.16	66 (Rh) 15 (ax CH_3CN) 12 (F-form) 7 (eq CH_3CN)	-1.94	63 (Rh) 14 (ax CH_3NC) 14 (F-form) 9 (eq CH_3NC)

[a]Not a dirhodium-based orbital.

Table 2.6 Bond character of orbitals, energy levels (eV) and orbital compositions (%) for the dirhodium units of **3** and **7**.

	3		**7**	
	Energy (eV)	Orbital Composition	Energy (eV)	Orbital Composition
δ*	-7.68	51 (NNN) 44 Rh	-9.32	43 Rh 28 (NNN) 25 (eq CH_3NC)
π	-8.63	74 Rh 12 (NNN) 11 (eq CH_3CN)	-9.19	63 Rh 14 (NNN) 12 (eq CH_3NC) 11 (ax CH_3NC)
π	-8.52	49 Rh 42 (NNN) 8 (eq CH_3CN)	-9.03	63 Rh 20 (eq CH_3NC) 12 (NNN) 5 (ax CH_3NC)
δ	-8.27	78 Rh 13 (eq CH_3CN) 9 (NNN)	-8.88	71 Rh 22 (eq CH_3NC) 6 (NNN)
π*	-7.54	86 Rh 6 (NNN)	-8.28	64 Rh 21 (NNN) 9 (eq CH_3NC) 6 (ax CH_3NC)
π*	-7.54	86 Rh 6 (NNN)	-8.28	53 Rh 32 (NNN) 11 (eq CH_3NC)
σ	-7.42	45 (NNN) 40 Rh 13 (ax CH_3CN)	-6.92	46 Rh 24 (ax CH_3NC) 22 (NNN) 7 (eq CH_3NC)
σ*	-2.32	66 Rh 15 (ax CH_3CN) 12 (NNN) 7 (eq CH_3CN)	-2.06	65 Rh 16 (NNN) 11 (ax CH_3NC) 9 (eq CH_3NC)

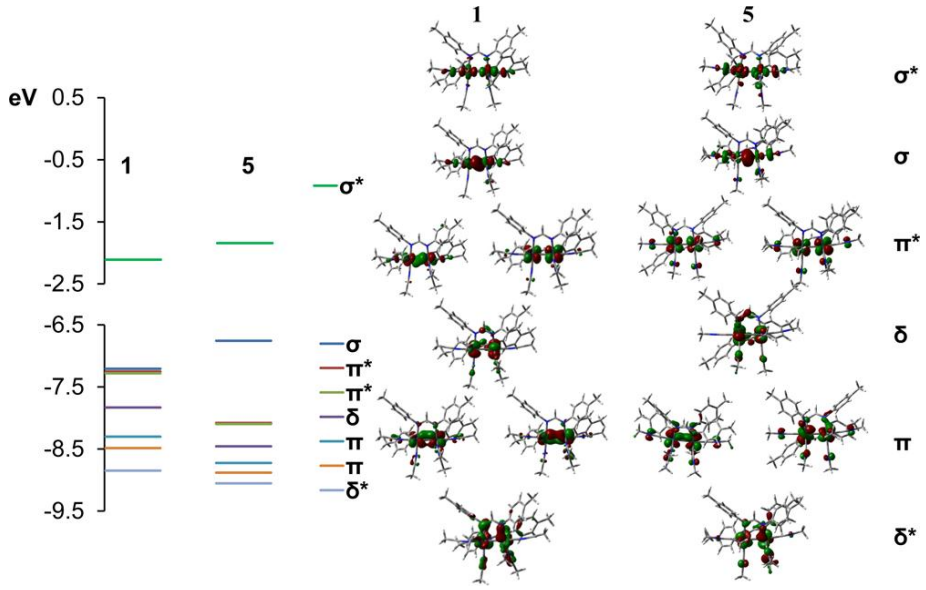

Figure 2.11 MO diagrams involving the Rh_2(II,II) units in **1** and **5** obtained by DFT calculations (iso-value=0.04).

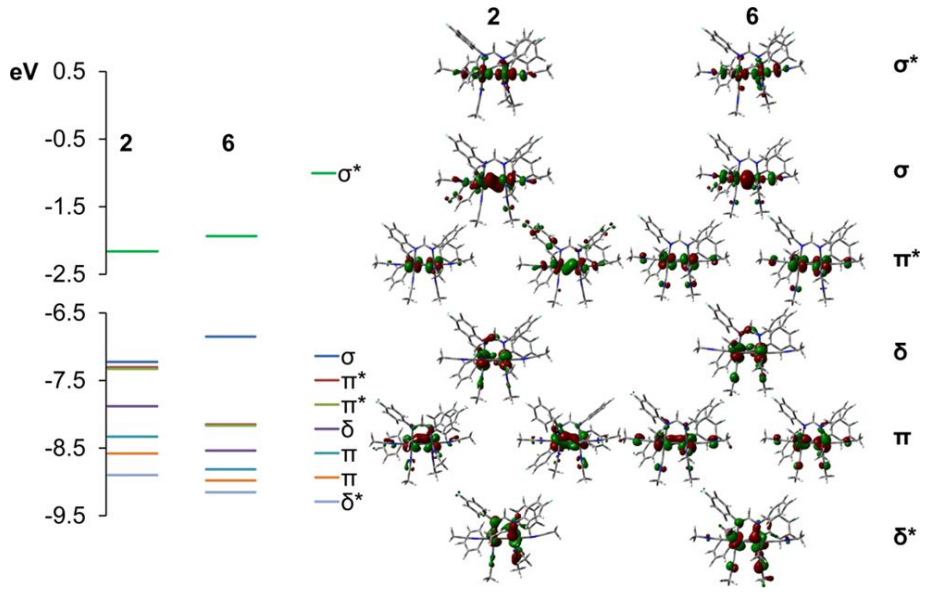

Figure 2.12 MO diagrams involving the Rh_2(II,II) units in **2** and **6** obtained by DFT calculations (iso-value=0.04).

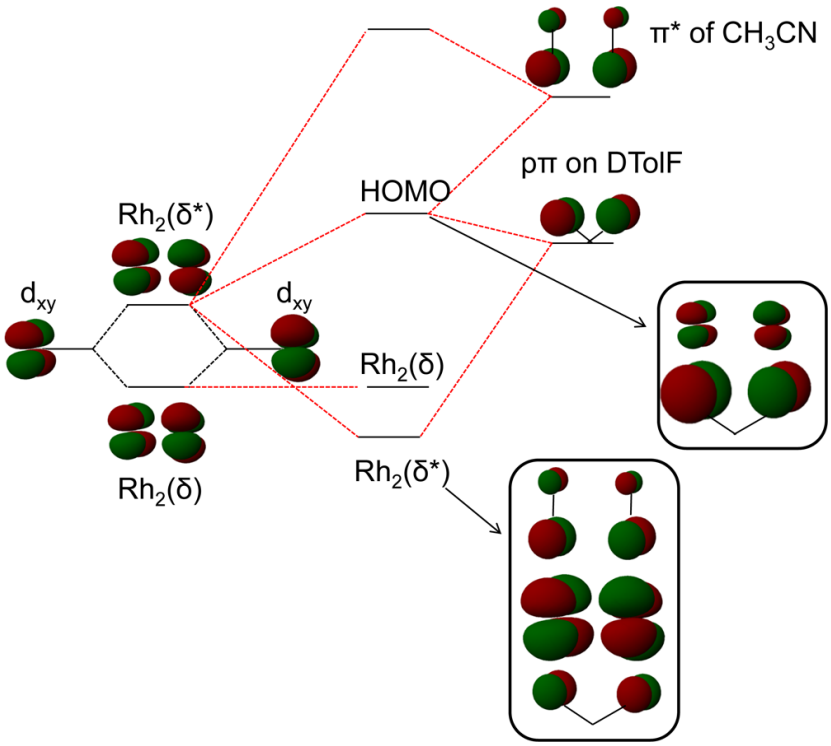

Figure 2.13 Representation of the orbital interactions between $Rh_2(\delta^*)$, pπ lone pairs on the bridging ligand and the low lying π*orbital on the CH_3NC ligands.

Apart from the $Rh_2(\delta^*)$ orbital becoming stabilized due to its interactions with two staggered $[DTolF]^-$ ligands in **1**, the $Rh_2(\sigma)$ orbital increases in energy as compared to the $Rh_2(\pi^*)$ orbital (Figure 2.11, Table 2.4) due to the interactions with the two ax CH_3CN ligands present in **1** but not in $Rh_2(DTolF)_4$. Analogous observations were made for the orbital levels in **2** and **3** (Figure 2.12, Table 2.5 for **2**, Table 2.6 for **3**). Importantly, the increase in energy for the $Rh_2(\sigma)$ and $Rh_2(\sigma^*)$ orbitals for the methyl isocyanide analogs **5-7** (Figures 2.11 and 2.12, Tables 2.4 and 2.5 for **5** and **6**, Table 2.6 for **7**) is even more pronounced as compared to **1-3** due to the better σ-donating ability of CH_3NC. Additionally in **5-7**, the $Rh_2(\pi)$, Rh_2 (π^*) and Rh_2 (δ), $Rh_2(\delta^*)$ orbitals are

stabilized by 0.2 to 0.8 eV as compared to **1-3**, respectively. This is attributed to the increased π-accepting ability of CH_3NC (*vide supra*) as the $Rh_2(\pi)$, $Rh_2(\pi^*)$ orbitals have significant contributions from both the ax and eq CH_3NC ligands and the $Rh_2(\delta^*)$ orbital has ~20% contribution from the eq CH_3NC ligands (Table 2.4), *e.g.*, the energy difference between the $Rh_2(\pi^*)$ and $Rh_2(\sigma^*)$ orbitals is ~ 1.32 and ~0.05 eV in **5** and **1**, respectively (Figure 2.12 and Table 2.5 for compounds **2** and **6)**.

In **8**, the MOs pertaining to Rh_2(II,II), which are primarily metal-based orbitals (Table 2.7), are in the order of $\pi^4\delta^2\delta^{*2}\pi^{*4}\sigma^2\sigma^{*0}$ (Figure 2.14). The stabilization of the π symmetry orbitals is attributed to significant π-backbonding from the dirhodium unit to the CH_3NC ligands, as in compounds **5-7**. In the case of **8**, however, the much stronger interactions of the dirhodium core with the ax CH_3NC ligands lead to a significant increase in the energy of the $Rh_2(\sigma)$ orbital to the extent that it actually becomes the HOMO level. As indicated from the MO diagram for **8** (Figure 2.14), the energy difference between the $Rh_2(\sigma)$ and $Rh_2(\pi^*)$ orbitals is 1.66 eV, *i.e.*, ~ 0.32 eV higher than that for **5 (**Table 2.4). In contrast to **5**, the $Rh_2(\delta)$ and $Rh_2(\delta^*)$ orbitals in **8** are very close in energy as larger distortions from the eclipsed configuration occur for the CH_3NC (the groups are twisted by $\omega \sim 30°$); this situation results in decreased orbital overlap which reduces the energy difference between the $Rh_2(\delta)$ and $Rh_2(\delta^*)$ orbitals. The graphical representation also indicates that both $Rh_2(\delta)$ and $Rh_2(\delta^*)$ orbitals have similar and strong interactions with the eq CH_3NC ligands (Figure 2.14).

Table 2.7 Bond character of orbitals, energy levels (eV) and orbital compositions (%) for the dirhodium units of **8**.

	8		
		Energy (eV)	Orbital Composition
π	HOMO-20	-8.59	68 Rh 14 (eq CH_3NC) 12 [$Ph_2P(C_6H_4)$] 6 (ax CH_3NC)
π	HOMO-19	-8.53	67 Rh 13 (eq CH_3NC) 13 [$Ph_2P(C_6H_4)$] 8 (ax CH_3NC)
δ	HOMO-18	-8.38	49 Rh 28 [$Ph_2P(C_6H_4)$] 21 (eq CH_3NC)
δ*	HOMO-17	-8.35	56 Rh 22 [$Ph_2P(C_6H_4)$] 18 (eq CH_3NC)
π*	HOMO-14	-7.89	55 Rh 29 [$Ph_2P(C_6H_4)$] 10 (eq CH_3NC) 6 (ax CH_3NC)
π*	HOMO-13	-7.81	79 Rh 8 [$Ph_2P(C_6H_4)$] 7 (ax CH_3NC) 6 (eq CH_3NC)
σ	HOMO	-6.17	59 Rh 18 (ax CH_3NC) 15 [$Ph_2P(C_6H_4)$] 9 (eq CH_3NC)
σ*	LUMO	-1.67	52 Rh 26 [$Ph_2P(C_6H_4)$] 11 (eq CH_3NC) 11 (ax CH_3NC)

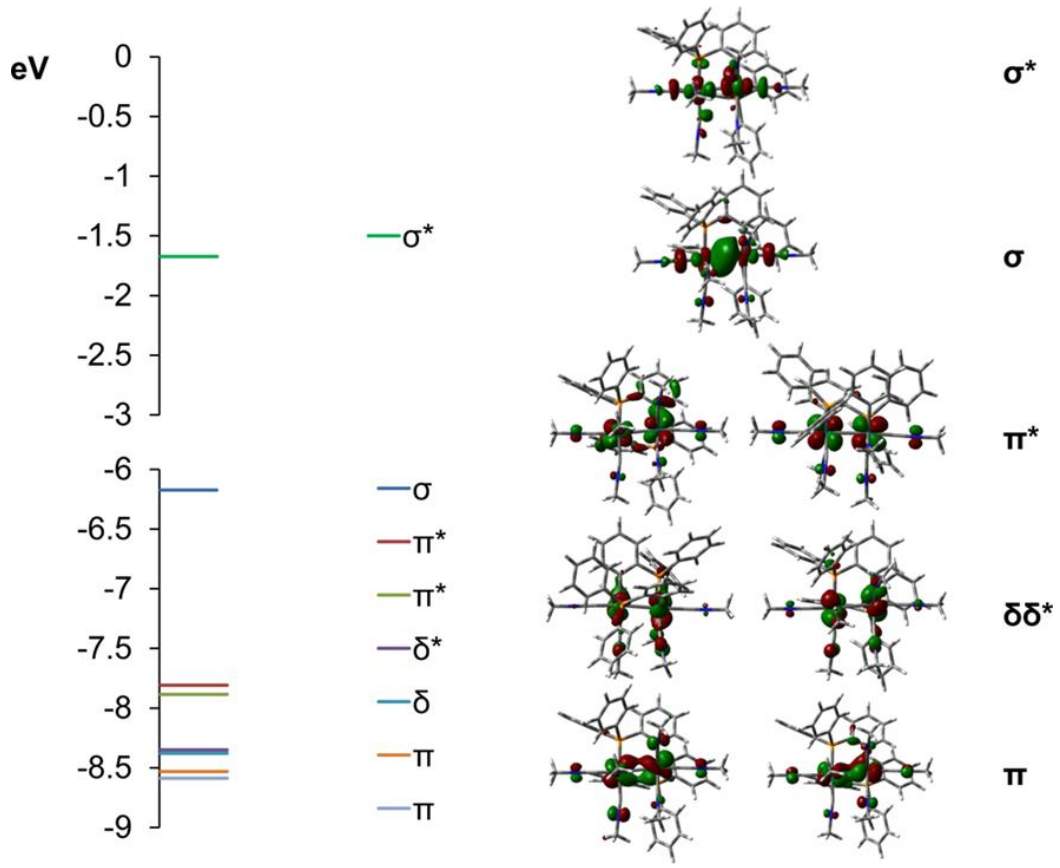

Figure 2.14 Diagram of the MO levels for the dirhodium unit in **8** with visualization of the corresponding orbitals generated by agui (iso-value = 0.04).

TD-DFT calculations

The calculated and experimental electronic absorption spectra for **1**-**4**, **5**-**8** are overlaid in Figures 2.15 and 2.16. The similarities between the spectra confirm the reliability of the calculations. The compositions of selected frontier MOs of the calculated cationic units for **1**-**8** are listed in Table 2.8.

The orbital compositions for HOMO-2 to LUMO+2, which were found to be mainly involved in the electronic transitions derived from the TD-DFT/PCM calculations for **1**-**8**, are listed in Table 2.8 and the spatial plots for **1**-**4**, **5**-**8** are displayed in Figures 2.17 and 2.18. The unoccupied orbitals for compounds **1**, **2**, **5** and **6** exhibit similar character, namely the LUMOs $Rh_2(\sigma^*)$ are primarily rhodium based orbitals (~ 65%) with ~ 15% contribution from the ax ligands (CH_3CN for **1**, **2** and CH_3NC for **5**, **6**; Table 2.8**)**. The other two low-lying orbitals, *i.e.*, the LUMO+1 ($\sigma^*_{\text{L-Rh-DTolF}}$) and LUMO+2 ($\sigma^*_{\text{L-Rh-DTolF}}$), have 45% Rh, 35% bridging ligand ($[DTolF]^-$ for **1**, **5** and $[F\text{-form}]^-$ for **2**, **6**) and 20% eq monodentate ligand (CH_3CN in **1**, **2** and CH_3NC in **5**, **6**) contributions.

Variable contributions were obtained, however, for the occupied orbitals of **1**, **2** and **5**, **6**. For **1**, the formamidinate orbitals mainly contribute to the HOMO-2 (π^*_{phenyl}), HOMO-1 ($p\pi_{\text{DTolF}}$) and HOMO ($\pi^*_{\text{Rh-DTolF}}$) (Figure 2.17, Table 2.8). Similar orbital characters are encountered in **2**. As discussed earlier, however, the HOMO-2 in **5** and **6** have $Rh_2(\sigma)$ character, whereas the HOMO-1 ($p\pi_{\text{bridging}}$) and HOMO ($p\pi_{\text{bridging}}$) comprise a set of closely lying orbitals with $p\pi$ lone-pair character from the bridging formamidinate ligands and much smaller contributions from metal-based orbitals (ratio ~5:1) (Figure 2.18, Table 2.8). For **3** and **7**, which are supported by triazenide bridging

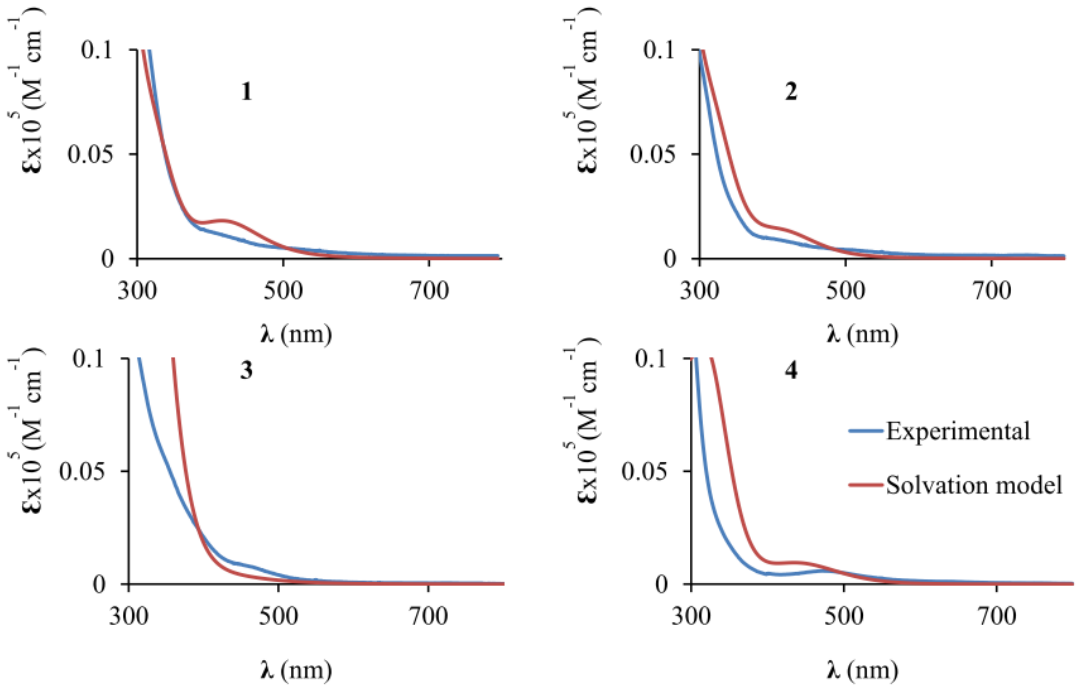

Figure 2.15 Overlay of the experimental and calculated electronic absorption spectra (in solvation model with CH_3CN as solvent) for **1**-**4**.

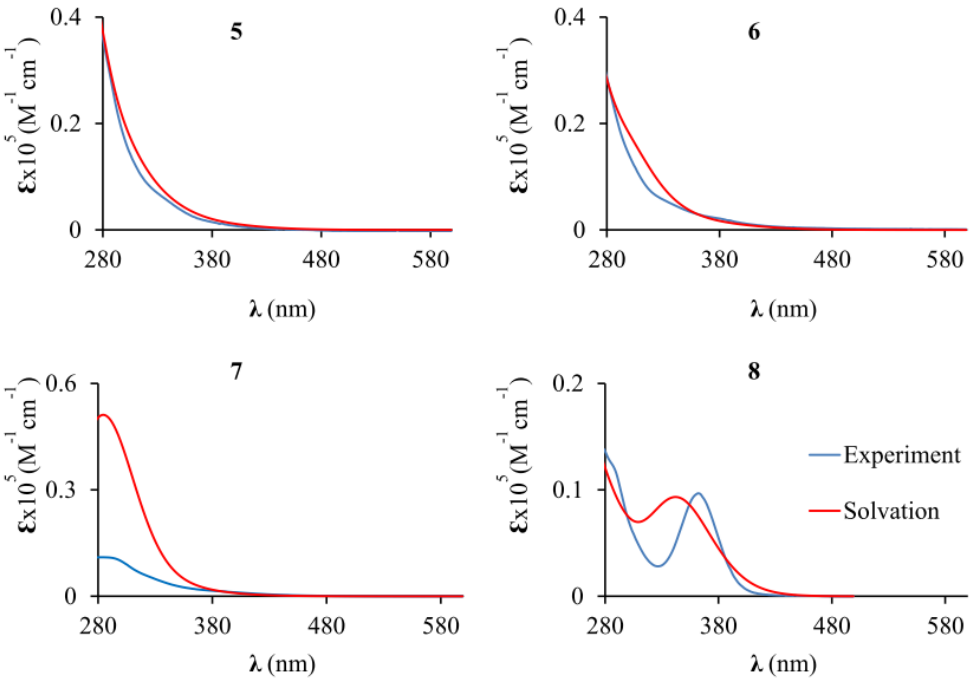

Figure 2.16 Overlay of the experimental and calculated electronic absorption spectra (in solvation model with CH_3CN as solvent) for **5-8**.

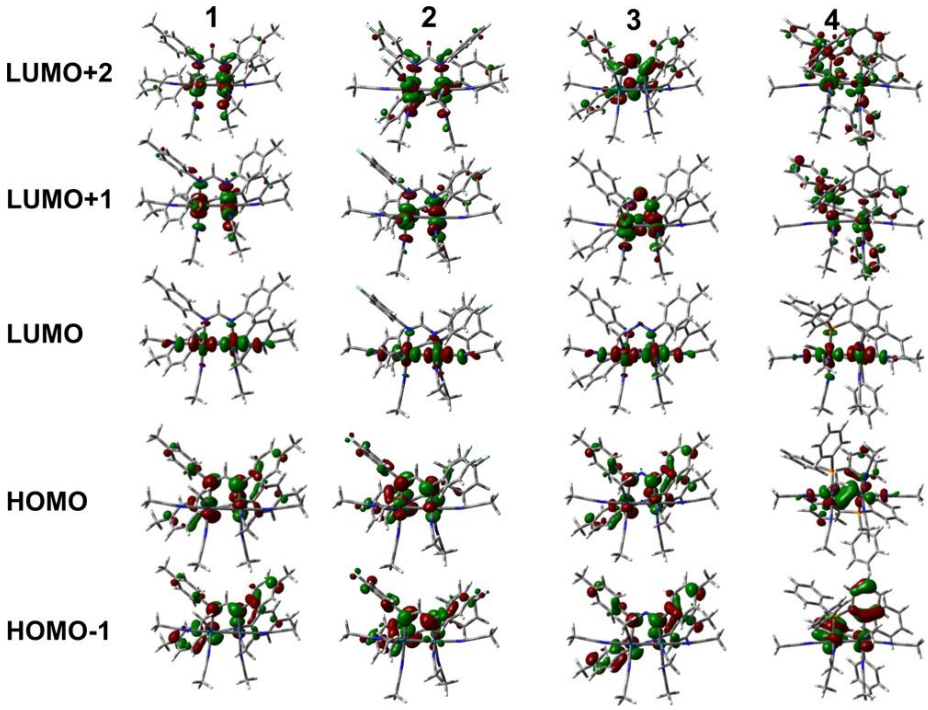

Figure 2.17 Visualization of the frontier molecular orbitals primarily involved in the electronic transitions for the DFT calculations of **1**-**4** (iso-value 0.04).

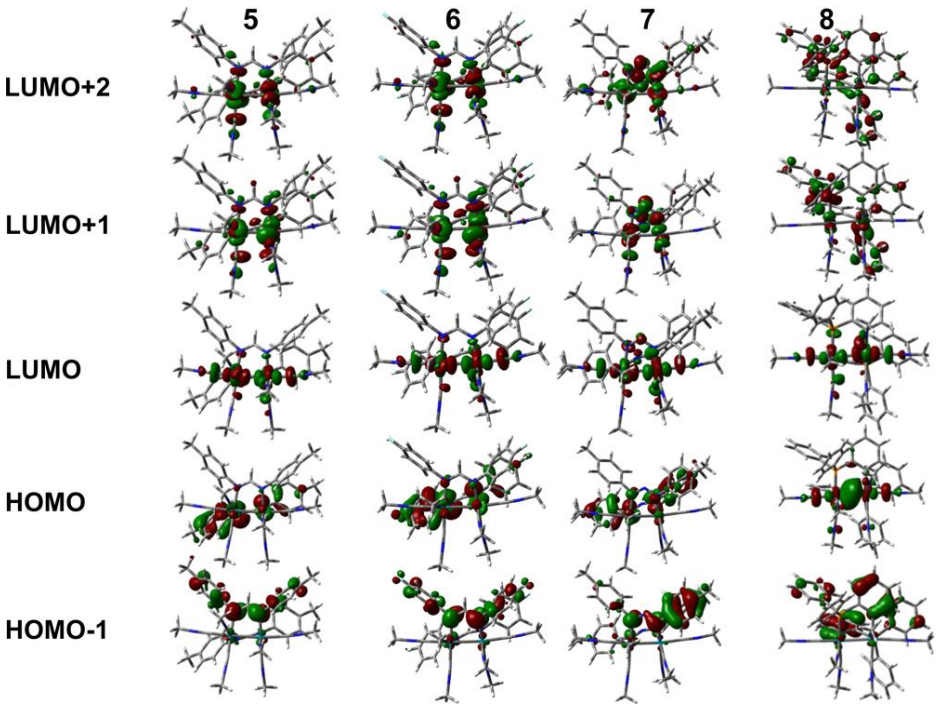

Figure 2.18 Visualization of the frontier molecular orbitals primarily involved in the electronic transitions for the TD-DFT calculations of **5**-**8** (iso-value 0.04).

Table 2.8 Composition (%) of selected frontier molecular orbitals, derived from TD-DFT calculations for **1-8**.

	1	**2**	**3**	**4**
HOMO-2	91 (DTolF) 7 Rh	80 (F-form) 17 Rh	92 (NNN) 7 Rh	54 [$Ph_2P(C_6H_4)$] 40 Rh
HOMO-1	93 (DTolF) 5 Rh	90 (F-form) 8 Rh	94 (NNN)	51 [$Ph_2P(C_6H_4)$] 46 Rh
HOMO	71 (DTolF) 27 Rh	69 (F-form) 29 Rh	79 (NNN) 20 (Rh)	68 Rh 20 [$Ph_2P(C_6H_4)$] 10 (ax CH_3CN)
LUMO	66 Rh 16 (ax CH_3CN) 7 (eq CH_3CN)	66 Rh 15 (ax CH_3CN) 12 (F-form) 7 (eq CH_3CN)	66 Rh 15 (ax CH_3CN) 12 (NNN) 7 (eq CH_3CN)	55 Rh 29 [$Ph_2P(C_6H_4)$] 11 (ax CH_3CN) 5 (eq CH_3CN)
LUMO+1	43 Rh 35 (DTolF) 21 (eq CH_3CN)	43 Rh 37 (F-form) 20 (eq CH_3CN)	44 (NNN) 39 (Rh) 16 (eq CH_3CN)	61 [$Ph_2P(C_6H_4)$] 33 Rh 6 (eq CH_3CN)
LUMO+2	45 Rh 33 (DTolF) 22 (eq CH_3CN)	44 Rh 35 (F-form) 21 (eq CH_3CN)	60 (NNN) 36 Rh	63 [$Ph_2P(C_6H_4)$] 29 Rh 7 (eq CH_3CN)

Table 2.8 Continued

	5	**6**	**7**	**8**
HOMO-2	51 Rh 26 (ax CH_3NC) 14 (DTolF) 9 (eq CH_3NC)	52 Rh 26 (ax CH_3NC) 13 (F-form) 9 (eq CH_3NC)	46 Rh 24 (ax CH_3NC) 22 (NNN) 7 (eq CH_3NC)	76 [$Ph_2P(C_6H_4)$] 21 Rh
HOMO-1	86 (DTolF) 11 Rh	86 (F-form) 10 Rh	90 (NNN) 7 Rh	86 [$Ph_2P(C_6H_4)$] 13 Rh
HOMO	80 (DTolF) 15 Rh	80 (F-form) 15 Rh	86 (NNN) 12 Rh	59 Rh 18 (ax CH_3NC) 15 [$Ph_2P(C_6H_4)$] 9 (eq CH_3NC)
LUMO	63 Rh 14 (ax CH_3NC) 13 (DTolF) 10 (eq CH_3NC)	63 Rh 14 (ax CH_3NC) 14 (F-form) 9 (eq CH_3NC)	65 Rh 16 (NNN) 11 (ax CH_3NC) 9 (eq CH_3NC)	52 Rh 26 [$Ph_2P(C_6H_4)$] 11 (eq CH_3NC) 11 (ax CH_3NC)
LUMO+1	43 Rh 34 (DTolF) 21 (eq CH_3NC)	44 Rh 34 (F-form) 21 (eq CH_3NC)	47 (NNN) 35 Rh 16 (eq CH_3NC)	60 [$Ph_2P(C_6H_4)$] 35 Rh
LUMO+2	41 Rh 36 (DTolF) 19 (eq CH_3NC)	41 Rh 36 (F-form) 19 (eq CH_3NC)	51 (NNN) 38 Rh 8 (eq CH_3NC)	49 [$Ph_2P(C_6H_4)$] 47 Rh

groups, the electronic transitions mainly involve the orbitals from HOMO-2 to LUMO+2. These orbitals in **3** and **7** exhibit very similar characters to the corresponding orbitals in **1** and **5**, respectively.

For **4** and **8**, the spatial plots of the LUMOs indicate that they are also of $Rh_2(\sigma^*)$ character but with slightly lower Rh orbital contributions (50%) as compared to **1-3** and **5-7**. The two low-lying unoccupied orbitals LUMO+1 and LUMO+2 in **4** are composed of ~60/40% bridging ligand/metal characters. A similar composition is also found for the LUMO+1 in **8**, whereas the LUMO+2 has ~50/50% bridging ligand/metal based characters. For the occupied orbitals, the HOMOs of both compounds are mainly metal-

based, but their spatial plots reveal $Rh_2(\pi^*)$ and $Rh_2(\sigma)$ characters in **4** and **8**, respectively (Figures 2.17 and 2.18). The HOMO-1 (π^*_{phenyl}) and HOMO-2 (π^*_{phenyl}**)** in **8** comprise a set of closely lying orbitals residing on the two bridging ligands; in contrast, both orbitals in **4** have ~40% metal character. Other orbitals with dirhodium character, which are involved in the excited states of **4**, derived from TD-DFT calculations, include the HOMO-18 to HOMO-14 and HOMO-5 to HOMO-3 (*vide infra*). A notable point, however, is that most of these orbitals also have significant contributions from bridging ligands with several of them having equal or even higher bridging ligand components, thus no $Rh_2(\sigma, \pi, \delta)$ character can be assigned to them.

The different substituents on the formamidinate ligands affect the energy differences between the orbitals of **1**, **2** and **5**, **6**. As shown in the MO diagrams (Figure 2.19), the orbitals in **2** and **6** lie at lower energies than in **1** and **5**, respectively, but the energy differences between the orbital sets are different for each compound. For example, the energies of the HOMO (-5.91 eV) and LUMO (-2.16 eV) for **2** are by ~ 0.16 and 0.05 eV lower than the corresponding orbital energies for **1** due to the electron withdrawing fluorine groups on the bridging formamidinate ligands in **2**. Furthermore, the various contributions from the bridging ligands result in different degrees of stabilization for the different orbitals in **1** and **2**. As shown in Table 2.8, the bridging ligands have major contributions to the HOMOs but with only minor participation in the LUMOs. Similar trends are also observed for **5** and **6**. On the other hand, the HOMOs of **5** and **6** are stabilized as compared to their CH_3CN congeners **1** and **2**, due to their antibonding character in **1** and **2**, as opposed to their non-bonding nature in **5** and **6**. Furthermore, the

LUMOs $Rh_2(\sigma^*)$ for **5**, **6** become destabilized, as compared to **1** and **2**, due to the better σ-donating ability of the ax CH_3NC ligands, which essentially leads to larger HOMO-LUMO energy gaps in **5** and **6** *vs.* **1** and **2**, respectively (Figure 2.19). Similarly, in **7**, the HOMO is stabilized by ~ 0.27 eV, whereas the LUMO is destabilized by ~ 0.26 eV, as compared to the corresponding orbitals in **3**, for the same reason that accounts for the larger HOMO-LUMO energy gap in **5** as compared to **1**. In compound **4**, the HOMO and LUMO lie at -6.42 and -1.92 eV respectively, *i.e.*, they are by ~ 0.25 eV lower than the corresponding orbitals in **8**. The destabilization of the $Rh_2(\sigma)$ (HOMO) and $Rh_2(\sigma^*)$

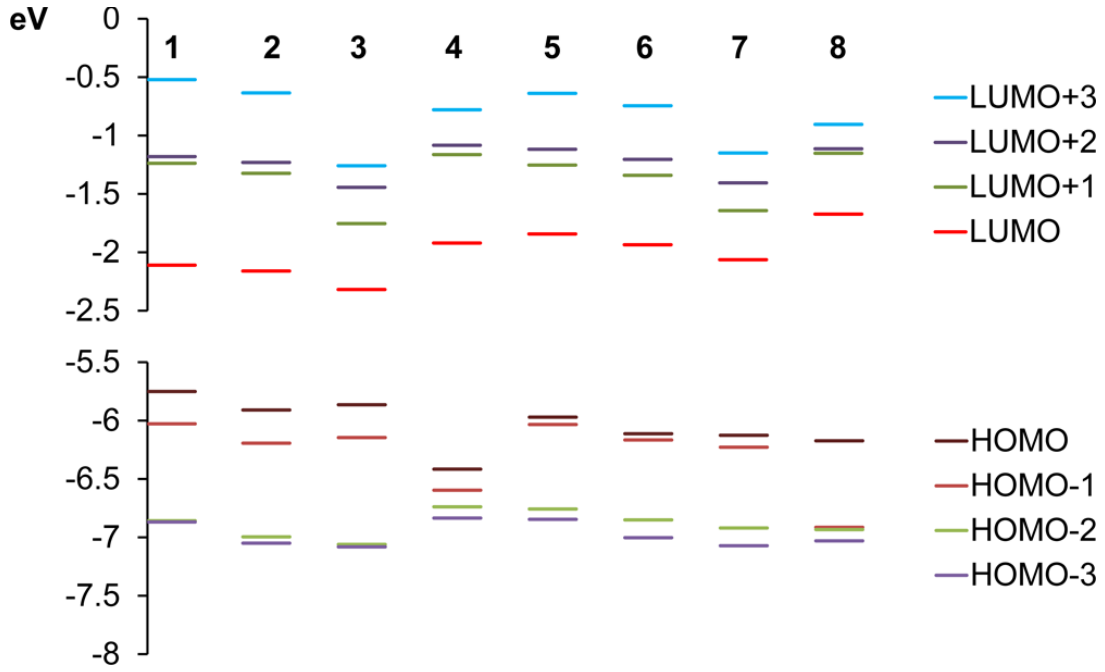

Figure 2.19 Energy levels of the MOs for **1**-**8** derived from TD-DFT calculations.

(LUMO) in **8** are attributed to the better σ-donating ability of the ax CH_3NC. The destabilization of the HOMO $Rh_2(\sigma)$ thus results in a weaker Rh-Rh bond in **8**.

The electronic transitions for **1** and **2** computed by TD-DFT calculations are summarized in Table 2.9. As the results of the TD-DFT calculation with the solvation model indicate, the lowest energy band in **1** involves a HOMO→LUMO transition occurring at 538 nm (f = 0.0015), thus it is primarily a ligand-to-metal charge-transfer transition (LMCT) with minor $Rh_2(\delta^*)\rightarrow Rh_2(\sigma^*)$ character (Tables 2.4 and 2.8). The corresponding transition in **2** occurs at 525 nm (f = 0.0011) and exhibits a hypsochromic shift as compared to **1**, which is attributed to the larger HOMO-LUMO energy gap in **2** due to the reasons we noted in the aforementioned section. The next higher energy absorption bands in **1** and **2** are in the range 435-440 nm (Table 2.9), involving transitions from HOMO-5 and HOMO-6 to LUMO in **1** and HOMO-5, HOMO-4 to LUMO in **2**. As indicated in Table 2.9, these occupied orbitals have significant $Rh_2(\pi^*)$ contribution, thus attributing metal-centered character (MC) to these transitions. The excited states 4-7 in **1** and **2** involve transitions from HOMO, HOMO-1 to LUMO+1 and LUMO+2, and occur in the broad range 330-410 nm. The involvement of HOMO and HOMO-1 orbitals leads to a bathochromic shift in **1** as compared to **2** (Table 2.9). The next set of transitions in the range 300-320 nm originates primarily from HOMO-15, HOMO-14, HOMO-13 to LUMO in both **1** and **2**. Since the three occupied orbitals mainly consist of $Rh_2(\pi)$ and $Rh_2(\sigma)$ related orbitals (*vide supra*), the transitions are considered MC with moderate oscillator factors due to being allowed by the Laporte rules.

Table 2.9 Excited states calculated by TD-DFT/PCM (CH_3CN as the solvent) with major transitions* involved in the excitations, transition coefficients, vertical excitation energies (nm), and oscillator strengths (*f*) for **1** and **2**.

1				**2**			
excitations		E/ nm	*f*	excitations		E/ nm	*f*
H ->L	94.1%	538	0.0015	H ->L	93.6%	525	0.0011
H-6 ->L H-1 ->L	30.2% 39.8%	441	0.0099	H-1 ->L	22.3%	442	0.0019
H-5 ->L	88.3%	435	0.0001	H-5 ->L H-4->L	64.2% 20.51%	436	0.0001
H-6 ->L H-1 ->L	22.5% 37.0%	424	0.0201	H-1->L H->L+1	21.84% 44.81%	419	0.0150
H-1 ->L H ->L+1	20.4% 58.9%	417	0.0001	H-1->L H->L+1	50.20% 27.31%	411	0.0066
H ->L+2	73.6%	405	0.0153	H->L+2	67.97%	399	0.0097
H-1 ->L+1	82.2%	332	0.0001	H-1->L+1	58.27%	333	0.0305
H-13 ->L H-2 ->L	22.8% 27.2%	330	0.0404	H-15->L H-12->L	17.00% 12.88%	330	0.0268
H-14 ->L	32.9%	326	0.0010	H-13->L	27.34%	326	0.0064
H-13 ->L	27.0%	325	0.0044	H-13->L	36.90%	323	0.0016

* $2|\text{coefficient}|^2 > 0.2$

For the isocyanide analogs **5** and **6**, the first two excited states are mainly HOMO, HOMO-1 to LUMO (LMCT) transitions (Table 2.10) which occur at 413 nm (*f* = 0.0016) and 392 nm (*f* = 0.0154) for **5** and 409 nm (*f* = 0.0011) and 387 nm (*f* = 0.0167) for **6**. The participation of HOMO and HOMO-1 orbitals leads to slight hypsochromic shifts from **5** to **6**, in agreement with the more stabilized HOMO in **6**. Furthermore, their hypsochromic shifts, as compared to the CH_3CN analogs **1** and **2**, are attributed to the larger HOMO-LUMO energy gaps in **5**, **6**. The next series of bands involve HOMO, HOMO-1 to LUMO+1 and LUMO+2 transitions in the absorption region 320-350 nm.

Similar bathochromic shifts from **6** to **5** are observed for these transitions due to the involvement of the HOMO and HOMO-1 orbitals. The excited states 7-10, in the range 295 to 300 nm, correspond to transitions from $Rh_2(\pi^*)$, $Rh_2(\sigma)$ to $Rh_2(\sigma^*)$ orbitals (MC), which renders them insensitive to the bridging ligand identity and thus gives rise to the same energies for both **5** and **6** (Table 2.10).

Table 2.10 Excited states calculated by TD-DFT/PCM (CH_3CN as the solvent) with major transitions* involved in the excitations, transition coefficients, vertical excitation energies (nm), and oscillator strengths (*f*) for **5** and **6**.

5				**6**			
Excitations		E/ nm	*f*	excitations		E/ nm	*f*
H-1 ->L	20.17%	413	0.0016	H->L	77.15%	409	0.0011
H ->L	75.05%						
H-1 ->L	75.81%	392	0.0154	H-1->L	78.10%	387	0.0167
H ->L	20.77%						
H ->L+1	74.6%	348	0.0259	H ->L+1	76.39%	345	0.0211
H ->L+2	68.89%	337	0.0037	H ->L+2	70.46%	334	0.0044
H-1->L+1	63.51%	334	0.0501	H-1 ->L+1	64.84%	331	0.0386
H-1->L+2	68.86%	326	0.0192	H-1 ->L+2	69.27%	324	0.0146
H-12->L	21.07%	301	0.1654	H-12 ->L	29.91%	301	0.1480
H-2->L	44.98%			H-2 ->L	38.4%		
H-11->L	43.58%	298	0.0189	H-11 ->L	65.98%	299	0.0234
H-2->L+1	50.98%	296	0.0403	H-2 ->L+1	46.97%	296	0.0192
H-12->L	26.65%	295	0.0349	H-12 ->L	25.90%	295	0.1088
H-3->L	24.71%			H-2 ->L	25.93%		

* $2|\text{coefficient}|^2 > 0.2$

The lowest energy transition in **3** is of the same character as the transitions in **1** and **2** and it occurs at λ = 538 nm (f = 0.0006) (Table 2.11). The second set of absorption bands in the region 440-450 nm corresponds to transitions from HOMO, HOMO-1 to LUMO, LUMO+1 orbitals. The excited states 4, 5 centered at λ ~ 425 nm, with low oscillator factors, mainly are $Rh_2(\pi^*) \rightarrow Rh_2(\sigma^*)$ transitions. The bands in the region 340-380 nm are predicted to be strong and originate from HOMO, HOMO-1 to the low lying orbitals including LUMO+1 to LUMO+4 orbitals. Similarly to **5** and **6**, the first two electronic transitions for **7** are mainly HOMO and HOMO-1 to LUMO occurring at λ = 413 and 388 nm (f = 0.0024 and 0.0008, respectively). These hypsochromic shifts, as compared to **3**, are also due to the larger HOMO-LUMO energy gap. The excited states 3-5 arise from HOMO, HOMO-1 to LUMO+1 and LUMO+2 transitions in the region 340-360 nm, and have similar characters and energies to those in **5** and **6**.

In the orthometalated complex **4**, the lowest energy transition at 442 nm (f = 0.0223) corresponds to HOMO-4 and HOMO to LUMO transitions, rendering it $Rh_2(\pi^*) \rightarrow Rh_2(\sigma^*)$ MC in character (Table 2.12). The absorption at ~ 360 nm involves a series of transitions from orbitals including the HOMO-4 and HOMO→LUMO and thus they have dual LMCT and MC characters. The strong absorptions at ~320 nm are mainly transitions from orbitals with both bridging ligand and metal contributions to the LUMO, thus also rendering them LMCT/MC in character but with much stronger oscillator factors as compared to the transitions at ~360 nm. Remarkably, in the methyl isocyanide analog **8**, the lowest energy transition is expected at 376 nm with a very strong oscillator factor f = 0.2222; this is mainly the HOMO $Rh_2(\sigma) \rightarrow$ LUMO $Rh_2(\sigma^*)$ transition and it

has a high molar absorptivity because it is allowed by the Laporte rules ($\sigma_g \rightarrow \sigma_u$ orbital transition). The absorption shoulder at ~ 310 nm arises from transitions from the HOMO to the vacant LUMO and LUMO+1 orbitals, whereas the absorption at ~ 290 nm involves transitions from the HOMO to orbitals ranging from LUMO+2 to LUMO+4. Depopulation of the high energy HOMO $Rh_2(\sigma)$ orbital essentially induces cleavage of the Rh-Rh bond, which explains the instability of compound **8** (*vide supra*).

Table 2.11 Excited states calculated by TD-DFT/PCM (CH_3CN as the solvent), with major transitions involved in the excitations, transition coefficients, vertical excitation energies (nm), and oscillator strengths (*f*) for **3** and **7**.

3				**7**			
excitations		E/ nm	*f*	excitations		E/ nm	*f*
H ->L	94.15%	538	0.0006	H ->L	91.41%	413	0.0024
H ->L+1	62.21%	452	0.0030	H-1 ->L	90.98%	388	0.0008
H-1 ->L	56.63%	437	0.0029	H ->L+1	81.08%	361	0.0298
H-10 ->L	81.03%	430	0.0003	H-1 ->L+1	72.77%	349	0.0060
H-9 ->L H-1 ->L	61.44% 24.54%	424	0.0005	H ->L+2	75.31%	336	0.0028
H ->L+4	69.52%	382	0.0107	H-2 ->L H-1 ->L+2	47.27% 30.88%	325	0.0282
H-1 ->L+1	88.11%	366	0.0006	H-2 ->L+1	63.75%	318	0.0078
H ->L+2	94.51%	347	0.0198	H-1 ->L+2	36.39%	315	0.0853
H ->L+3	44.82%	340	0.1346	H ->L+3	52.51%	302	0.2781
H-10 ->L+1	48.22%	331	0.0428	H-13 ->L H-3 ->L	34.27% 30.09%	302	0.0175

* $2|\text{coefficient}|^2 > 0.2$

Table 2.12 Excited states calculated by TD-DFT/PCM (CH_3CN as the solvent), with major transitions involved in the excitations, transition coefficients, vertical excitation energies (nm), and oscillator strengths (*f*) for **4** and **8**.

4				**8**			
excitations		E/ nm	*f*	excitations		E/ nm	*f*
H-4 ->L	24.82%	442	0.0223	H ->L	87.54%	346	0.2222
H ->L	48.85%						
H-3 ->L	67.17%	441	0.0000	H ->L+1	83.60%	312	0.0012
H-1 ->L	22.08%						
H-3 ->L	22.51%	364	0.0012	H ->L+2	67.77%	306	0.0183
H-1 ->L	64.24%						
H-4 ->L	32.91%	359	0.0074	H-2 ->L	72.75%	294	0.0007
H-2 ->L	34.18%						
H ->L	20.00%						
H-14 ->L	15.07%	327	0.1063	H ->L+2	20.60%	290	0.0108
H-2 ->L	18.65%			H ->L+3	38.38%		
H-17 ->L	22.26%	322	0.0027	H-13 ->L	65.68%	288	0.0021
H-2 ->L	26.04%	317	0.1262	H-3 ->L	50.27%	287	0.0349
H ->L+1	44.44%	312	0.0017	H-1 ->L	43.00%	285	0.0959
				H ->L+3	22.18%		
H ->L+2	29.04%	308	0.0009	H ->L+4	79.91%	284	0.0010
H-3 ->L+1	32.76%	299	0.0056	H ->L+5	80.72%	269	0.0007

* $2|\text{coefficient}|^2 > 0.2$

Infrared spectroscopy

A summary of the ν(NC) stretching frequencies for **5-8**, and other reported Rh(II) and Rh(I) isocyanide compounds is provided in Table 2.13. As explained in the computational section (*vide supra*), the strength of the CN bond (and thus the stretching frequencies) in methyl isocyanide can be influenced by two interdependent factors: on the one hand, methyl isocyanide donates electron density to the $Rh_2(\sigma^*)$ orbitals from its σ^*(CN) orbital (HOMO), which is antibonding in character;[138] this fact is expected to increase the ν(NC) stretching frequency as compared to free CH_3NC.[139] Conversely, as a good π-acceptor, methyl isocyanide can accept electron density by backbonding from the Rh-Rh centers into the low lying π^* molecular orbital, which results in elongation of the CN bond and a decrease in the ν(NC) stretching frequencies as compared to free CH_3NC (similar to π-backbonding for CO,[75,79-80] *e.g.*, ν(CO) in $Rh_2(O_2CC_3H_7)_4(CO)_2$[79] and *cis*-$[Rh_2[Ph_2P(C_6H_4)]_2(O_2CCH_3)_2(CO)(CH_3CO_2H)]$ is shifted to 2095 cm^{-1} and 2028 cm^{-1}, respectively, as compared to 2143 cm^{-1} for free CO. In the case of compounds **5-8** (Table 2.13), the net result is a large shift for ν(NC) by ~60-80 cm^{-1} to higher frequencies as compared to CH_3NC,[139] which reflects the dominant effect of σ-donation from the methyl isocyanide groups to the $Rh_2(\sigma^*)$ orbital in these complexes.[80]

Table 2.13 The ν(NC) (cm^{-1}) stretching bands for isocyanide groups in the free ligands and **5-8**.

Compound	ν(NC) (cm^{-1})	Ref.
CH_3NC	2161[a]	139
5	2241(s), 2265(s)[b]	This work
6	2233(s)[b]	This work
7	2244(s), 2264(s)[b]	This work
8	2219(s)[b]	This work
$Rh_2(O_2CCH_3)_4$•$2CNC_6H_5$ [c]	2139	84
$Rh_2(O_2CCH_3)_4$•$2(CNBu^t)$ [c]	2150, 2130(s)[d]	84
$Rh_2(pz)_2(CNBu^t)_4I_2$ [c]	2199, 2173	97
$[Rh_2(pz)_2(CNBu^t)_4(CH_3CN)_2][PF_6]_2$ [c]	2224, 2203(s)	97
$[Rh_2(CNC_6H_{11})_8Cl_2][BF_4]_2$ [c]	2219	96
$[Rh_2(p\text{-}CH_3C_6H_4NC)_8I_2][PF_6]_2$	2194	95
$[Rh_2(p\text{-}CH_3C_6H_4NC)_8Br_2][PF_6]_2$	2199	95
$[Rh_2(dppm)_2(CNCH_3)_4I_2][BPh_4]_2$[e]	2215[f]	92
$[Rh_2(dppm)_2(CNCH_3)_2(SCF_3)_2][PF_6]_2$[e]	2214[f]	93
$[Rh_2(dppm)_2(CNCH_3)_4][PF_6]_2$[d]	2174[f]	92
$[Rh_2(dpam)_2(CNCH_3)_4][BPh_4]_2$[f]	2196, 2172[b]	93

[a]Sample at partial pressure 0.025 atm in N_2 (1 atm). [b]Nujol mull, KBr. [c]ν(NC) (cm^{-1}): C_6H_5NC, 2117; Bu^tNC, 2139; $C_6H_{11}NC$, 2138.[140] [d]In CH_2Cl_2. [e]dppm: $(C_6H_5)_2PCH_2P(C_6H_5)_2$. [f]dpam: $(C_6H_5)_2AsCH_2As(C_6H_5)_2$.

In dirhodium complexes with ax isocyanide groups only, *e.g.*, $Rh_2(O_2CCH_3)_4$•$2CNC_6H_5$, $Rh_2(O_2CCH_3)_4$•$2(NCBu^t)$, there is a moderate shift of ν(NC) of ~20 cm^{-1} to higher frequencies relative to the unperturbed isocyanide molecules [84, 140] (Table 2.13). In the case of the methyl isocyanide complexes **5-8**, however, the effect is more pronounced due to the σ-donation of both axially and equatorially bound isocyanide groups. Analogous large shifts of ν(NC) by ~80 cm^{-1} to higher frequencies have been reported for other dirhodium complexes with eq isocyanide groups, *e.g.*, $[Rh_2(pz)_2(CNBu^t)_4(CH_3CN)_2][PF_6]_2$, $[Rh_2(p\text{-}CH_3C_6H_4NC)_8I_2][PF_6]_2$, $[Rh_2(CNC_6H_{11})_8Cl_2][BF_4]_2$ and others (Table 2.13). This σ-donation from the eq bonds has a substantial effect, as it is well established for compounds with Rh-Rh bonds that the eq bonds to the Rh atoms are stronger than the ax interactions for the same ligand. Moreover, the strong σ-donation from the methyl isocyanide groups to the $Rh_2(\sigma^*)$ orbital for Rh(II) complexes is also corroborated by the fact that the ν(NC) is smaller in Rh(I) complexes, as in these cases, the π-backbonding, which results in a weakening of the CN bond, is more prominent, *e.g.*, the last two Rh(I) isocyanide compounds listed in Table 2.13.[92]

For complexes **1-4**, the stretching frequencies ν(CN) of CH_3CN also shift to higher frequencies by ~60-80 cm^{-1} (Table 2.14) as compared to free CH_3CN (2253 cm^{-1}) which indicates a strengthening of the CN bond attributed to σ-donation from the nitrogen lone pair of the acetonitrile, which is antibonding in character, to the metal orbitals.[141]

Table 2.14 The ν(CN) (cm^{-1}) for the CH_3CN stretches in the free ligand and **1-4**.

Compound	ν(CN) (cm^{-1})
CH_3CN	2253
1	2326(w), 2303(m), 2276(w)[a]
2	2334(w), 2308(m), 2276(w)[a]
3	2330(m), 2310(m), 2280(w)[a]
4	2314(m), 2286(sh), 2268(m)[a]
$[Rh_2(CH_3CN)_{10}][BF_4]_4$[b]	2300(w), 2317(m), 2342(m)[c]
$[Rh_2(CH_3CN)_{10}][CF_3SO_3]_4$[b]	2286(m), 2316(w), 2345(m)[c]

[a]Nujol mull, KBr. [b] Ref.142 [c]Nujol mull, CsI.

Electrochemistry

The electrochemical data for **1-8** are summarized in Table 2.15 and representative cyclic voltammograms are displayed in Figure 2.20 (for **2** and **6**). The dirhodium compounds **1-3** and **5-7**, supported by N-N type bridging ligands, exhibit two metal-centered one-electron reductions and two one-electron oxidation processes (the first oxidation event is reversible). There is a second reduction at ~ -1.20 V unlike the series of dirhodium substituted tetraformamidinate complexes reported by Ren *et al.*,[143] an indication of the better π-accepting ability of both CH_3NC and CH_3CN *vs.* the formamidinate groups. The second reductions for **5-7** are irreversible, however, an indication that the doubly reduced species for these electron-rich adducts are unstable. Furthermore, the oxidation processes of **1-3** and **5-7** shift to higher potentials as compared to $Rh_2(DPhF)_4$, which further supports the effect of the π-accepting ability of the CH_3NC and CH_3CN ligands. In this respect, compounds **1-3** are easier to oxidize than the methyl isocyanide analogs **5-7**, respectively, which attests to the improved π-accepting ability of CH_3NC relative to

Table 2.15 Electrochemical data (V) for **1**-**8** in CH_3CN.[a]

Compound		$E_{1/2(red)1}$ (V)	$E_{1/2(red)2}$ (V)	$E_{1/2(ox)1}$ (V)	$E_{1/2(ox)2}$ (V)
$[Rh_2(DTolF)_2(CH_3CN)_6][BF_4]_2$	**1**[b]	-0.50	-1.33	+0.98	+1.40
$[Rh_2(F\text{-}form)_2(CH_3CN)_6][BF_4]_2$	**2**[b]	-0.47	-1.26	+1.13	+1.63
$[Rh_2(NNN)_2(CH_3CN)_6][BF_4]_2$	**3**[b]	-0.35[e]	-1.22	+1.19	+1.49
$[Rh_2[Ph_2P(C_6H_4)]_2(CH_3CN)_6][BF_4]_2$	**4**[b,c]			+1.54	
$[Rh_2(DTolF)_2(CNCH_3)_6][BF_4]_2$	**5**[b]	-0.67	-1.20[f]	+1.13	+1.43
$[Rh_2(F\text{-}form)_2(CNCH_3)_6][BF_4]_2$	**6**[b]	-0.61	-1.09[f]	+1.32	+1.70[f]
$[Rh_2(NNN)_2(CNCH_3)_6][BF_4]_2$	**7**[d]	-0.58[f]	-1.18[e]	+1.28	+1.50
$[Rh_2[Ph_2P(C_6H_4)]_2(CNCH_3)_6][BF_4]_2$	**8**[b]	-1.38[f]		+1.23	
$Rh_2(DTolF)_4$[g]		-1.40		+0.17	+0.68

[a]Data collected in ~ 0.10 M [n-Bu_4N][PF_6] as supporting electrolyte at a scan rate of 0.2 V/s at 25° C. [b]*vs.* Ag/AgCl. [c]In CH_2Cl_2. [d]Glassy carbon working electrode. [e]Quasi-reversible. [f]Irreversible. [g]Ref.143

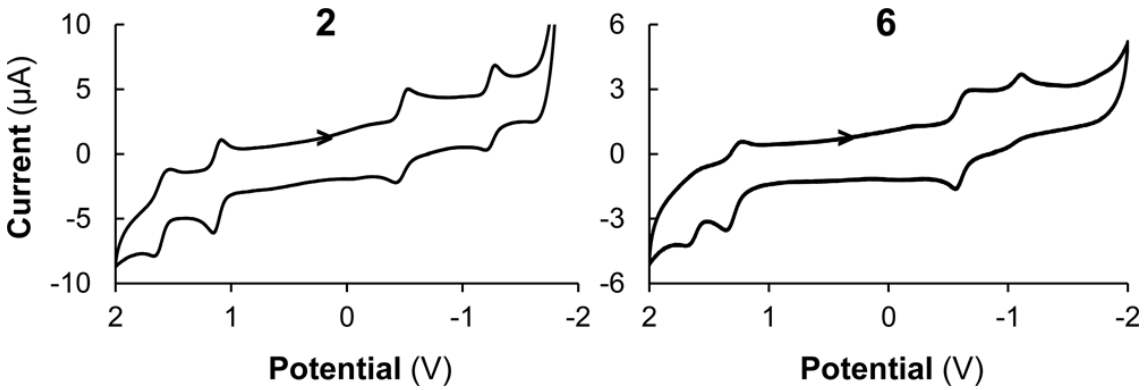

Figure 2.20 Cyclic voltammograms of **2** and **6** *vs.* Ag/AgCl in CH_3CN (~ 0.10 M [n-Bu_4N][PF_6] as supporting electrolyte) at a scan rate of 0.2 V/s at 25°C.

CH_3CN. Also, as expected, the methyl isocyanide analogs **5-7** are more difficult to reduce than the respective acetonitrile adducts **1**-**3** (the potentials for **5**-**7** shift to more negative values by ~ 0.15 V; Table 2.14) owing to the enhanced σ-donating ability of CH_3NC as compared to CH_3CN, which renders the dirhodium core more electron-rich in the isocyanide series.

The axial isocyanide adduct $Rh_2(DPhF)_4(CNC_6H_5)$ is not reduced within the negative potential limit of CH_2Cl_2 (- 1.8 V) in contrast to $Rh_2(DPhF)_4$, which is reduced at - 1.21 V under the same experimental conditions.[82] Compounds **1** and **5** undergo more facile oxidations, as compared to **2** and **6**, respectively, which is ascribed to the strong electron-withdrawing ability of the fluorine substituents on the formamidinate bridging ligands of the latter (based on the calculations, there is significant contribution to the HOMO from the bridging formamidinate ligands, Tables 2.5-2.7); similar trends were observed for the substituted $Rh_2(R\text{-}DPhF)_4$ series reported by Ren *et al.*,[143] but the differences in the reduction potentials between **1**, **2** and **5**, **6** are much smaller, findings that are corroborated by the proximity between the LUMO orbitals of each set of complexes (Figure 2.19).

In the case of **4**, there is only one reversible oxidation at ~ +1.54 V, whereas this oxidation is shifted to ~ +1.23 V for **8**, indicating the destabilization of the HOMO. This oxidation is assigned to the $Rh_2(II,II)/Rh_2(II,III)$ redox couple as in the case of *cis*-$Rh_2[Ph_2P(C_6H_4)_2]_2(O_2CCH_3)_2$. No reduction was observed within the solvent limit for compound **4**. A reduction for **8** occurs at ~ - 1.38 V but the irreversibility of the process indicates the instability upon reduction. The electrochemical behavior of **4** and **8**, with

respect to reduction, is attributed to the strong σ-donating ability of the phosphine groups,[81]which increases the electron density of the dirhodium core.

Discussion

Two series of partial paddlewheel dirhodium compounds supported by σ-donating bridging N-N or orthometalated phosphine ligands and either monodentate acetonitrile (**1**-**4**) or methyl isocyanide (**5**-**8**) groups in the unoccupied eq/ax positions were synthesized and investigated by X-ray crystallography, ^{1}H, ^{31}P NMR, electronic and infrared spectroscopies, cyclic voltammetry and theoretical calculations. In each series, the dirhodium core is supported by substituted formamidinates, triazenide or phosphine bridging groups. The substitution of the acetonitrile for methyl isocyanide ligands in **5**-**8** leaves the dirhodium core framework intact but results in substantial differences in the structural, spectrochemical and electrochemical behavior of the two classes of compounds. The findings from the X-ray crystallography, the electronic and infrared spectroscopies as well as the cyclic voltammetric and computational studies nicely converge and support the conclusions presented for the two series of complexes.

Compounds **5**-**8** are unprecedented partial paddlewheel Rh_2(II,II) compounds with a single metal-metal bond, with four eq and two ax positions occupied by methyl isocyanide ligands. The substitution of the CH_3CN ligands with CH_3NC results in marked differences in the corresponding distances between the two series **1**-**4**/**5**-**8** and allows for pertinent correlations that reflect the differences in the electronic structures of the monodentate ligands. The distances to the atoms engaged in short contacts with the Rh_2(II,II) units for **1**-**8** are summarized in Tables 2.16 and 2.17. It is important to note

Table 2.16 Summary of important bond distances (Å) in **1**-**3** and **5**-**7**.

	Rh-Rh (Å)	Rh-L_{ax} (Å)	Rh-L_{eq} (Å)[c]	Donor Atom[d]	L (CN)[c,d] (Å)	Rh-N (Å)[c]
1	2.5594(8)	2.208(7)[a]	2.020(6)[a]	N	1.132(9)[a]	2.026(6)
		2.235(7)	2.029(7)		1.138(8)	2.037(6)
2	2.571(1)	2.195(4)[a]	2.032(5)[a]	N	1.134(8)[a]	2.038(5)
		2.251(4)	2.040(5)		1.140(7)	2.046(5)
3	2.5135(9)	2.202(7)[a]	2.004(6)[a]	N	1.12(1)[a]	2.024(6)
		2.225(7)	2.024(6)		1.13(1)	2.023(6)
5	2.6262(4)	2.080(2)[b]	1.935(2)[b]	C	1.137(3)[b]	2.081(2)
		2.099(2)	1.948(2)		1.139(3)	2.093(2)
6	2.6104(9)	2.074(4)[b]	1.937(5)[b]	C	1.131(5)[b]	2.081(3)
		2.133(4)	1.951(4)		1.143(5)	2.094(3)
7	2.5852(6)	2.089(4)[b]	1.943(5)[b]	C	1.137(7)[b]	2.078(3)
		2.093(4)	1.950(5)		1.143(6)	2.089(3)
CH_3CN					1.158[e]	
CH_3NC					1.167[e]	

[a]L is CH_3CN. [b]L is CH_3NC. [c]Representative distances are listed. [d]Ax and eq ligands are the same. [e]Distances within monodentate ligands; Ref. 144.

Table 2.17 Summary of important bond distances (Å) in **4** and **8**.

Cmpd	Rh-Rh (Å)	Rh-L_{ax} (Å)	Rh-L_{eq} (Å)[c,d]	Donor	Rh-C[e] (Å)	Rh-P (Å)
4-*R*	2.656(1)	2.196(6)[a]	2.104(6)[a]	N[c]	2.01(2)	2.232(7)
			2.142(6)			
4-*S*	2.655(1)	2.202(6)[a]	2.127(5)[a]	N[c]	2.024(5)	2.228(2)
			2.131(5)			
8-*R*	2.766(1)	2.033(3)[b]	2.005(3)[b]	C[c]	2.096(3)	2.3056(8)
		2.040(2)	2.011(3)		2.099(3)	2.3076(8)
8-*S*	2.7682(6)	2.023(4)	2.007(2)[b]	C[c]	2.078(2)	2.2929(9)
		2.037(4)[b]	2.009(2)		2.090(3)	2.3077(9)

[a]CH_3CN groups. [b]CH_3NC groups. [c]Ax and eq ligands are the same. [d]Representative bonds are listed. [e]C atoms of bridging orthometalated phosphine groups. [f] Ref.134

that, in contrast to compounds **5-8**, which are the first of their kind to be prepared by substitutions of the ax/eq monodentate ligands with methyl isocyanide, the few reported Rh_2(II,II) compounds with isocyanide groups occupying eq positions (Table 2.18) were synthesized by oxidative addition of halogens to Rh(I) isocyanide precursors [93,94] or by the reaction of Rh(I) and Rh(III) mononuclear complexes. [92] These compounds exhibit significantly different structural parameters than those found for **5-8** (Tables 2.16, 2.17). The dearth of the type of compounds of the type in this study is likely related to the fact that the stabilization of isocyanide metal-metal bonded compounds is non-trivial due to the non-innocent character of the isocyanide ligands, which leads to reduction of the metal centers and cleavage of the metal-metal bonds.[84]

Table 2.18 Summary of important bond distances (Å) in dirhodium compounds with isocyanide ligands.

Compound	Rh-Rh (Å)	Rh-C (Å)	Ref
$Rh_2(O_2CCH_3)_4$•$2CNC_6H_4N(CH_3)_2$	2.4245(4)	2.148(4)[a]	133
$Rh_2(O_2CCH_3)_4$•$2CNC_6H_5$	2.4271(3)	2.133(3)[a]	133
$Rh_2(O_2CCH_3)_4$•$2CNC_6H_5CF_3$	2.4182(3)	2.122(3)[a]	133
$Rh_2(DPhF)_4$•(CNC_6H_5)	2.4798(4)	1.991(4)[a]	82
$Rh_2(DPhF)_4(CNC_6H_4NC)Rh_2(DPhF)_4$	2.496(1)	1.988(9)[a]	82
$[\{Rh_2(\mu\text{-}pz)_2(I)(CN^tBu)_4\}_2(\eta\text{-}I)][CF_3SO_3]$	2.632(3) 2.605(3)	1.90(1)[b] 1.93(1)	97
$[Rh_2(\mu\text{-}dppm)_2(pz)(CN^tBu)_2Cl_2][PF_6]$	2.768(1)	1.933(5)	98
$[Rh_2[CN(CH_2)_3NC]_4Cl_2]Cl_2$	2.8377(9)	1.9887(7)[b]	89
$[Rh_2(CNC_6H_{11})_8Cl_2][BF_4]_2$	2.6944(4)	1.980(3)[b]	96
$[Rh_2(TMB)_4Cl_2][PF_6]_2$[c]	2.773(2)	1.96(2)[b]	91
$[Rh_2(DMB)_4Cl_2]Cl_2$[d]	2.8464(3)	1.982(4)[b]	100
$[Rh_2(p\text{-}CH_3C_6H_4NC)_8I_2][PF_6]_2$	2.785(2)	1.97-1.99[b]	95

[a]Ax isocyanide groups. [b]Eq isocyanide groups. [c]TMB: 2,5-diisocyano-2,5-dimethylhexane. [d]DMB: 2,2-dimethyl-1,3-diisocyanopropane.

*Dirhodium coordination sphere, σ-bonding and π-backbonding in **1-8***

It is notable that the Rh-Rh bond distances in **5-7** are elongated by up to ~ 0.07 Å relative to **1-3** (Table 2.16), respectively, and by ~0.10 Å in **8** as compared to **4** (Table 2.17**)**, which indicates stronger interactions between the ax CH_3NC ligands and the rhodium centers in the isocyanide series. This fact is also confirmed by the shorter Rh-C (ax CH_3NC) bond distances in **5-8** as compared to the Rh-N distances in **1-4** (Tables 2.16, 2.17). The aforementioned findings are the result of two interdependent factors, which are reflected in the differences in the MOs of the two ligands. As noted earlier, the superior σ-donating ability of CH_3NC relative to CH_3CN is attributed to the fact that the HOMO of CH_3NC is at higher energy than that of CH_3CN, whereas the enhanced π-accepting ability of CH_3NC is due to the lower lying LUMO+1, LUMO+2 (Figure 2.10) orbitals. On the one hand, the strong σ-donation from the ax CH_3NC groups to the $Rh_2(\sigma^*)$ orbitals results in elongation of the Rh-Rh bond distances[145] and shortening of the CN bond distances in CH_3NC (the distances in the **5-8** are shorter than in the free ligand; Tables 2.16, 2.17) due to the π* antibonding character of the HOMO for CH_3NC. On the other hand, the donation of electron density from the $Rh_2(\pi^*)$ orbitals to the low-lying π* orbitals of the CH_3NC ligands, due to the good π-accepting ability of CH_3NC, results in a reduction of the Rh-Rh bond distances and elongation of the CN bonds. The net elongation of the Rh-Rh bond distances in **5-8** and the shortening of the CN bonds by ~ 0.02-0.04 Å as compared to free CH_3NC (Tables 2.16, 2.17) strongly suggest that the σ-donation of the ax CH_3NC ligands is more dominant than the backbonding in **5-8**. This

conclusion is also clearly corroborated by the ν(CN) frequencies of the methyl isocyanide groups in **5**-**8**, which are higher by $\nu\sim$ 60-80 cm^{-1} as compared to free methyl isocyanide (Table 2.13); as explained earlier, this is due to donation of electron density from the σ* NC antibonding HOMO orbital to the Rh_2(σ*) orbitals of the complexes, thus rendering the NC bonds in the bound methyl isocyanide groups shorter than the free ligand (Tables 2.16, 2.17). A similar shortening of the CN bonds in CH_3CN is also observed for the acetonitrile series **1**-**4** (Table 2.16). The strengthening of the CN bonds in **1**-**4** is also in agreement with the observed increase in the stretching frequencies ν(CN) by ~ 60-80 cm^{-1} of the bound ligand as compared to free CH_3CN (Table 2.14).[141] The contraction of the CN bonds for the bound CH_3CN groups in **1**-**4**, however, is less than the corresponding one in **5**-**8**, as compared to the free ligands in each case (Tables 2.16, 2.17), reflecting the better σ-donating ability of CH_3NC as compared to CH_3CN.

Apart from the aforementioned Rh-Rh and CN distances in **1**-**8**, of pertinence to this discussion are the Rh-N and Rh-C distances in **1**-**4** and **5**-**8**, respectively. Due to the smaller covalent radius of N *vs.* C, the Rh-N (CH_3CN) distances in **1**-**4** would be expected to be shorter than the Rh-C (CH_3NC) distances in **5**-**8**, in the absence of π-backbonding. In our series, however, the bond distances Rh-C (CH_3NC) in **5**-**8** are considerably shorter as compared to Rh-N (to CH_3CN) in **1**-**4** (Tables 2.16, 2.17), which strongly supports the presence of significant π-backbonding in the case of the methyl isocyanide series. An analogous shortening of the Rh-C bond distances has been observed for other reported dirhodium isocyanide complexes (Table 2.18) for which the Rh-C bond distances are typically in the range 1.98-2.1 Å, *i.e.*, shorter by 0.20-0.5 Å

than the Rh-C bond distances in dirhodium complexes with weak π-donor molecules such as (-)-*trans*-caryophyllene (~2.46, 2.62 Å),[146] other olefins, substituted alkynes, benzene and hexamethylbenzene, polycyclic aromatic hydrocarbons, and the geodesic polyarene corannulenes and hemibuckminsterfullerenes which exhibit considerably longer ax Rh-C bonds (~2.5-2.7 Å). In agreement with the presence of considerable π-backbonding from $Rh_2(\pi^*)$ to π* (CH_3NC) and shorter Rh-C bond distances in **5**-**8**, the Rh-Rh bond distances are also longer in the latter series as compared to **1**-**4** (Tables 2.16, 2.17).[141] The presence of significant π-backbonding from the dirhodium core to the methyl isocyanide groups in **5**-**8** accounts for the more positive oxidation potentials of **5**-**8** with respect to **1**-**4** (Table 2.15), as there is reduced electron density on the dirhodium core in **5**-**8**, thus rendering it more difficult to oxidize the isocyanide series. On the other hand, the more negative reduction potentials for **5**-**8** are in accord with the enhanced σ-donation of CH_3NC.

As reported by Christoph *et al.* and Eagle *et al*., both the σ-donor and π-acceptor abilities of the ligands have an impact on the Rh-Rh and Rh-L (ax) structural parameters,[22,133] which is clearly demonstrated by comparing **1**-**4** with **5**-**8**. The strong *trans* influence that gives rise to the inverse relationship of the Rh-Rh and Rh-N/Rh-C (ax) distances,[22, 147] namely isocyanide adducts with the shorter Rh-C ax bonds exhibit longer Rh-Rh distances as compared to the acetonitrile series with shorter Rh-Rh and longer ax Rh-N distances (Tables 2.16, 2.17). Furthermore, the *trans* influence is also obvious when comparing the Rh-L (eq) monodentate ligand and the Rh-N (bridge) distances between the two series. The shorter bond distances Rh-C (eq CH_3NC) in **5**-**7**,

indicating the stronger interactions between the Rh centers and the eq CH_3NC ligands due to π-backbonding, result in the elongation of the *trans* Rh-N (bridging group) distances by ~0.05 Å as compared to their CH_3CN analogs **1**-**3** with weaker Rh-N eq bonds to the acetonitrile ligands. The short bond distances Rh-C (eq CH_3NC) in **5**-**7** (and thus stronger bonds) are also supported by the absence of CH_3NC ligand exchange with the solvent in the ^1H NMR spectra of the isocyanide complexes even after 1 week (*e.g.*, Figure 2.7). Short Rh-C (CH_3NC) contacts are also encountered in both isomers of **8** with remarkably short Rh-C (ax $CNCH_3$) bond distances that are only ~ 0.02 Å longer than the Rh-C (eq $CNCH_3$) distances (Table 2.17). To the best of our knowledge, the latter finding is unprecedented for Rh_2(II,II) compounds, as it is well-known that the ax ligands typically establish weaker contacts with the dirhodium core as compared to the same identity eq ligands, *e.g.*, in the case of **1**-**3** the contacts to the eq CH_3CN groups are up to 0.2 Å shorter than the ax distances, and in the cases of **4**-**7**, the eq contacts are shorter by ~ 0.10 Å. In particular, the Rh-N (ax CH_3CN) bond distances (2.202(6) and 2.196(6) Å) for compound **4** are much longer than Rh-N (eq CH_3CN) (in the range 2.104(6)-2.142(6) Å). The extremely short Rh-C (ax CH_3NC) bonds in **8** as well as the considerably shorter Rh-C (ax CH_3NC) in **5**-**7**, as compared to other dirhodium compounds with ax C atom donors,[146 146] are correlated to the increased electron density on the dirhodium core (arising from the strong σ-donation of the orthometalated phosphine bridging groups, which increases the degree of π-backbonding to the π-acceptor isocyanide ligands and thus strengthens the Rh-C bonds). In this respect, for example, the Rh-C (ax CH_3NC) bond distances in **5**-**7** are shorter than the distances in

the tetra-acetate adducts with isocyanide $Rh_2(\mu\text{-}O_2CCH_3)_4$•2L (L = $2CNC_6H_4N(CH_3)_2$, CNC_6H_5, $CNC_6H_5CF_3$; ~ 2.14 Å) but longer than the corresponding ax distances in $Rh_2(DPhF)_4(CNC_6H_5)$ and $Rh_2(DPhF)_4(CNC_6H_4NC)Rh_2(DPhF)_4$ (~ 1.99 Å; Table 10)[82] as well as in **8** (~ 2.03 Å; Table 2.17). The previous Rh-C (ax CH_3NC) bond distances decrease in the order of increasing number of strong σ-donor formamidinate or phosphine bridging ligands bound to the dirhodium core, rendering it progressively more electron-rich and thus a better candidate for π-backbonding and shorter Rh-C (ax CH_3NC) distances. The higher degree of π-backbonding in the case of **8** as compared to **5-7** is also reflected by the lower ν(NC) frequency of the CH_3NC groups in **8** (by ~20-30 cm^{-1}; Table 2.13) *vs.* **5-7**.

As previously detailed, the short Rh-C (eq $CNCH_3$) contacts and the concomitant significant π-backbonding from the dirhodium unit to the CH_3NC ligands in **5-7** relative to **1-3** lead to the stabilization of the $Rh_2(\pi^*)$ orbitals (due to the higher contribution from the low-lying π* orbitals of CH_3NC in **5-7**; Tables 2.4-2.7), which result in the $Rh_2(\pi^*)$ being of lower energy than that of the $Rh_2(\sigma)$ level (Figures 2.11, 2.12). In the case of **8**, however, apart from the strong eq CH_3NC contacts, the strong Rh-C bonds with the ax CH_3NC ligands, which are shorter by 0.05 Å as compared to **5-7**, greatly destabilize the $Rh_2(\sigma)$ bond (Figure 2.14), which complies with the considerably longer Rh-Rh distances in **8** (~ 2.76 Å; Table 9) as compared to **4**, as well as with the observed relative instability of **8** in solution, as evidenced by the ^1H, ^{31}P NMR data (Figure 2.8) and the ESI-MS fragmentation pattern. The previous findings are in accord with the strong *trans* influence of the ax Rh-C bonds on the Rh-Rh bond in **8**. Similarly, the

shorter Rh-C (eq $CNCH_3$) contacts in **8** exert a strong *trans* influence on the bridging orthometalated ligands, thus resulting in elongation of the Rh-C (bridge) and Rh-P bonds by ~0.1 and 0.08 Å, respectively (Table 9), as compared to the orthometalated adducts *cis*-$[Rh_2(O_2CCH_3)_2[Ph_2P(C_6H_4)]_2]\bullet 2CH_3CO_2H$ and *cis*-$[Rh_2(O_2CCH_3)_2[Ph_2P(C_6H_4)]_2]\bullet 2C_5H_5N$ with bridging carboxylate groups. [134]

*Molecular orbital energy levels, spectroscopic and electrochemical studies for **1**-**8***

The stronger σ-donating ability of the ax isocyanide groups in **5**-**8** leads to the destabilization of the LUMO $Rh_2(\sigma^*)$ orbitals (Figures 2.11, 2.12 and 2.14) in **5**-**8** *vs.* **1**-**4**. Furthermore, the non-bonding HOMOs of **5**-**7** are stabilized as compared to the antibonding HOMOs of their CH_3CN analogs **1**-**3** (Figures 2.11, 2.12). The aforementioned shifts in the HOMO/LUMO relative energy levels, resulting in larger HOMO-LUMO energy gaps in **5**-**8** *vs.* **1**-**4** (Figures 2.11, 2.12), clearly account for the experimentally observed hypsochromic shifts of the lowest energy transitions in the visible spectra (~360-450 nm) of the isocyanide series **5**-**8**, by ~80-100 nm, relative to the corresponding acetonitrile analogs **1**-**4** (comparisons between **1** and **5**, **2** and **6**, **3** and **7**, **4** and **8**; Table 2.3); an increase in the lowest energy bands of the dirhodium core with increasing donor strength of the ax ligands was previously recorded.[148] Importantly, the results from the TD-DFT calculations (Tables 2.9 – 2.12 and Figures 2.15, 2.16) provide strong support for the previous hypsochromic shifts of the low energy bands in the electronic spectra of **5**-**8** as compared to **1**-**4**. In particular, in the case of **8**, the TD-DFT calculations are not only in agreement with the experimentally observed hypsochromic shift of the low-energy MC band to 362 nm (from ~478 nm in **4**), but they also support the

nearly 20-fold increase of the band intensity in **8** ($\varepsilon \sim 10^4$ $M^{-1}cm^{-1}$) with respect to **4** ($\varepsilon \sim 6$ x 10^2 M^{-1} cm^{-1}; Table 2.3, Figure 2.9d) based on the calculated strong oscillator factor for **8** (Table 2.12). The MC band at 362 nm, which is assigned to the HOMO $Rh_2(\sigma)\rightarrow$LUMO $Rh_2(\sigma^*)$ transition in **8**, exhibits a high molar absorptivity, as compared to a typical d-d electronic transition because it is allowed by the Laporte rules ($\sigma_g\rightarrow\sigma_u$ transition). The stronger interactions of the dirhodium core with the ax CH_3NC ligands increase the energy of the $Rh_2(\sigma)$ orbital considerably, rendering it the HOMO in **8** (Figure 2.14) as opposed to **4** where the lowest energy transition is the HOMO $Rh_2(\pi^*)\rightarrow$LUMO $Rh_2(\sigma^*)$ and thus of considerably lower intensity (Figure 2.9d, Table 2.3). The $Rh_2(\sigma)$ orbital has been reported to become the HOMO for dirhodium tetracarboxylate complexes with strong ax ligands, *e.g.*, phosphines.[79,149-151] Larger energy gaps for the MC $Rh_2(\pi^*)\rightarrow Rh_2(\sigma^*)$ transitions were also rightfully anticipated by the TD-DFT calculations, which corroborate the hypsochromic shifts of the electronic transitions in **5-7** as compared to **1-3**, respectively (in the range 425-440 nm for **1-3** *vs.* 295-300 nm for **5-7**; Tables 2.9-2.12). Accordingly, the slight hypsochromic shift of the lowest energy HOMO-LUMO transition in **2** as compared to **1** (Table 2.3, Figure 2.9a) is in agreement with the TD-DFT calculations (Table 2.9) and is attributed to the greater stabilization of the HOMO (primarily of bridging formamidinate ligand character) in **2** (Figure 2.19) due to the electron-withdrawing F substituents on the formamidinate bridging ligands.

It is notable that the DFT calculations are also in excellent agreement with the findings from the electrochemical studies. In particular, the stabilization of the HOMO orbitals in compounds **5-7**, as compared to **1-3** (Figure 2.19) is corroborated by the

higher oxidation potentials of the isocyanide series **5-7** *vs.* the acetonitrile analogs **1-3**, respectively (Table 2.15); this is ascribed to the π-backbonding from the dirhodium core to the CH_3NC groups. Correspondingly, the higher energy of the LUMO orbitals for compounds **5-7** (Figure 2.19) is in agreement with the isocyanide analogs **5-7** being more difficult than **1-3** to reduce as a result of the more electron-rich dirhodium cores in **5-7**, arising from the superior σ-donating ability of CH_3NC as compared to CH_3CN. Furthermore, the expected correlations are found by comparing the electrochemical behavior of **1** with **2** and **5** with **6**, *i.e.,* **1** and **5** more easily oxidized and less easily reduced than **2** and **6**, respectively, which is reflected by the lower-lying LUMO and HOMO orbitals for **2** and **6** with respect to **1** and **5** (Tables 2.4 and 2.5, Figure 2.19) due to the strong electron withdrawing ability of the fluorine groups on the formamidinate bridging ligands.

Concluding remarks

In this comprehensive investigation, two analogous classes of dirhodium compounds with two strong σ-donating bridging groups and eq/ax monodentate acetonitrile (**1-4**) or isocyanide (**5-8**) ligands were synthesized and characterized by X-ray crystallography, ^{1}H, ^{31}P NMR, electronic and infrared spectroscopies as well as electrochemical studies, the collective results of which are in agreement with the theoretical studies. The isocyanide analogs **5-8** are unprecedented with respect to their geometrical features and are a rarity in the metal-metal bond literature with isocyanide ligands given the synthetic challenges of isolating products that have not undergone reduction. The substitution of acetonitrile for isocyanide in the eq/ax positions leads to notable changes in the

isocyanide series **5**-**8** as compared to **1**-**4** and allows for intriguing correlations between the two classes of dirhodium compounds to be made. The combined experimental data gleaned from the crystallographic, spectroscopic and theoretical studies all converge to the conclusion that the improved σ-donating and π-accepting abilities of isocyanide *vs.* acetonitrile have a profound effect on the structural and spectroscopic features of **5**-**8**. In particular, the longer Rh-Rh bonds (by up to ~ 0.07 Å) in **5**-**8** *vs.* **1**-**4** are in agreement with the better σ-donation of the ax CH_3NC as compared to CH_3CN; the latter conclusion is also supported by the short CN distances in CH_3NC and the increase in the stretching frequencies ν(CN) by ~ 60-80 cm^{-1} for the bound ligands in **5**-**8** *vs.* free CH_3NC. Furthermore, the short Rh-C (ax CH_3NC) distances in **5**-**8**, which exert a strong *trans* influence on the Rh-Rh bonds, attest to the enhanced π-accepting ability of CH_3NC as compared to CH_3CN. The significant π-backbonding from the dirhodium core to the isocyanide groups in **5**-**8** is also evidenced by the shorter bond distances Rh-C (eq CH_3NC), which result in elongation of the Rh-bridging group distances *trans* to the eq isocyanide groups, as compared to their CH_3CN analogs **1**-**4** with longer Rh-N (eq CH_3CN) bonds. In accord with the π-backbonding to the isocyanide groups for **5**-**8**, are their more positive oxidation potentials and the lower energy levels of the HOMO orbitals as compared to **1**-**4**. The more negative reduction potentials and the destabilization of the LUMO orbitals for **5**-**8** *vs.* **1**-**4** are consistent with the enhanced σ-donation of CH_3NC. Accordingly, the TD-DFT calculations are in excellent agreement with the larger HOMO-LUMO energy gaps in **5**-**7** *vs.* **1**-**3** as well as with the experimentally observed hypsochromic shifts of the lowest-energy transitions in the

isocyanide series **5-7** with respect to the corresponding acetonitrile analogs **1-3**. Interestingly, for **8**, the TD-DFT calculations corroborate the experimentally observed hypsochromic shift of the low energy MC band and the ~20-fold increase of the band intensity in **8** ($\varepsilon \sim 10^4$ $M^{-1}cm^{-1}$) with respect to **4.** The latter increase originates from a Laporte allowed HOMO $Rh_2(\sigma)\rightarrow$LUMO $Rh_2(\sigma^*)$ transition due to the increase in the energy of the $Rh_2(\sigma)$ orbital with respect to **4**, which renders it the HOMO in **8**. This considerable destabilization of the $Rh_2(\sigma)$ in **8** is attributed to the stronger interactions of the dirhodium core with the ax CH_3NC ligands. These interactions account for the weaker Rh-Rh bond (by ~ 0.1 Å relative to the acetonitrile analog **4**) and the remarkably short ax Rh-C (CH_3NC) distances (2.01-2.04 Å) in **8**, and, in fact the latter become comparable in length to the eq Rh-C (CH_3NC) contacts which is an unprecedented structural feature among all reported dirhodium(II,II) compounds.

To this stage, two series of partial paddlewheel dirhodium complexes featuring two electron-rich bridging ligands with the *cis* configuration have been developed, namely the acetonitrile complexes **1-4** and their corresponding methyl isocyanide anologs **5-8**. The strong electron donating ability of the bridging ligands renders the CH_3CN ligands *trans* to them labile, and conversely, due to π-backbonding, leads to substitutional inertness for CH_3NC ligands. To achieve the dark stability and photolability of the eq monodentate ligands for this type of dirhodium complexes, further tuning of the ligand field around the dimetal center is required. The use of less electron accepting ligands, *e.g.* CF_3NC and C_6H_5NC are promising for this purpose and these studies are currently in progress.

CHAPTER III

INVESTIGATION OF PARTIAL PADDLEWHEEL DIRHODIUM COMPLEXES WITH ELECTRON ACCEPTOR LIGANDS*

Introduction

Photocatalytic reduction of H_2O to generate H_2 is one of the most promising and effective methods for meeting the demand for increasing global fuel consumption. Transition metal complexes hold great potential as molecular water reduction photocatalysts as exemplified by the extensive studies of Ni(II)[64], Co(II)[152], Pt(II)[153], Pd(II)[154], Rh(III)[155] and Mo(III)[65] complexes. Among the aforementioned catalysts, mononuclear Rh(III) complexes represent one of the earliest examples in this category.[156] A few years ago Bernhard and co-workers reported a multicomponent H_2O reduction system, $[Rh(dtbbpy)_3]^{3+}$ (dtbbpy = 4,4'-di-tert-butyl-2,2'-bipyridine) as the catalyst and $[Ir(f\text{-}mppy)_2(dtbbpy)]^+$ (f-mppy = 5-methyl-2-(4-fluorophenyl)pyridine) as the photosensitizer that achieves a turnover number (TON) of > 5000 upon 22 h irradiation under optimal conditions.[157] Another example relevant to the current study involves the series of dirhodium(II,II) complexes, *cis*–$[Rh_2(\mu\text{-}O_2CCH_3)_2(L)_2][O_2CCH_3]_2$ (L = bpy, phen; bpy = 2,2'-bipyridine, phen = 1,10-phenanthroline) which were recently shown to act as catalysts for H_2 evolution from H^+ in the presence of external photosensitizer, $[Ir(ppy)_2(dtbbpy)]^+$ (ppy = 2-phenylpyridine) and the sacrificial electron donor triethylamine (TEA).[14] It was proposed by the researchers that the reduced

* Reprinted with permission from "Directional charge transfer and highly reducing and oxidizing excited states of new dirhodium(II,II) complexes: potential applications in solar energy conversion" by Zhanyong Li, Nicholas A. Leed, Nicole M. Dickson-Karn, Kim R. Dunbar and Claudia Turro, 2014. Chem. Sci, 5, 727-737, Copyright [2014] by The Royal Society of Chemistry (RSC). http://pubs.rsc.org/en/Content/ArticleLanding/2014/SC/C3SC52366G#!divAbstract

photosensitizer (this reduction is achieved by TEA) undergoes electron transfer process to the Rh_2(II,II) catalysts to generate the active catalysts upon light irradiation; the identities of the active catalysts, however, remain unknown. Interestingly, the performance of this multicomponent system depends on the concentration of the catalysts. For example, at the concentration of 16.7 μM (*cis*-$[Rh_2(\mu\text{-}O_2CCH_3)_2(phen)_2]^{2+}$), the TON for H_2 production reached 2622 after 50 h of irradiation, which is the maximum efficiency for the system. Another series of excellent complexes in this vein are developed by Nocera and coworkers as shown earlier in chapter I. They were able to eliminate electron transfer steps between the sensitizer and the catalyst in the excited state because both the light absorber and the catalytic unit are in one molecule. [15-17]

The present work in this chapter focuses on the synthesis and characterization of series of *cis*-$[Rh_2(\mu\text{-DTolF})_2(L)_2][BF_4]_2$ and *cis*-$[Rh_2(\mu\text{-F-form})_2(N\text{-}N)_2][BF_4]_2$ complexes (DTolF = p-ditolylformamidinate, F-Form = di-pfluorobenzylformamidinate; N-N = chelating diimine ligands, dpq dipyrido[3,2-f:2',3'-h]-quinoxaline), dppz (dipyrido[3,2-a:2',3'-c]phenazine) and dppn (benzo[i]dipyrido[3,2-a:2',3'-h]quinoxaline)). In addition, the computational modeling studies are also conducted for the better understanding of their photophysical properties. These complexes, the structural representation of which are depicted in Figure 3.1, were chosen based on our prior finding that $Rh_2(form)_4$ (form = formamidinate ligands with various substituents) exhibit highly reducing excited states capable of transferring electrons to alkyl halides via outer-sphere mechanism. The photophysical and redox properties of the new

complexes were also investigated, and the data reveal highly reducing and oxidizing ligand-to-ligand charge-transfer (LLCT) excited states.

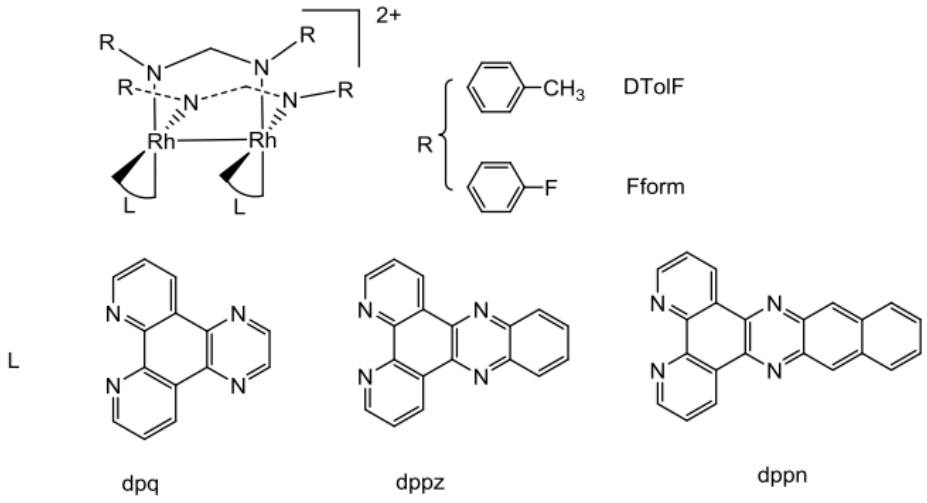

Complex	L	R
9	dpq	DTolF
10	dppz	DTolF
11	dppn	DTolF
12	dpq	Fform
13	dppz	Fform
14	dppn	Fform

Figure 3.1 Schematic representations of the molecular structures of selected complexes.

Experimental section

Starting materials

The precursor $(RhClCOD)_2$ was purchased from Pressure Chemicals and used without further purification. The compounds $[Rh(F\text{-}form)(COD)]_2$, $[Rh(DTolF)(COD)]_2$,[102] dpq (dipyrido[3,2-f:2',3'-h]-quinoxaline), dppz (dipyrido[3,2-a:2',3'-c]phenazine) and dppn (benzo[i]dipyrido[3,2-a:2',3'-h]quinoxaline) [158] were synthesized by published procedures. The synthesis of *cis*-$[Rh_2(F\text{-}form)_2(CH_3CN)_6][BF_4]_2$ was achieved by adapting the published procedure for *cis*-$[Rh_2(DTolF)_2(CH_3CN)_6][BF_4]_2$.[104] Acetonitrile was pre-dried over 3 Å molecular sieves and distilled under a nitrogen atmosphere. All reactions were conducted using standard Schlenk-line techniques unless otherwise stated. Filtration and further manipulation of the products were conducted in air.

***cis*-$[Rh_2(DTolF)_2(dpq)_2(CH_3CN)][BF_4]_2$ (9).** A sample of *cis*-$[Rh_2(DTolF)_2(CH_3CN)_6][BF_4]_2$ (68 mg, 0.063 mmol) was dissolved in 10 mL of CH_3CN and combined with 20 mL of CH_3CN suspended with 37 mg (0.16 mmol) of the dpq ligand. The color of the solution changed gradually from red to dark brown and was refluxed under N_2 for 48 h after which time it was concentrated to 5 mL and filtered through a medium frit to remove any insoluble materials. Addition of 20 mL of diethyl ether induced the precipitation of 68 mg of green product which was washed three times with 10 mL of diethyl ether and collected by filtration. It was dried under vacuum for 24 h (yield: 79% based on rhodium). ^{1}H NMR (CD_3CN-d_3) δ ppm: 9.02 (s, dpq), 8.88 (dd, dpq), 8.79(d, dpq), 8.29 (t, NCHN), 7.76 (dd, dpq), 7.10 (dd, phenyl H of DTolF), 2.28 (s, -CH_3 of DTolF), 1.96 (s, CH_3CN). ESI-MS: $[Rh_2(DTolF)_2(dpq)_2]^{2+}$, 558.08. Anal.

Calcd for $C_{62}H_{55}B_2Cl_4F_8N_{13}ORh_2$ (**1**•$2CH_2Cl_2$ •H_2O): C 48.89, N 11.98, H 3.65%. Found C 48.84, N 12.10, H 3.56%.

***cis*-[Rh$_2$(DTolF)$_2$(dppz)$_2$(CH$_3$CN)][BF$_4$]$_2$ (10)**. A sample of *cis*-[$Rh_2(DTolF)_2(CH_3CN)_6][BF_4]_2$ (63 mg, 0.058 mmol) was dissolved in 10 mL of CH_3CN and combined with 36 mg (0.13 mmol) of dppz suspended in 20 mL CH_3CN. The red solution was refluxed under N_2 for 48 h which led to an eventual color change to dark brown. The volume was reduced to 5 mL and filtered through a medium frit to remove any insoluble impurities. A subsequent addition of 30 mL of diethyl ether induced the precipitation of 60 mg of the green product which was collected by filtration in air, washed with 3 x 10 mL of diethyl ether, and dried under vacuum for 24 h. The yield is 72% based on rhodium. ^{1}H NMR (CD_3CN-*d*$_3$) δ ppm: 8.97 (d, dppz), 8.81 (d, dppz), 8.31 (t, NCHN), 8.05 (dd, dppz), 7.84 (dd, dppz), 7.12 (dd, phenyl H of DTolF), 2.28 (s, -CH_3 of DTolF), 1.96 (s, CH_3CN); ESI-MS: $[Rh_2(DTolF)_2(dppz)_2]^{2+}$, 608.12. Crystals suitable for X-ray diffraction were obtained by slow diffusion of diethyl ether into a CH_3CN solution of the compound. Anal. Calcd for $C_{69}H_{55}B_2F_8Cl_2N_{13}Rh_2$ (**2**•CH_2Cl_2): C 54.61, N 12.01, H 3.66%. Found: C 54.27, N 11.75, H 3.78%.

***cis*-[Rh$_2$(DTolF)$_2$(dppn)$_2$(CH$_3$CN)][BF$_4$]$_2$ (11).** A sample of *cis*-[$Rh_2(DTolF)_2(CH_3CN)_6][BF_4]_2$ (49 mg, 0.045 mmol) was added to 10 mL of CH_3CN, mixed 20 mL of CH_3CN containing a suspension of 38 mg (0.11 mmol) dppn and refluxed under N_2 for 6 days. The dark red solution was concentrated to 5 mL and filtered through a medium frit to remove any insoluble solids. The red product was precipitated by adding 30 mL of diethyl ether to the concentrated solution. The yield is

55 mg (72% based on rhodium). ^{1}H NMR (CD_3CN-d_3) δ ppm: 9.03 (d, dppn), 8.82 (d, dppn), 8.31 (t, NCHN), 8.22 (s, dppn), 7.90(dd, dppn), 7.82 (dd, dppn), 7.72 (dd, dppn), 7.12 (dd, phenyl H of DTolF), 2.29 (s, -CH_3 of DTolF), 1.96 (s, CH_3CN); ESI-MS: $[Rh_2(DTolF)_2(dppn)_2]^{2+}$, 658.14; Anal. Calcd for $C_{76}H_{57}N_{13}Rh_2B_2F_8$ (**3**): C 59.33, N 11.65, H 3.86%. Found: C 59.56, N 11.89, H 3.75%.

***cis*-[Rh$_2$(F-form)$_2$(dpq)$_2$(CH$_3$CN)$_2$][BF$_4$]$_2$ (12).** A sample of *cis*-$[Rh_2(F\text{-}form)_2(CH_3CN)_6][BF_4]_2$ (53 mg, 0.049 mmol) was dissolved in 10 mL of CH_3CN and combined with 20 mL of CH_3CN that contained 32 mg (0.138 mmol) of suspended dpq. The red solution was refluxed under N_2 for 48 h, reduced in volume to 5 mL, and then treated with a copious volume of diethyl ether to precipitate the product along with a small amount of the free dpq ligand. Recrystallization by slow diffusion of diethyl ether into a CH_3CN solution containing the product produced crystals which were used for further studies including X-ray diffraction. The overall yield is 50% based on rhodium. ^{1}H NMR (CD_3CN-d_3) δ ppm: 9.02 (s, dpq), 8.88 (dd, dpq), 8.81(d, dpq), 8.27 (t, NCHN), 7.79 (dd, dpq), 7.15 (m, phenyl H of F-form), 1.96 (s, CH_3CN). Anal. Calcd for $C_{59}H_{44}B_2F_{12}Cl_2N_{14}ORh_2$ (**5**•CH_2Cl_2•H_2O): C 47.48, N 13.15, H 2.97%. Found: C 47.42, N 13.13, H 3.11%.

***cis*-[Rh$_2$(F-form)$_2$(dppz)$_2$(CH$_3$CN)$_2$][BF$_4$]$_2$ (13).** A sample of *cis*-$[Rh_2(F\text{-}form)_2(CH_3CN)_6][BF_4]_2$ (55 mg, 0.050 mmol) was dissolved in 10 mL of CH_3CN and combined with a suspension of 30 mL of CH_3CN containing 34 mg (0.12 mmol) of dppz ligand. The solution was refluxed under N_2 for ~ 72 h, concentrated to 5 mL and filtered to remove unreacted dppz. Addition of 30 mL of diethyl ether induced the precipitation

of 61 mg of the red product. The yield is 86% based on rhodium. Crystals suitable for X-ray diffraction were produced from slow diffusion of diethyl ether to a CH_3CN solution containing the product. ^{1}H NMR (CD_3CN-d_3) δ ppm: 9.00 (d, dppz), 8.85 (d, dppz), 8.27 (t, NCHN), 8.05 (dd, dppz) 7.84 (dd, dppz), 7.26 (m, phenyl H of F-form), 7.05 (m, phenyl H of F-form), 1.96 (s, CH_3CN). Anal. Calcd for $C_{67}H_{48}B_2Cl_2F_{12}N_{14}ORh_2$ (**6**•CH_2Cl_2•H_2O): C 50.53, N 12.32, H 3.04%. Found: C 50.71, N 11.93, H 2.76%.

***cis*-[Rh$_2$(F-form)$_2$(dppn)$_2$(CH$_3$CN)$_2$][BF$_4$]$_2$ (14).** A quantity (55 mg, 0.050 mmol) of *cis*-[Rh_2(F-Form)$_2$(CH_3CN)$_6$][BF_4]$_2$ was dissolved in 10 mL of CH_3CN and combined with a suspension of 20 mL of CH_3CN containing 35 mg (0.1 mmol) dppn ligand. The solution was refluxed under N_2 for 4 days and condensed to 20 mL after which time it was filtered through a fine frit. Subsequent addition of 40 mL of diethyl ether induced the precipitation of 54 mg of a red product, which was washed with 3 x 10 mL of diethyl ether and dried under vacuum for 24 h. The yield is 70% based on rhodium. Crystals suitable for X-ray diffraction were obtained by slow diffusion of diethyl ether into a CH_3CN solution of the product. ^{1}H NMR (CD_3CN-d_3) δ ppm: 9.06 (dd, dppn, 4H), 8.87 (dd, dppn, 4H), 8.28 (t, NCHN, 2H), 7.91-7.84 (m, dppn, 8H), 7.71(dd, dppn, 4H) 7.26 (m, phenyl of F-form, 8H), 7.06(m, phenyl of F-form, 8H), 1.96 (s, CH_3CN). Anal. Calcd for $C_{71}N_{12}H_{44}B_2F_{12}Cl_2Rh_2$ (**7**•CH_2Cl_2): C 53.55, N 10.56, H 2.79%. Found: C 53.46, N 10.78, H 3.02%.

Instrumentation and methods

X-ray data sets for **10**, and **12**-**14** were collected on a Bruker CCD APEX diffractometer with graphite monochromated Mo Kα radiation (λ = 0.71073 Å). X-ray data for **9** and **11** were collected at beamline 15-ID-B at the Advanced Photon Source at Argonne National Laboratory using synchrotron radiation (λ= 0.41328 Å). A hemisphere of data for **10**, **12**-**14** were collected by a combination of four sets of X-ray exposures. Each set used a different ϕ angle for the crystals and covered 0.5˚ in ω for **10** and **14**, 0.3˚ for **12** and **13**. The exposure times were 20 s for **10**, **12** and **14** and 30 s for **13**. Crystal data for **9** and **11** were collected by a combination of two sets of X-ray exposures. The first set of data covers the whole sphere of the crystal whereas the second set of data covers the half sphere with an exposure time of 0.3 s. Crystal decay was monitored by analyzing duplicate reflections and was found to be less that 1%, therefore no decay corrections were applied.

Cyclic voltammetry and Uv-vis spectroscopic measurements were done in the similar fashion to the ones in the previous chapter II. The methods for the computational studies are also detailed in the same chapter.

Results and discussion

Synthesis and solution characterization

The complex *cis*-$[Rh_2(DTolF)_2(CH_3CN)_6]^{2+}$ reacts with the diimine ligands dpq, dppz, and dppn to produce *cis*-$[Rh_2(DTolF)_2(dpq)_2]^{2+}$ (**9**), *cis*-$[Rh_2(DTolF)_2(dppz)_2]^{2+}$ (**10**), and *cis*-$[Rh_2(DTolF)_2(dppn)_2]^{2+}$ (**11**), respectively. Similarly, *cis*-$[Rh_2(F\text{-form})_2(CH_3CN)_6]^{2+}$ was used to produce *cis*-$[Rh_2(F\text{-form})_2(dpq)_2]^{2+}$ (**12**), *cis*-$[Rh_2(F\text{-form})_2(dppz)_2]^{2+}$ (**13**),

and *cis*-$[Rh_2(F\text{-}form)_2(dppn)_2]^{2+}$ (**14**). The schematic representations of the structures of **9**-**11** and **12**-**14** are shown in Figure 3.1.

The reaction of *cis*-$[Rh_2(DTolF)_2(CH_3CN)_6][BF_4]_2$ with 2.2 equivalents of dppz was monitored by ^1H NMR spectroscopy as a function of reaction time; the aromatic regions of the spectra collected after 7 and 35 hours are shown in Figure 3.2. After refluxing for 7 hours, the ^1H NMR spectrum is consistent with a mixture of the starting material *cis*-$[Rh_2(DTolF)_2(CH_3CN)_6][BF_4]_2$ and a new product (labeled as * and †, respectively, in Figure 3.2a). The new product, labeled †, exhibits resonances from bound dppz ligand at δ = 9.84, 9.43, 8.51, 8.25, 8.17 ppm, together with a new triplet at δ = 7.92 ppm arising from the NCHN on the $[DTolF]^-$ ligand. The ratio between the integrations of the resonances at 9.84 and 7.92 ppm is approximately 1:1, consistent with the formation of the mono-dppz intermediate product *cis*-$[Rh_2(DTolF)_2(CH_3CN)_{3,4}(dppz)][BF_4]_2$ (†). This species with the dppz ligand bound in an eq-eq fashion is similar to those reported for the related complexes *cis*-$[Rh_2(DTolF)_2(CH_3CN)_{3,4}(bpy)][BF_4]_2$ and *cis*-$[Rh_2(DTolF)_2(CH_3CN)_{3,4}(phen)][BF_4]_2$,[129] but no eq CH_3CN resonances were observed in this case, presumably due to their fast exchange with the CD_3CN molecules.

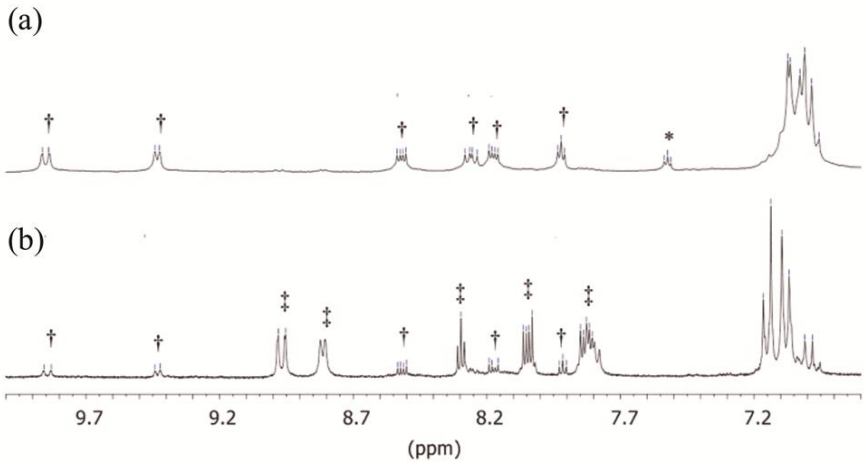

Figure 3.2 Aromatic region of the ^{1}H-NMR spectra of the products of the reaction between *cis*-$[Rh_2(DTolF)_2(CH_3CN)_6](BF_4)_2$ and 2.2 equiv of dppz in CD_3CN after refluxing in CH_3CN for (a) 7 hours and (b) 35 hours, where * = *cis*-$[Rh_2(DTolF)_2(CH_3CN)_6](BF_4)_2$, † = *cis*-$[Rh_2(DTolF)_2(CH_3CN)_{3–4}(dppz)](BF_4)_2$, and ‡ = **10**.

After 35 hours the resonance at 7.52 ppm (labeled *) disappeared, indicating total consumption of the *cis*-$[Rh_2(DTolF)_2(CH_3CN)_6][BF_4]_2$ starting material. Moreover, the intensities of the resonances for the mono-dppz *cis*-$[Rh_2(DTolF)_2(CH_3CN)_{3,4}(dppz)][BF_4]_2$ intermediate decreased (†), with concomitant appearance of a new set of dppz resonances at 8.97, 8.81, 8.05, 7.84, 7.80 ppm and bridgehead protons (NCHN) of $[DTolF]^-$ at 8.31 ppm, corresponding to the final product (labeled ‡ in Figure 3.2b). The integration ratio between the resonances at 8.97 and at 8.31 ppm is ~ 2:1, consistent with the formation of final product **10**. Three days of refluxing followed by purification led to the generation of a single final product indicated by the appearance of only one set of dppz and bridgehead (NCHN) ^{1}H-NMR resonances (Figure 3.3b) with the same chemical shifts as those labeled ‡ in Figure 3.2b.

X-ray crystallography confirmed the identity of **10** and will be discussed in the next section.

It is evident from Figure 3.3b that the resonances for the dppz ligands in **10** are shifted downfield as compared to those of the free ligand, but are positioned upfield relative to those of *cis*-$[Rh_2(DTolF)_2(CH_3CN)_{3,4}(dppz)][BF_4]_2$ (labeled † in Figure 3.2). These shifts are similar to those reported for the free dppz ligand, *cis*-$[Rh_2(\mu\text{-}O_2CCH_3)_2(dppz)_2]^{2+}$, and *cis*-$[Rh_2(\mu\text{-}O_2CCH_3)_2(dppz)(\eta^1\text{-}O_2CCH_3)(CH_3OH)]^+$. [45-47]

A slightly greater amount than two equivalents of dpq, dppz, dppn ligands were used in the reactions with *cis*-$[Rh_2(F\text{-}form)_2(CH_3CN)_6][BF_4]_2$ combined with refluxing conditions to induce the full substitution of all four eq CH_3CN ligands by the diimine ligands. In general, the addition of excess diethyl ether to the CH_3CN reaction mixture results in precipitation of the desired product along with an admixture of excess diimine ligand in some cases. In the latter instances, the pure products were obtained by recrystallization from slow diffusion of diethyl ether into the CH_3CN solution.

The purity of compounds **9**-**14** was confirmed by ^1H NMR spectroscopy. Upon coordination of the diimine ligands to the Rh_2^{4+} core, the characteristic triplet resonance of the bridgehead protons (NCHN) on the $[DTolF]^-$ ligands typically shift to lower field as compared to that in *cis*-$[Rh_2(DTolF)_2(CH_3CN)_6][BF_4]_2$ at 7.52 ppm, observed at 8.29, 8.31 and 8.31 ppm in **9**-**11**, respectively (Figure 3.3). Similarly, this triplet is observed at 7.49 ppm in *cis*-$[Rh_2(F\text{-}form)_2(CH_3CN)_6][BF_4]_2$ as compared to 8.27, 8.27 and 8.28 ppm in **12**-**14**, respectively (Figure 3.4). The resonance associated with the ax CH_3CN ligands, is present at 1.96 ppm as free CH_3CN due to the rapid exchange of them with CD_3CN

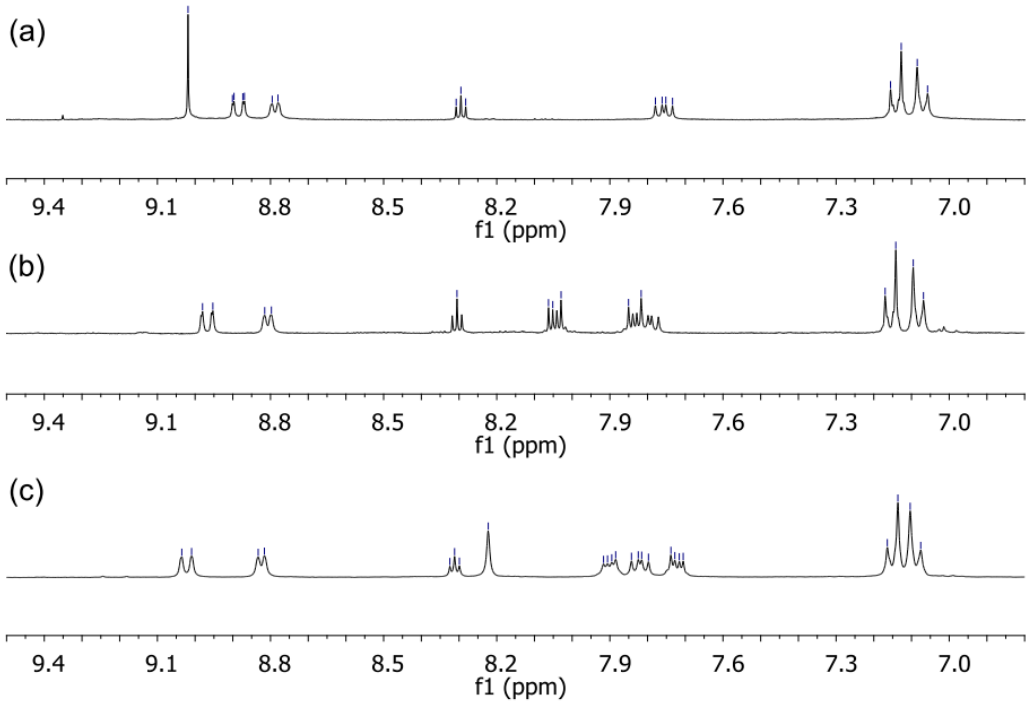

Figure 3.3 The aromatic region of the ^{1}H NMR spectra for **9-11** in CD_3CN.

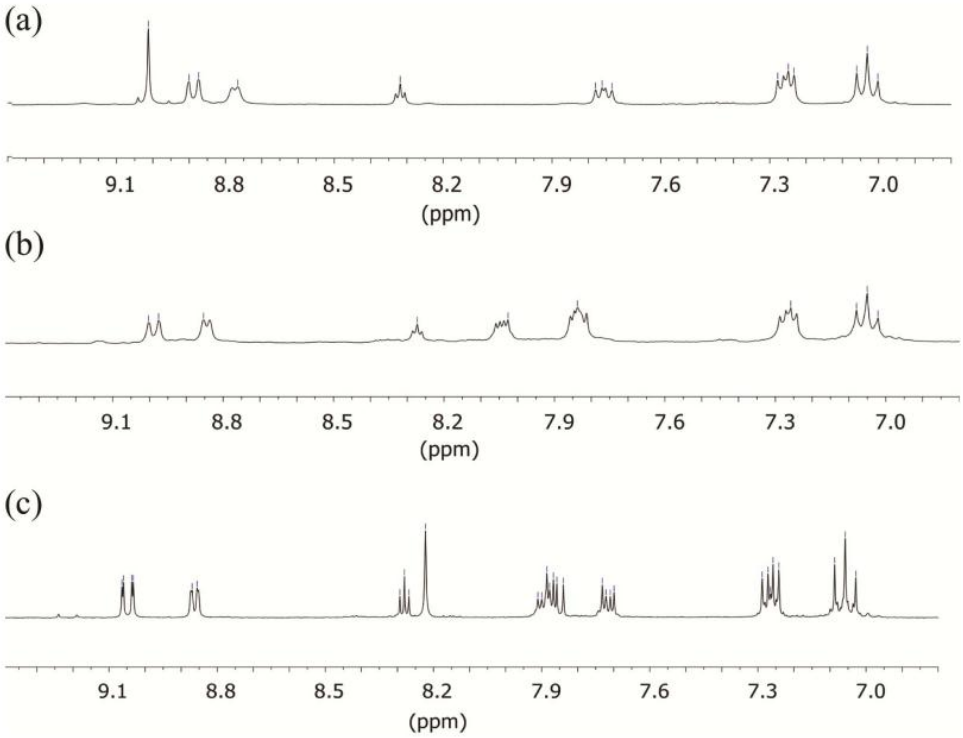

Figure 3.4 The aromatic region of the ^{1}H NMR spectra for **12-14** in CD_3CN.

solvent molecules, as is typical for Rh_2(II,II) complexes.[21] Only one set of resonances for the diimine ligands is observed in the ^{1}H NMR spectra of **9**-**11** and **12**-**14**, as illustrated in Figures 3.3 and 3.4 which supports the conclusion that the two diimine ligands are magnetically equivalent in each complex. The major species in the mass spectra of **9**, **10** and **11** correspond to the intact 2^+ cationic unit of the parent compound with the correct isotope distribution.

X-ray crystallography

***cis*-$[Rh_2(DTolF)_2(dpq)_2(CH_3CN)][BF_4]_2$ (9).** Compound **9** crystallizes in the space group of *P*bca. Its molecular structure consists of a cationic dirhodium unit bridged by two $[DTolF]^-$ ligands in a *cisoid* disposition (Figure 3.5). Two outer-sphere $[BF_4]^-$ anions are present as well. Each Rh(II) center is further chelated by a dpq ligand that occupies two eq positions (Figure 3.5). One of the two ax positions is occupied by a solvent acetonitrile molecule at a bond distance of 2.094(4) Å. The occupation of only one axial site is not uncommon for dirhodium(II,II) compounds equipped with $[DTolF]^-$ ligands and is attributed to its strong electron donating ability as well as the steric hindrance afforded by the bulky tolyl groups. The Rh-Rh bond distance is 2.5684(7) Å, which is comparable to that found in the related compounds *cis*-$[Rh_2(DTolF)_2(CH_3CN)_6][BF_4]_2$,[104] *cis*-$[Rh_2(DTolF)_2(bpy)(CH_3CN)_3][BF_4]_2$, and *cis*-$[Rh_2(DTolF)_2(bpy)_2(CH_3CN)][BF_4]_2$.[129] The Rh-N (dpq) bond distances are in a small range, from 2.029(4) to 2.064(4) Å. The two dpq ligands in the molecule adopted a staggered geometry to reduce the repulsion between them, with the dihedral angles defined by N5-Rh1-Rh2-N7 ~ 27.3(2)º.

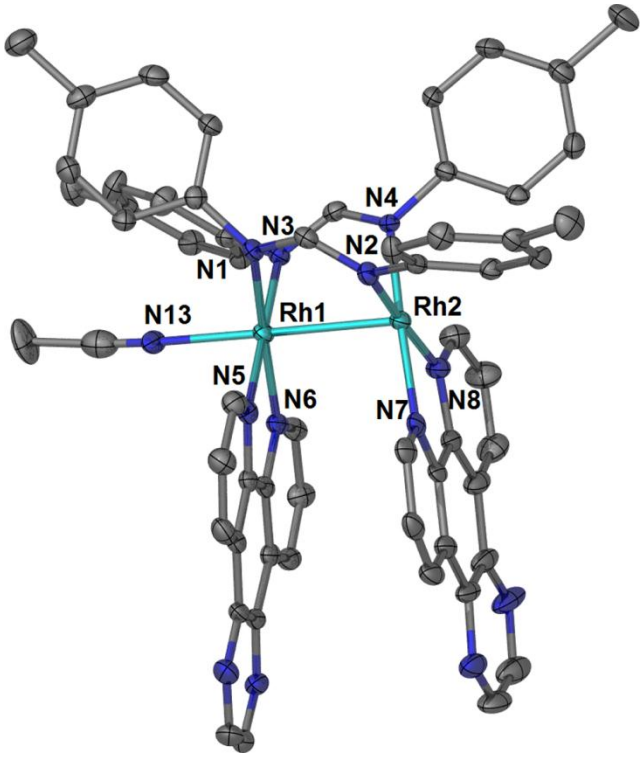

Figure 3.5 Cationic unit of **9** drawn at 50% probability level.

***cis*-[Rh$_2$(DTolF)$_2$(dppz)$_2$(CH$_3$CN)][BF$_4$]$_2$ (10).** The molecular structure of **10** is similar to **9**, with a distance of 2.158(6) Å for Rh-N (ax CH_3CN) bond. The Rh-Rh bond distance is 2.597(1) Å, which is slightly longer than that was found in **9**. The Rh-N bond distances (dppz) range from 2.040(5) to 2.060(2) Å, longer than those reported for *cis*-[$Rh_2(\mu\text{-}O_2CCH_3)_2(dppz)_2][O_2CCH_3]_2$.[46] The longer Rh-diimine N bond in **10** is explained on the basis of a stronger *trans* influence induced by the more electron-rich $[DTolF]^-$ ligand as compared to $[CH_3CO_2]^-$ ligand.

The presence of the Rh-Rh single bond brings the two dppz ligands into close proximity, leading to the splay from a parallel alignment to reduce the steric repulsions. The twist angle of the two dppz ligands away from the eclipsed geometry is 15.6º, similar to the angle of 13º in *cis*-$[Rh_2(\mu\text{-}O_2CCH_3)_2(dppz)_2][O_2CCH_3]_2$. The view along the b axis of the crystal packing diagram of **10** (Figure 3.6b), reveals π-stacking interactions of the dppz ligands between two adjacent dirhodium cations along the c axis. Since these ligands are not parallel to each other, no definitive distances can be determined between the two planes defined by them, but it is noted that the distances between C43 and C46 and the plane defined by C43-C44-C45-C46-C47-C48 in the adjacent dppz ligands are 3.47 and 3.42 Å, respectively, as depicted in Figure 3.6b. Such short intermolecular distances are indicative of π-stacking interactions between the two adjacent molecules. The crystal packing diagrams of **10** viewed along the b and c axes are provided in Figure 3.6c and 3.6d respectively.

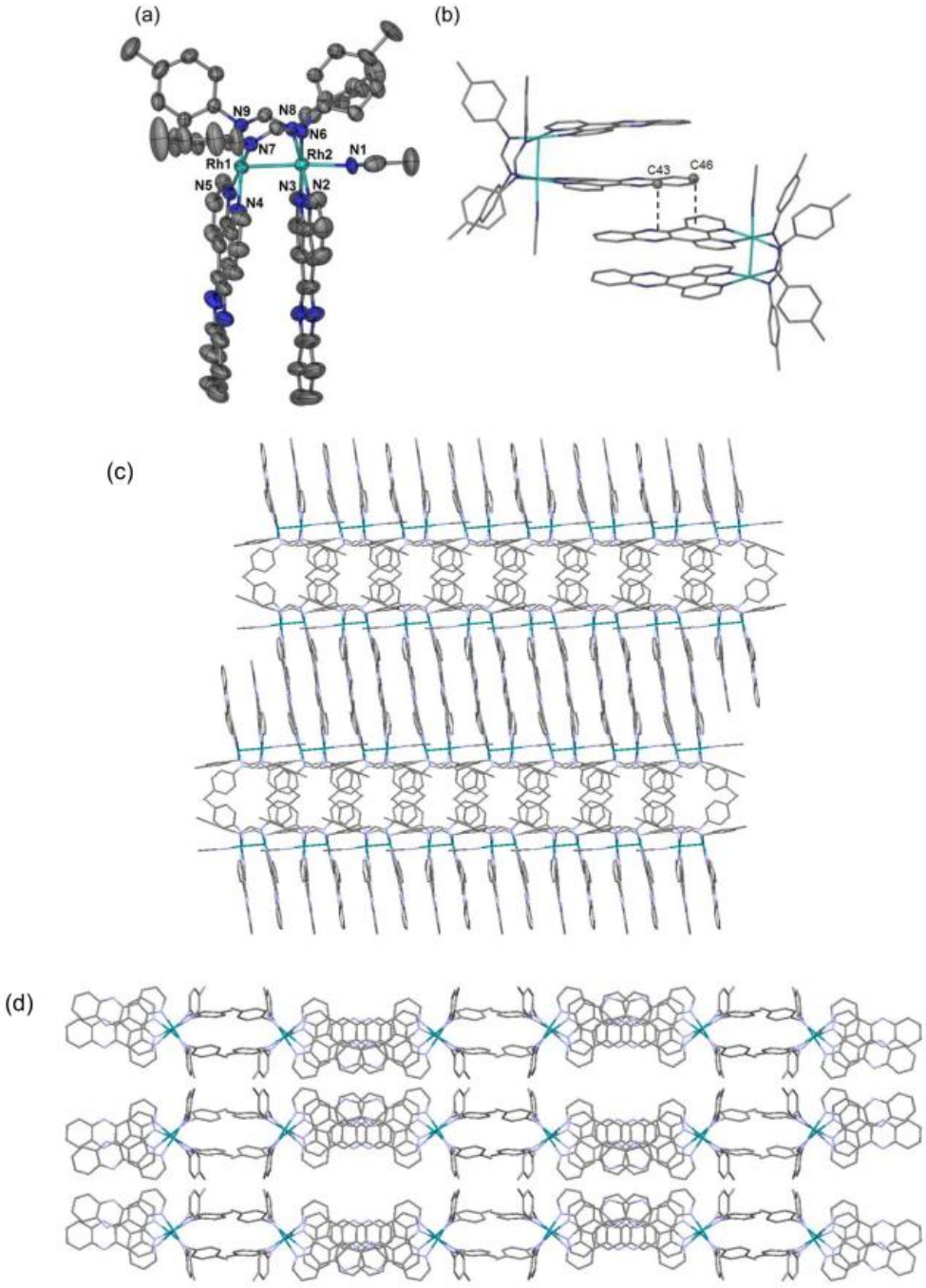

Figure 3.6 Crystal structure of **10** showing (a) thermal ellipsoid plot of the cation drawn at 50% probability level and (b) the crystal packing of the cations showing intermolecular π-stacking; the $[BF_4]^-$ anions and hydrogen atoms are omitted for the sake of clarity.

***cis*-[Rh_2(DTolF)$_2$(dppn)$_2$)Cl][BF_4]•Et_2O•3CH_3CN (3•Et_2O•3CH_3CN).** The cation in complex **11** crystallizes in the space group *P*-1 along with one $[BF_4]^-$ as well as three acetonitrile and one diethyl ether interstitial solvent molecules. The coordination sphere of the Rh(II) centers is similar to that found in **10** except that one ax position is occupied by a Cl^- ligand (Figure 3.7a). The Rh–Cl distance of 2.4562(7) Å is comparable to that reported for [Rh_2(1,3-diisocyanopropane)$_4Cl_2$]Cl_2, in which Rh-Cl (ax) is 2.4472(8) Å,[159] but is significantly longer than the Rh-N (ax CH_3CN) bond length in **10**, which is not surprising given the larger size of the Cl^- ion. The Rh-Rh bond distance is 2.5818(3) Å and the Rh-N (dppn) bond distances range from 2.032(2) to 2.053(3) Å, comparable the corresponding metrical parameters found in **9** and **10**. The two dppn ligands are twisted away from the eclipsed configuration with a dihedral angle of ~ 28º. This value is significantly larger than was found for the dppz ligands in **10**, indicating the stronger repulsions between the two adjacent dppn ligands in **11**.

***cis*-[Rh_2(F-form)$_2$(dpq)$_2$(CH_3CN)$_2$)][BF_4]$_2$ (12).** The molecular structure of the cationic unit of **12** depicted in Figure 3.7b is similar to that of **10**, but with both ax positions being occupied by CH_3CN ligands as a result of the smaller size and less electron-rich nature of the $[F\text{-form}]^-$ *vs.* the $[DTolF]^-$ ligands. The Rh-Rh distance is 2.599(1) Å and the Rh-N ($[F\text{-form}]^-$) distances range from 2.034(5) to 2.052(5) Å, similar to that found in *cis*-[Rh_2(F-form)$_2$(CH_3CN)$_6$][BF_4]$_2$. The Rh-N (dpq) distances are in the range of 2.035(3)-2.053(3) Å, similar to the Rh-N (dppz) lengths in **10**. The internal twist angles away from the eclipsed geometry of the two dpq ligands defined by N5-Rh1-Rh2-N7 and N6-Rh1-Rh2-N8 are -18.6(1)º and -18.9(1)º.

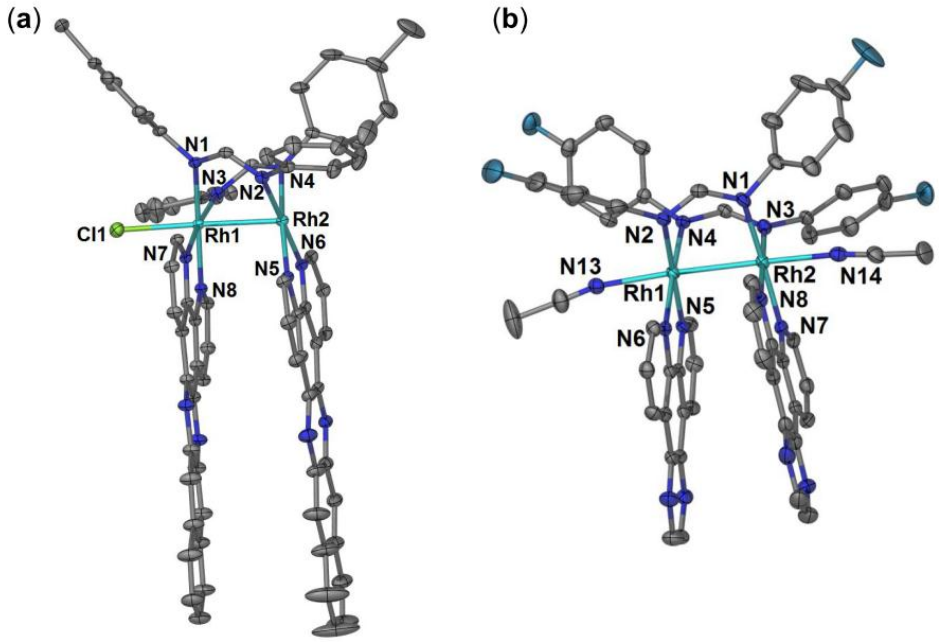

Figure 3.7 Thermal ellipsoid plot of (a) **11** an (b) **12** drawn at the 50% probability level; hydrogen atoms, $[BF_4]^-$ anion, and interstitial solvent molecules are omitted for the sake of clarity.

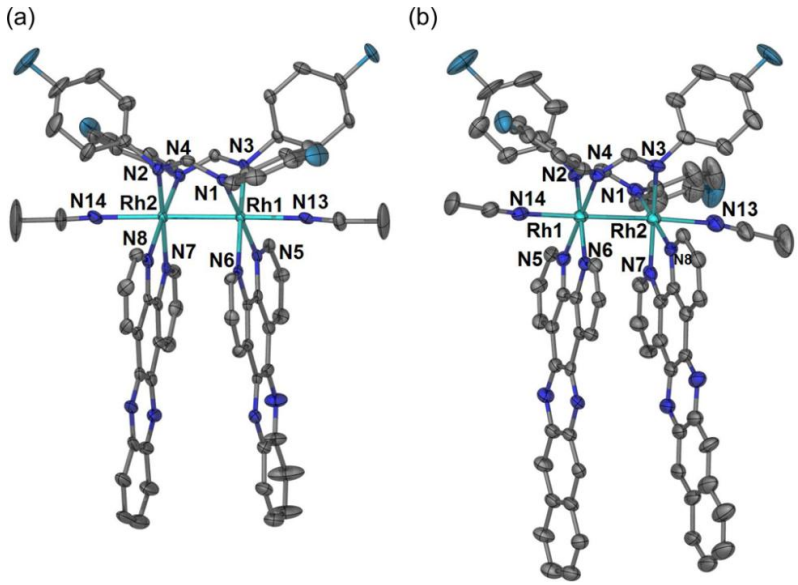

Figure 3.8 Thermal ellipsoid plots drawn at the 50% probability level; the anions, hydrogen atoms and interstitial solvent molecules are omitted for the sake of clarity (a) **13** (b) **14**.

***cis*-[Rh_2(F-form)$_2$(dppz)$_2$(CH_3CN)$_2$][BF_4]$_2$ (13).** Compound **13** crystallizes in the *P*-1 space group. The thermal ellipsoid plot of the cationic unit is shown in Figure 3.8a. Both ax positions of **13** are occupied by solvent CH_3CN molecules with the distances of 2.210(6) and 2.256(6) Å. The Rh-Rh bond distance of 2.6190(9) Å is slightly longer than the corresponding distances in **12**. The Rh-N ([F-form]$^-$) bond distances are in the range 2.043(5)-2.065(5) Å, similar to those found in **12**. The Rh-N (dppz) bond distances are ~2.06 Å, similar to those in **10**. The two dppz ligands in one molecule of **13** are twisted away from the eclipsed configuration with dihedral angles of 16.8(2)º (defined by N7-Rh2-Rh1-N5).

***cis*-[Rh_2(F-form)$_2$(dppn)$_2$(CH_3CN)$_2$)][BF_4]$_2$•2CH_3CN (14•2CH_3CN).** As in the case of the dirhodium cations in **12** and **13**, both ax positions are occupied by CH_3CN ligands in **14** with bond distances of 2.202(7) and 2.245(9) Å (Figure 3.8b). The Rh-Rh bond distance is 2.614(1) Å, slightly longer than those found in **12** but comparable to that in **13**. The Rh-N ([F-form]$^-$) bond distances are in the range 2.047(5)-2.069(4) Å, similar to that for **12** and **13**. The Rh-N (dppn) bond distances range from 2.042(8) to 2.064(6) Å, comparable to those in **12**. Much larger distortions between the two diimine ligands is evident in **14** as compared to that of **12** and **13**, with the angles defined by N5-Rh1-Rh2-N7 and N6-Rh1-Rh2-N8 being -21.7(2)º and -21.8(2)º respectively, due to considerable repulsion between the two dppn ligands.

The detailed crystal refinement parameters are listed in Table 3.1 whereas the bond distances and dihedral angles are compiled in Table 3.2

Table 3.1 Crystallographic data and refinement parameters for **9**-**14**.

	9	**10**	**11** Et_2O•$3CH_3CN$	**12**	**13**	**14**•$2CH_3CN$
Formula	$C_{60}H_{49}B_2N_{13}F_8Rh_2$	$C_{68}H_{53}B_2N_{13}F_8Rh_2$	$C_{80}H_{63}B_1N_{15}F_4Cl_1Rh_2$	$C_{58}H_{40}B_2N_{14}F_{12}Rh_2$	$C_{66}H_{44}B_2N_{14}F_{12}Rh_2$	$C_{78}H_{54}B_2F_{12}N_{16}Rh_2$
Mol. Wt. (g/mol)	1331.55	1431.67	1636.67	1388.46	1488.59	1670.81
Space group	Pbca	C2/c	P-1	P-1	P-1	$P2_1/c$
a, *b*, *c*/ Å	13.964(3) 19.803(4) 40.072(8)	50.745(10) 19.810(4) 13.614(3)	10.0565(4) 19.2440(7) 19.4311(8)	12.764(3) 13.196(3) 20.352(4)	13.104(3) 13.114(3) 22.820(5)	14.698(3) 26.636(5) 23.354(7)
α, β, γ/ º	90.00	90, 99.70(3), 90	97.1760(10) 94.0670(10) 102.6250(10)	83.78(3), 72.12(3), 66.51(3)	73.63(3) 86.21(3) 66.42(3)	90 123.59(2) 90
Z	8	8	2	2	2	4
2θ range for data collection/º	49.47	50.02	58.26	53.67	49.43	48.14
R(int)	0.1010	0.0737	0.0467	0.0368	0.0365	0.0960
Completeness to θ max/ %	99.7	99.9	0.937	98.6	97.8	97.2
Goodness-of-fit (all data)[a]	1.025	1.038	1.224	0.996	1.089	1.065
R_1,[b] wR_2[c] (all data)	*R* = 0.0754 *wR* = 0.1076	*R* = 0.0852 *wR* = 0.1962	*R = 0.0611* *wR = 0.1485*	*R* = 0.0592 *wR* = 0.1116	*R = 0.0760* *wR = 0.1752*	*R = 0.0871* *wR* = 0.1709

[a]Goodness-of-fit = $\{\sum[w(F_o^2 - F_c^2)^2]/(n-p)\}^{1/2}$, where *n* is the number of reflections and *p* is the total number of parameters refined. [b]$R = \sum||F_o|-|F_c||/\sum|F_o|$. [c]$wR = \{\sum[w(F_o^2 - F_c^2)^2]/\sum w(F_o^2)^2]\}^{1/2}$.

Table 3.2 Selected bond distances and dihedral angles in **9**-**14**.

9		**10**	
Bond distances	Å	Bond distances	Å
Rh1-Rh2	2.5684(7)	Rh1-Rh2	2.597(1)
Rh1-N13	2.094(4)	Rh1-N4	2.041(5)
Rh1-N1	2.047(4)	Rh1-N9	2.015(5)
Rh1-N5	2.050(4)	Rh1-N7	2.021(6)
Rh1-N6	2.064(4)	Rh1-N5	2.048(6)
Rh1-N3	2.042(4)	Rh2-N1	2.158(6)
Rh2-N8	2.029(4)	Rh2-N6	2.045(6)
Rh2-N2	2.026(4)	Rh2-N8	2.047(5)
Rh2-N4	2.023(4)	Rh2-N3	2.040(5)
Rh2-N7	2.064(4)	Rh2-N2	2.062(6)
Dihedral angles	º	Dihedral angles	º
N3-Rh1-Rh2-N4	19.9(2)	N4-Rh1-Rh2-N2	-15.6(2)
N5-Rh1-Rh2-N7	27.3(2)	N9-Rh1-Rh2-N8	-13.9(2)
N1-Rh1-Rh2-N2	22.0(2)	N7-Rh1-Rh2-N6	-15.7(2)
N6-Rh1-Rh2-N8	27.2(2)	N5-Rh1-Rh2-N3	-16.9(2)
11		**12**	
Bond distances	Å	Bond distances	Å
Rh1-Rh2	2.5818(3)	Rh1-Rh2	2.5991(9)
Rh1-Cl1	2.4562(7)	Rh1-N13	2.233(3)
Rh1-N8	2.033(2)	Rh1-N5	2.035(3)
Rh1-N7	2.048(3)	Rh1-N6	2.053(3)
Rh1-N3	2.065(3)	Rh1-N2	2.052(3)
Rh1-N1	2.084(3)	Rh1-N4	2.042(3)
Rh2-N2	2.026(3)	Rh2-N8	2.045(3)
Rh2-N5	2.032(2)	Rh2-N7	2.053(3)
Rh2-N6	2.053(3)	Rh2-N3	2.057(3)
Rh2-N4	2.041(3)	Rh2-N1	2.031(3)
		Rh2-N14	2.200(3)
Dihedral angles	º	Dihedral angles	º
N8-Rh1-Rh2-N6	28.29(9)	N6-Rh1-Rh2-N8	-18.9(1)
N7-Rh1-Rh2-N5	28.70(9)	N5-Rh1-Rh2-N7	-18.6(1)
N1-Rh1-Rh2-N2	25.8(1)	N2-Rh1-Rh2-N1	-14.4(1)
N3-Rh1-Rh2-N4	23.4(1)	N4-Rh1-Rh2-N3	-14.7(1)

Table 3.2 Continued

13		**14**	
Bond distances	Å	Bond distances	Å
Rh1-Rh2	2.6190(9)	Rh1-Rh2	2.615(1)
Rh1-N13	2.210(6)	Rh1-N2	2.056(5)
Rh1-N3	2.043(5)	Rh1-N4	2.054(4)
Rh1-N6	2.054(5)	Rh1-N5	2.053(4)
Rh1-N5	2.056(4)	Rh1-N6	2.063(4)
Rh1-N1	2.059(4)	Rh1-N14	2.202(7)
Rh2-N14	2.256(6)	Rh2-N1	2.047(5)
Rh2-N8	2.060(5)	Rh2-N3	2.069(4)
Rh2-N7	2.066(4)	Rh2-N7	2.055(4)
Rh2-N2	2.058(4)	Rh2-N8	2.048(5)
Rh2-N4	2.065(5)	Rh2-N13	2.245(9)
Dihedral angles	º	Dihedral angles	º
N3-Rh1-Rh2-N4	14.5(2)	N2-Rh1-Rh2-N1	-17.4(2)
N1-Rh1-Rh2-N2	14.0(2)	N4-Rh1-Rh2-N3	-17.5(2)
N5-Rh1-Rh2-N7	17.4(2)	N5-Rh1-Rh2-N7	-21.7(2)
N6-Rh1-Rh2-N8	16.8(2)	N6-Rh1-Rh2-N8	-21.8(2)

Electronic absorption and electrochemistry

Data regarding the photophysical properties of **9**-**14** in CH_3CN are compiled in Table 3.3. The relatively distinct transitions in the region between 280 and 420 nm for all the complexes are attributed to the intramolecular $^1\pi\pi^*$ electronic transitions resulting from the free diimine ligands; *e.g.* the dpq ligand absorbs at 254 nm (ε = 53,000 $M^{-1}cm^{-1}$) in $CHCl_3$, comparing well with the maxima of **9** and **12** at 289 nm (ε = 54,000 $M^{-1}cm^{-1}$) and 291 nm (ε = 50,000 $M^{-1}cm^{-1}$), respectively. Similarly, the dppz and dppn ligands exhibit absorption maxima at 370 nm (ε = 17,200 $M^{-1}cm^{-1}$) and 414 nm (ε = 12,500 $M^{-1}cm^{-1}$) respectively in $CHCl_3$,[36] similar to those measured for **10** and **13** (~ 370 nm) and **11** and **14** (~ 418 nm), respectively (Table 3.3). It is also noted that these transitions are also observed in the related complexes *cis*-$[Rh_2(\mu\text{-}O_2CCH_3)_2(L)(\eta^1\text{-}O_2CCH_3)(CH_3OH]^+$ (L = dpq, dppz, dppn), *cis*-$[Rh_2(\mu\text{-}O_2CCH_3)_2(dppz)_2]^{2+}$, *cis*-$[Rh_2(\mu\text{-}O_2CCH_3)_2(dppn)_2]^{2+}$,[44-48]as well as in Ru(II) and Os(II) complexes containing dpq, dppz, and dppn ligands.[36, 37,160-163] More intense bands are observed at higher energies in the 250-280 nm rage, namely 256 nm for **9** and **12**, 275 nm for **10** and **13**, and 261 nm for **11** and **14**. Although a small dependence is apparent as a function of the diimine ligands, it is likely that these are metal-centered transitions involving orbitals participating in bonding interactions with the diimine ligands. Similar transitions are also observed in Rh_2(F-form)$_4$ at 230 nm (ε = 42,000 $M^{-1}cm^{-1}$) and 275 nm (ε = 23,900 $M^{-1}cm^{-1}$) and in Rh_2(DTolF)$_4$ at 265 nm (ε= 61,800 $M^{-1}cm^{-1}$) in CH_3CN.

Table 3.3 Electronic absorption maxima, λ_{abs}, molar absorptivities, ε, and redox potentials for **9-14** in CH_3CN.

Complex	λ_{abs} / nm (ε/ $\times 10^3$ $M^{-1}cm^{-1}$)	V[a]
9	256 (98), 289 (54), 525 (1.3)	–1.55, –1.36, –1.03,[b] –0.40, +1.05, +1.59[c]
10	276 (143), 368 (25), 541 (1.3)	–1.49, –1.16, –0.94,[b] –0.42, +1.06,[b] +1.64[c]
11	261 (100), 314 (110), 418 (17), ~553 (3.0)	–1.50, –0.92, –0.67,[b] –0.40, +1.06,[b] +1.55[c]
12	256 (116), 291 (50), 520 (0.80)	–1.55, –1.29, –0.98,[b] –0.45, +1.17,[b] +1.68[c]
13	275 (107), 371 (17), 537 (1.0)	–1.40, –1.13, –0.91,[b] –0.39, +1.18,[b] +1.74[c]
14	260 (92), 315 (101), 419 (14), ~525 (1.8)	–1.39, –0.88, –0.61,[b] –0.38, +1.16,[b] +1.73[c]

[a]*vs.* Ag/AgCl; 0.1 M [n-Bu_4N][PF_6]; 0.2 V/s. [b]Quasi reversible. [c]Irreversible.

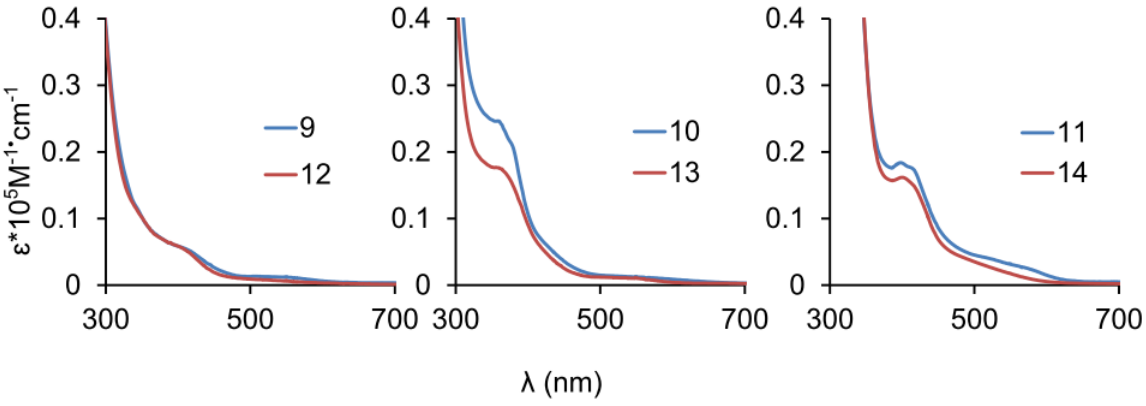

Figure 3.9 Electronic absorption spectra of **9** and **12** (left), **10** and **13** (middle), and **11** and **14** (right) in CH_3CN.

In addition to the higher energy transitions there is a tail in the absorption profile for each complex that extends to lower energies as listed in Table 3.3 and illustrated in Figure 3.9. The dependence of the absorption maxima on the identity of the diimine ligands as well as the bridging formamidinate ligands for each series taken together with the intensities being in the ~ 1-3 x10^3 $M^{-1}cm^{-1}$, points to the assignment of these lower energy bands as charge-transfer transitions from the formamidinate to the diimine ligands. Such charge-transfer features are also observed in the related *cis*-$[Rh_2(\mu\text{-}O_2CCH_3)_2(L)_2]^{2+}$ complexes where L is dpq, dppz and dppn with maxima in the range 609-620 nm with similar intensities (ε = 1,100-3,800 $M^{-1}cm^{-1}$).[48] The increased electron donation from the formamidinate ligands to the bimetallic core as compared to acetate is consistent with the lower energies of these charge-transfer transitions in **9-11** and **12-14**. In addition, these transitions are observed at lower energies for the $[DTolF]^-$ complexes as compared to the corresponding $[F\text{-form}]^-$ compounds, which is in accord with that the formamidinate ligands participate in the transition.

The observed redox couples measured for **9-11** and **12-14** are compiled in Table 3.3. A redox couple is observed at approximately – 0.4 V *vs.* Ag/AgCl in **9-11** and **12-14** (Table 3.3, Figure 3.10 for complex **13**). This process represents oxidation of the complexes which has been confirmed by a color change observed in the presence of oxidizing agents such as TCNQ, 7,7,8,8-tetracyanoquinonedimethane, (E' = – 0.14 *vs.* SCE in CH_3CN, ΔG = – 0.30 V), $AgBF_4$ in CH_3CN (E' = + 0.44 V *vs.* SCE, ΔG = – 0.88 V) and $NOBF_4$ (E' = + 1.03 V *vs.* SCE, ΔG = – 1.47 V).[164] Following the oxidation of **9** and **10** with TCNQ, an IR stretch at ~ 2186 cm^{-1} is observed which is known to

correspond to the TCNQ radical anion, $TCNQ^{\bullet -}$.[165] The product of the reaction of **10** with $NOBF_4$ was isolated; the absorption spectrum is shown in Figure 3.11. The facile oxidation of these dirhodium(II,II) complexes is not unexpected given the presence of the electron-rich formamidinate ligands.

The second oxidation process is at ~ +1.06 V *vs.* Ag/AgCl for the $[DTolF]^-$ complexes **9**-**11** and ~ + 1.17 V *vs.* Ag/AgCl for the $[F\text{-form}]^-$ series **12**-**14** (Table 3.3). This couple is reversible in the case of **9** and quasi-reversible for **10**-**11**, and **12**-**14** and is independent of the nature of the diimine ligand in each series but dependent on the substituents on the formamidinate ligand. As expected, the complexes with $[DTolF]^-$ ligands are more easily oxidized than those containing the electron withdrawing fluoride substituents, *viz.*, $[F\text{-form}]^-$ (Table 3.3). The difference of ~ 0.1 V for the $[DTolF]^-$ and

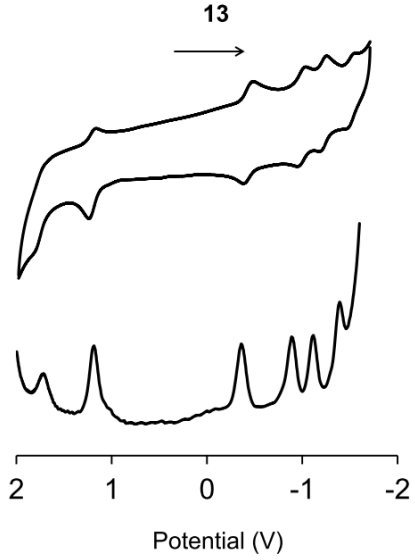

Figure 3.10 Cyclic voltammogram (top) and differential pulse voltammogram (bottom) of complex **13** in ~ 0.1 M $[n\text{-}Bu_4N][PF_6]$ CH_3CN solution at room temperature.

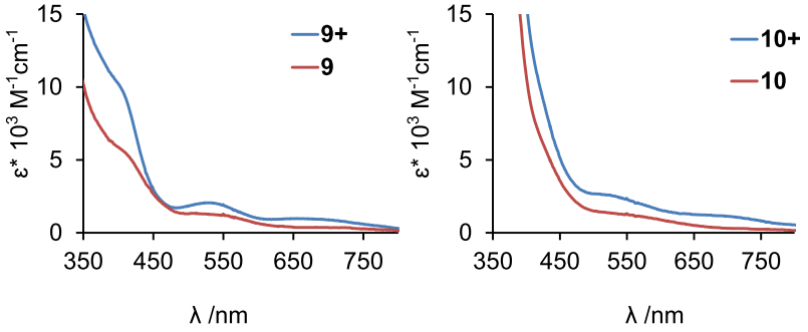

Figure 3.11 Comparison of the electronic absorption spectra of $[\mathbf{9}]^+$ and **9** (left) and of $[\mathbf{10}]^+$ and **10** (right) in CH_3CN.

$[F\text{-form}]^-$ complexes is similar to the difference in the second oxidation potentials of $Rh_2(DTolF)_4$ and $Rh_2(F\text{-form})_4$ of 0.14 V; the $E_{1/2}$ values are + 0.85 V and + 0.99 V *vs.* SCE, respectively.[143] The third oxidation process is irreversible for all the complexes with E_{pa} ~ + 1.6 V *vs.* Ag/AgCl for **9**-**11** and ~ + 1.7 V *vs.* Ag/AgCl for **12**-**14** (Table 3.3). The 0.1 V difference between the two series is consistent with this oxidation correspondent to the removal of one electron from orbital with significant formamidinate character.

The first reduction occurs at – 1.03 V, – 0.94 V, and – 0.67 V *vs.* Ag/AgCl for **9**, **10**, and **11** (Table 3.3), respectively, and is clearly dependent on the nature of the diimine ligand. These values are similar to those found for the corresponding $[F\text{-form}]^-$ complexes **12**, **13**, and **14**, at – 0.98, – 0.91, and – 0.61 *vs.* Ag/AgCl (Table 3.3). The trends for each series of complexes, considering the fact that the diimine ligand L is easier to reduce in the order dppn > dppz > dpq, is consistent with the first reduction being centered on this ligand. These values are also comparable to those reported for

Ru(II) complexes with dpq, dppz, and dppn ligands.[166] The potential of the second reduction process is also dependent on the diimine ligand L(Table 3.3), which is also the case for Ru(II) complexes, and may be assigned to the placement of an electron on the remaining neutral diimine ligand. A third reduction process is observed in the range of – 1.39 to – 1.55 V *vs.* Ag/AgCl for **9-11** and **12-14**, in accord with a metal-centered reduction. On the basis of the typical electronic structure of d^7–d^7 paddlewheel complexes, it is reasonable to expect that the third reduction corresponds to the population of the $Rh_2(\sigma^*)$ orbital.[21] These values are similar to the corresponding data for $Rh_2(DTolF)_4$ at – 1.23 V *vs.* Ag/AgCl that do not possess diimine ligands.[143]

Electronic structure calculations

Computational studies of the $[DTolF]^-$ and $[F\text{-form}]^-$ series of compounds were performed in order to gain a deeper understanding of their electronic structures. Geometric parameters for the gas phase optimizations were obtained from the crystal structures. For the calculations of **9-11**, two CH_3CN ligands were placed in both ax positions given that only one set of dpq, dppz and dppn resonances was observed in the solution ^1H NMR spectra, indicating a symmetrical coordination environment. The calculated structures of **12-14** are depicted in Figure 3.12.

The calculated MO diagrams of **9-11** and **12-14** are shown in Figure 3.13, and the contributions to the orbitals from the metal and the ligands are listed in Tables 3.4 and 3.5.

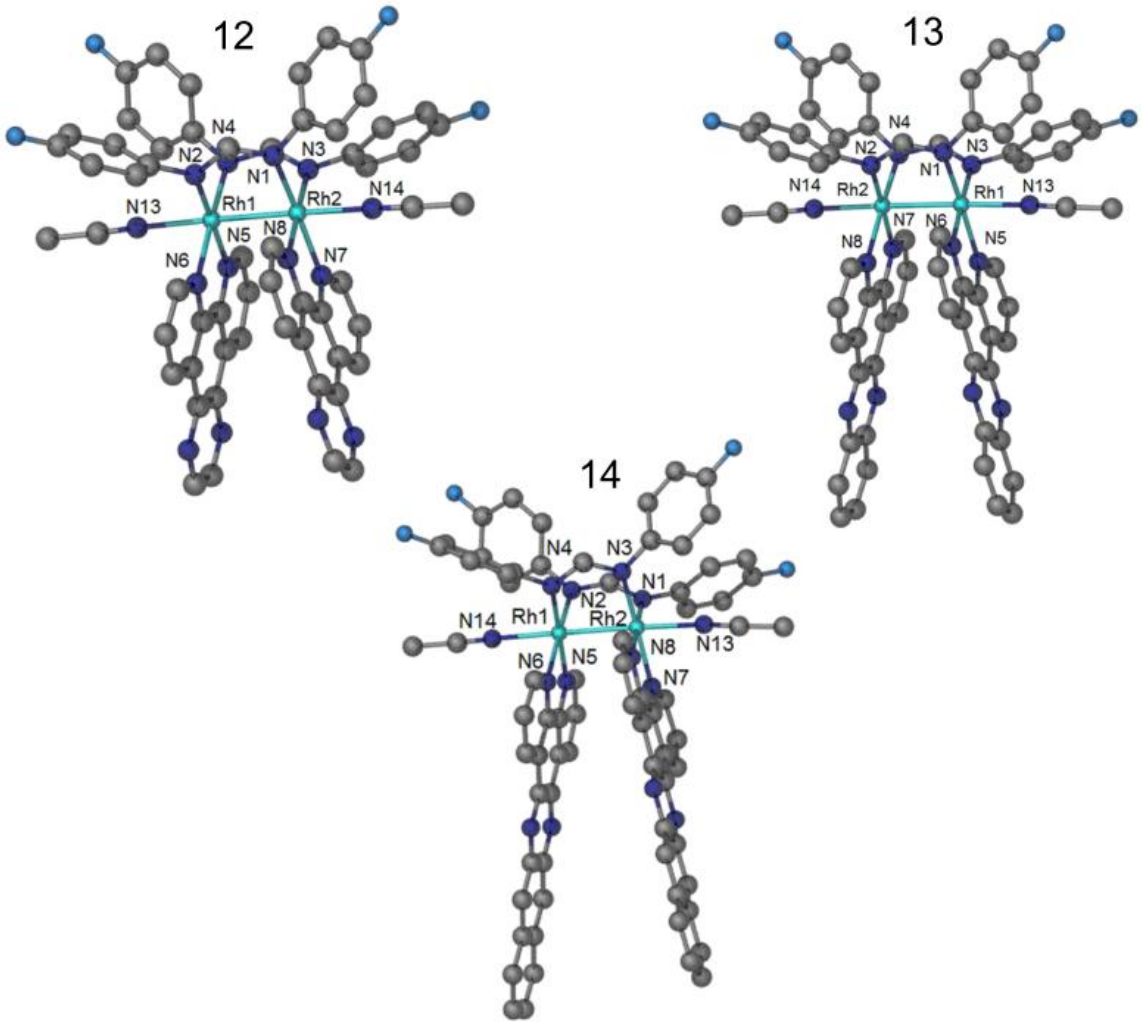

Figure 3.12 Calculated structures for complexes **12-14**.

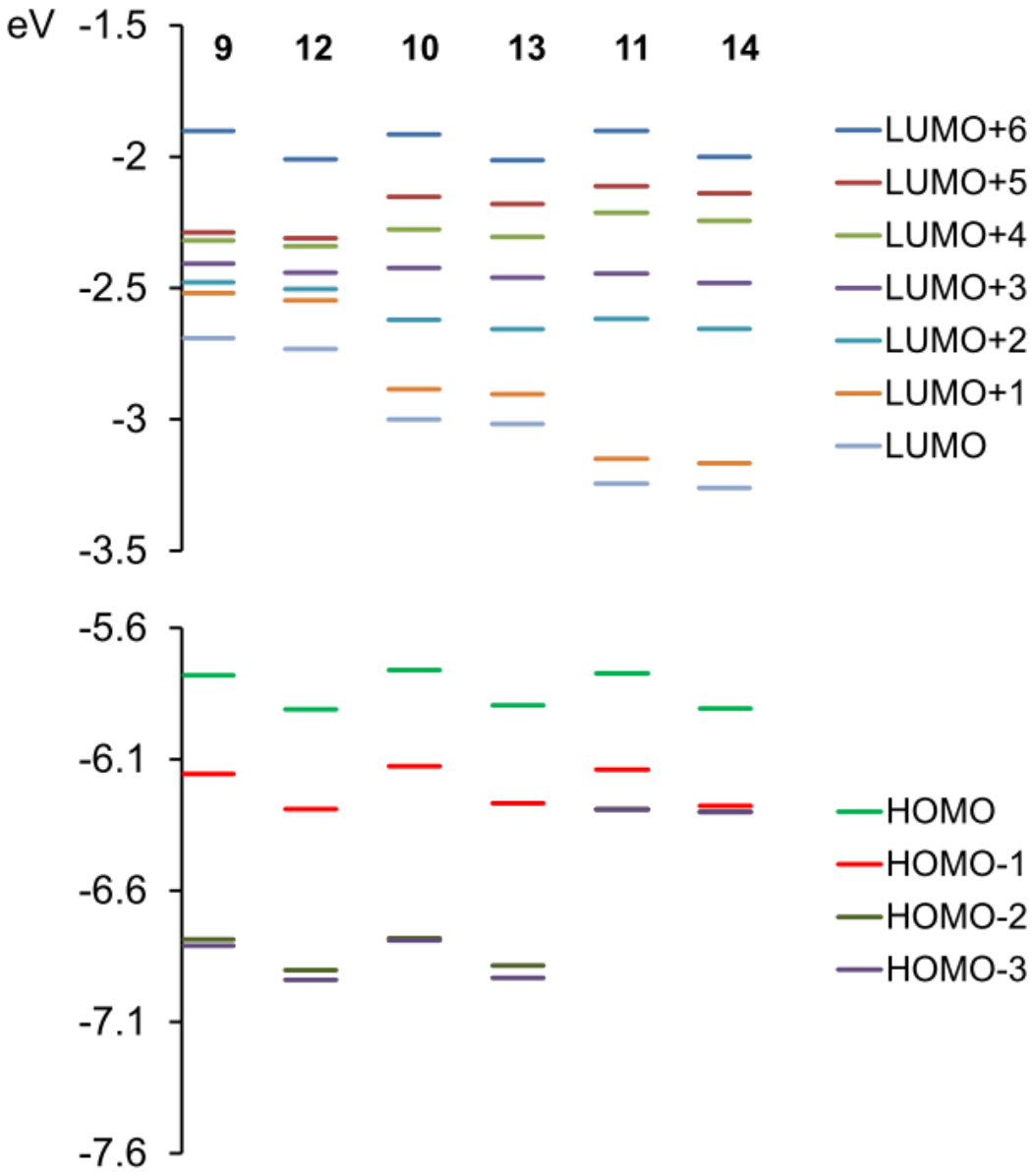

Figure 3.13 Calculated MO diagrams for **9**-**14**.

Table 3.4 Orbital contributions for **9-11** predicted by DFT calculations in CH_3CN.

	9	**10**	**11**
HOMO-5	77 Rh 10 DTolF 7 ax CH_3CN 6 dpq	78 Rh, 11 dppz, 9 DTolF	77 Rh 10 ax CH_3CN 7 dppn 6 DTolF
HOMO-4	91 DTolF	91 DTolF	66 DTolF 30 Rh
HOMO-3	78 Rh 9 ax CH_3CN 7 dpq 6 DTolF	78 Rh, 10 ax CH_3CN 7 dppz 6 DTolF	100 dppn
HOMO-2	65 DTolF, 30 Rh	66 DTolF 30 Rh	100 dppn
HOMO-1	83 DTolF, 11 Rh	85 DTolF 10 Rh	82 DTolF 11 Rh 5 dppn
HOMO	63 DTolF 33 Rh	64 DTolF 32 Rh	62 DTolF 32 Rh 5 dppn
LUMO	89 dpq 8 Rh	98 dppz	99 dppn
LUMO+1	88 dpq 11 Rh	79 dppz 21 Rh	80 dppn 20 Rh
LUMO+2	94 dpq	86 dppz 10 Rh	86 dppn 10 Rh
LUMO+3	82 dpq 15 Rh	63 dppz 36 Rh	65 dppn 33 Rh
LUMO+4	58 dpq 41 Rh	97 dppz	97 dppn
LUMO+5	96 dpq	96 dppz	96 dppn
LUMO+6	66 Rh 15 ax CH_3CN 11 DTolF 9 dpq	66 Rh 15 ax CH_3CN 11 DTolF 8 dppz	66 Rh 15 ax CH_3CN 11 DTolF 9 dppn

Table 3.5 Orbital contributions for **12-14** predicted by DFT calculations in CH_3CN.

	12	**13**	**14**
HOMO-5	72 Rh 16 F-form 10 dpq	69 F-form 25 Rh	61 F-form 35 Rh
HOMO-4	76 Rh 10 Fform 7 ax CH_3CN 7 dpq	61 Fform 35 Rh	79 Rh 9 ax CH_3CN 8 dppn
HOMO-3	61 F-form 35 Rh	79 Rh 9 ax CH_3CN 7 dppz	91 dppn 7 F-form
HOMO-2	79 Rh 9 ax CH_3CN 7 dpq	79 Rh 9 ax CH_3CN 7 dppz	100 dppn
HOMO-1	84 F-form 10 Rh	85 F-form 10 Rh	79 F-form 10 Rh 9 dppn
HOMO	63 F-form, 33 Rh	63 F-form 33 Rh	63 F-form 33 Rh
LUMO	89 dpq 8 Rh	98 dppz	99 dppn
LUMO+1	87 dpq 11 Rh	80 dppz 20 Rh	81 dppn 18 Rh
LUMO+2	94 dpq	86 dppz 10 Rh	86 dppn 10 Rh
LUMO+3	85 dpq 13 Rh	62 dppz 36 Rh	65 dppn 33 Rh
LUMO+4	58 dpq 41 Rh	97 dppz	96 dppn
LUMO+5	96 dpq	96 dppz	95 dppn
LUMO+6	66 Rh 15 ax CH_3CN 11 F-form 9 dpq	66 Rh 15 ax CH_3CN 11 F-form 8 dppz	66 Rh 15 ax CH_3CN 11 F-form 9 dppn

The HOMO and HOMO-1 are of all the complexes are calculated to contain significant contributions from the formamidinate ligands. In general, the HOMO of each complex exhibits ~63% contribution from the $[DTolF]^-$ or $[F\text{-form}]^-$ ligand and ~33% from Rh, whereas the HOMO-1 typically contains ~84% formamidinate and ~10% Rh character (Tables 3.4 and 3.5). Consistent with the ligand contributions to these orbitals, the relative energy of the HOMO and HOMO-1 vary with the nature of the formamidinate ligand by ~0.1 eV. The HOMO-2 has ~65% $[DTolF]^-$ and 30% Rh contributions in **9** and **10**, but this orbital is metal-centered in **12** and **13**, with 79% $Rh_2(\sigma)$ character and 9% contribution from the ax CH_3CN ligands. In the dppn complexes **11** and **14**, however, the HOMO-2 is completely localized on the dppn ligand.

It is evident from Tables 3.4 and 3.5 that the LUMO to LUMO+5 orbitals in **9**-**14** are centered on the corresponding diimine ligand. The relative energies of the LUMOs are consistent with the ease of reduction of the complexes, *i.e.*, **9** and **12** are more difficult to reduce than **10** and **13**, and **11** and **14** are easier to reduce (Table 3.3). In each complex, the LUMO+6 is calculated to possess 66% $Rh_2(\sigma^*)$ character with 15% contribution from ax CH_3CN ligands. The HOMO, LUMO and LUMO+6 levels of **9** are depicted in Figure 3.14 and are representative of the ones calculated for **10**, **11**, and **12**-**14**.

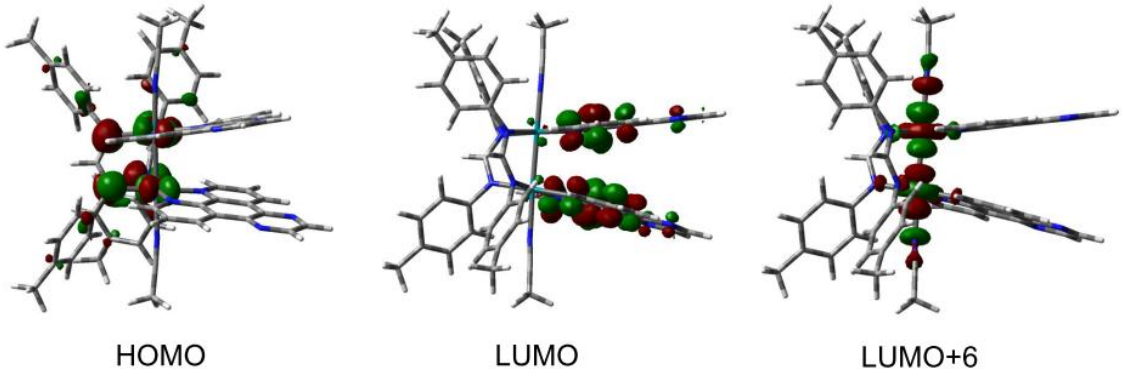

Figure 3.14 Electron density maps of the HOMO, LUMO and LUMO+6 of **9** drawn with iso-value = 0.04.

The vertical energies and orbital contributions for the lowest eight singlet excited states of **9-11** and **12-14** are listed in Tables 3.6 and 3.7, respectively. In all complexes, the major contribution to the lowest energy singlet excited state (≥82% in **9- 11** and ≥78% in **12-14**) corresponds to the transfer of electron density from the HOMO to the LUMO of each complex. Because the HOMO exhibits a high degree of formamidinate character (~66%) and the LUMO is localized on the corresponding diimine ligands, this state may be assigned as a ligand-to-ligand charge transfer (^{1}LLCT). The calculated oscillator strengths, f, of the vertical transitions from the ground state, ^{1}GS, to the lowest energy state, ^{1}LLCT state listed in Tables 3.6 and 3.7 are relatively low in **9** (f = 0.0014), **10** (f = 0.0004), **12** (f = 0.0012), and **13** (f = 0.0004), but the calculated transition energies are in good agreement with the experimental maxima in these complexes (Table 3.3). For example, the calculated energy of the ^{1}GS→^{1}LLCT transitions in **9** and **12** are 536 nm and 518 nm, which compare well with the estimated experimental maxima of 525 nm

Table 3.6 Vertical energies of the singlet excited states, λ (in nm), oscillator strengths, *f*, and major orbital contributions [a] calculated for **9**-**11** in CH_3CN (H = HOMO; L = LUMO).

Excited State	**9**	**10**	**11**
1	536 nm, *f* = 0.0014 H → L (91.0%)	562 nm, *f* = 0.0004 H → L (82.0%)	611 nm, *f* = 0.0000 H → L (96.7%)
2	514 nm, *f* = 0.0000 H → L+6 (91.2%)	528 nm, *f* = 0.0002 H → L+1 (87.6%)	580 nm, *f* = 0.0001 H → L+1 (97.7%)
3	493 nm, *f* = 0.0003 H → L+1 (82.5%)	518 nm, *f* = 0.0011 H → L+2 (79.6%)	523 nm, *f* = 0.0022 H → L+3 (94.5%)
4	461 nm, *f* = 0.0009 H → L+3 (80.4%)	518 nm, *f* = 0.0000 H → L+6 (89.0%)	516 nm, *f* = 0.0001 H–3 → L (70.6%), H–2 → L+1 (25.7%)
5	457 nm, *f* = 0.0015, H–5 → L+4 (32.9%), H–3 → L+4 (34.0%), H → L+2 (20.2%)	478 nm, *f* = 0.0001 H → L+3 (89.1%)	515 nm, *f* = 0.0275 H–3 → L+1 (25.6%), H–2 → L (72.9%)
6	454 nm, *f* = 0.0005 H → L+2 (70.3%)	470 nm, *f* = 0.0108 H–1 → L (90.6%)	515 nm, *f* = 0.0001 H → L+6 (92.0%)
7	446 nm, *f* = 0.0130 H–1 → L (48.8%), H–6 → L+6 (28.8%)	458 nm, *f* = 0.0026 H–7 → L+6 (43.8%), H–3 → L+6 (45.9%)	507 nm, *f* = 0.0102 H–1 →L (95.6%)
8	438 nm, *f* = 0.0022 H → L+3 (94.9%)	447 nm, *f* = 0.0017 H–1 → L+1 (95.2%)	486 nm, *f* = 0.0013 H–1 → L+1 (97.9%)

[a]Only contributions of ≥20% are listed.

Table 3.7 Vertical energies of the singlet excited states, λ (in nm), oscillator strength, *f*, and major orbital contributions [a] calculated for **12-14** in CH_3CN (H = HOMO; L = LUMO).

Excited State	**12**	**13**	**14**
1	518 nm, *f* = 0.0012 H → L (92.1%)	537 nm, *f* = 0.0004 H → L (78.2%), H → L+2 (20.6%)	579 nm, *f* = 0.0000 H → L (96.2%)
2	511 nm, *f* = 0.0000 H → L+6 (92.4%)	514 nm, *f* = 0.0001 H → L+6 (88.6%)	551 nm, *f* = 0.0002 H → L+1 (97.3%)
3	475 nm, *f* = 0.0003 H → L+1 (85.0%)	504 nm, *f* = 0.0002 H → L+1 (86.4%)	517 nm, *f* = 0.0003 H–3 → L (66.0%), H–2 → L+1 (26.8%)
4	459 nm, *f* = 0.0016 H–4 → L+6 (36.5%), H–2 → L+6 (51.5%)	497 nm, *f* = 0.0010 H → L (21.0%), H → L+2 (76.2%)	517 nm, *f* = 0.0287 H–3 → L+1 (24.5%), H–2 → L (72.3%)
5	447 nm, *f* = 0.0002 H–5 → L+6 (25.7%), H → L+3 (41.8%)	461 nm, *f* = 0.0001 H → L+3 (86.8%)	509 nm, *f* = 0.0001 H → L+6 (92.7%)
6	443 nm, *f* = 0.0047 H–4 → L+6 (34.4%), H → L+3 (44.2%)	460 nm, *f* = 0.0021 H–6 → L+6 (31.4%), H–2 → L+6 (50.0%)	503 nm, *f* = 0.0011 H → L+2 (93.7%)
7	438 nm, *f* = 0.0002 H → L+2 (91.3%)	451 nm, *f* = 0.0122 H–1 → L (73.5%)	483 nm, *f* = 0.0104 H–1 → L (91.4%)
8	427 nm, *f* = 0.0091 H–1 → L (82.5%)	444 nm, *f* = 0.0000 H–5 → L+6 (50.9%)	477 nm, *f* = 0.0030 H–3 → L+1 (64.2%), H–2 → L (26.9%)

[a]Only contributions of ≥20% are listed.

and 520 nm, respectively (Table 3.3 and Figure 3.9a). We also note that the only other transitions calculated with a greater oscillator strength in the visible region are those at 457 nm (f = 0.0015), 446 nm (f = 0.013) and 438 nm (f = 0.0022) for **9** and 459 nm (f = 0.0016), 447 nm (f = 0.0047), and 427 nm (f = 0.0091) for **12**. These calculated values are consistent with the increasing intensity of the absorption at $\lambda < 500$ nm, but, because these are shoulders, it is difficult to estimate an experimental maxima.

The calculated maxima for the lowest energy $^1GS \rightarrow {}^1LLCT$ transitions at 562 nm and 537 nm for **10** and **13**, respectively, are bathochromic shifted from those of **9** and **12** (Tables 3.6 and 3.7), consistent with ease of reduction for the diimine ligands in the former as compared to the latter compounds (Table 3.3). This trend is also observed in the maxima of the lowest energy transitions of **10** and **13** at 541 nm and 537 nm, respectively, which compare well with the calculated values. In addition to the lowest energy transition, absorptions are also predicted to occur between 447 nm and 518 nm for **10**, the strongest of which is at 470 nm (f = 0.0108), listed in Table 3.6. Similarly, transitions at 497 nm (f = 0.0010), 460 nm (f = 0.0021), and 451 nm (f = 0.0122) are calculated for **13** (Table 3.7).

A value of f = 0.0000 is calculated for the $^1GS \rightarrow {}^1LLCT$ lowest energy transitions of **11** and **14** at 611 nm and 579 nm, respectively (Tables 3.6 and 3.7); accordingly these transitions are not expected to have significant intensity. It should be noted, however, that the absorption spectrum of **11** (Figure 3.9) extends beyond 600 nm whereas that of **14** does not (Figure 3.9), a trend that is consistent with the calculated values. Other stronger electronic transitions are predicted at 523 nm (f = 0.0022) and 515 nm (f =

0.0275) for **11** and 517 (f = 0.0287) for **14** which are consistent with the estimated maxima of the shoulders at ~553 nm and ~525 nm for **11** and **14**, respectively (Table 3.3). The low energy transitions of **11** are red-shifted relative to those of **14**, which is rationalized by the fact that $[DTolF]^-$ is a better electron donor than is $[F\text{-form}]^-$ which influences the transitions that involves depletion of electron density from the formamidinate ligands (Tables 3.6 and 3.7).

Concluding remarks

The two series of dirhodium complexes in this chapter exhibit unusual photophysical properties involving low energy Ligand-to-Ligand Charge Transfer (LL'CT) transitions. This conclusion was confirmed by both experimental and theoretical data. The oxidation of these complexes is facile, as evidenced by their cyclic voltammetric diagrams. This is also in accord with the results of a series of chemical oxidation experiments. The data obtained in this project indicate that electronic properties tuning of dirhodium complexes can be readily achieved by a systematic ligand design approach.

CHAPTER IV

STUDY OF PARTIAL PADDLEWHEEL DIRHODIUM COMPLEXES WITH PYRIDINATE BRIDGING LIGANDS

Introduction

The serendipitous discovery of the anticancer activity of cisplatin (*cis*-$Pt(NH_3)_2Cl_2$) launched a new era of metals in medicinal research[167,168] which was approved officially by the FDA in 1978 for the treatment of testicular and ovarian cancers. It has been well documented that the complex undergoes hydrolysis upon administration to generate the active aqua species *cis*-$[Pt(NH_3)_2Cl(H_2O)]^+$ and *cis*-$[Pt(NH_3)_2(H_2O)_2]^{2+}$, which preferentially bind to the N-7 guanine site in DNA to form 1,2-intrastrand crosslinks.[169-180] These lesions induce DNA distortions, inhibit transcription and the DNA replication process and ultimately lead to the cell death.[169-180] In spite of the efficacy of the drug, severe nephrotoxicity as well as intrinsic and acquired resistance[181-186] have necessitated the development of second and third generation platinum-based anticancer drugs. During the past three decades, only two other platinum drugs, namely carboplatin[187,188] and oxaliplatin,[189,190] were approved for clinical use by the FDA in addition to several other platinum based drugs being approved in other countries.[191] Considering the fact that platinum-based anticancer agents are highly effective and are the leading drugs for the current cancer therapy, there is a pressing need for new platinum-containing anticancer agents.[192-205] Despite the efficacy of platinum anticancer drugs, other transition metal containing complexes also deserve further exploration, *e.g.* various dirhodium(II,II)

compounds that are active towards cisplatin-resistant cancer cell lines as well as some anticancer active complexes that are operative in different modes from cisplatin. [3-7,10]

Photodynamic Therapy (PDT) has emerged as a promising treatment for cancer as well as some other diseases with the advantage over conventional chemotherapy being that active toxic species are generated only in selectively irradiated tissues. The clinically approved drug for PDT treatment, Photofrin®, functions by the production of reactive oxygen species including $^1O_2$ (singlet oxygen) upon irradiation with visible light (~630 nm). [206] These cytotoxic species damage subcellular organelles and macromolecules, leading to apoptosis and/or necrosis of the affected cells.[206] The low concentration of O_2 or the slow diffusion of O_2 from adjacent tissues, however, restricts the use of these drugs in dense hypoxic tumors.[207-209] A different approach to the same problem can be to use transition metal complexes which can also produce $^1O_2$ but which can also bind covalently to relevant biomolecules upon irradiation due to the dissociation of photo-labile ligands in the excited states via an O_2 independent pathway.[210 - 219] Moreover, biologically active molecules can be attached to the metal complexes as the photo-labile ligands which, when released upon irradiation, will generate two active species, namely a metal complex with an open coordination site and an organic drug, from a single precursor.[220-222]

A recent study by the Turro group revealed the potential of the partial paddlewheel dirhodium(II,II) compound *cis*-$[Rh_2(\mu\text{-}O_2CCH_3)_2(CH_3CN)_6][BF_4]_2$ as a PDT agent (Scheme 4.1). It is postulated that the photo-lability of the stable eq CH_3CN ligands in the dark is crucial for the formation of the active species upon light irradiation.[9] As such,

different dirhodium(II,II) complexes with photo-labile CH_3CN ligands were jointly developed by our research groups, *e.g.* head to head (H-H), head to tail (H-T) *cis*-$[Rh_2(NHOCCH_3)_2(CH_3CN)_6][BF_4]_2$ [223] and unbridged $[Rh_2(phen)_2(CH_3CN)_6][BF_4]_4$ (phen: 1,10-phenanthroline)[224] and found to have promising potential as effective PDT anticancer agents. To construct a structure/activity relationship for the dirhodium(II,II) partial paddlewheel complex with monodentate CH_3CN ligands, the substituted oxopyridine (Scheme 4.1b) ligands were chosen as bridging ligands in the current study due to the easy tuning of the ligand field in these complexes. The results in this chapter involve the syntheses and characterization of series of dirhodium(II,II) complexes featuring two *cis* 6-R-oxo-pyridinate (R = -CH_3, 6-methyl-oxo-pyridine, **mhp**; R = -Cl, 6-chloro-oxo-pyridine, **chp**; R = -F, 6-fluoro-oxo-pyridine, **fhp**.) bridging ligands; the investigation of their potential as PDT agents is also presented.

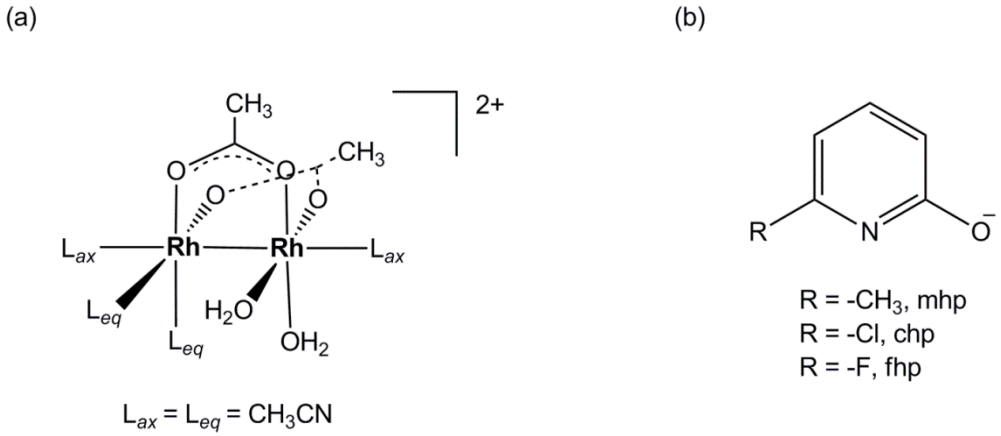

Scheme 4.1 Structural representation of (a) active species generated from *cis*-$[Rh_2(\mu\text{-}O_2CCH_3)_2(CH_3CN)_6]^{2+}$ upon irradiation; (b) bridging 6-R-oxo-pyridine ligands.

Experimental section

Starting materials

The compound $Rh_2(\mu\text{-}O_2CCH_3)_4\bullet 2CH_3OH$ was either purchased from Pressure Chemical Company or synthesized from $RhCl_3\bullet 3H_2O$ as reported.[225] The ligands 2-hydoxy-6-methylpyridine (Hmhp), 2-hydroxy-6-chloropyridine (Hchp) were purchased from Sigma Aldrich and used as received whereas 2-hydroxy-6-fluoropyridine was purchased from VWR and used without further purification. The reagent Et_3OBF_4 (1 M in CH_2Cl_2) was purchased from Sigma Aldrich. The solvents acetonitrile, dichloromethane, diethyl ether, chlorobenzene, dimethyl sulfoxide (DMSO) and tetrahydrofuran (THF) were of ACS grade and used as received. The NMR solvents D_2O (d_2) and CD_3CN (d_3) were purchased from Cambridge Isotope Laboratory. The compound $Rh_2(mhp)_4$ (**15**) was synthesized according to a slightly modified literature procedure.[226]

Preparation of $Rh_2(chp)_4$ (16). A quantity of ~ 4.4 equivalents of Hchp ligand (220 mg, 1.70 mmol) was mixed with 50 mL of chlorobenzene suspended with $Rh_2(\mu\text{-}O_2CCH_3)_4\bullet 2CH_3OH$ (195 mg, 0.39 mmol) and refluxed for 36 h, forming a slightly green colored solution with a large quantity of yellow precipitate. The solid was collected by filtration and then washed with copious volumes of CH_3OH (50 mL) to remove unreacted Hchp ligand. The yield is 235 mg, which is 85% based on rhodium.

Preparation of $Rh_2(fhp)_4$ (17). A quantity of ~ 4.1 equivalents of Hfhp ligand (186 mg, 1.65 mmol) was mixed with a suspension of $Rh_2(\mu\text{-}O_2CCH_3)_4\bullet 2CH_3OH$ (200 mg, 0.40 mmol) in 50 mL of chlorobenzene and refluxed for 48 h. The resulting teal colored solution which contained a large amount of green precipitate was dried under vacuum

after which time 50 mL CH_3OH was added and the solution was filtered through a medium frit to remove unreacted Hfhp ligand. The product was collected as a green solid (240 mg, 93% yield). Crystals suitable for X-ray diffraction were obtained from slow evaporation of an acetone solution containing the product in the presence of several drops of DMSO. ^{1}H-NMR ($(CD_3)_2CO$~d_6): 7.29 (m, fhp), 6.22 (d, fhp), 6.09(d, fhp).

Preparation of *cis*-[Rh_2(mhp)$_2$(CH_3CN)$_6$][BF_4]$_2$ (18). An amount of $Rh_2(mhp)_4$ (81 mg, 0.13 mmol) was added to 30 mL of a mixture of CH_3CN:CH_2Cl_2 (v:v = 1:2). An aliquot of 0.5 mL of Et_3OBF_4 (1.0 M in CH_2Cl_2) was added to this suspension, leading to instantaneous formation of a clear green solution which eventually turned into red color over the course of 6 hours. The solution was stirred at room temperature for 24 h and then concentrated to 5 mL and treated with 50 mL of diethyl ether which led to the precipitation of the product in an oily form. The oil was washed with copious quantities of diethyl ether and recrystallized by slow diffusion of diethyl ether into the CH_3CN solution of the product at room temperature. The yield is 82mg (75% based on rhodium). X-ray quality crystals were obtained in a similar fashion. ^{1}H NMR (CD_3CN-d_3) δ ppm: 7.21 (t, 2H, mhp), 6.36 (d, 2H, mhp), 6.22 (d, 2H, mhp), 2.63 (s, 6H, -CH_3 of mhp), 2.47 (s, 6H, eq CH_3CN), 2.46 (s, 6H, eq CH_3CN).

Preparation of H-T (19) and H-H (20) *cis*-[Rh_2(chp)$_2$(CH_3CN)$_6$][BF_4]$_2$. An amount of $Rh_2(chp)_4$ (90.4 mg, 0.13 mmol) was suspended in 30 mL of CH_2Cl_2/CH_3CN(v:v = 1:2) and a 0.4 mL aliquot of Et_3OBF_4 (1 M in CH_2Cl_2) was then added to the flask. The solution gradually became clear over the course of the next 6 h and was then stirred at room temperature for a total of 28 h. The solution eventually became clear red and was

concentrated to 5 mL and treated with 80 mL of diethyl ether, which led to the formation of an oily residue which was washed with copious diethyl ether to obtain a red powder (98 mg). As evidenced by ^{1}H-NMR spectroscopy, this solid contains both H-H and H-T isomers of *cis*-$[Rh_2(chp)_2(CH_3CN)_6][BF_4]_2$. The material was redissolved in 5 mL of CH_3CN and slow diffusion of diethyl ether into this solution at -4ºC led to the crystallization of the H-T isomer and the yield is 50 mg (44% based on rhodium). The crystals were collected by filtration and the filtrate was condensed to 2 mL. The recrystallization of the H-H isomer was achieved by slow diffusion of diethyl ether into the CH_3CN solution at room temperature. H-T isomer (**19**): ^{1}H NMR (CD_3CN-d_3) δ ppm: 7.44 (t, 2H, chp), 6.71 (d, 2H, chp), 6.33 (d, 2H, chp), 2.57 (s, 6H, eq CH_3CN, *trans* to N), 2.38 (s, 6H, eq CH_3CN, *trans* to O), 1.96(s, ax CH_3CN). H-H isomer (**20**): ^{1}H NMR (CD_3CN-d_3) δ ppm: 7.38 (t, chp), 6.74 (d, chp), 6.57 (d, chp), 2.55 (s, eq CH_3CN, *trans* to N), 2.48 (s, eq CH_3CN, *trans* to O), 1.96(s, ax CH_3CN).

Preparation of *cis*-$[Rh_2(fhp)_2(CH_3CN)_6][BF_4]_2$ (21). An amount of $Rh_2(fhp)_4$ (184 mg, 0.28 mmol) was suspended in 30 mL of CH_3CN/CH_2Cl_2 (v:v = 1:1). An aliquot of 1.2 mL of Et_3OBF_4 (1 M CH_2Cl_2) was added and the mixture was stirred for 4 days at room temperature. The initially green turbid mixture changed to violet and finally to red. The reaction solution was filtered to remove any insoluble materials and the filtrate was concentrated to 5 mL and treated with 50 mL of diethyl ether which led to precipitation of the desired product which was washed with copious amounts of diethyl ether to obtain a red powder. Yield: 194 mg, 81%. ^{1}H-NMR (CD_3CN-d_3) δ ppm: 7.49 (dd, fhp), 6.29(d,

fhp), 6.21(d, fhp), 2.49 (eq CH_3CN, *trans* to N), 2.48(eq CH_3CN, *trans* to O), 1.96 (free CH_3CN).

Instrumentation and methods

X-ray data sets for all the complexes were collected on a Bruker CCD APEX diffractometer with graphite monochromated Mo Kα radiation (λ = 0.71073 Å). Hemispheres of data for **15** and **18-20** were collected by a combination of four sets of X-ray exposures. Each set used a different ϕ angle for the crystals and covered 0.3° in ω for all the complexes. The exposure times were 10s for **15**, 20 s for **18**, **19** and 30 s for **20**. The crystal parameters and information pertaining to the data collection and refinement of the crystals for **15**, **18**-**20** are summarized in Table 4.1.

Results and discussion

Synthesis and solution characterization

Molten reactions were performed for the syntheses of **15** and **16** with an excess of Hmhp and Hchp ligands. After completion of the reactions, the excess ligands were removed by dissolution in CH_3OH which led to the formation of pure (*trans*, *syn*-2, 2) isomers as evidenced by ^{1}H-NMR spectra (Figures 4.1, 4.2 respectively), and X-ray crystallographic studies which are detailed in the following section. The crystal structures of both complexes were published in previous reports, [226] but the structure obtained herein for compound **15** exhibits different unit cell parameters from the published one. Therefore, the detailed crystal data parameters are also provided in Table 4.1. Compound **17** was synthesized by a different method from the published one and in improved yields. [227] Unlike the complex reported previously, it is only slightly soluble in

Table 4.1 Crystallographic data for $Rh_2(mhp)_4$ (**15**), *cis*-$[Rh_2(mhp)_2(CH_3CN)_6][BF_4]_2$ (**18**), H-T *cis*-$[Rh_2(chp)_2(CH_3CN)_6][BF_4]_2$•$CH_3CN$ (**19**•CH_3CN) and H-H *cis*-$[Rh_2(chp)_2(CH_3CN)_6][BF_4]_2$•$2CH_3CN$(**20**•$2CH_3CN$).

	15	**18**	**19**	**20**
Formula	$C_{24}H_{24}N_4Rh_2O_4$	$C_{24}H_{30}N_8O_2Rh_2B_2F_8$	$C_{24}H_{27}N_9O_2Cl_2Rh_2B_2F_8$	$C_{24}H_{27}N_9Rh_2Cl_2O_2B_2F_8$
Formula weight (g/mol)	638.29	841.97	923.86	923.86
Space group	*Pbca*	$P2_12_12_1$	$P2_1$/c	P-1
a, *b*, *c*/ Å	15.489(3) 15.961(3) 18.567(4)	12.194(2) 12.462(3) 22.014(4)	16.222(3) 12.319(3) 21.796(4)	11.609(2) 11.712(2) 15.189(3)
α, β, γ/ º	90,90,90	90, 90, 90	90.00, 96.88(3), 90.00	70.72(3), 76.07(3), 86.12(3)
Z	8	4	4	2
2θ range for data collection/º	57.44	54.83	46.53	57.31
Completeness to θmax/ %	95.3	99.9	99.5	90.1
R_1,[a] wR_2,[b] [$I > 4\sigma(I)$]	R = 0.0191, wR = 0.0464	R = 0.0314, wR = 0.0912	R = 0.0796, wR = 0.2067	R = 0.0301 wR = 0.0794
R_1,[a] wR_2,[b] (all data)	*R = 0.0231* *wR = 0.0485*	R = 0.0334, wR = 0.0930	R = 0.1013, wR = 0.2173	R = 0.0342, wR = 0.0817
Goodness-of-fit parameter (all data)[c]	1.042	1.061	0.964	1.060

[a] $R = \sum||F_o|-|F_c||/\sum|F_o|$. [b] $wR = \{\sum[w(F_o^2 - F_c^2)^2]/\sum w(F_o^2)^2]\}^{1/2}$. [c] Goodness-of-fit = $\{\sum[w(F_o^2 - F_c^2)^2]/(n-p)\}^{1/2}$, where *n* is the number of reflections and *p* is the total number of parameters refine

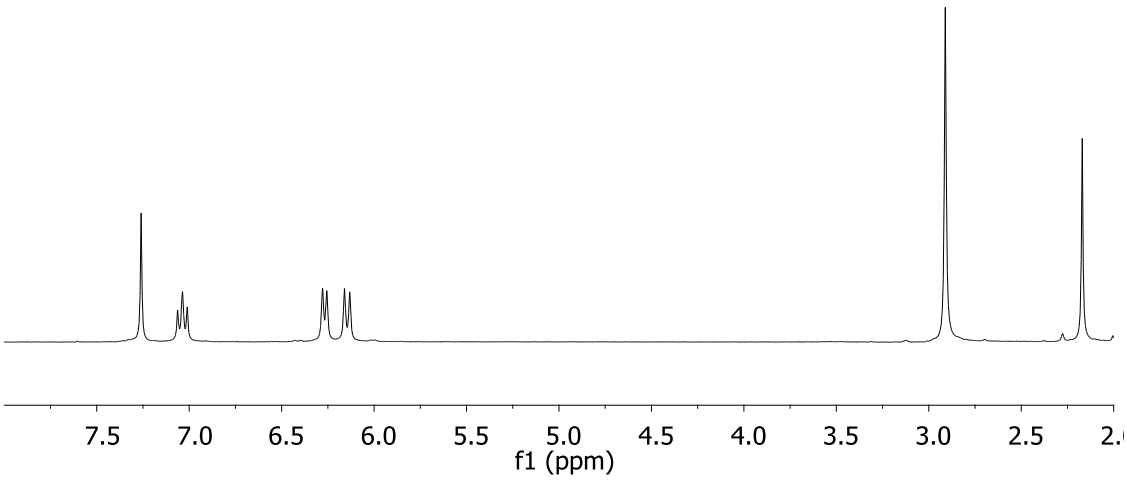

Figure 4.1 ^{1}H-NMR spectrum of compound **15** in $CDCl_3$.

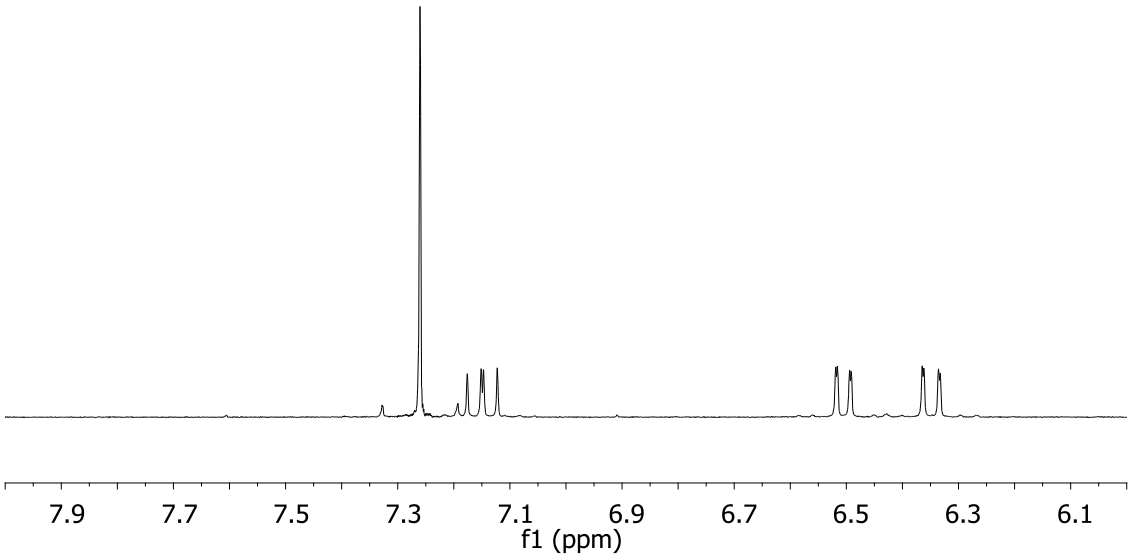

Figure 4.2 ^{1}H-NMR spectrum of compound **16** in $CDCl_3$.

THF, acetone and ethanol. With the presence of several drops of DMSO, several pink solutions containing **17** with THF, acetone and ethanol were obtained.

The alkylating agent Et_3OBF_4 was used to synthesize the partial paddlewheel complex *cis*-$[Rh_2(xhp)_2(CH_3CN)_6][BF_4]_2$ (**18-21**), similar to the method adopted by Turro *et al.* to prepare H-H and H-T *cis*-$[Rh_2(HNOCCH_3)_2(CH_3CN)_6][BF_4]_2$.[223] The reaction between Et_3OBF_4 and $Rh_2(mhp)_4$ produces only one isomer as indicated by its ^{1}H-NMR (Figure 4.3) spectrum which was identified as the H-T isomer by an X-ray crystallographic study. The synthetic route adopted for *cis*-$[Rh_2(chp)_2(CH_3CN)_6][BF_4]_2$, however, resulted in the formation of both the H-H and H-T isomers as indicated by ^{1}H-NMR spectroscopy (Figure 4.4). This finding indicates that the alkylating agent Et_3OBF_4 does not react discriminately with the two chp ligands in the *cis*-positions leading to the

formation of **19**, but also with the two bridging ligands occupying *trans*-positions which then undergo rearrangement into the more stable *cis* isomer to produce compound **20**. Compound **21** was synthesized by a similar procedure to the one used for complexes **18** and **19** but with much longer reaction times due to the low solubility of **17** in the solvent. Many trials to obtain a single crystal of compound **21** were unsuccessful. From the structure of precursor **17**, however, we can conclude that compound **21** adopts the H-H configuration.

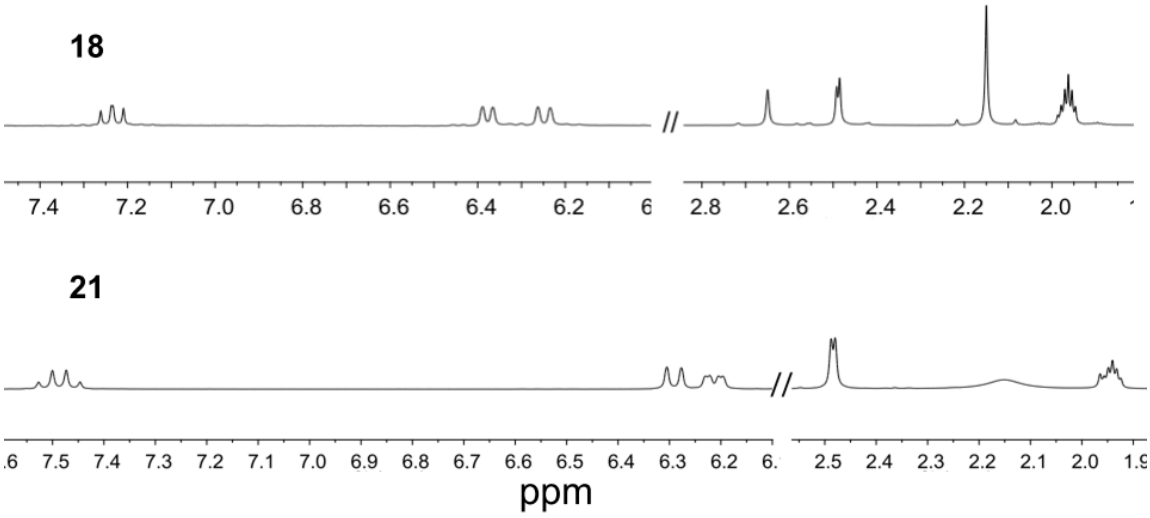

Figure 4.3 ^{1}H-NMR spectra for compounds **18** and **21**.

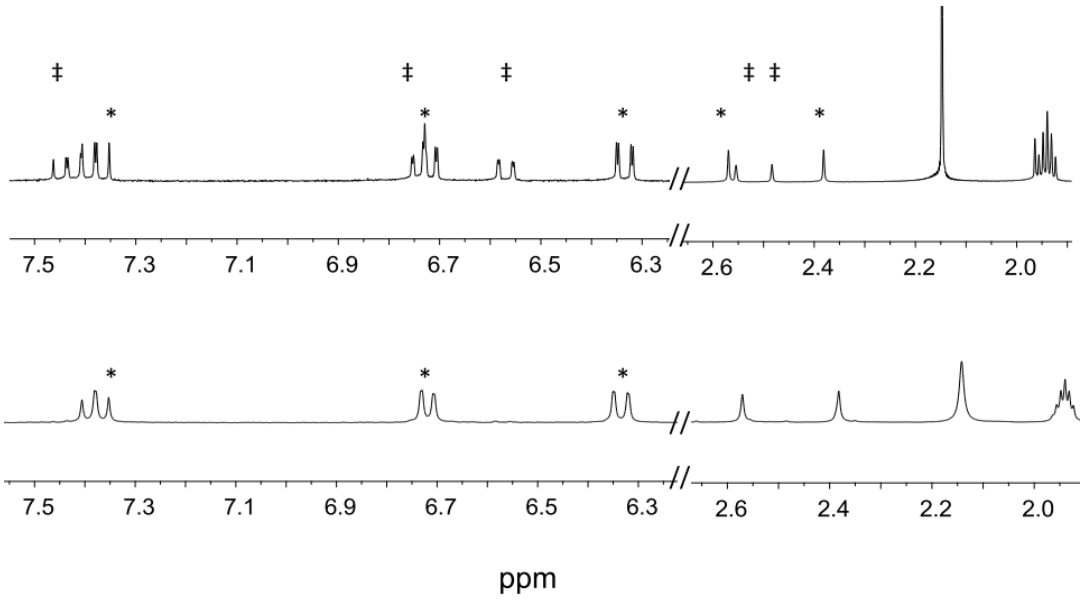

Figure 4.4 ^{1}H-NMR spectra of a mixture of **19** * and **20** ‡ (top) and pure **19** * (bottom) in the aromatic region in CD_3CN.

X-ray crystallographic studies

***cis*-$[Rh_2(mhp)_2(CH_3CN)_6][BF_4]_2$ (18).** The compound crystallizes in the chiral space group $P2_12_12_1$ and the cation contains two *cis* bridging mhp ligands in a H-T fashion. Six CH_3CN ligands complete the pseudo-octahedral coordination sphere of the central rhodium atoms (Figure 4.5) and there are two $[BF_4]^-$ present as counterions. One of the eq CH_3CN ligands and a $[BF_4]^-$ counterion are disordered between two different positions with site occupancies of 0.6366/0.3634 and 0.3765/0.6235 respectively. Racemic twinning was refined during the last cycle, with the flack parameter 0 and the esd value 0.9416. The Rh-Rh bond distance is 2.4794(5) Å, which is ~ 0.12 Å longer than that found for **15** which we ascribe to the less sterically demanding bridging mhp ligands in **18**. The Rh-N (ax CH_3CN) bond distances are 2.234(4) and 2.201(4) Å, significantly longer than the Rh-N (eq CH_3CN) bond distances which are in the range of 1.999(4)-2.014(4) Å. The Rh-N (mhp) and Rh-O (mhp) bond distances are comparable to the corresponding distances in **15** respectively. The distorted eq CH_3CN and mhp ligands away from the eclipsed confirmation reflect the repulsion between them. The dihedral angles defined by N5-Rh1-Rh2-N7 and N6-Rh1-Rh2-N8 are -36.5(1)º and -36.9(2)º respectively, larger than those in *cis*-$[Rh_2(DTolF)_2(CH_3CN)_6][BF_4]_2$ and *cis*-$[Rh_2(F\text{-}form)_2(CH_3CN)_6][BF_4]_2$.[229] Slightly smaller distortions are obserbved for the two mhp bridging ligands, with the dihedral angles defined by O1-Rh1-Rh2-N2, N1-Rh1-Rh2-O2 being -30.3(1) and -30.8(1)º.

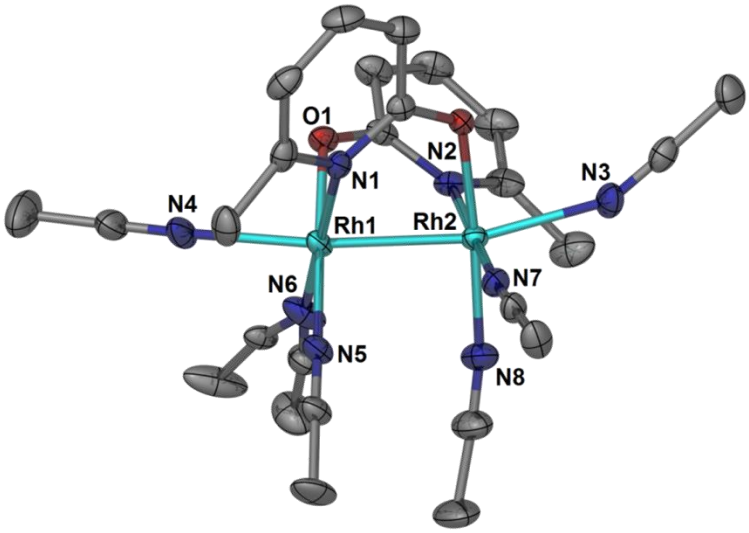

Figure 4.5 Thermal ellipsoid plot of the cationic part of compound **18** at the 50% probability level; the anions and hydrogen atoms are omitted for the sake of clarity.

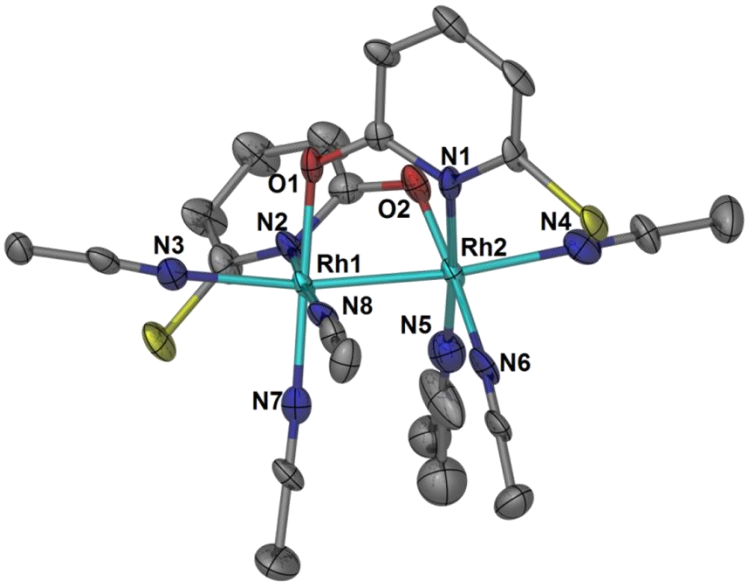

Figure 4.6 Thermal ellipsoid graph of the cationic unit in compound **19** at the 50% probability level; the anions and hydrogen atoms are omitted for the sake of clarity.

H-T *cis*-[$Rh_2(chp)_2(CH_3CN)_6$][BF_4]$_2$•CH_3CN (19•CH_3CN): Compound **19** crystallizes in the space group of $P2_1/c$ with a coordination sphere similar to that of compound **18** as seen in Figure 4.6. One of the eq CH_3CN ligands is disordered over two positions with a site occupancy of 0.5199/0.4801. The Rh-Rh bond distance is 2.492(1) Å, ~ 0.11 Å longer than that of $Rh_2(chp)_4$ due to the less constraints from the two bridging ligands in **19**. The Rh-N (ax CH_3CN) bond distances are 2.21(1) and 2.25(1) Å, longer than the Rh-N (eq CH_3CN) bond distances ranging from 1.97(1) to 2.031(9) Å. Similar distortions from the eclipsed configuration of the eq CH_3CN ligands occur, with larger distortions for the eq CH_3CN ligands than those defined by the chp ligand.

H-H *cis*-[$Rh_2(chp)_2(CH_3CN)_6$][BF_4]$_2$•2CH_3CN (20): Compound **20** crystallizes in the space group *P*-1. The thermal ellipsoid plot of the cationic unit is displayed in Figure 4.7 and can be seen to consist of two *cisoid* bridging chp ligands in the H-H fashion, four eq CH_3CN ligands and one ax CH_3CN coordinated to the Rh center that is bonded to the O atoms of the bridging chp ligands. The Rh-Rh bond distance is 2.505(1) Å, slightly longer than those in **18** and **19**. The Rh-N (ax CH_3CN) bond distance is 2.114(2) Å, ~ 0.1 Å shorter than that in **18**, **19** and H-T *cis*-[$Rh_2(HNOCCH_3)_2(CH_3CN)_6$][$BF_4$]$_2$.[223] The Rh-N (eq CH_3CN) bond distances fall in a small range of 1.989(3) to 2.002(2) Å, similar to those in **18** and **19**. Much smaller distortions from the eclipsed configuration defined by the eq CH_3CN ligands in **20** occur as compared to that found for **18** and **19**, with the dihedral angles defined by N4-Rh1-Rh2-N6 and N3-Rh1-Rh2-N5 being 23.55(9)º and 23.51(9)º. Distortions of the bridging chp ligands are only slightly smaller, with the angles being 19.35(9)º and 21.74(8) º respectively.

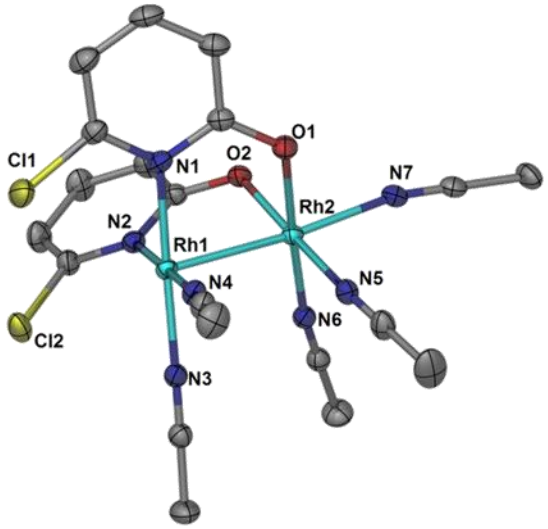

Figure 4.7 Thermal ellipsoid graph of the cationic part in compound **20** at the 50% probability level; the anions and hydrogen atoms are omitted for the sake of clarity.

*^{1}H-NMR investigations of compounds **18**, **19** and **21***

The exchange process of the monodentate eq CH_3CN ligands in **18**, **19**, and **21** with the NMR solvent molecule CD_3CN or D_2O in the dark was monitored by ^{1}HNMR spectroscopy and the results are detailed in the following section.

As shown in Figure 4.8, three different resonances in the aliphatic region are present in the ^{1}H-NMR spectrum of **18** obtained ~2 min after dissolution in CD_3CN, with chemical shifts of 2.63, 2.47 and 2.46 ppm, respectively. The peak at ~2.63 ppm is assigned to the $–CH_3$ groups on the mhp ligands since its intensity does not change over the course of the experiment (*vide infra*). The other two closely spaced resonances are attributed to the two different sets of eq CH_3CN ligands which are *trans* to O and N atoms of the mhp ligands respectively. After 15 min, a distinct decrease in intensity for

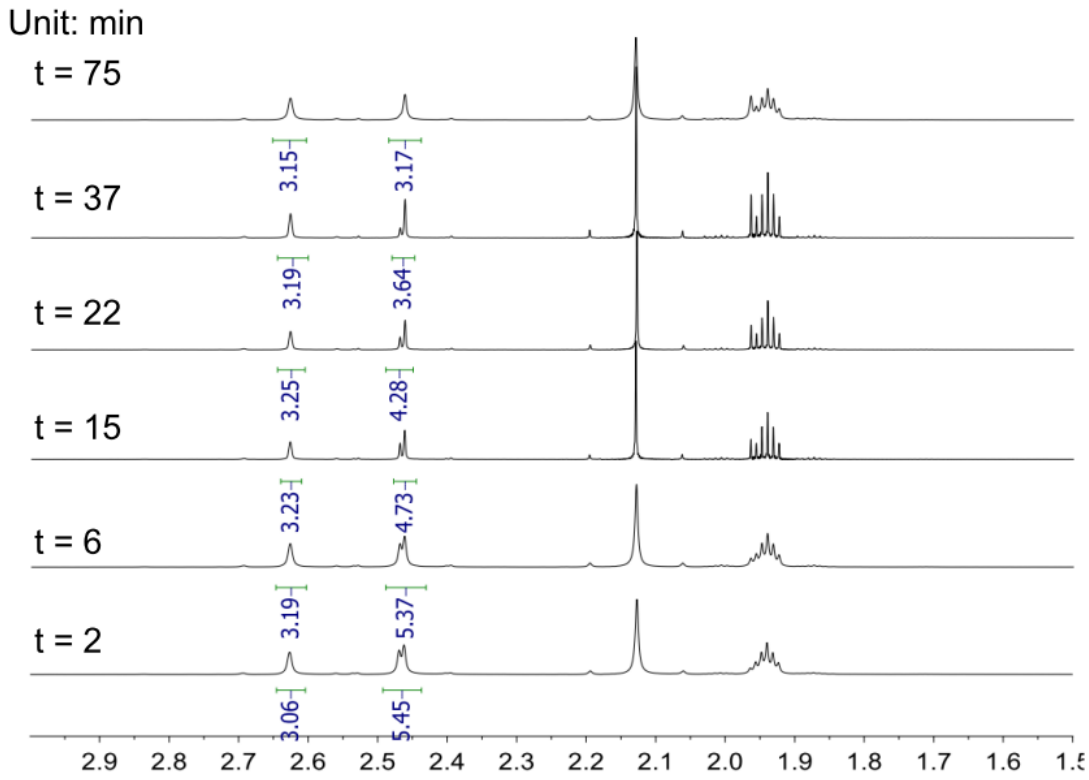

Figure 4.8 ^{1}H-NMR spectral changes of complex **18** in the dark in CD_3CN.

the resonance ~ 2.47 ppm is observed, attributed to fast exchange with the CD_3CN molecules. This peak disappeared after 75 min in the dark, indicating the much faster exchange process with the CD_3CN molecules than that in *cis*-$[Rh_2(\mu\text{-}O_2CCH_3)_2(CH_3CN)_6][BF_4]_2$.[8]

The investigation of the lability of the eq CH_3CN ligands in compound **19** was conducted in a similar fashion. In this case, two resonances at 2.57 and 2.38 ppm were observed corresponding to the eq CH_3CN ligands *trans* to O and N atoms of the chp ligand respectively. As shown in Figure 4.9, the intensity of both peaks decrease simultaneously over the course of 65 h with the exchange rate for the latter resonance being much faster than that for the former one. Both exchange processes are much slower, however, than that of compound **18**, presumably due to the weaker *trans* effect exerted by bridging chp ligands owing to the presence of electron withdrawing Cl substituents in **19**.

For compound **21**, the two types of eq CH_3CN ligands, namely either *trans* to the N or to the O atoms of the fhp ligands, exhibit only slightly different chemical shifts (δ = 2.49 and 2.48 ppm). The former resonance disappears over a period of ~ 340 h, indicating its complete substitution by CD_3CN molecules whereas the latter one has only negligible changes in intensity during the same period of time (Figure 4.10). These features are ascribed to the much stronger electron withdrawing ability of the F substituents on the bridging fhp ligands.

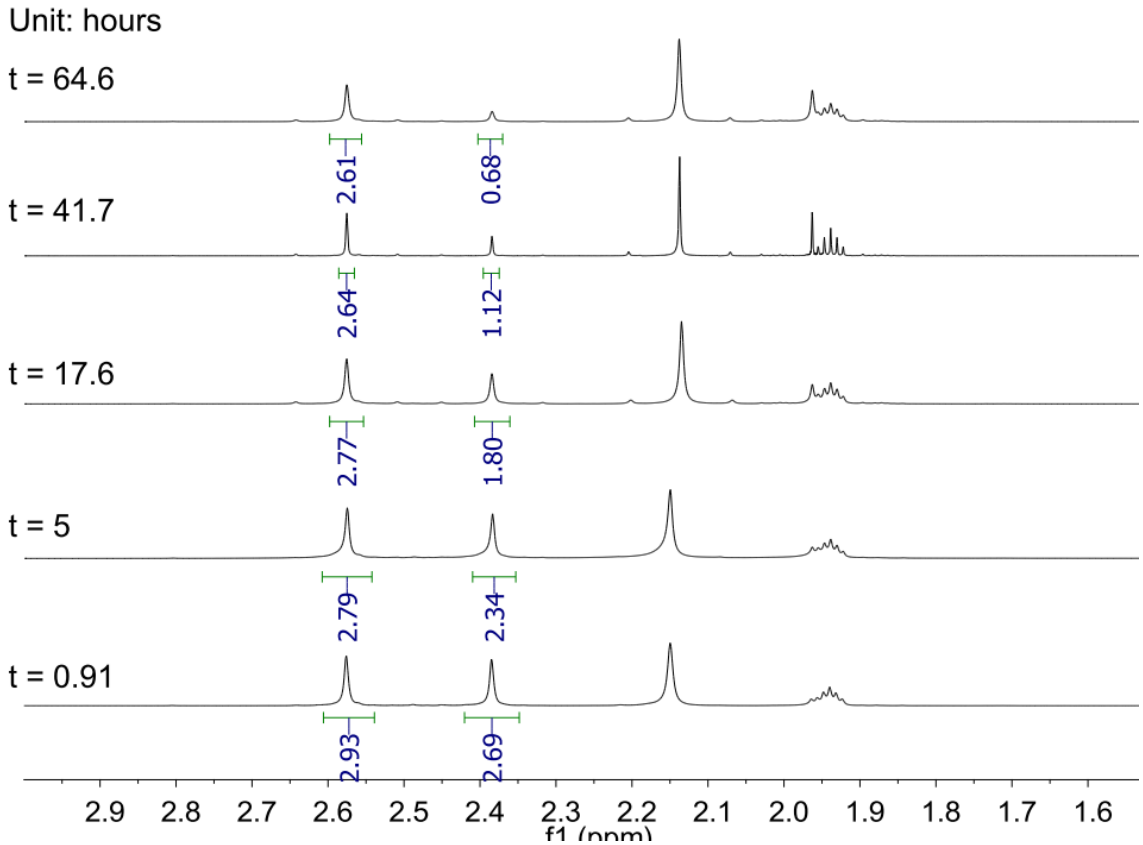

Figure 4.9 ^{1}H-NMR spectral changes in complex **19** in the dark in CD_3CN; only the region involving the change in the spectra is shown.

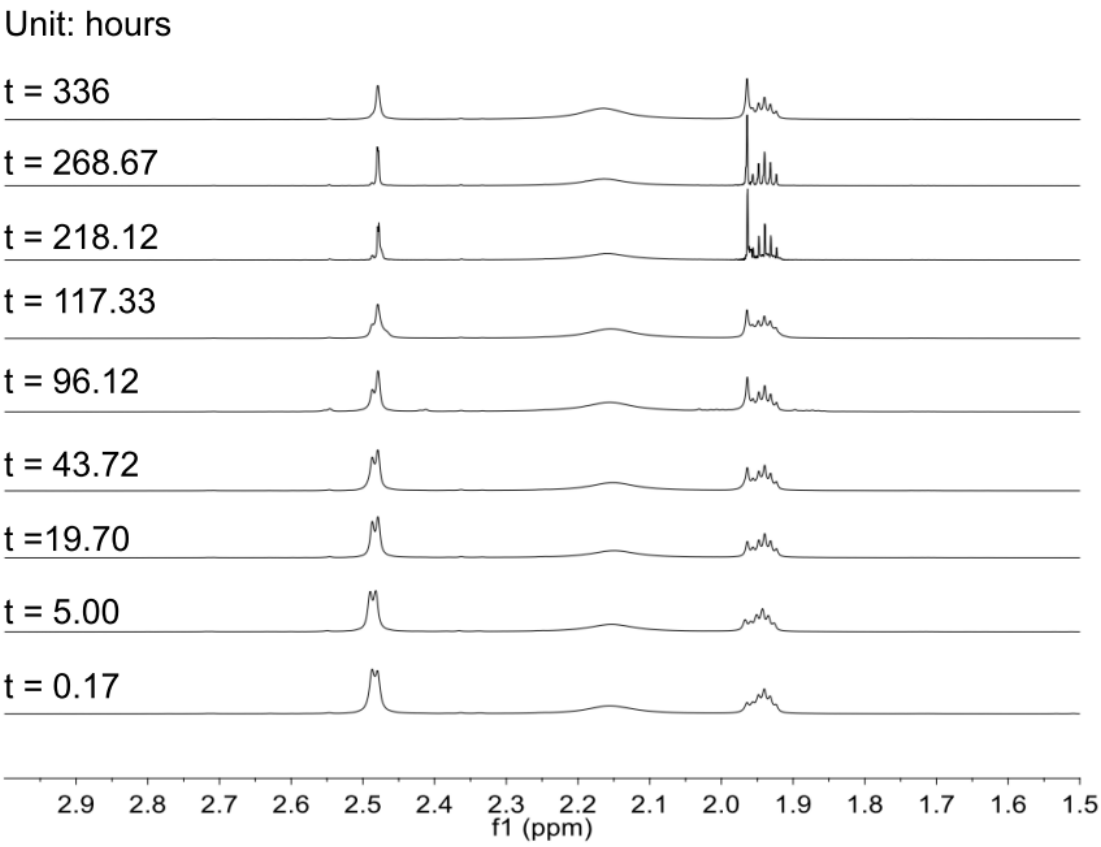

Figure 4.10 ^{1}H-NMR spectral change for complex **21** in the dark in CD_3CN; only the region involving the changes in the spectra are shown.

The exchange of eq CH_3CN with H_2O molecules in **18** was also monitored by ^{1}H-NMR spectroscopy in the dark. Upon dissolution in D_2O the solution turns green in contrast to its red color in CD_3CN. A very fast substitution process involving the D_2O molecules is apparently occurring, a fact that is further corroborated by the very complicated ^{1}H-NMR spectrum and the intense signal at 2.06 ppm for free CH_3CN (Figure 4.11). Similarly, for both compounds **19** and **21**, there is also exchange of eq

CH_3CN ligands with D_2O molecules but at a significant slower rate as compared to that in compound **18** as indicated by Figures 4.12 and 4.13 respectively.

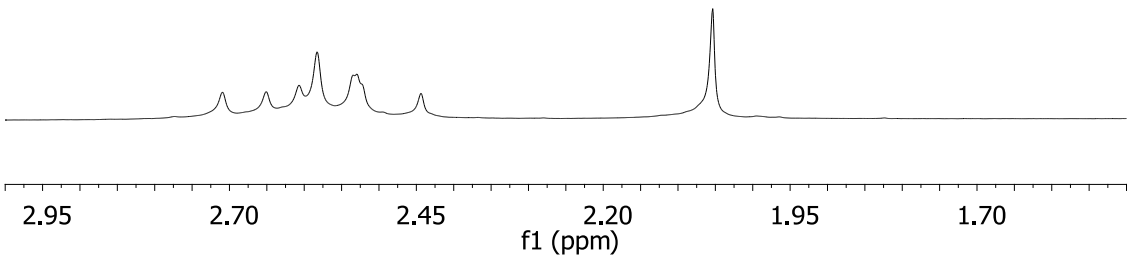

Figure 4.11 ^{1}H-NMR spectrum of **18** after dissolution in D_2O for 10 min, indicating very fast exchange of eq CH_3CN with D_2O molecules.

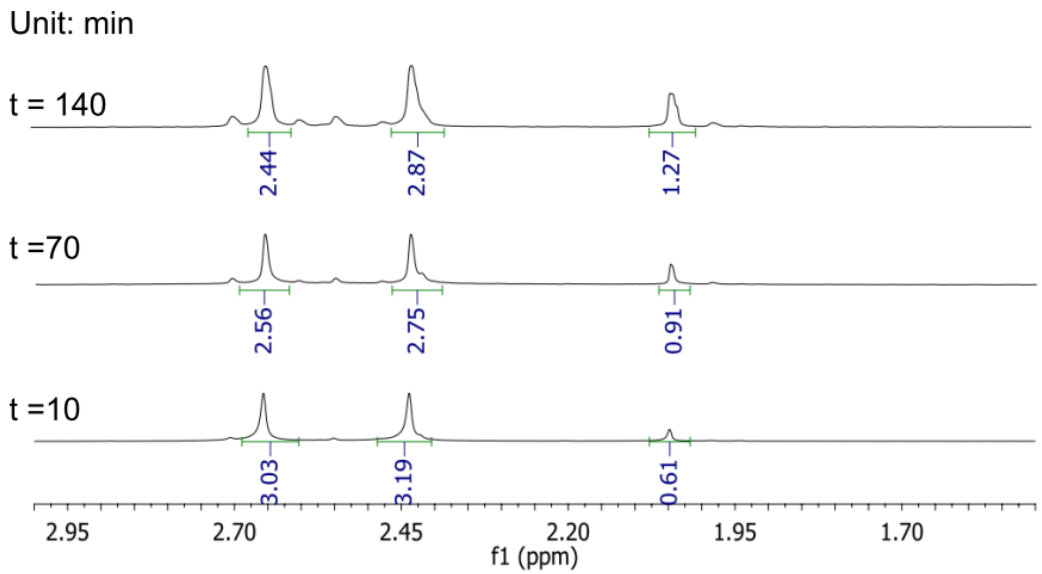

Figure 4.12 ^{1}H-NMR spectral changes of **19** after its dissolution in D_2O over the course of 140 min.

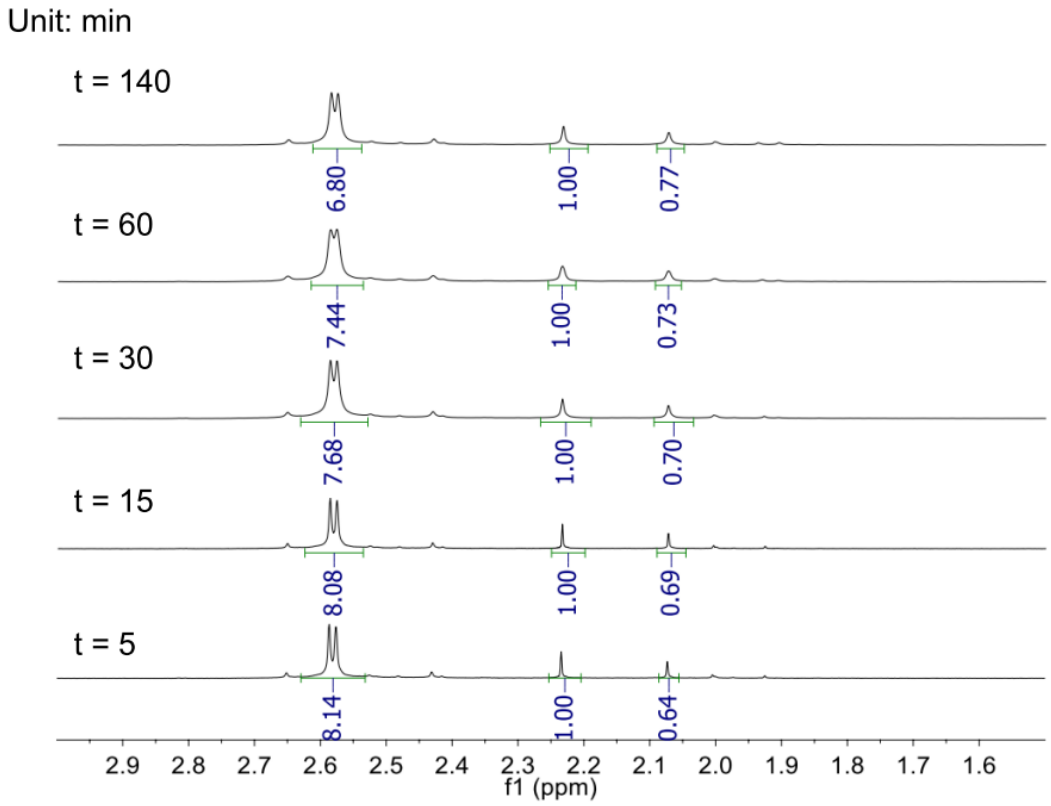

Figure 4.13 Changes in the ^{1}H-NMR spectra of **21** after dissolution in D_2O over the course of 140 min.

Electronic absorption and electrochemical studies

The electronic absorption spectra of compounds **18**, **19** and **21** were measured at room temperature in both CH_3CN and H_2O respectively and are summarized in Table 4.2.

Compounds **18**, **19** and **21** exhibit similar electronic absorption spectroscopic properties in CH_3CN at room temperature. The transitions at $\lambda \sim 498$ nm in **18**, $\lambda \sim 473$ nm for **19** and $\lambda \sim 491$ nm for **21** have very similar low molar absorptivities (Table 4.2). They are tentatively assigned as the $Rh_2(\pi^*)$ to $Rh_2(\sigma^*)$ charge-transfer bands but with minor LMCT character due to the dependence on the bridging ligands. Another weak but distinct feature of this series of compounds is the absorption in the region of 380-390 nm, similar to the transitions at ~350 nm for both the H-H and H-T isomers of *cis*-$[Rh_2(HNOCCH_3)_2(CH_3CN)_6][BF_4]_2$[223] and the transition at ~363 nm in *cis*-$[Rh_2(OOCCH_3)_2(CH_3CN)_6][BF_4]_2$.[8] These features are ascribed to combinations of

Table 4.2 Photophysical properties of **18**, **19** and **21** in CH_3CN and H_2O at room temperature.

	λ (nm), (ε x $10^3(M^{-1}\bullet cm^{-1})$) in CH_3CN	λ (nm), (ε x 10^3 $(M^{-1}\bullet cm^{-1})$) in H_2O
18	239 (36.9), 259 (29.0), 303 (6.0), ~ 389 (0.78), 498 (0.20)	N/A
19	239(31.5), 256(21.2), 294 (7.5), ~ 382 (0.68) ~ 473 (0.22)	236(20.0), 259(17.4), 302(3.4), 381 (0.37), 550 (0.12)
21	230(39.8), 257(31.4), 291 (5.8), ~ 380 (0.61), 491 (0.20)	226 (35.9), 257(33.5), 294(4.8), 397(0.47), 558 (0.18)

electronic transitions from $Rh_2(\pi^*)$ to Rh-CH_3CN(eq) (σ^*) and $Rh_2(\sigma^*)$ orbitals. As shown in Table 4.2 and Figure 4.14a, medium intensity absorptions at ~ 290-300 nm are also present in all three compounds. Due to the independence of the energies on the bridging ligands, these bands are also assigned as metal-centered (MC) transitions. Since they have slightly higher molar absorptivities, they correspond to the transitions originating from $Rh_2(\pi)$, $Rh_2(\sigma)$ to Rh-CH_3CN(eq) (σ^*), $Rh_2(\sigma^*)$ orbitals. The electronic absorption spectra of compounds **19** and **21** in H_2O are displayed in Figure 4.14b. The electronic absorption spectrum of compound **18**, however, was not possible to obtain due to the fast exchange of eq CH_3CN with H_2O upon dissolution (*vide supra*). Slight bathochromic shifts of the lowest energy transitions occur for both compounds **19** and **21** when dissolved in H_2O as compared to their CH_3CN solutions (Table 4.2). This is similar to the situation for *cis*-$[Rh_2(OOCH_3)_2(CH_3CN)_6][BF_4]_2$ in H_2O as compared to CH_3CN solution.[8] The transitions at ~ 380-390 nm, however, are not shifted, in accord with the involvement of only the eq CH_3CN ligands but not the ax ones.

The redox potentials of the synthesized compounds as well as the free bridging ligands were determined by cyclic voltammetry with the detailed results listed in Table 4.3.

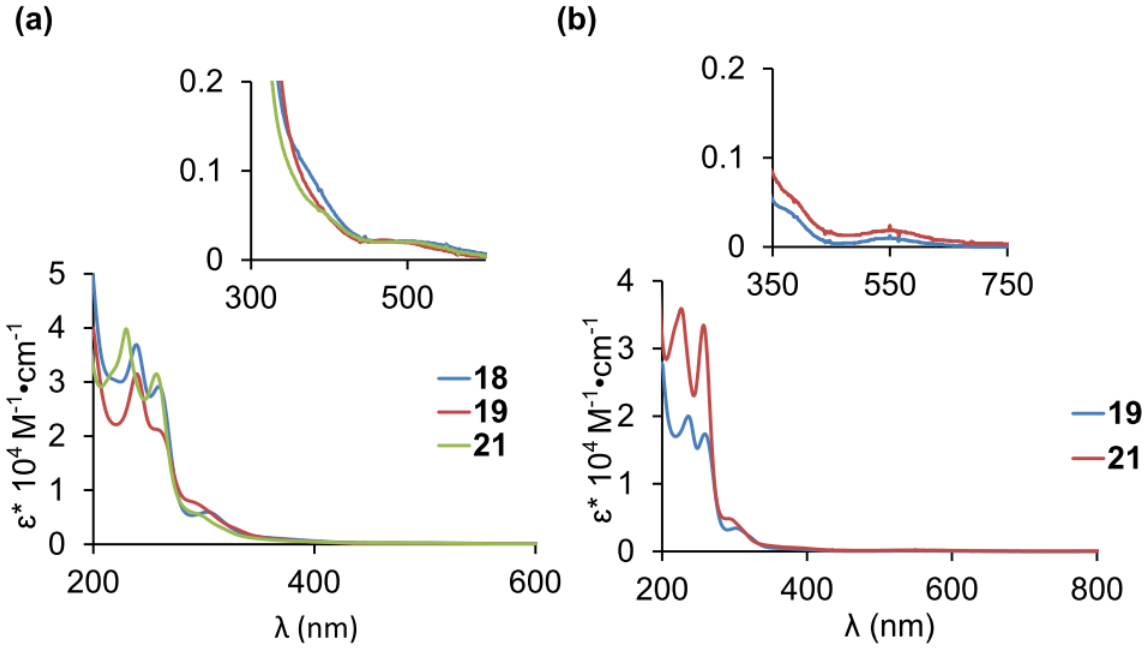

Figure 4.14 Electronic absorption spectra of: (a) compounds **18**, **19** and **21** obtained in CH_3CN and (b) compounds **19** and **21** obtained in H_2O.

Table 4.3 Electrochemical data of complexes **15**-**19**, **21** as well as the free ligands mhp, chp and fhp.

		$E_{pc,\,1}$	$E_{pc,\,2}$	$E_{pc,3}$	$E_{ox,\,1}$	$E_{ox,2}$
mhp					1.51[a]	
chp		-1.03	-1.44		1.85[a]	
fhp		-0.92				
$Rh_2(mhp)_4$[b]	**15**	-1.36[c]			0.91	
$Rh_2(chp)_4$[d]	**16**	-1.20[c]			1.23	
$Rh_2(fhp)_4$[d]	**17**	-1.49			0.99[a]	1.20[c]
cis-$[Rh_2(mhp)_2(CH_3CN)_6][BF_4]_2$	**18**	-0.45	-1.27		1.61[e]	
cis-$[Rh_2(chp)_2(CH_3CN)_6][BF_4]_2$	**19**	-0.24	-1.13	-1.44		
cis-$[Rh_2(fhp)_2(CH_3CN)_6][BF_4]_2$	**21**	-0.66	-1.18	-1.34	1.27[e]	1.48[e]

a. Irreversible. *b.* in CH_2Cl_2 *c.* reversible *d.* in CH_3CN, with the presence of drops of DMSO *e.* quasi-reversible

The strong electron donating ability of the mhp ligands renders the dimetal center electron-rich, thus leading to a cathodic shift of the first oxidation potential by ~ 0.30 V in **15** as compared to that in $Rh_2(\mu\text{-}O_2CCH_3)_4$.[21] On the other hand, it occurs at a more positive potential ~ 1.23 V in **16**, most likely due to the electron withdrawing Cl groups on the bridging chp groups. Both **15** and **16** exhibit one reversible reduction at -1.36 and -1.20 V respectively, attributed to the Rh_2^{4+}/ Rh_2^{3+} redox couple. The more difficult reduction for **15** is also in accord with the electron donating -CH_3 groups resulting in an electron-rich dimetal core. Complex **17** exhibits different electrochemical properties as compared to **15** and **16**, presumably because of the different ligand configuration. It exhibits one irreversible reduction at -1.49V, one irreversible oxidation at ~ 0.99 V and another quasi-reversible oxidation at ~ 1.20 V. For the partial paddlewheel Rh_2(II,II) compounds **18**, **19** and **21**, there are two irreversible reductions for compound **18** and three irreversible reductions for compounds **19** and **21**. The two reductions for **18**, the first two reductions for **19** as well as the first and third reductions for **21** are ascribed to stepwise reductions of the dimetal center, namely the Rh_2^{4+}/Rh_2^{3+} and Rh_2^{3+}/Rh_2^{2+} redox couples respectively. The third reduction in **19** and second reduction in **21** are tentatively assigned as bridging-ligand based redox events since similar features occur for the free chp and fhp ligands at -1.44 and -0.92 V respectively. One quasi-reversible oxidation appears for **18** and two for **21**, tentatively assigned as a metal-centered oxidation but with contributions from the bridging ligands unlike the case of **19**.

Computational studies

To aid in the interpretation of the electronic structures of **18**, **19** and **21**, computational studies of their cationic units were conducted. For **18** and **19**, the gas phase optimizations began with the cationic units from the crystal structures respectively while for **21**, it was built in 'agui' by the modification of the crystal structure for **20** but with both ax positions occupied by CH_3CN ligands. The calculated structures are very similar to the experimental ones for both **18** and **19**, indicating the accuracy of the levels of theory chosen and the basis sets. Important bond parameters are summarized in Table 4.4 and graphic representations of the calculated structures are displayed in Figure 4.15. TD-DFT calculations using both CH_3CN and H_2O as solvents were conducted based on the gas phase optimized structures. One issue that needs to be pointed out is that, due to the lability of the ax CH_3CN upon solvation in H_2O, the TD-DFT calculations in H_2O were started from the optimized *cis*-$[Rh_2(chp)_2(CH_3CN)_4(H_2O_{ax})_2]^{2+}$ and *cis*-$[Rh_2(fhp)_2(CH_3CN)_4(H_2O_{ax})_2]^{2+}$ for **19** and **21** respectively.

As can be seen in Tables 4.5 and 4.6, the MO compositions of all three compounds are very similar in the two different solvents (Table 4.5 for results in CH_3CN and Table 4.6 for results in H_2O). Thus, only the results from using CH_3CN as solvent are presented in the following section. Orbitals HOMO and HOMO-1 are mainly the bridging ligands (mhp in **18**, chp in **19** and fhp in **21**) characters (~ 75% in HOMO, ~ 85% in HOMO-1); conversely, orbitals ranging from HOMO-8 to HOMO-2 are mainly Rh based orbitals. For the unoccupied orbitals, the LUMO is mainly rhodium based and the visualization indicates $Rh_2(\sigma^*)$ character. The LUMO+1 and LUMO+2 have significant

Table 4.4 Comparisons between the calculated structures and X-ray crystallographic data for **18** and **19**.

	18	
	Experimental	Calculated
Bond	Å	Å
Rh1-Rh2	2.4794(5)	2.515
Rh1-N1	2.057(4)	2.074
Rh1-O1	2.007(3)	2.001
Rh2-N2	2.050(4)	2.073
Rh2-O2	2.006(3)	2.001
Rh1-N4	2.201(4)	2.243
Rh1-N5	1.999(4)	2.013
Rh1-N6	2.012(4)	2.028
Rh2-N7	2.014(4)	2.014
Rh2-N8	2.008(4)	2.028
Rh2-N3	2.234(4)	2.244
Dihedral	º	º
O1-Rh1-Rh2-N2	-30.3(1)	-30.1
N1-Rh1-Rh2-O2	-30.8(1)	-30.1
N5-Rh1-Rh2-N7	-36.5(1)	-37.3
N6-Rh1-Rh2-N8	-36.9(2)	-37.3
	19	
	Experimental	Calculated
Bond	Å	Å
Rh1-Rh2	2.492(1)	2.518
Rh1-N2	2.071(8)	2.085
Rh1-O1	2.005(6)	2.004
Rh2-N1	2.080(8)	2.085
Rh2-O2	2.017(7)	2.004
Rh1-N3	2.21(1)	2.222
Rh1-N7	1.987(9)	2.016
Rh1-N8	2.031(9)	2.010
Rh2-N4	2.25(1)	2.221
Rh2-N5	1.97(1)	2.016
Rh2-N6	1.996(9)	2.010
Dihedral	º	º
O1-Rh1-Rh2-N1	30.9(3)	29.3
N2-Rh1-Rh2-O2	30.7(3)	29.2
N5-Rh1-Rh2-N8	37.6(4)	36.1
N6-Rh1-Rh2-N7	36.4(4)	36.2

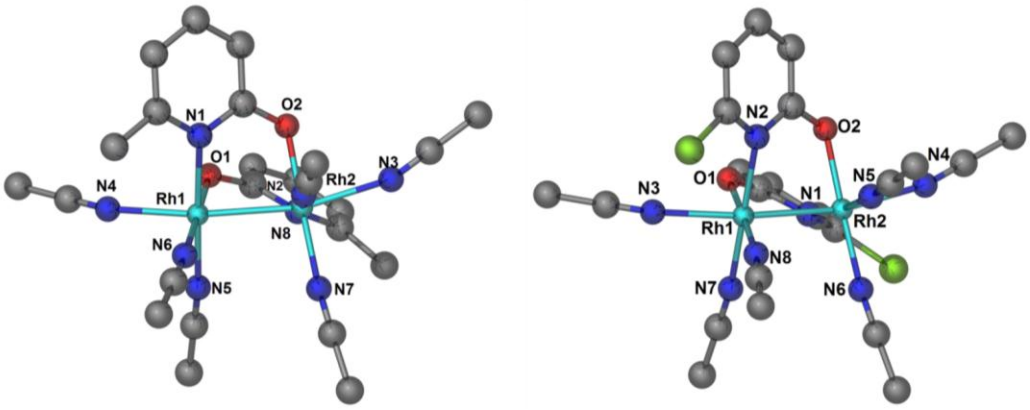

Figure 4.15 Optimized cationic units for compounds **18** (left) and **19** (right); hydrogen atoms were omitted for the sake of clarity.

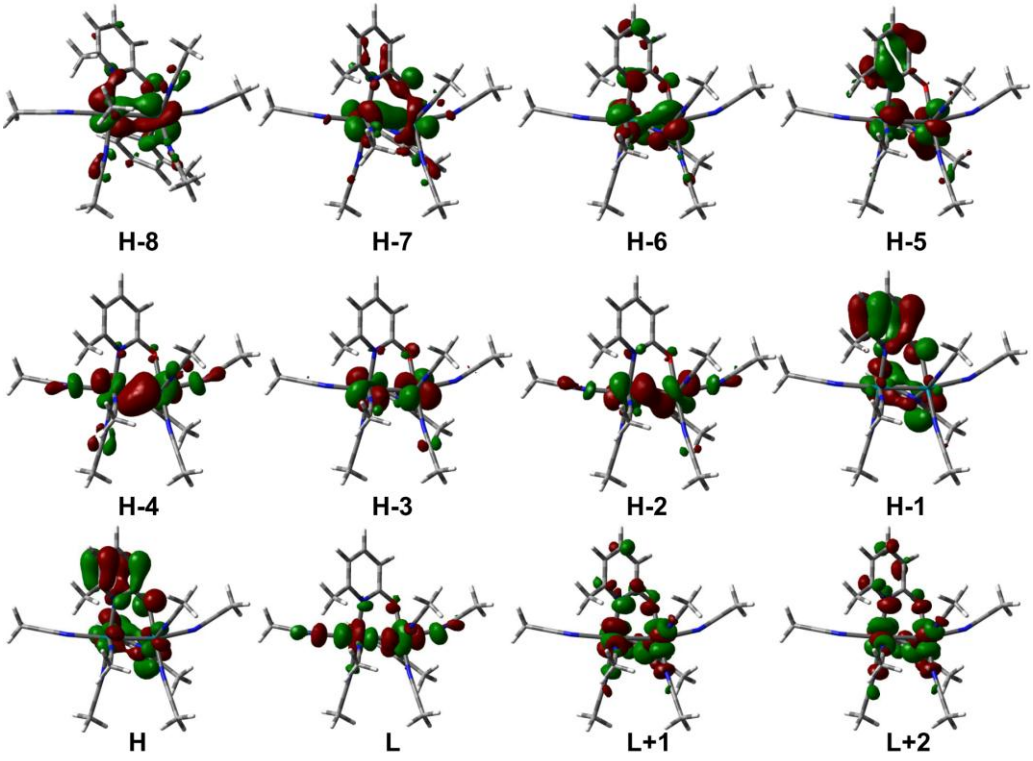

Figure 4.16 MO visualizations of **18** in the solvation model with CH_3CN as the solvent, generated by agui with iso-value = 0.04; H = HOMO, L = LUMO.

Table 4.5 MO components (%) of the frontier orbitals related to the electronic transitions based on the TD-DFT calculation using CH_3CN as the solvent.

	18 in CH_3CN	**19** in CH_3CN	**21** in CH_3CN
HOMO-8	71 Rh 19 mhp 8 eq CH_3CN	72 Rh 15 mhp 10 eq CH_3CN	69 Rh 19 fhp 9 eq CH_3CN
HOMO-7	62 Rh 28 mhp 6 eq CH_3CN	61 Rh 28 chp 9 eq CH_3CN	55 Rh 35 fhp 7 eq CH_3CN
HOMO-6	66 Rh 28 mhp	65 Rh 26 chp 8 eq CH_3CN	73 Rh 16 fhp 11 eq CH_3CN
HOMO-5	52 Rh 44 mhp	48 Rh 45 chp 6 eq CH_3CN	63 Rh 28 fhp 7 eq CH_3CN
HOMO-4	76 Rh 11 ax CH_3CN 7 eq CH_3CN 6 mhp	78 Rh 12 ax CH_3CN 7 eq CH_3CN	71 Rh 12 fhp 11 ax CH_3CN 6 eq CH_3CN
HOMO-3	85 Rh 8 mhp 6 eq CH_3CN	85 Rh 7 chp 6 eq CH_3CN	85 Rh 7 fhp 5 eq CH_3CN
HOMO-2	80 Rh 8 mhp 7 ax CH_3CN	79 Rh 9 ax CH_3CN 8 chp	82 Rh 8 ax CH_3CN 5 fhp 5 eq CH_3CN
HOMO-1	89 mhp 9 Rh	89 chp 9 Rh	83 fhp 13 Rh
HOMO	74 mhp 23 Rh	75 chp 23 Rh	75 fhp 23 Rh
LUMO	69 Rh 14 ax CH_3CN 10 mhp 7 eq CH_3CN	68 Rh 13 ax CH_3CN 11 chp 8 eq CH_3CN	70 Rh 14 ax CH_3CN 9 fhp 7 eq CH_3CN
LUMO+1	46 Rh 35 mhp 19 eq CH_3CN	44 Rh 37 chp 19 eq CH_3CN	47 Rh 33 fhp 20 eq CH_3CN
LUMO+2	45 Rh 32 mhp 22 eq CH_3CN	46 Rh 34 chp 20 eq CH_3CN	51 Rh 25 eq CH_3CN 24 fhp

Table 4.6 MO components (%) of the frontier orbitals related to the electronic transitions based on the TD-DFT calculation using H_2O as the solvent.

	18 in H_2O	**19** in H_2O	**21** in H_2O
HOMO-8	69 Rh 20 mhp 10 eq CH_3CN	72 Rh 17 mhp 11 eq CH_3CN	70 Rh 19 fhp 11 eq CH_3CN
HOMO-7	60 Rh 27 mhp 9 eq CH_3CN	57 Rh 32 chp 8 eq CH_3CN	55 Rh 36 fhp 7 eq CH_3CN
HOMO-6	71 Rh 19 mhp 7 eq CH_3CN	69 Rh 21 chp 10 eq CH_3CN	71 Rh 18 fhp 11 eq CH_3CN
HOMO-5	57 Rh 35 mhp 7 eq CH_3CN	50 Rh 42 chp 7 eq CH_3CN	69 Rh 17 fhp 7 eq CH_3CN 6 ax H_2O
HOMO-4	70 Rh 14 mhp 9 ax H_2O 7 eq CH_3CN	76 Rh 13 ax H_2O 6 eq CH_3CN	69 Rh 17 fhp 8 ax H_2O 6 eq CH_3CN
HOMO-3	87 Rh 6 mhp 6 eq CH_3CN	87 Rh 6 eq CH_3CN 6 chp	87 Rh 6 fhp 6 eq CH_3CN
HOMO-2	83 Rh 7 mhp 6 ax H_2O	82 Rh 7 ax H_2O 6 chp	83 Rh 8 ax H_2O
HOMO-1	90 mhp 8 Rh	90 chp 8 Rh	88 fhp 10 Rh
HOMO	73 mhp 24 Rh	72 chp 25 Rh	72 fhp 25 Rh
LUMO	77 Rh 9 ax H_2O 9 mhp 5 eq CH_3CN	75 Rh 10 ax H_2O 9 chp 6 eq CH_3CN	76 Rh 10 ax H_2O 8 fhp 6 eq CH_3CN
LUMO+1	45 Rh 35 mhp 20 eq CH_3CN	43 Rh 38 chp 19 eq CH_3CN	47 Rh 33 fhp 21 eq CH_3CN
LUMO+2	43 Rh 34 mhp 22 eq CH_3CN	42 Rh 37 chp 20 eq CH_3CN	51 Rh 25 eq CH_3CN 24 fhp

anti-bonding interactions between the Rh and eq CH_3CN ligands (Figure 4.16), similar to those found in *cis*-$[Rh_2(\mu\text{-}O_2CCH_3)_2(CH_3CN)_6][BF_4]_2$.[8]

As displayed in Figure 4.17, the orbitals in **19** lie slightly lower than the corresponding ones in **18**, probably due to the stabilization by the electron-withdrawing Cl groups on the bridging ligands (Table 4.5). However, different levels of stabilization occur for each orbital set, a result of different degrees of contributions from the bridging ligands to those orbitals. For example, the HOMO in **19** is ~ 0.25 eV lower than that in **18** while the LUMO is only by ~ 0.08 eV lower. This, therefore, leads to a larger HOMO-LUMO gap in **19** as compared to **18**. For compound **21**, its MO compositions, as listed in Table 4.5, are very similar to those in **18** and **19**; however, no trend was observed for the energy of each orbital as compared to the corresponding ones in **18** and **19** presumably due to the H-H orientation of two bridging ligands in **21**. Nevertheless, its HOMO-LUMO gap was predicted to be ~ 0.05 eV smaller than that of **19**, while ~ 0.12 eV larger than that of **18**.

On the basis of TD-DFT calculations using CH_3CN as the solvent, the lowest energy bands mainly correspond to the HOMO, HOMO-3 to LUMO charge-transfer transition as shown in Tables 4.7-4.9, rendering it dual MC and MLCT characters. It is predicted at λ = 485, 462 and 473 nm respectively for **18**, **19** and **21**, in accord with the experimental data (*vide supra*). The bands in the region of 390-400 nm in all three compounds are predicted to be the transitions to the LUMO+1 σ^*[Rh-CH_3CN(eq)]. Therefore, the population of the LUMO+1 orbital leads to labilization of eq CH_3CN ligands. The

absorption bands in the 330-360 nm region correspond to the transitions from HOMO-6, HOMO-3 to LUMO, LUMO+1, thus mainly of MC character.

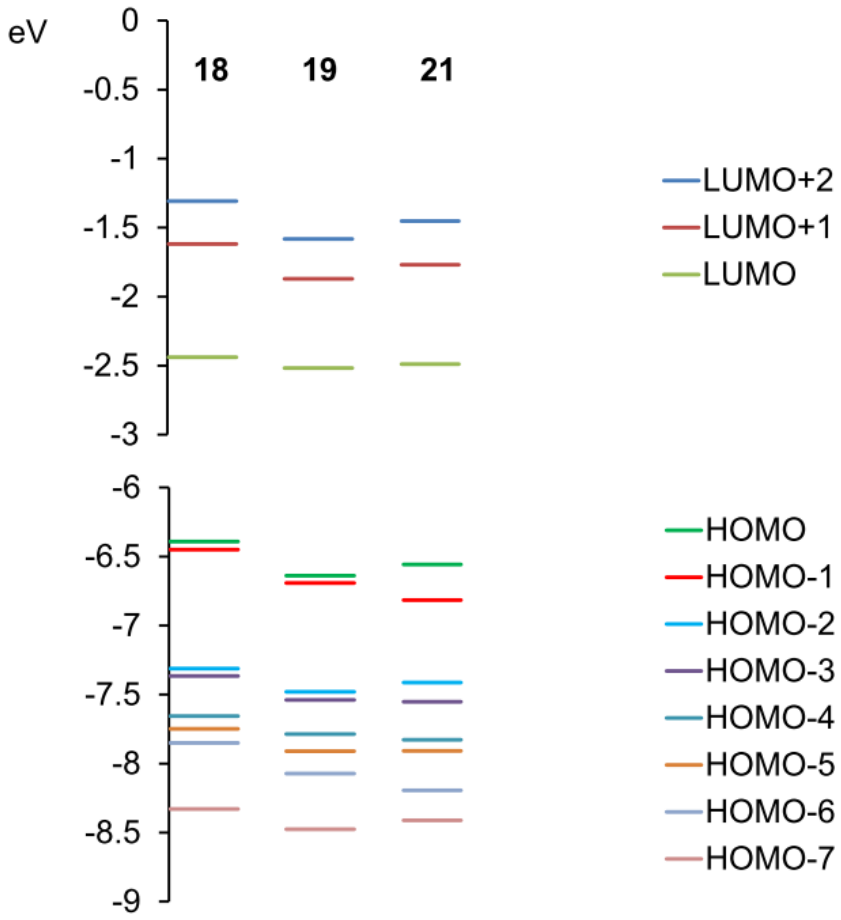

Figure 4.17 MO diagram of **18**, **19** and **21** obtained from DFT calculations using CH_3CN as solvent.

Table 4.7 First ten electronic transitions of **18** predicted by TD-DFT calculations in solvation model with CH_3CN and H_2O as solvents respectively, H=HOMO, L=LUMO.

	18 in CH_3CN	**18** in H_2O
1	485 nm *f*=0.0002 H-3 ->L 29.47% H ->L 59.20%	537 nm *f*=0.0005 H-3 ->L 54.70% H ->L 34.91%
2	461 nm *f*=0.0033 H-2 ->L 73.92%	523 nm *f*=0.0022 H-2 ->L 80.48%
3	451 nm *f*=0.0003 H-3 ->L 62.28% H ->L 31.02%	497 nm *f*=0.0004 H-3 ->L 39.39% H ->L 52.44%
4	422 nm *f*=0.0019 H-1 ->L 90.75%	447 nm *f*=0.0008 H-1 ->L 93.99%
5	391 nm *f*=0.0030 H ->L+1 56.54%	385 nm *f*=0.0029 H ->L+1 49.24%
6	373 nm *f*=0.0023 H ->L+2 35.63%	371 nm *f*=0.0047 H-4 ->L 36.48%
7	353 nm *f*=0.0065 H-6 ->L 26.19% H-4 ->L 24.97%	368 nm *f*=0.0027 H ->L+2 31.81%
8	338 nm *f*=0.0028 H-2 ->L+1 36.60% H-1 ->L+1 29.36%	346 nm *f*=0.0011 H-8 ->L 33.78%
9	332 nm *f*=0.0000 H-3 ->L+2 29.00%	343 nm *f*=0.0044 H-6 ->L 47.29%
10	332 nm *f*=0.0022 H-6 ->L 30.47% H-3 ->L+1 46.73%	337 nm *f*=0.0003 H-5 ->L 37.07% H-2 ->L+1 29.05%

Table 4.8 First ten electronic transitions of **19** predicted by TD-DFT calculations in solvation model with CH_3CN and H_2O as solvents respectively, H=HOMO, L=LUMO.

	19 in CH_3CN	**19** in H_2O
1	462 nm *f*=0.0002 H-3 ->L 49.52% H ->L 38.09%	511 nm *f*=0.0004 H-3 ->L 71.81% H ->L 20.01%
2	447 nm *f*=0.0023 H-4 ->L 23.91% H-2 ->L 66.52%	496 nm *f*=0.0014 H-2 ->L 74.37%
3	430 nm *f*=0.0000 H-3 ->L 39.83% H ->L 50.31%	463 nm *f*=0.0000 H-3 ->L 21.89% H ->L 68.23%
4	401 nm *f*=0.0014 H-1 ->L 67.97%	412 nm *f*=0.0007 H-1 ->L 89.65%
5	391 nm *f*=0.0034 H-1 ->L 25.82% H ->L+1 38.21%	387 nm *f*=0.0032 H ->L+1 48.72%
6	377 nm *f*=0.0023 H ->L+2 34.48%	373 nm *f*=0.0026 H ->L+2 34.84%
7	350 nm *f*=0.0030 H-3 ->L+1 34.95%	361 nm *f*=0.0069 H-4 ->L 23.03%
8	340 nm *f*=0.0014 H-2 ->L+1 55.37%	344 nm *f*=0.0004 H-8 ->L 30.07% H-3 ->L+2 34.10%
9	337 nm *f*=0.0007 H-3 ->L+2 39.67%	341 nm *f*=0.0026 H-6 ->L 27.07% H-3 ->L+1 47.43%
10	332 nm *f*=0.0083 H-6 ->L 35.38% H-3 ->L+1 30.87%	341 nm *f*=0.0007 H-2 ->L+1 62.83%

Table 4.9 First ten electronic transitions of **21** predicted by TD-DFT calculations in solvation model with CH_3CN and H_2O as solvents respectively. H=HOMO, L=LUMO.

	21 in CH_3CN	**21** in H_2O
1	473 nm f=0.0007 H-3 ->L 28.80% H ->L 51.34%	516 nm f=0.0011 H-2 ->L 33.51% H ->L 31.03%
2	458 nm f=0.0022 H-2 ->L 62.36%	506 nm f=0.0014 H-3 ->L 29.52% H-2 ->L 38.63%
3	430 nm f=0.0010 H-3 ->L 51.81% H ->L 35.57%	461 nm f=0.0009 H-3 ->L 45.70% H ->L 41.87%
4	402 nm f=0.0052 H ->L+1 46.19%	397 nm f=0.0050 H ->L+1 34.17% H ->L+2 18.21%
5	374 nm f=0.0087 H-1 ->L 76.17%	386 nm f=0.0041 H-1 ->L 66.03%
6	355 nm f=0.0022 H-5 ->L+2 16.81% H ->L+2 22.07%	356 nm f=0.0019 H ->L+2 17.63%
7	347 nm f=0.0003 H-2 ->L+1 24.03% H-2 ->L+2 15.95%	352 nm f=0.0007 H-2 ->L+1 11.86% H-2 ->L+2 13.62%
8	339 nm f=0.0035 H-3 ->L+1 25.89% H-2 ->L+1 13.93%	343 nm f=0.0059 H-8 ->L 17.22% H-2 ->L+2 10.35%
9	330 nm f=0.0031 H-5 ->L 17.35% H-2 ->L+1 19.96%	342 nm f=0.0021 H-5 ->L 28.71% H-2 ->L+1 23.14%
10	326 nm f=0.0076 H-3 ->L+1 22.86% H-2 ->L+2 11.59%	335 nm f=0.0035 H-4 ->L 17.45% H-2 ->L+1 17.91%

Concluding remarks

A series of partial paddlewheel dirhodium complexes of general formula *cis*-$[Rh_2(xhp)_2(CH_3CN)_6][BF_4]_2$ (xhp = mhp, chp and fhp) were synthesized and fully characterized by X-ray diffraction and ^{1}H NMR spectroscopy. The eq CH_3CN ligands in this family of compounds were determined to be kinetically labile upon dissolution in CH_3CN or H_2O in the dark, as indicated by the ^{1}H NMR and electronic spectroscopic studies. Importantly, the lability of the eq CH_3CN ligands can be tuned through judicious choice of the substituents on the bridging ligands and in this case the ligand lability decreases in the order mhp> chp> fhp, which is in agreement with the hypothesis that the stronger electron donating ligands exert stronger *trans* effects. Irradiation of the aqueous solutions of compounds **19** and **21** with white light significantly accelerates the exchange rate of eq CH_3CN ligands for the solvent H_2O molecules. This is well understood from the TD-DFT calculation results, which indicate that population of the σ* Rh-N (eq CH_3CN) bonds occurs in their excited states. Consequently, compounds **19** and **21** hold great potential as PDT agents for cancer, investigations that are currently in progress.

CHAPTER V

INVESTIGATION OF PARTIAL PADDLEHWEEL DIRHODIUM COMPLEXES BRIDGED BY ORTHOMETALATED PHOSPHINE LIGANDS

Introduction

Our previous studies revealed the exciting results that partial paddlewheel Rh_2(II,II) complexes with electron-rich bridging formamidinate and chelating electron-accepting diimine ligands, namely *cis*-$[Rh_2(DTolF)_2(N\text{-}N)_2]^{2+}$ and *cis*-$[Rh_2(F\text{-}form)_2(N\text{-}N)_2]^{2+}$ (N-N = dpq, dppz, dppn) exhibit directional Ligand-to-Ligand-Charge-Transfer (LLCT) excited states. Comprehensive experimental and computational studies indicate that the excited states of these complexes exhibit superior reducing and oxidizing abilities than the commonly used Ru(II) mononuclear complexes.[230] To better understand the nature of these intriguing excited states, it is imperative to investigate the charge distributions in the excited states by time-resolved techniques (transient infrared and transient absorption spectroscopies). It is also important to design other Rh_2(II,II) complexes with similar structural features but with different bridging ligands. The orthometalated phosphine ligand $[Ph_2P(C_6H_4)]^-$ discussed in chapter II is another excellent example of an electron-rich bridging ligand for dirhodium(II,II) compounds. It was shown by Cotton and coworkers that compound *cis*-$[Rh_2[Ph_2P(C_6H_4)]_2(CH_3CN)_6][BF_4]_2$ is an excellent synthetic precursor for a series of supramolecular arrays because the eq CH_3CN ligands are highly labile due to the strong *trans* effect exerted by the two bridging $[Ph_2P(C_6H_4)]^-$ ligands.[105] As such, we chose the compound and one of its derivatives, namely, tris(4-methoxyphenyl)phosphine (PMP) as bridging ligands and synthesized two series of

partial paddlewheel complexes and fully characterized them by NMR spectroscopy and X-ray crystallography. In addition, theoretical calculations were conducted which provide useful insight into the electronic structures of those complexes.

Experimental section

Starting materials

The starting material $Rh_2(\mu\text{-}O_2CCH_3)_4$•2MeOH was purchased from Pressure Chemical and purified by recrystallization from CH_3OH. The ligands tris(4-methoxyphenyl)phosphine (PMP) and triphenylphosphine (PPh_3) were obtained from Sigma Aldrich and used as received. The ligands dpq (dipyrido[3,2-f:2',3'-h]-quinoxaline), dppz (dipyrido[3,2-a:2',3'-c]phenazine) and dppn (benzo[i]dipyrido[3,2-a:2',3'-h]quinoxaline) were synthesized according to published procedures and their purities were confirmed by ^{1}H-NMR spectroscopy. The compound *cis*-$[Rh_2(PMP)_2(\mu\text{-}O_2CCH_3)_2(CH_3CN)_2]$ was synthesized according to a slightly modified published procedure.[228] The solvents acetic acid, diethyl ether and acetonitrile are of ACS grade and were used as received whereas dry CH_3CN was obtained by distillation over 3 Å molecular sieves under a flow of dry N_2. The CH_2Cl_2 was pre-dried over 4 Å molecular sieves and distilled over P_2O_5 under a flow of dry N_2.

Synthesis of *cis*-$[Rh_2[Ph_2P(C_6H_4)]_2(dpq)_2(CH_3CN)][BF_4]_2$ (22). A quantity of *cis*-$[Rh_2[Ph_2P(C_6H_4)]_2(CH_3CN)_6][BF_4]_2$ (51 mg, 0.044 mmol) was added to 20 mL of a suspension of the dpq ligand CH_2Cl_2/CH_3CN (a 1:1/v:v mixture) (23 mg, 0.098 mmol) in the dark. The solution was stirred at room temperature for 72 h, after which time the color was observed to have changed to dark red. The solution was then concentrated to 5

mL under reduced pressure and filtered through a medium frit to remove any insoluble materials. The addition of 50 mL of diethyl ether to the filtrate led to the precipitation of the desired product as a red solid; upon drying under vacuum for 24 h, an amount of 54 mg green product was obtained. The yield is 55 mg, ~ 85% based on rhodium. ^{1}H-NMR (CD_3CN-d_3) δ ppm: 9.38(d, dpq), 9.10 (d, dpq), 8.90 (d, dpq), 8.73(s, dpq), 8.12(m, $Ph_2P(C_6H_4)$), 7.84 (dd, dpq), 7.50 (m, $Ph_2P(C_6H_4)$), 7.30(m, $Ph_2P(C_6H_4)$), 7.19 (m, $Ph_2P(C_6H_4)$), 7.17 (dd, dpq), 6.73 (t, $Ph_2P(C_6H_4)$), 6.27 (dd, $Ph_2P(C_6H_4)$), 6.21 (d, $Ph_2P(C_6H_4)$); ^{31}P-NMR (CD_3CN-d_3) δ ppm: 19.59 ppm ^{1}J (Rh-P) = 330 Hz, ^{2}J (Rh-P) = 45 Hz. Anal. Calcd for $Rh_2C_{64}H_{44}P_2N_8B_2F_8$•$2CH_2Cl_2$: C, 51.74; N, 7.99; H, 3.26 %. Found: C, 51.42; N, 7.71; H, 3.69%.

Synthesis of *cis*-$[Rh_2[Ph_2P(C_6H_4)]_2(dppz)_2(CH_3CN)_2][BF_4]_2$ (23). A sample of *cis*-$[Rh_2[Ph_2P(C_6H_4)]_2(CH_3CN)_6][BF_4]_2$ (50 mg, 0.043 mmol) was added to 20 mL of a 1:1/v:v CH_2Cl_2/CH_3CN mixture containing 27 mg (0.097 mmol) of suspended dppz. The resulting orange solution which was stirred in the dark at room temperature for 72 hours eventually turned to red and was concentrated to 5 mL and filtered through a medium frit to remove any insoluble materials. The addition of 50 mL diethyl ether to the filtrate led to the precipitation of the desired product as a brown solid, yielding 60 mg of green product after drying under vacuum for 24 h (90% based on rhodium). ^{1}H-NMR (CD_3CN-d_3) δ ppm: 9.51 ppm (d, dppz), 8.74 (s, dppz), 8.43(d, dppz), 8.14(m, $Ph_2P(C_6H_4)$), 8.02 (dd, dppz), 7.86 (dd, dppz), 7.38 (m, dppz), 7.33 (m, $Ph_2P(C_6H_4)$), 7.35 (m, $Ph_2P(C_6H_4)$), 7.22(m, $Ph_2P(C_6H_4)$), 6.73 (t, $Ph_2P(C_6H_4)$), 6.27 (dd, $Ph_2P(C_6H_4)$), 6.21 (d, $Ph_2P(C_6H_4)$); ^{31}P-NMR (CD_3CN-d_3) δ ppm: 19.36 ppm ^{1}J (Rh-P) = 330 Hz, ^{2}J

(Rh-P) = 45 Hz. Anal. Calcd for $Rh_2C_{72}H_{48}P_2N_8B_2F_8$•$CH_2Cl_2$•$H_2O$-$CH_3CN$: C, 55.90; N, 7.83; H, 3.44 %. Found: C, 55.63; N, 7.54; H, 3.53%.Crystals suitable for X-ray diffraction were obtained by slow diffusion of diethyl ether into a CH_3CN solution containing the product.

Synthesis of *cis*-[$Rh_2[Ph_2P(C_6H_4)]_2(dppn)_2(CH_3CN)][BF_4]_2$ (24). An orange slurry of *cis*-[$Rh_2[Ph_2P(C_6H_4)]_2(CH_3CN)_6][BF_4]_2$ (50 mg, 0.044 mmol) in 10 mL of CH_3CN solution was mixed with a red slurry of dppn ligand (32 mg, 0.097 mmol) in 15 mL CH_2Cl_2 in the dark. The red slurry was stirred at room temperature for 72 h and was then concentrated to 5 mL and filtered through a medium frit to remove the insoluble materials. To the mother liquor was added 50 mL diethyl ether, which led to the precipitation of the desired product as a red solid. The material was collected by filtration and dried under vacuum, yielding 63 mg of desired product (87% based on rhodium). ^{1}H-NMR (CD_3CN-d_3) δ ppm: 9.49(d, dppn), 9.11(s, dppn), 8.74 (s, b, dppn), 8.43(d, dppn), 8.10 (d, $Ph_2P(C_6H_4)$), 7.84 (m, dppn), 7.80 (m, dppn), 7.36(m, $Ph_2P(C_6H_4)$), 7.21(m, $Ph_2P(C_6H_4)$) 7.18 (m, $Ph_2P(C_6H_4)$), 6.77(t, $Ph_2P(C_6H_4)$), 6.34 (dd, $Ph_2P(C_6H_4)$), 6.21(d, $Ph_2P(C_6H_4)$). ^{31}P-NMR (CD_3CN-d_3) δ ppm: 19.43 ppm ^{1}J (Rh-P) = 330 Hz, ^{2}J (Rh-P) = 45 Hz. Anal. Calcd for $Rh_2C_{80}H_{52}P_2N_8B_2F_8$•$2CH_2Cl_2$: C, 57.04; N, 7.22; H, 3.64 %. Found: C, 57.16; N, 6.91; H, 3.74%.

Synthesis of *cis*-[$Rh_2(PMP)_2(CH_3CN)_6][BF_4]_2$ (25). A quantity of 70 mg of *cis*-[$Rh_2(PMP)_2(\mu$-$O_2CCH_3)_2(CH_3CN)_2$] was added to 30 mL of CH_3CN to form a suspension. Upon addition of 0.8 mL of Et_3OBF_4 (1.0 M solution in CH_2Cl_2), the solution gradually became a clear orange color which was stirred under N_2 for an

additional 12 h after which time it was evaporated to dryness under reduced pressure. The orange residue was re-dissolved in 3 mL of CH_3CN. Subsequent addition of 50 mL of diethyl ether to the solution induced the precipitation of the desired product as an orange solid which was washed with copious quantities of diethyl ether. The yield is 84 mg (85% based on rhodium). ^{1}H-NMR (CD_3CN-d_3) δ ppm: 7.68(t, PMP), 7.10(dd, PMP), 6.45(dt, PMP), 5.98(t, PMP), 3.85(s, OCH_3 of PMP), 3.78(s, OCH_3 of PMP), 3.34(s, OCH_3 of PMP). ^{31}P-NMR (CD_3CN-d_3) δ ppm: 19.36 ppm ^{1}J (Rh-P) = 330 Hz, ^{2}J (Rh-P) = 45 Hz.

Synthesis of *cis*-$[Rh_2(PMP)_2(dpq)_2(CH_3CN)_2][BF_4]_2$ (26). An amount of *cis*-$[Rh_2(PMP)_2(CH_3CN)_6][BF_4]_2$ (40 mg, 0.030 mmol) was added to 20 mL of a 1:1/v:v mixture of CH_2Cl_2 and CH_3CN which contained a suspension of 16 mg dpq (0.067 mmol) ligand. The mixture was stirred in the dark for 72 h resulting in the formation of a dark red solution. The solution was then concentrated to 3 mL under reduced pressure and filtered through a medium frit to remove any insoluble materials. The addition of 30 mL diethyl ether into the filtrate induced the precipitation of the desired product as a reddish brown solid. It was collected by filtration and dried under vacuum for 24 h. The yield is 88% (43mg) based on rhodium. ^{1}H-NMR (CD_3CN-d_3) δ ppm: 9.39 (d, dpq), 9.10 (d, dpq), 8.90 (d, dpq), 8.80 (s, dpq), 8.14 (d, dpq), 7.89(dd, dpq), 7.08 (m, PMP), 6.74(d, PMP), 6.51(s, PMP), 6.27(m, PMP), 3.90 (s, OCH_3 of PMP), 3.80 (s, OCH_3 of PMP), 3.35 (OCH_3 of PMP). ^{31}P-NMR (CD_3CN-d_3) δ ppm: 16.90 ppm ^{1}J (Rh-P) = 330 Hz, ^{2}J (Rh-P) = 45 Hz. Anal. Calcd for $Rh_2C_{74}H_{62}N_{10}O_6P_2B_2F_8$•$CH_3CN$•$3CH_2Cl_2$: C, 48.30; N, 8.16; H, 3.79%. Found: C, 48.35; N, 7.96; H, 3.94%.

Synthesis of *cis*-[$Rh_2(PMP)_2(dppz)_2(CH_3CN)(H_2O)][BF_4]_2$ (27). An amount of *cis*-[$Rh_2(PMP)_2(CH_3CN)_6][BF_4]_2$ (40 mg, 0.030 mmol) was added into 20 mL of a 1:1/v:v mixture of CH_2Cl_2 and CH_3CN which contained a suspension of 20 mg of dppz (0.072 mmol) ligand. The solution rapidly turned to dark red and was stirred for 72 h in the dark. The solution was concentrated to 5 mL under reduced pressure with subsequent addition of 30 mL diethyl ether leading to the precipitation of the desired product. The solid was collected by filtration and dried under vacuum to yield 46 mg (89% based on rhodium) of the desired product. Slow diffusion of diethyl ether into a CH_3CN solution containing **27** led to the formation of crystals that were suitable for X-ray diffraction studies. ^{1}H-NMR (CD_3CN-*d_3*) δ ppm: 9.53 (d, dppz), 8.81 (s, dppz), 8.11-8.17 (m, dppz), 8.03 (dd, dppz), 7.90 (dd, dppz), 7.08 (m, PMP), 6.74(d, PMP), 6.51(s, PMP), 6.27(m, PMP), 3.92 (s, OCH_3 of PMP), 3.81 (s, OCH_3 of PMP), 3.39 (OCH_3 of PMP). ^{31}P-NMR (CD_3CN-*d_3*) δ ppm: 16.73 ppm ^1J (Rh-P) = 330 Hz, ^2J (Rh-P) = 45 Hz. Anal. Calcd for $Rh_2C_{80}H_{65}P_2N_9O_7B_2F_8 \bullet CH_2Cl_2$: C, 54.30; N, 7.04; H, 3.77%. Found: C, 54.37; N, 7.06; H 3.98%.

Synthesis of *cis*-[$Rh_2(PMP)_2(dppn)_2(CH_3CN)(H_2O)][BF_4]_2$ (28). An orange slurry of 10 mL of dry CH_3CN containing *cis*-[$Rh_2(PMP)_2(CH_3CN)_6][BF_4]_2$ (50 mg, 0.037 mmol) was treated with 20 mL of CH_2Cl_2 which contained 28 mg of undissolved dppn ligand (0.085 mmol). The was stirred in the dark for 72 h, after which time it was concentrated to 5 mL under reduced pressure and filtered through a medium frit to remove any insoluble materials. The addition of 30 mL of diethyl ether to the filtrate led to the precipitation of the desired product as a red solid which was collected by filtration and

dried under vacuum for 24 h to yield 61 mg (90% based on rhodium) of the desired product. ^{1}H-NMR (CD_3CN-d_3) δ ppm: 9.51 (d, dppn), 9.12 (s, dppn), 8.81(s, dppn), 8.44 (d, dppn), 8.12 (d, dppn), 7.94 (m, PMP), 7.87 (m, dppn), 7.10-7.17 (m, PMP), 6.75(d, PMP), 6.62(m, PMP), 6.45-35(m, PMP), 3.94 (s, OCH_3 of PMP), 3.81 (s, OCH_3 of PMP), 3.41 (OCH_3 of PMP). ^{31}P-NMR (CD_3CN-d_3) δ ppm: 16.64 ppm ^{1}J (Rh-P) = 330 Hz, ^{2}J (Rh-P) = 45 Hz. Anal. Calcd for $Rh_2C_{88}H_{69}P_2N_9O_7B_2F_8$•$CH_2Cl_2$: C, 56.50; N, 6.67; H, 3.79%. Found: C, 56.65; N, 6.79; 3.96%.

Instrumentation and methods

Hemispheres of data for **22**, **23** and **27** were collected by a combination of four sets of X-ray exposures. Each set used a different ϕ angle for the crystals and covered 0.5˚ in ω for **22** and 0.3˚ for **23** and **27**. The exposure times were 45 s for **22** and 20 s for **23** and **27**. The electron density corresponding to heavily disordered solvent molecules observed during the data refinement was removed using the SQUEEZE routine implemented in PLATON.

Results and discussion

Syntheses and characterization

The synthetic route for compound **25** follows the published procedure for *cis*-$[Rh_2[Ph_2P(C_6H_4)]_2(CH_3CN)_6][BF_4]_2$.[105] A slight excess of Et_3OBF_4 was used to replace each bridging $[O_2CCH_3]^-$ group with two monodentate CH_3CN ligands by alkylation of the carboxylates to the corresponding ester. The purity of **25** was confirmed by ^{1}H-NMR and ^{31}P-NMR spectroscopic data. The ^{1}H-NMR spectrum of *cis*-$[Rh_2[Ph_2P(C_6H_4)]_2(CH_3CN)_6][BF_4]_2$ in CD_3CN, *i.e.*, indicated all four eq CH_3CN ligands

in compound **25** undergoes fast exchange process with the CD_3CN solvent molecules, as evidenced by the presence of only free CH_3CN resonances in its ^{1}H-NMR spectrum.

Syntheses of **22**-**24**, **26**-**28** (structural representation shown in Figure 5.1) followed a similar procedure as described below.

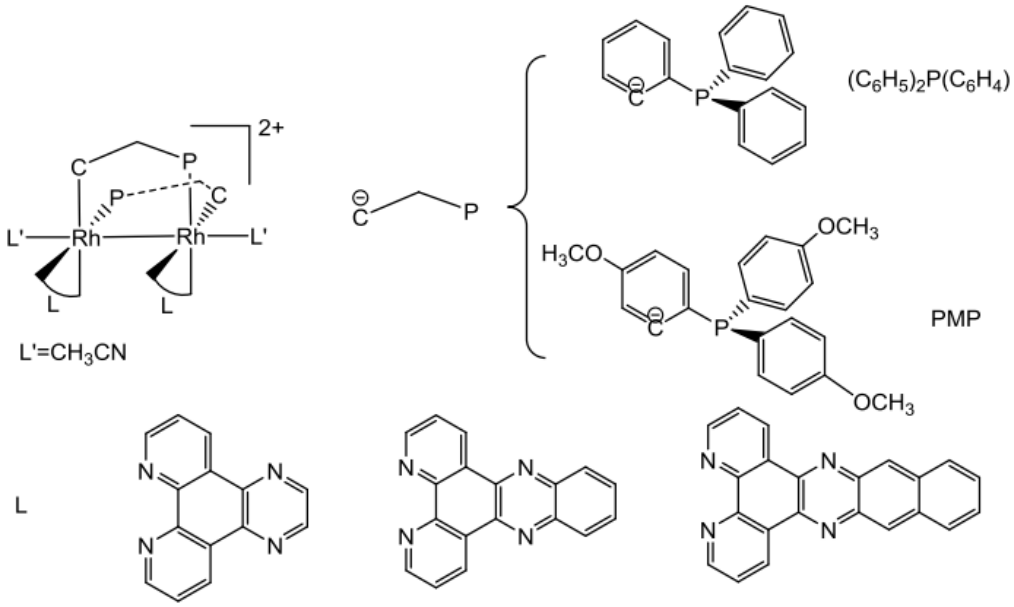

Complex	Bridging Ligands	L
22	$[(C_6H_5)_2P(C_6H_4)]^-$	dpq
23	$[(C_6H_5)_2P(C_6H_4)]^-$	dppz
24	$[(C_6H_5)_2P(C_6H_4)]^-$	dppn
26	$[PMP]^-$	dpq
27	$[PMP]^-$	dppz
28	$[PMP]^-$	dppn

Figure 5.1 Schematic representations of the complexes **22**-**24** and **26**-**28**.

A suspension of slightly more than two equivalents of diimine (dpq, dppz, dppn) ligands in CH_3CN/CH_2Cl_2 solution was mixed with the CH_3CN solution of *cis*-$[Rh_2[Ph_2P(C_6H_4)]_2(CH_3CN)_6][BF_4]_2$ or **25**. An immediate color change to dark red was observed. Stirring at room temperature for 72 h led to full substitution of the four labile eq CH_3CN ligands with the corresponding diimine ligands, as evidenced by the ^{31}P-NMR spectra of the products. The purity of each compound was also confirmed by ^{1}H-NMR spectroscopy.

X-ray crystallography

The crystal parameters and information pertaining to the data collection and refinement are summarized in Table 5.1.

***cis*-$[Rh_2[Ph_2P(C_6H_4)]_2(dpq)_2(CH_3CN)][BF_4]_2$.** Compound **22** crystallizes in the space group *P*-1. The two rhodium centers are bridged by two *cisoid* $[Ph_2P(C_6H_4)]^-$ ligands in the H-T fashion with P and C atoms as the coordination sites, akin to the starting material *cis*-$[Rh_2[Ph_2P(C_6H_4)]_2(CH_3CN)_6][BF_4]_2$.[105] Each rhodium center is further chelated by one dpq ligand but with only one of the ax positions being occupied by CH_3CN solvent molecule (Figure 5.2). As is the case for the compounds *cis*-$[Rh_2[Ph_2P(C_6H_4)]_2(CH_3CN)_6][BF_4]_2$[105] and *cis*-$[Rh_2[Ph_2P(C_6H_4)]_2(CNCH_3)_6][BF_4]_2$ [229], the product is a racemic mixture of both R and S isomers and they are related to each other by an inversion center. The Rh-Rh bond distance is 2.702(2) Å, ~ 0.04 Å longer than those in *cis*-$[Rh_2[Ph_2P(C_6H_4)]_2(CH_3CN)_6][BF_4]_2$ and ~ 0.06 Å shorter than those in *cis*-$[Rh_2[Ph_2P(C_6H_4)]_2(CNCH_3)_6][BF_4]_2$. [229] The Rh-P and Rh-C bond distances are ~ 2.24 and ~ 2.02 Å respectively. The Rh-N (dpq, *trans* to C) bond length is ~ 0.05 Å

Table 5.1 Crystal data for compounds **22**•$(CH_3)_2CO$, **23**•CH_3CN•$C_4H_{10}O$ and **27**.

	22•$(CH_3)_2CO$	**23•CH_3CN•$C_4H_{10}O$**	**27**
Formula	$C_{69}N_9O_1B_2F_8P_2$ Rh_2 H_{53}	$C_{82}H_{67}B_2N_{11}$ $F_8P_2Rh_2O_1$	$C_{82}H_{66}N_{10}Rh_2$ $P_2O_6B_2F_8$
Space group	*P-1*	*P2₁/c*	*P*-1
a, *b*, *c*/ Å	12.097(9)	16.067(3)	13.871(3)
	12.996(10)	15.486(3)	14.085(3)
	21.095(16)	29.969(6)	23.870(5)
α, β, γ/ º	85.270(10)	90.00	87.84(3)
	82.340(10)	102.08(3)	79.11(3)
	70.230(9)	90.00	66.22(3)
V/Å^3	3091(4)	7292(3)	4187.1(15)
Z	2	4	2
2θ range for data collection/º	52.93	46.49	48.11
Independent reflections	12351	10457	13057
Completeness to θ max/ %	96.8	99.9	98.6
Goodness-of-fit parameter (all data)[a]	0.935	1.051	1.060
Residual factors [$I > 4\sigma(I)$][b]	*R = 0.0602*	*R = 0.0338*	*R* = 0.0388
	wR = 0.1441	*wR = 0.0811*	*wR* = 0.0921
Residual factors (all data)[c]	*R = 0.1151*	*R = 0.0409*	*R* = 0.0537
	wR = 0.1661	*wR = 0.0859*	*wR* = 0.0969

[a]Goodness-of-fit = $\{\sum[w(F_o^2 - F_c^2)^2]/(n-p)\}^{1/2}$, where *n* is the number of reflections and *p* is the total number of parameters refined. [b]$R = \sum ||F_o| - |F_c|| / \sum |F_o|$. [c]$wR = \{\sum[w(F_o^2 - F_c^2)^2] / \sum w(F_o^2)^2]\}^{1/2}$.

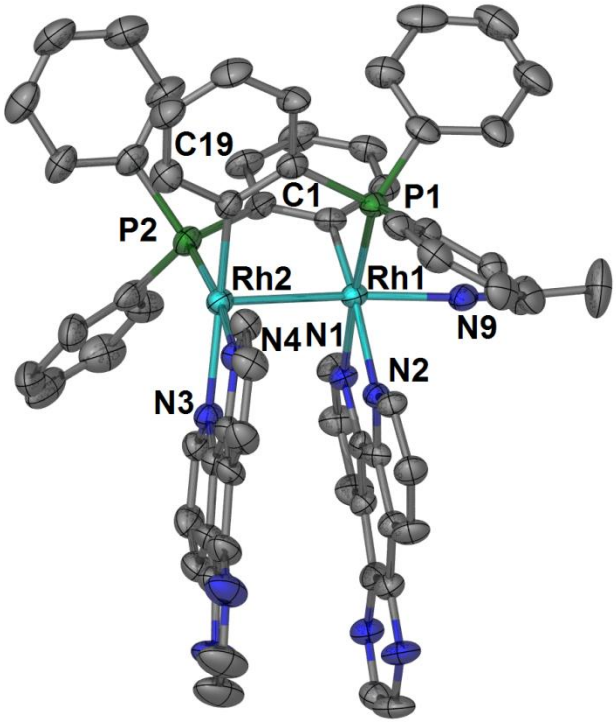

Figure 5.2 Thermal ellipsoid plot for compound **22** at the 50% probability level; anions $[BF_4]^-$, hydrogen atoms and interstitial solvent molecules omitted for the sake of clarity.

longer than the Rh-N (dpq, *trans* to P), with the former distance being ~ 2.20 Å. Quite noticeably, the Rh-N (ax CH_3CN) is 2.106(6) Å, which is shorter than the Rh-N (dpq) bond distances. The internal twists from the eclipsed configuration occur for the two dpq ligands to reduce the steric repulsion between them, with the dihedral angle values of 28.82º and 28.42º. This is larger than those found for *cis*-$[Rh_2(Fform)_2(dpq)_2(CH_3CN)_2][BF_4]_2$ (~ 19º), indicating the stronger repulsions operative in this compound.[230]

***cis*-[Rh$_2$[Ph$_2$P(C$_6$H$_4$)]$_2$(dppz)$_2$(CH$_3$CN)$_2$][BF$_4$]$_2$.** Compound **23** crystallizes in the space group $P2_1/c$. The coordination spheres of the rhodium centers are similar to that of **22**, except that both ax positions are occupied by CH_3CN ligands as shown in Figure 5.3. As in the case of **22**, compound **23** is a racemic mixture, but the two isomers are related to each other by glides located at 1/4b and 3/4b. The Rh-Rh bond distance is 2.7186(6) Å, comparable to that in **22**. The Rh-P and Rh-C bond distances are ~ 2.2503(4) and ~ 2.0400(3) Å, similar to those in *cis*-[Rh$_2$[Ph$_2$P(C$_6$H$_4$)]$_2$(CH$_3$CN)$_6$][BF$_4$]$_2$ and **22**, but shorter than those found in *cis*-[Rh$_2$[Ph$_2$P(C$_6$H$_4$)]$_2$(CNCH$_3$)$_6$][BF$_4$]$_2$.[229] The Rh-N (dppz, *trans* to C atoms) bond distances are ~ 2.19 Å, ~ 0.05 Å longer than the Rh-N (dppz, *trans* to P atoms) bond distances. On average, both of them are longer than those in *cis*-[Rh$_2$(μ-O$_2$CCH$_3$)$_2$(dppz)$_2$(η^1-O$_2$CCH$_3$)(CH$_3$CH$_2$OH)][BF$_4$][46] (from 2.005(4) to 2.016(4) Å) and *cis*-[Rh$_2$(DTolF)$_2$(dppz)$_2$(CH$_3$CN)][BF$_4$]$_2$ (from 2.040(5) to 2.060(2) Å),[230] indicating the much stronger *trans* influence of the bridging orthometalated phosphine ligands. The Rh-N (ax CH_3CN) bond distances are 2.2437(5) and 2.1953(5) Å, respectively, in a similar range to Rh-N (dppz, *trans* to C atoms). The internal twist angles from the eclipsed configuration for two dppz ligands are - 21.65º and - 21.61º, which are larger than those in *cis*-[Rh$_2$(μ-O$_2$CCH$_3$)$_2$(dppz)$_2$(η^1-O$_2$CCH$_3$)(CH$_3$CH$_2$OH)][BF$_4$] (~ 13º) and *cis*-[Rh$_2$(DTolF)$_2$(dppz)$_2$(CH$_3$CN)][BF$_4$]$_2$ (~ 16º).

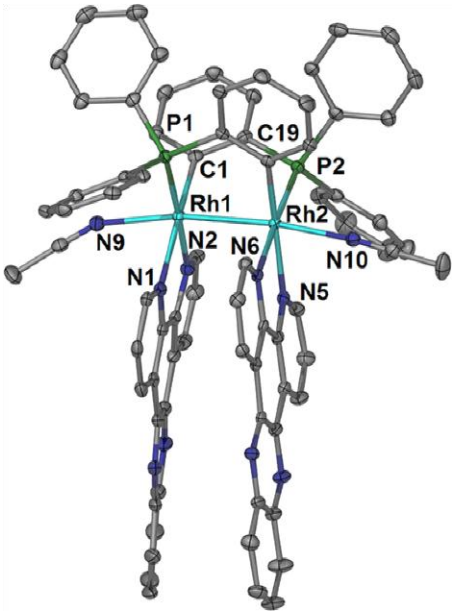

Figure 5.3 Thermal ellipsoid representation of compound **23** at the 50% probability level; anions and hydrogen atoms were omitted for the sake of clarity.

***cis*-[Rh$_2$[PMP]$_2$(dppz)$_2$(CH$_3$CN)$_2$][BF$_4$]$_2$.** Compound **27** crystallizes in the triclinic *P*-1 space group, with the coordination environment around the two rhodium centers similar to **23** being depicted in Figure 5.4a. Compound **27** is also a racemic mixture with the isomers related to each other by an inversion center. The Rh-Rh bond distance is 2.723(1) Å, in a similar range to that found for **22** and **23**. The Rh-N (dppz) bond distances *trans* to the P atoms are ~2.12 Å while those *trans* to C atoms are ~2.19 Å, and both distances are in a similar range to those in **23**. The Rh-N (ax CH_3CN) bond distances are ~2.19 Å, similar to the Rh-N (dppz, *trans* to C) bond distances. Distortions from the eclipsed configuration for the two dppz ligands also occur in the crystal structure, and the dihedral angles defined by N1-Rh1-Rh2-N3 and N2-Rh1-Rh2-N4 are -24.5(1)º and -24.4(1)º respectively. As shown in Figure 5.4b, intermolecular π-π stacking interactions

are present in the crystal packing diagram of **27**, with a distance of ~ 3.36 Å from C75 to the plane that is defined by the dppz ligand from another molecule.

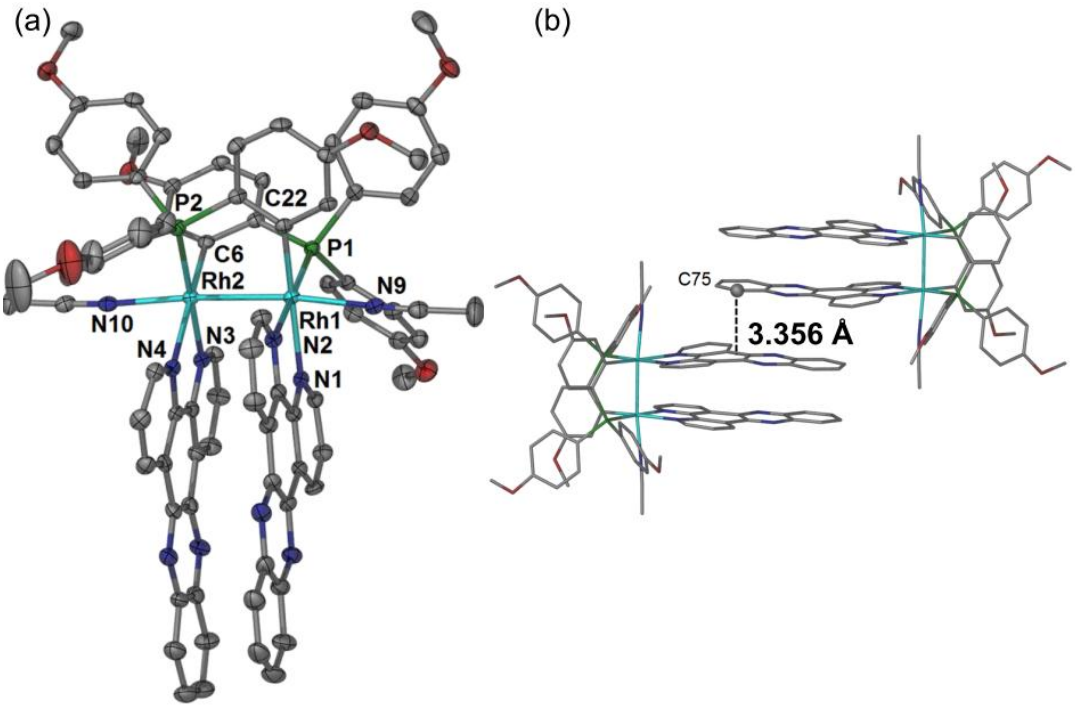

Figure 5.4 (a) Thermal ellipsoid representation of compound **27** at the 50% probability level; anions and hydrogen atoms were omitted for the sake of clarity; (b) crystal packing representations of **27**, indicating the π-π stacking interactions between two dppz ligands in two adjacent molecules.

Electronic absorption and electrochemical studies

Since there are structural similarities between **22**/**26**, **23**/**27**, **24**/**28**, respectively, each pair is expected to exhibit analogous electronic properties in CH_3CN at room temperature (Figures 5.5 and 5.6) which are detailed in this section. Although the ε values are low, two distinct shoulder peaks are observed in the region λ> 410 nm for all the complexes. The first shoulder peak, at ~420 nm for **22**/**26**, ~440 nm for **23**/**27** and ~470 nm for **24**/**28** (Table 5.2), is clearly dependent on the identity of the diimine ligands with the absorption bands for compounds containing more conjugated π system ligands occurring at relative lower energies. Therefore, they can be assigned as the electronic transitions from the metal centers to the diimine ligands (MLCT). As featured in Figure 5.5 and Table 5.2, the lowest energy transitions in **22** and **23** are of nearly the same energy with similar molar absorptivities (~ 477 nm, ε = 1250 $M^{-1}cm^{-1}$ in **22** and ~ 474 nm, 1250 $M^{-1}cm^{-1}$ in **23**). For compound **24**, however, the transition occurs at a lower energy with a slightly higher molar absorptivity (~ 518 nm, ε = 2000 $M^{-1}cm^{-1}$), an indication of the different character in **24**. Furthermore, as shown in Figure 5.6 and Table 5.2, the lowest energy transitions in **26** and **27** also occur in a very similar energy range as compared to that of **22** and **23**. The independence of these transitions on both the bridging and chelating ligands indicates that they are MC dd transitions, not uncommon for Rh_2(II,II) compounds.[21] The relatively high ε value (~ 1000 $M^{-1}cm^{-1}$), however, indicates that they are likely of different characters from the lowest energy transition band in $Rh_2(\mu\text{-}OOCCH_3)_4 \bullet 2H_2O$ (~ 584 nm, ~ 240 $M^{-1}cm^{-1}$ in H_2O) which corresponds to the $Rh_2(\pi^*)$ to $Rh_2(\sigma^*)$ transition. The absorptions at λ ~ 302 and 339 nm

for **22**, 361 and 378 nm for **23**, 398 and 418 nm for **24** are assigned as the diimine centered intramolecular $^1\pi\pi^*$ transitions, given that similar absorption bands are also present in the free dpq ligand at ~ 326-340 nm, the free dppz ligand at ~ 340-370 nm and the free dppn ligand at ~ 390 and 414 nm. In addition, similar absorptions are also observed for compounds **26**-**28** with similar molar absorptivities, the series of Rh_2(II,II) compounds with different bridging ligands ($[DTolF]^-$, $[F\text{-}form]^-$ and $[OAc]^-$), as well as

Table 5.2 Electronic absorption maxima, λ_{abs}, molar absorptivities, ε, and redox potentials for **22-24** and **26-28** in CH_3CN.

Complex	λ_{abs}/nm ($\varepsilon\times10^3$ $M^{-1}cm^{-1}$)	Potential/ V
22	257 (66), 302 (31), 339 (14), 415 (3.2), ~ 477 (1.25)	1.44(E_{pa}), -0.76, -1.03, -1.49, -1.77
23	275 (115), 361 (25), 378 (22), 441 (2.5) ~ 484 (1.15)	1.33(E_{pa})
24	242 (92), 261 (71), 313 (128), 398 (17.7), 418 (17.4), 470 (5.0), ~ 518 (2.0)	1.36(E_{pa})
26	252 (117), 301 (45), 347 (15), 420 (3.3), ~ 474 (1.25)	1.35(E_{pa}), -0.86, -1.08, -1.52,
27	274 (127), 361 (28), 378 (24), 444 (2.8), ~ 490 (1.05)	1.24(E_{pa})
28	241 (110), 261 (77), 313 (118), 398 (16.5), 418 (16.4), 470 (4.6), ~ 518(1.7)	1.27(E_{pa})

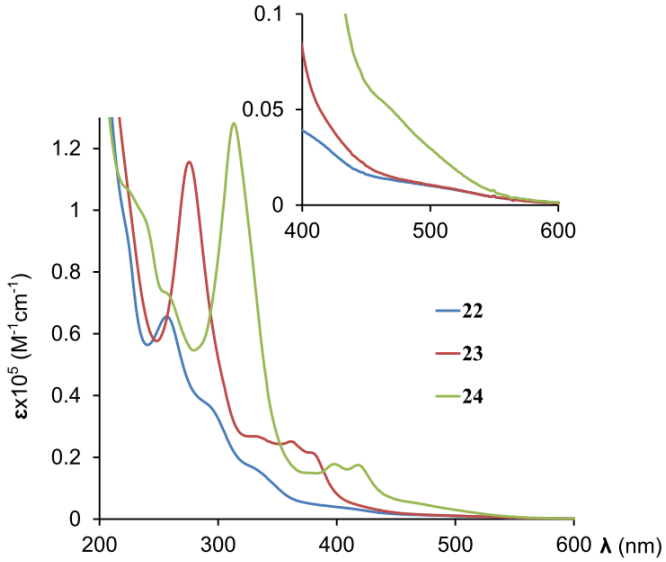

Figure 5.5 Overlay of the electronic absorption spectra of compounds **22**-**24** in CH_3CN at room temperature.

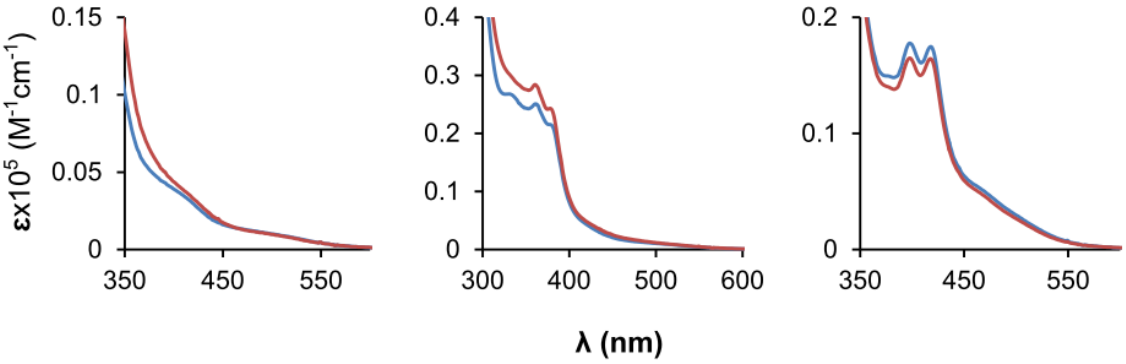

Figure 5.6 Comparisons of the electronic absorption spectra between **22**/**26**, **23**/**27** and **24**/**28.**

several Ru(II) compounds containing these diimine ligands.[36,37,44-48, 230] Other strong absorption maxima in these compounds are located at λ ~ 250 nm in **22** and **26**, ~ 270

nm in **23** and **27**, ~ 260 nm in **24** and **28**, ascribed to the electronic transitions between the metal based orbitals but perturbed by mixing with the diimine ligands.

Upon a strong reducing potential to the working electrode of CH_3CN solutions containing compounds **23**, **24**, **27** and **28**, changes in the cyclic voltammogram were observed, indicating the decomposition of those complexes; positive voltages do not casue degradation. Of all the compounds, there is one quasi-reversible oxidation, occurring at ~1.30 V for compounds **22**-**24**, and at ~1.25 V for compounds **26**-**28**. A similar process is also observed in *cis*-$[Rh_2[Ph_2P(C_6H_4)]_2(CH_3CN)_6][BF_4]_2$ at ~1.41 V, assigned as the Rh_2^{4+}/Rh_2^{5+} redox couple.[105] In the case of compounds **22**-**24**, **26**-**28**, these events are independent of the diimine ligands while electron-donating groups on the bridging ligands result in a cathodic shift which idicates a Rh_2^{4+}/Rh_2^{5+}oxidation process influenced by the bridging ligands.

There are four consecutive reduction processes for compounds **22** and **26**. The first two reduction processes occur at ~ -0.76 and -1.03 V in **1**, -0.86 and -1.08 V in **26**, tentatively assigned as the stepwise reductions of the two diimine ligands. Compared to **22**, these processes for compound **26** occur at a more negative potential (~ 0.1 V), underscoring the involvement of the bridging ligands which is also in accord with the electron donating groups resulting in greater difficulty to reduce them. The third and fourth reduction events are tentatively assigned to the stepwise reduction of the dimetal centers, namely, the Rh_2^{4+}/Rh_2^{3+} and Rh_2^{3+}/Rh_2^{2+} redox couples.

Computational studies

DFT and TD-DFT calculations of the cationic units in **22-24**, **26-28** were conducted to gain further understanding of their electrochemical and photophysical properties. Geometric parameters for the gas phase optimizations were obtained from the crystal structures of **22**, **23**, **27** with appropriate modifications of the diimine ligands for different compounds (dpq for **26**, dppn for **24** and **28**). The optimized cationic units of **23** and **27** are shown in Figure 5.7. The comparisons of the bond distances and bond angles between the calculated structures and the crystal structures are listed in Table 5.3.

In all six compounds, orbitals ranging from LUMO to LUMO+5 are mainly diimine based orbitals, whereas the LUMO+6 is mainly of $Rh_2(\sigma^*)$ character (Table 5.4). For the HOMOs in **22-24**, different compounds vary in character and they are detailed as follows. For **22** and **23**, they possess similar compositions, mainly $Rh_2(\sigma)$ character with small contributions from ax CH_3CN (~10%) and bridging ligands (~10%), whereas it is a dppn-centered orbital in **24**. The HOMO-1 in **24**, on the other hand, has the same character as the HOMOs in **22** and **23** ($Rh_2(\sigma)$ orbital). Metal-centered $Rh_2(\pi^*)$ orbitals are HOMO-3, HOMO-4 in **22** and **23** (Table 5.4) and HOMO-5 [83% (Rh), 9% ($Ph_2PC_6H_4$)] and HOMO-6 [70% (Rh), 22% ($Ph_2PC_6H_4$)] in **24**. For the HOMOs in **26-28**, they are mainly $Rh_2(\sigma)$ character (70% Rh_2, 15% PMP and 10% ax CH_3CN). The metal-centered $Rh_2(\pi^*)$ orbitals are HOMO-9 in **26** [72% (Rh), 19% (PMP)] and **27** [71% (Rh), 22% (PMP)] and HOMO-11 in **28**. One point worth mentioning is that the HOMO-1 and HOMO-2 in **28**, are mainly dppn-based orbitals.

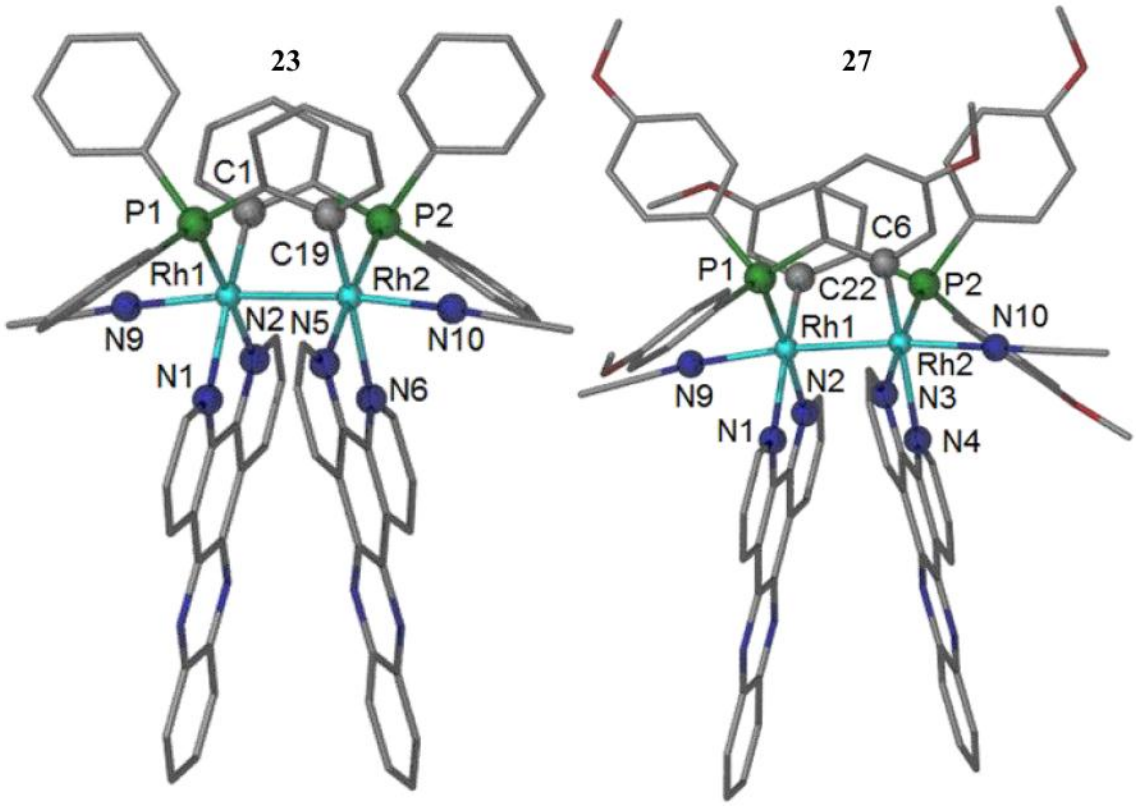

Figure 5.7 Calculated cationic structures of compounds **23** and **27**; the hydrogen atoms were omitted for the sake of clarity.

Table 5.3 Comparisons of the structural parameters in compounds **23** and **27** between the calculated structures and X-ray diffraction data.

23	Experimental	Calculated
	Bond distances (Å)	Bond distances (Å)
Rh1-Rh2	2.7186(6)	2.7110
Rh1-P1	2.2391(4)	2.285
Rh1-C1	2.0313(3)	2.032
Rh2-C19	2.0400(3)	2.032
Rh2-P2	2.2503(4)	2.285
Rh1-N9	2.2437(5)	2.226
Rh2-N10	2.1953(5)	2.226
Rh1-N1	2.2026(4)	2.239
Rh1-N2	2.1300(4)	2.162
Rh2-N5	2.1983(4)	2.161
Rh2-N6	2.1413(4)	2.240
	Experimental	Calculated
	Dihedral angle (º)	Dihedral angle (º)
P1-Rh1-Rh2-C19	-9.28	-14.9
C1-Rh1-Rh2-P2	-9.34	-14.9
N1-Rh1-Rh2-N6	-21.61	-29.2
N2-Rh1-Rh2-N5	-21.65	-29.3
27	Experimental	Calculated
	Bond distances (Å)	Bond distances (Å)
Rh1-Rh2	2.723(1)	2.7116
Rh1-N9	2.196(4)	2.233
Rh2-N10	2.185(4)	2.211
Rh1-P1	2.252(1)	2.284
Rh1-C22	2.029(4)	2.030
Rh2-C6	2.043(3)	2.030
Rh2-P2	2.252(1)	2.284
Rh1-N1	2.182(3)	2.165
Rh1-N2	2.123(3)	2.237
Rh2-N3	2.126(3)	2.169
Rh2-N4	2.195(3)	2.239
	Experimental	Calculated
	Dihedral angle (º)	Dihedral angle (º)
P1-Rh1-Rh2-C6	-10.3(1)	-16.9
C22-Rh1-Rh2-P2	-10.9(1)	-16.9
N1-Rh1-Rh2-N3	-24.5(1)	-32.1
N2-Rh1-Rh2-N4	-24.4(1)	-32.1

Table 5.4 Compositions of the orbitals related to the electronic transitions in compounds **22**-**24**, **26**-**28** calculated by TD-DFT calculations in the solvation model with CH_3CN as the solvent.

	22	**23**	**24**	**26**	**27**	**28**
HOMO-4	69 Rh 23 $Ph_2PC_6H_4$ 5 dpq	70 Rh 22 $Ph_2PC_6H_4$ 5 dppz	56 $Ph_2PC_6H_4$ 40 Rh	48 PMP 47 Rh	56 PMP 39 Rh	79 PMP 19 Rh
HOMO-3	82 Rh 10 $Ph_2PC_6H_4$ 5 dpq	84 Rh 9 $Ph_2PC_6H_4$ 6 dppz	50 $Ph_2PC_6H_4$ 46 Rh	78 PMP 20 Rh	80 PMP 17 Rh	71 PMP 15 Rh 14 dppn
HOMO-2	57 $Ph_2PC_6H_4$ 39 Rh	56 $Ph_2PC_6H_4$ 40 Rh	68 dppn 25 Rh	80 PMP 19 Rh	78 PMP 19 Rh	75 dppn 22 PMP
HOMO-1	49 $Ph_2PC_6H_4$ 47 Rh	51 $Ph_2PC_6H_4$ 45 Rh	60 Rh 24 dppn 8 CH_3CN 8 $Ph_2PC_6H_4$	79 PMP 17 Rh	81 PMP 15 Rh	91 dppn 9 PMP
HOMO	74 Rh 10 CH_3CN 10 $Ph_2PC_6H_4$ 6 dpq	75 Rh 10 CH_3CN 10 $Ph_2PC_6H_4$ 5 dppz	99 dppn	71 Rh 16 PMP 9 CH_3CN	71 Rh 14 PMP 10 CH_3CN 5 dppz	71 Rh 15 PMP 10 CH_3CN
LUMO	80 dpq 13 Rh 6 $Ph_2PC_6H_4$	73 dppz 17 Rh 10 $Ph_2PC_6H_4$	85 dppn 14 Rh	79 dpq 15 Rh 6 PMP	80 dppz 19 Rh	80 dppn 16 Rh
LUMO+1	86 dpq 9 Rh	86 dppz 11 $Ph_2PC_6H_4$	97 dppn	81 dpq 9 Rh 8 PMP	96 dppz	93 dppn
LUMO+2	83 dpq 11 $Ph_2PC_6H_4$ 6 Rh	84 dppz 11 Rh	85 dppn 11 Rh	87 dpq 6 Rh 6 PMP	78 dppz 11 Rh 9 PMP	85 dppn 11 Rh

Table 5.4 Continued

	22	**23**	**24**	**26**	**27**	**28**
LUMO+3	63 dpq 31 Rh 5 $Ph_2PC_6H_4$	72 dppz 24 Rh	74 dppn 22 Rh	57 dpq 34 Rh 8 PMP	66 dppz 26 Rh 7 PMP	72 dppn 25 Rh
LUMO+4	95 dpq	93 dppz	95 dppn	84 dpq 13 PMP	94 dppz	95 dppn
LUMO+5	86 dpq 7 Rh 7 $Ph_2PC_6H_4$	84 dppz 9 $Ph_2PC_6H_4$ 6 Rh	81 dppn 9 $Ph_2PC_6H_4$ 9 Rh	78 dpq 16 PMP 6 Rh	85 dppz 10 PMP	88 dppn 6 PMP
LUMO+6	57 Rh 25 $Ph_2PC_6H_4$ 11 ax CH_3CN 7 dpq	57 Rh 24 $Ph_2PC_6H_4$ 11 CH_3CN 8 dppz	55 Rh 24 $Ph_2PC_6H_4$ 11 CH_3CN 10 dppn	58 Rh 24 PMP 12 CH_3CN 6 dpq	58 Rh 25 PMP 12 CH_3CN 5 dppz	58 Rh 23 PMP 12 CH_3CN 7 dppn

For all six compounds, the energies for the orbitals ranging from LUMO to LUMO+5 are closely related to the diimine ligands as displayed in Figure 5.8 due to their diimine ligand characters, which is similar to the observation in the other two series of dirhodium compounds equipped with $[DTolF]^-$ and $[F\text{-}form]^-$ ligands.[230] On the other hand, the LUMO+6 orbitals lie in very close energy range for all the complexes due to their $Rh_2(\sigma^*)$ character. The HOMOs in **22** and **23** and the HOMO-1 in **24** are of very similar energies due to their comparable $Rh_2(\sigma)$ character (Table 5.4). The HOMO and HOMO-2 in **24** (dppn-centered orbital) also lie in a very similar range as the HOMO-1 in **24** as depicted in Figure 5.8. The HOMOs in **26**-**28** lie very close in energy as displayed in Figure 5.8, but are of slightly higher energy than the HOMOs in **22**-**23** and HOMO-1 in **24** (Table 5.4), ascribed to the electron donating –OMe groups on the phenyl rings of the bridging ligand which is a minor component of the HOMOs in all six compounds. The HOMO-1 and HOMO-2 in **28** are of very similar energy to the HOMO and HOMO-2 in **24** due to their same dppn ligand character (Table 5.4).

The vertical energies, the orbital contributions and oscillating factors for the first 10 excited states in **22**-**24**, **26**-**28** are listed in Tables 5.5 and 5.6, respectively. The lowest energy transitions in **22**-**23**, **26**-**27** have similar character, mainly the electronic transitions from $Rh_2(\sigma)/Rh_2(\pi^*)$ orbitals to $Rh_2(\sigma^*)$ orbital (Tables 5.5 and 5.6). Therefore, they occur within a very small energy range of 470 to 475 nm with a similar oscillating factor of $f \sim 0.02$; the lowest energy transitions for **24** and **28**, however, occur at ~ 500-510 nm and they are of dual $^1\pi\pi^*$ dppn-centered and metal to dppn ligand charge transition character (MLCT) as revealed by the TD-DFT calculations.

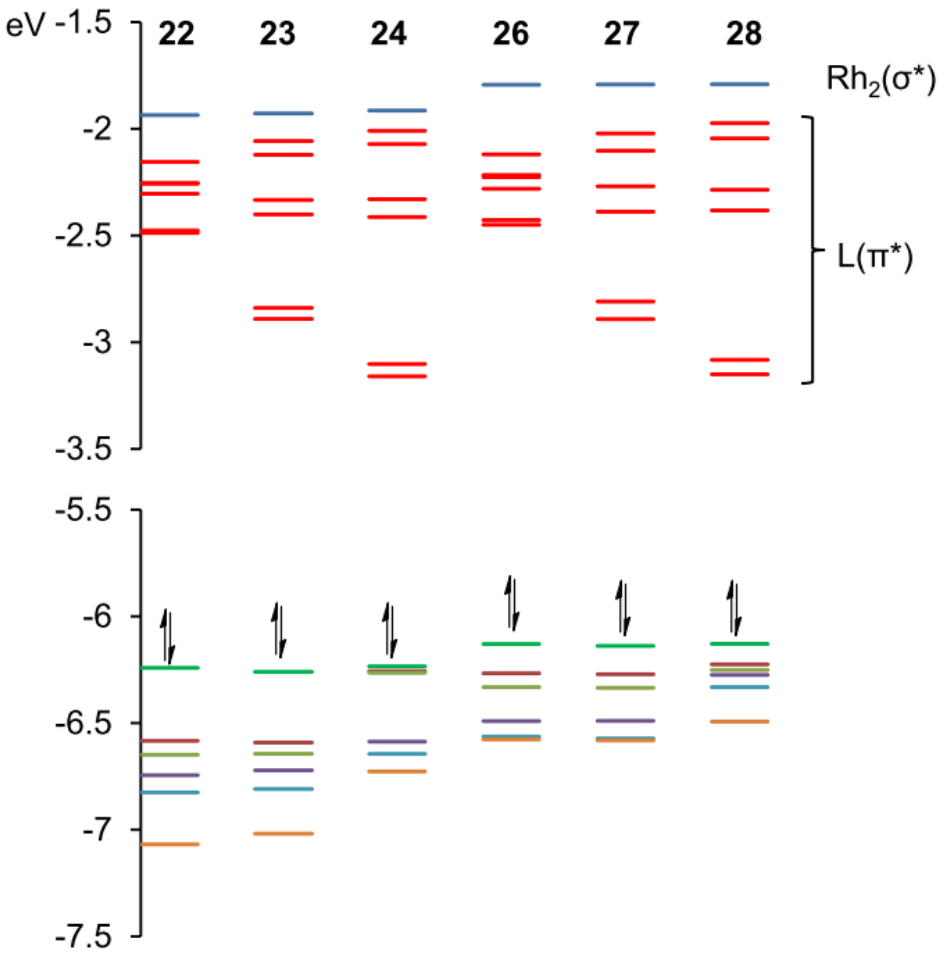

Figure 5.8 MO diagrams for **22-24**, **26-28** predicted by TD-DFT calculations with CH_3CN as the solvent.

Table 5.5 Electronic transitions in **22-24** predicted by TD-DFT calculations with CH_3CN as the solvent; only major transitions ($2|coefficient|^2$>20%) are listed in the table; H = HOMO, L = LUMO.

	22	**23**	**24**
1	474 nm f=0.0211 H-4 -> L+6 32.1% H -> L+6 48.8%	476 nm f=0.0187 H-4 -> L+6 33.2% H -> L+6 47.5%	508 nm f=0.0017 H-2 -> L+1 23.9% H -> L 66.0%
2	455 nm f=0.0005 H-3 -> L+6 67.5%	457 nm f=0.0008 H-3 -> L+6 72.9%	507 nm f=0.0311 H-2 -> L 40.8% H -> L+1 42.9%
3	430 nm f=0.0239 H -> L+1 88.1%	449 nm f=0.0035 H -> L 91.4%	488 nm f=0.0027 H-2 -> L 25.4% H-1 -> L 71.5%
4	419 nm f=0.0079 H -> L 72.6% H -> L+3 24.6%	442 nm f=0.0218 H -> L+1 80.7%	477 nm f=0.0192 H-2 -> L+1 23.9% H-1 -> L+1 71.0%
5	384 nm f=0.0004 H -> L+4 87.9%	413 nm f=0.0078 H -> L+2 78.0%	473 nm f=0.0226 H-5 -> L+6 31.4% H-1 -> L+6 34.8%
6	382 nm f=0.0072 H-3 -> L+1 24.5% H-1 -> L+1 30.5%	404 nm f=0.0050 H -> L+3 88.5%	461 nm f=0.0002 H-2 -> L 32.4% H -> L+1 56.4%
7	379 nm f=0.0039 H-1 -> L+6 51.3%	392 nm f=0.0175 H-1 -> L 68.3%	460 nm f=0.0000 H-2 -> L+1 50.2% H -> L 33.4%
8	378 nm f=0.0184 H -> L+3 39.4%	389 nm f=0.0115 H-1 -> L+1 43.7%	454 nm f=0.0000 H-5 -> L+6 68.9%
9	375 nm f=0.0010 H-3 -> L+1 29.2% H-2 -> L+6 21.8%	385 nm f=0.0322 H-3 -> L 65.6%	423 nm f=0.0136 H-3 -> L 79.7%
10	374 nm f=0.0019 H -> L+2 86.2%	384 nm f=0.0104 H-3 -> L+1 42.5%	419 nm f=0.0199 H-2 -> L+2 23.0% H-1 -> L+2 66.1%

Table 5.6 Electronic transitions in **26-28** predicted by TD-DFT calculations with CH_3CN as the solvent; only major transitions ($2|coefficient|^2$>20%) are listed in the table. H = HOMO, L = LUMO.

	26	**27**	**28**
1	476 nm *f*=0.0207 H-9 -> L+6 29.0% H -> L+6 43.3%	472 nm *f*=0.0204 H-9 -> L+6 30.4% H -> L+6 41.3%	511 nm *f*=0.0033 H -> L 94.64%
2	457 nm *f*=0.0011 H-7 -> L+6 26.4% H-4 -> L+6 32.1%	468 nm *f*=0.0063 H -> L 89.2%	507 nm *f*=0.0015 H-2 -> L+1 26.00% H-1 -> L 67.48%
3	438 nm *f*=0.0232 H -> L+1 76.9%	458 nm *f*=0.0196 H -> L+1 54.3%	505 nm *f*=0.0294 H-2 -> L 50.49% H-1 -> L+1 40.72%
4	429 nm *f*=0.0069 H -> L 67.3% H -> L+3 24.5%	451 nm *f*=0.0057 H-7 -> L+6 24.8% H -> L+1 23.9%	497 nm *f*=0.0192 H -> L+1 92.43%
5	391 nm *f*=0.0004 H -> L+4 90.8%	426 nm *f*=0.0081 H -> L+2 71.0%	474 nm *f*=0.0256 H-11 -> L+6 29.58% H -> L+6 43.76%
6	390 nm *f*=0.0019 H -> L+3 33.5%	418 nm *f*=0.0003 H-1 -> L 76.2%	460 nm *f*=0.0003 H-2 -> L 39.22% H-1 -> L+1 56.99%
7	388 nm *f*=0.0043 H-2 -> L+1 26.5%	413 nm *f*=0.0036 H-2 -> L 72.7%	459 nm *f*=0.0000 H-2 -> L+1 60.10% H-1 -> L 31.01%
8	385 nm *f*=0.0224 H -> L+3 23.6%	412 nm *f*=0.0082 H -> L+3 84.1%	455 nm *f*=0.0005 H-3 -> L 75.84%
9	384 nm *f*=0.0017 H -> L+2 80.1%	407 nm *f*=0.0082 H-1 -> L+1 65.0%	454 nm *f*=0.0001 H-9 -> L+6 29.43% H-7 -> L+6 25.66%
10	381 nm *f*=0.0098 H-1 -> L+1 38.0%	402 nm *f*=0.0054 H-2 -> L+1 70.4%	448 nm *f*=0.0036 H-4 -> L 70.40%

On the other hand, the transitions originating from $Rh_2(\sigma)/Rh_2(\pi^*)$ to $Rh_2(\sigma^*)$ in **24** and **28**, occur at $\lambda \sim 473$ nm, which is similar to the lowest energy transitions for **22**, **23** and **26**, **27**. Other distinct low energy transition are predicted to occur at $\lambda \sim 420$-430 nm in **22**, 430-440 nm in **23**, 480-490 nm in **24**. They are the transitions from metal-based orbitals to the low lying diimine based unoccupied orbitals, thus rendering them MLCT character. The bathochromic shifts on going from **22** through **24** are in accord with the order of the energy levels for those diimine based unoccupied orbitals being dpq> dppz> dppn. Similar bands also occur in compounds **26**-**28**, with all of them also bathochromic-shifted as compared to **22**-**24** respectively, attributed to the slight destabilization of the $Rh_2(\pi^*)$ orbitals by the more electron donating bridging PMP ligands in them (*vide supra*).

Concluding remarks

The complexes presented in this chapter comprise two new families of partial paddlewheel dirhodium compounds with orthometalated phosphines as bridging ligands that exhibit novel structural features, in particular the very long eq Rh-N bond distance. This finding is not surprising given the fact that the orthometalated phosphine ligands are very good electron donors (*vide supra*), that exert a strong *trans* influence on these eq Rh-N bonds. Preliminary studies indicate that the lowest energy transitions in the dpq, dppz complexes are mainly of metal-centered character whereas the dppn analogs are dual dppn $\pi\pi^*$ and $Rh_2(\pi^*)$ to $Rh_2(\sigma^*)$ character. As compared to the results obtained from the studies in Chapter III, the use of orthometalated phosphine ligands leads to a

drastic change of the electronic structures of the dirhodium complexes, indicating an ease of tuning of the ligand field.

CHAPTER VI

CONCLUDING REMARKS AND FUTURE WORK

As described in the previous chapters, the new dirhodium complexes exhibit potential for two very different applications, namely solar energy conversion (specifically water splitting to produce hydrogen) and anticancer photodynamic applications. These properties are directly related to the nature of the bridging ligands spanning the dirhodium metal-metal bond. To further improve their performance in each arena the ligand environment was tuned.

The ultimate goal for the partial paddlewheel dirhodium complexes in Chapters II and IV was to achieve stability of the complexes with respect to lack of substitution of the monodentate eq ligands and to induce photolability upon visible light irradiation; in this respect, the aim was a medicinal chemistry application. As demonstrated in this dissertation, the incorporation of electron rich bridging ligands, *e.g.* formamidinate or orthometalated phosphine ligands, leads to an electron rich dimetal core which renders the monodentate eq CH_3CN ligands labile even in the absence of light. The use of the better electron accepting CH_3NC ligand results in the formation of partial paddlewheel dirhodium isocyanide complexes, in which the eq CH_3NC ligands bind so strongly to the dimetal center that they are stable even with light irradiation. By using the less electron-donating pyridinate ligand with different substituents as described in Chapter IV, one can systematically tune the electronic structures of the dirhodium complexes which further sheds light on the structure/reactivity relationships for this class of partial paddlewheel dirhodium complexes.

Given the above issues, a promising idea is to coordinate CH_3NC ligands to *cis*-$[Rh_2(mhp)_2(CH_3CN)_6][BF_4]_2$ for which it is known that the eq CH_3CN ligands are less labile than those in *cis*-$[Rh_2(DTolF)_2(CH_3CN)_6][BF_4]_2$ but more labile than those in the case of *cis*-$[Rh_2(O_2CCH_3)_2(CH_3CN)_6][BF_4]_2$. Therefore, the resulting compound, namely *cis*-$[Rh_2(mhp)_2(CNCH_3)_6][BF_4]_2$, is expected to possess stable eq CH_3NC ligands in the dark but may achieve the desired photolability upon visible light irradiation.

Partial paddlewheel dirhodium complexes with formamidinate bridging ligands presented in Chapter III and those with orthometalated phosphine bridging ligands in Chapter IV exhibit very different photophysical properties, further underscoring the important role of the bridging ligands. Of particular interest, preliminary studies on compound **9** from Chapter III, namely *cis*-$[Rh_2(DTolF)_2(dpq)_2(CH_3CN)][BF_4]_2$ indicate its ability to catalytically reduce H^+ to H_2 upon visible light irradiation in the absence of any external photosensitizer. This result opens up a new strategy for incorporating the water reduction catalyst and photosensitizer into a single molecule without the complicated synthesis and purification processes. Moreover, compounds based on this strategy can also eliminate the undesired electron transfer process from the photosensitizer to the water reduction catalyst, thereby increasing the efficiency of the H_2 production process. We propose that the H_2 production ability of compound **9** is closely related to the highly reducing ^{3}MC excited state, which can facilitate the formation of Rh hydride species. Therefore, the development of other dirhodium complexes with a similar structural type should also utilize electron rich donating ligands to render the excited states of the dirhodium complexes highly reducing. For

example, oxopyridinate or acetamide ligands should be utilized to further tune the properties of this type of partial paddlewheel dirhodium complexes. In this vein, compounds *cis*-$[Rh_2(xhp)_2(CH_3CN)_6][BF_4]_2$ and *cis*-$[Rh_2(NHCOCH_3)_2(CH_3CN)_6][BF_4]_2$ are readily available as the synthetic precursors for compounds *cis*-$[Rh_2(xhp)_2(N\text{-}N)_2][BF_4]_2$ and *cis*-$[Rh_2(NHCOCH_3)_2(N\text{-}N)_2][BF_4]_2$ (N-N = dpq, dppz or dppn ligands).

Improving water solubility

For the better performance as catalysts or as anticancer agents, one goal of primary importance is to develop complexes with higher water compatibility as compared to the current ones. For example, the complexes *cis*-$[Rh_2(DTolF)_2(N\text{-}N)_2]^{2+}$ and *cis*-$[Rh_2(F\text{-}form)_2(N\text{-}N)_2]^{2+}$ in chapter III as well as *cis*-$[Rh_2[Ph_2P(C_6H_4)]_2(N\text{-}N)_2]^{2+}$ in chapter V (N-N = dpq, dppz, dppn) have very limited water solubility.

The introduction of hydrophilic groups (carboxylic acids[231], sulfonic acids[232-234] or ammonium groups[235]) onto the scaffold of organic ligands is an effective way of imparting higher water solubility to coordination complexes. Diarylformamidine ligands offer many possibilities for the improvement of water solubility through variation of the substituents at different positions on the phenyl groups. The proposed synthetic route for formamidine ligands with sulfonate/carboxylate groups is outlined in Figure 6.1.

Another commonly applied strategy to enhance water solubility of organic ligands is to incorporate hydrophilic peptides as functional groups. One common linker group between the organic ligands and the peptides is carboxylate,[236] which can be readily attached to the formamidine ligands according to the synthetic route depicted in Figure 6.1. The structures of the proposed peptides [237-238] are displayed in Figure 6.2 and the

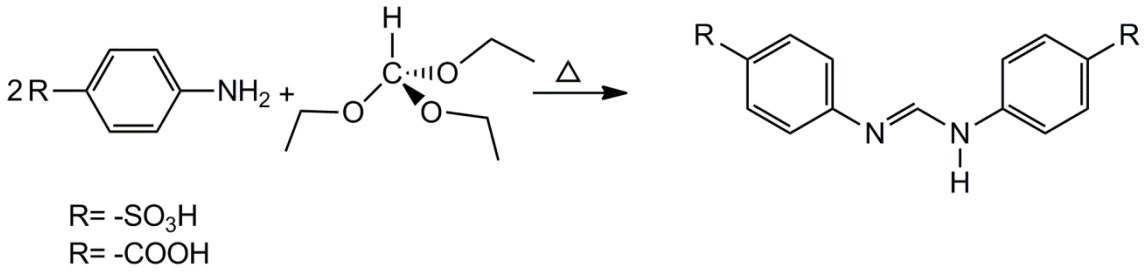

Figure 6.1 Synthetic route for formamidine ligands bearing sulfonate or carboxylate groups.

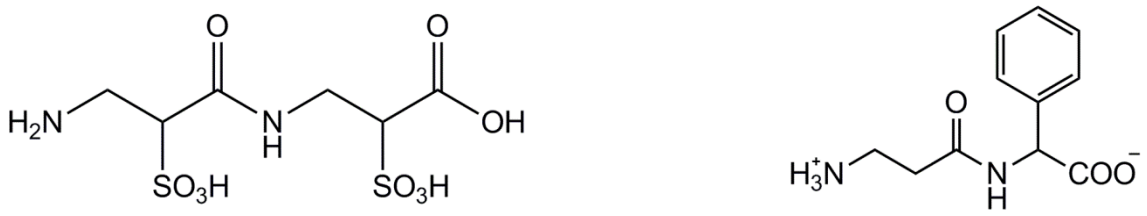

Figure 6.2 Structural representations of the proposed peptides to enhance the water solubility of the formamidine ligands.

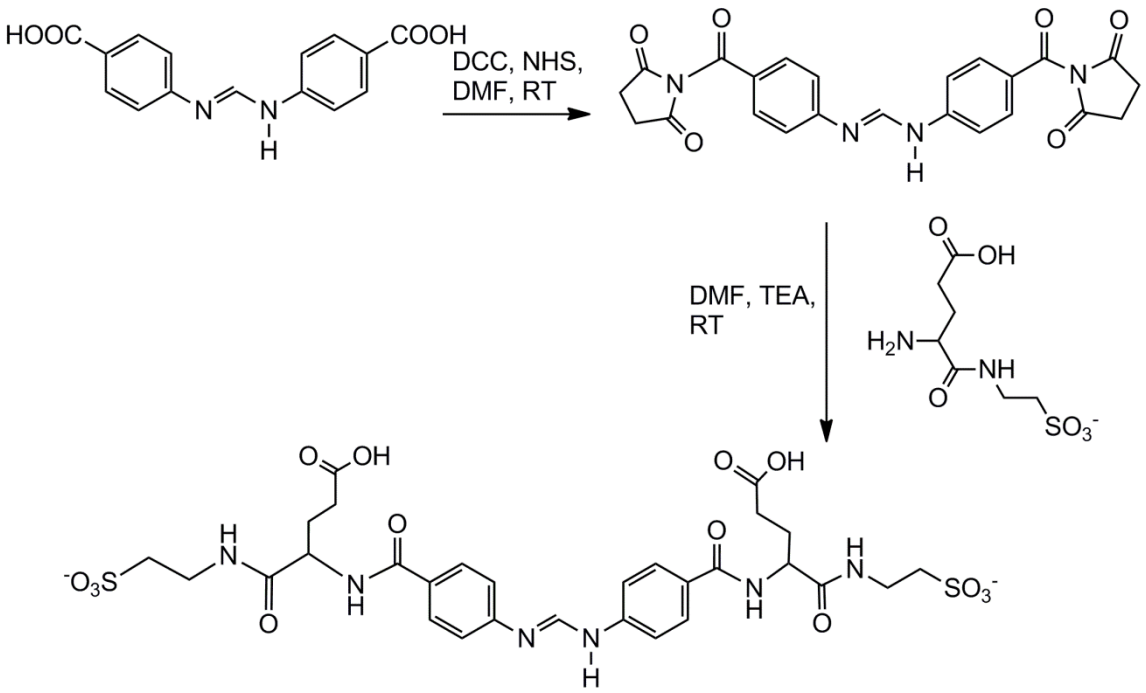

Figure 6.3 Synthetic routes for the coupling reaction between peptides and formamidine ligands.

detailed procedure for the coupling reactions between the carboxylate group and the peptides is described in Figure 6.3. [239]

Betaine (Figure 6.4) is a chemically neutral zwitterion with a positively charged cationic group and a negatively charged functional group. It is widely used in biology and biochemistry to increase the water solubility of various types of drugs and proteins. [240 - 241] The proposed synthetic route for formamidine ligands bearing a sulfobetaine group is detailed in Figure 6.4. The sulfobetaine can be easily obtained by the reaction of a tertiary amine with 1,3-propanesultone in toluene.[242] The resulting product is then reacted with the p-iodoaniline in DMF catalyzed by [Pd(0)(PPh_3)$_4$] through a Sonogashira cross-coupling reaction to form the para-substituted aniline.[243] Subsequent reaction with triethylorthoformate generates the desired formamidine ligands.

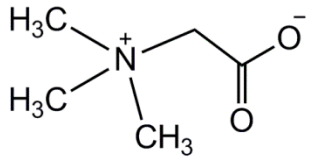

Figure 6.4 Schematic representation of trimethylglycine (betaine).

Design of dual functionality PDT agents for cancer therapy

One burgeoning area in the development of effective PDT anticancer drugs is the design and synthesis of dual-action phototherapeutic agents. For example, Turro and coworkers designed several Ru(II) complexes with 5-CNU (5-CNU = 5-cyanouracil, an anticancer active drug) as the monodentate ligands (the structural representation of cationic unit of

compound $[Ru(tpy)(5\text{-}CNU)_3]Cl_2$ is shown in Figure 6.5). Upon light irradiation, the 5-CNU molecule can be released from the parent compounds. Therefore, the *in situ* generated compounds, 5-CNU and Ru(II) complex have synergic effect and can achieve higher cytotoxicity towards cancer cell. [222,244]

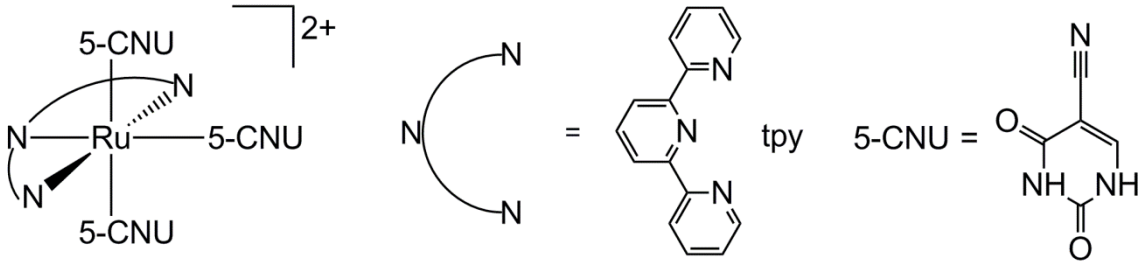

Figure 6.5 Structural representation of $[Ru(tpy)(5\text{-}CNU)_3]^{2+}$.

The same strategy can also be applied to synthesize photoactive Rh_2(II,II) compounds. For example, it has been shown in chapter V that the complex H-H *cis*-$[Rh_2(fhp)_2(CH_3CN)_6][BF_4]_2$ has two relatively labile eq CH_3CN in the dark which undergo ligand exchange with the CD_3CN molecules. Therefore, it is reasonable to react the complex with 1 eq of diimine ligand, *e.g.* dpq, to replace these two labile CH_3CN ligands. The resulting product, *cis*-$[Rh_2(fhp)_2(dpq)(CH_3CN)_3][BF_4]_2$ should be able to subsequently undergo substitution reactions with the 5-CNU ligands to generate *cis*-$[Rh_2(fhp)_2(dpq)(5\text{-}CNU)_3][BF_4]_2$. The detailed synthetic route is described in Figure 6.6 Presently, compound *cis*-$[Rh_2(fhp)_2(dpq)(CH_3CN)_3][BF_4]_2$ has been successfully synthesized, the identity of which was confirmed by an X-ray crystallographic study

(Figure 6.7); the purity was verified by ^{1}H-NMR spectroscopy (Figure 6.8). The four resonances at ~ 9.70, 9.29, 9.00 and 8.19 ppm correspond to the dpq ligand, while the

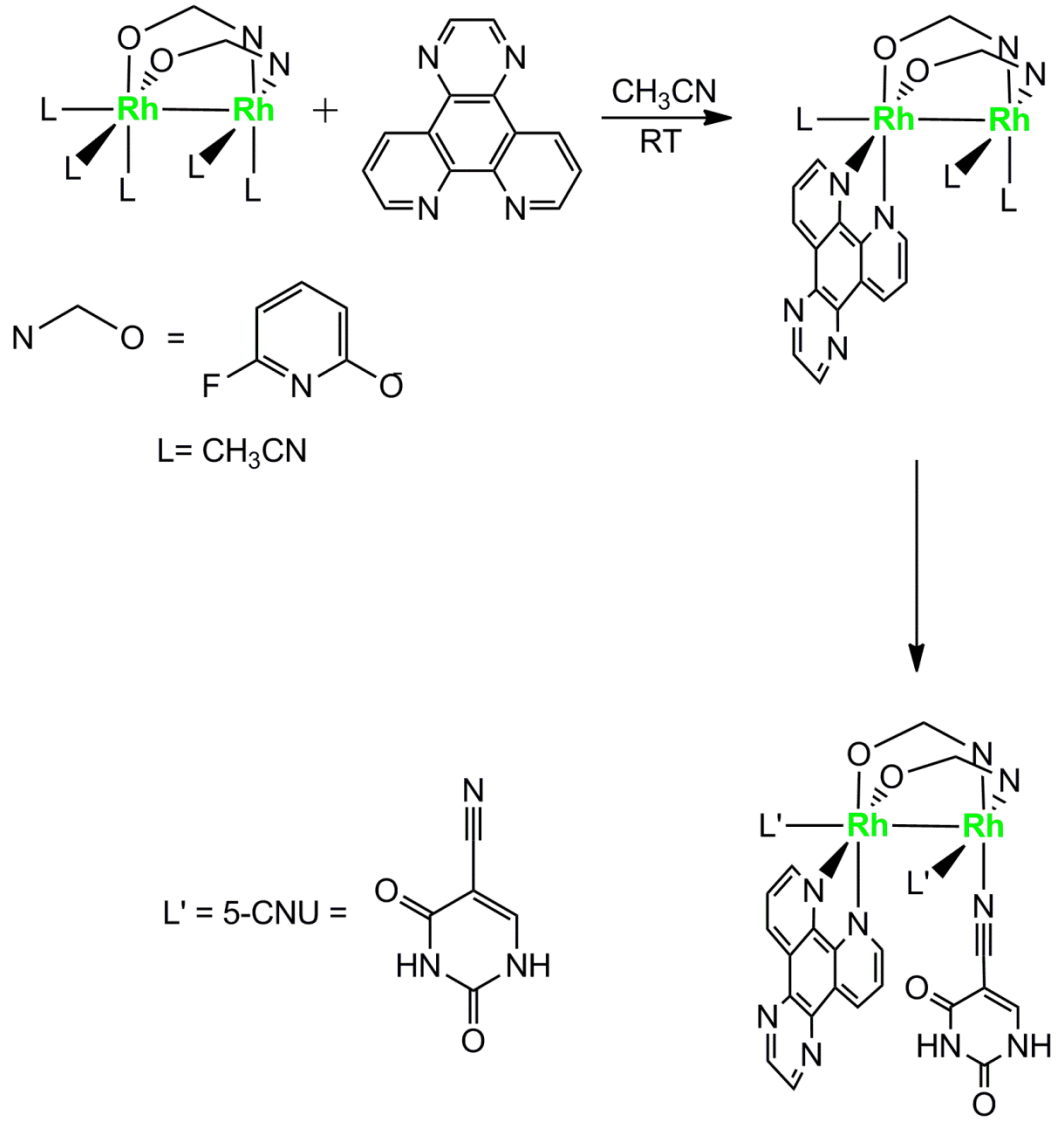

Figure 6.6 Detailed synthetic route to generate *cis*-$[Rh_2(fhp)_2(5\text{-}CNU)_3][BF_4]_2$.

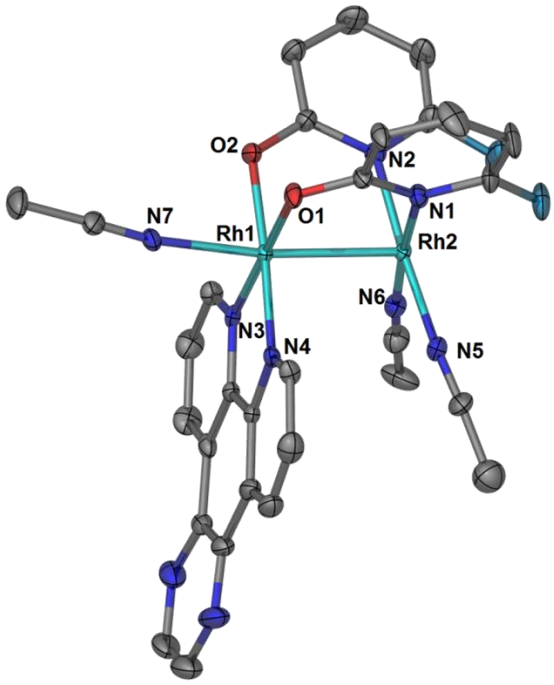

Figure 6.7 Thermal ellipsoid plot for compound *cis*-$[Rh_2(fhp)_2(dpq)(CH_3CN)_3][BF_4]_2$ at the 50% probability level. Anions and hydrogen atoms were omitted for the sake of clarity.

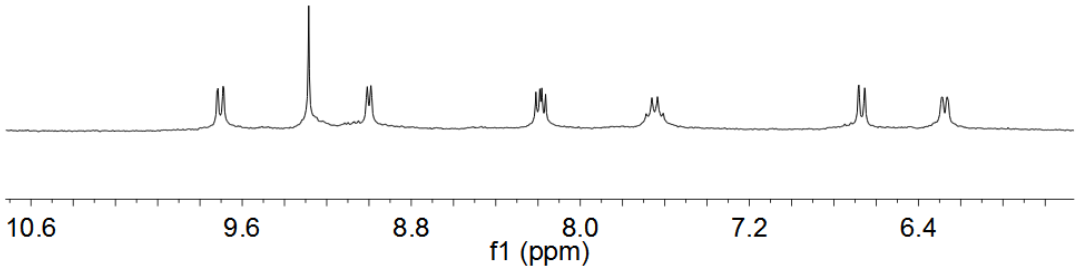

Figure 6.8 ^{1}H-NMR spectrum for *cis*-$[Rh_2(fhp)_2(dpq)(CH_3CN)_3][BF_4]_2$ in the aromatic region measured in CD_3CN at room temperature.

three resonances at ~ 7.64, 6.66, and 6.27 ppm result from the three different types of protons on the bridging fhp ligands.

In conclusion, the dirhodium complexes described in this thesis constitute new families of compounds that exhibit interesting and intriguing structural and electronic properties. Further studies involving the new compounds described in the chapter and their respective applications, such as photocatalyzing water reduction to generate H_2 and PDT agents for cancer, are currently in progress.

REFERENCES

1 Doyle, M. P.; Duffy, R.; Ratnikov, M.; Zhou, L. *Chem. Rev*. **2010**, *110*, 704-724.

2 Lou, Y.; Remarchuk, T. P.; Corey, E. J. *J. Am. Chem. Soc*. **2005**, *127*, 14223-14230.

3 Chifotides, H. T.; Koshlap, K. M.; Pérez, L. M.; Dunbar, K. R. *J. Am. Chem. Soc.* **2003**, *125*, 10703-10713.

4 Chifotides, H. T.; Koshlap, K. M.; Pérez, L. M.; Dunbar, K. R. *J. Am. Chem. Soc.* **2003**, *125*, 10714-10724.

5 Chifotides, H. T.; Dunbar, K. R. *J. Am. Chem. Soc.* **2007**, *129*, 12480-12490.

6 Kang, M.; Chouai, A.; Chifotides, H. T.; Dunbar, K. R. *Angew. Chem. Int. Ed*. **2006**, *45*, 6148-6151.

7 Chifotides, H. T.; Dunbar, K. R. *Acc. Chem. Res.* **2005**, *38*, 146-156 and references therein.

8 Lutterman, D. A.; Fu, P. K.-L.; Turro, C. *J. Am. Chem. Soc.* **2006**, *128*, 738-739.

9 Chifotides, H. T.; Lutterman, D. A.; Dunbar, K. R.; Turro, C. *Inorg. Chem.* **2011**, *50*, 12099-12107.

10 Aguirre, J. D.; Angeles-Boza, A. M.; Chouai, A.; Pellois, J.-P.; Turro, C.; Dunbar, K. R. *J. Am. Chem. Soc.* **2009**, *131*, 11353-1136.

11 Cotton, F. A.; Lin, C.; Murillo, C. A. *Acc. Chem. Res*. **2001**, *34*, 759-771 and reference therein

12 Kumar, D. K.; Filatov, A. S.; Napier, M.; Sun, J.; Dikarev, E. V.; Petrukhina, M. A. *Inorg. Chem.* **2012**, *51*, 4855-4861.

13 Tanaka, S.; Masaoka, S.; Yamauchi, K.; Annaka, M.; Sakai, K. *Dalton Trans.*, **2010**, *39*, 11218–11226.

14 Xie, J.; Li, C.;Zhou, Q.; Wang,W.; Hou,Y.; Zhang,B.; Wang, X. *Inorg. Chem.*, **2012**, *51*, 6376-6384.

15 Esswein, A. J.; Veige, A. S.; Nocera, D. G. *J. Am. Chem. Soc.* **2005**, *127*, 16641-16651.

16 Teets, T. S.; Cook, T. R.; McCarthy, B. D.; Nocera, D. G. *Inorg. Chem.* **2011**, *50*, 5223-5233.

17 Heyduk, A. F.; Nocera, D. G. *Science* **2001**, *293*, 1639-1641.

18 Hilderbrand, S. A.; Lim, M. H.; Lippard, S. J. *J. Am. Chem. Soc.* **2004**, *126*, 4972-4978.

19 Esteban, J.; Ros-Lis, J. V.; Martínez-Mánez, R.; Marcos, M. D.; Moragues, M.; Soto, J.; Sancenón, F. *Angew. Chem., Int. Ed.* **2010**, *49*, 4934-4937.

20 Moragues, M. E.; Esteban, J.; Ros-Lis, J. V.; Martínez-Mánez, R.; Marcos, M. D.; Martínez, M.; Soto, J.; Sancenón, F. *J. Am. Chem. Soc.* **2011**, *133*, 15762-15772.

21 Chifotides, H. T.; Dunbar, K. R. 'Rhodium Compounds', Chapter 12, In '*Multiple Bonds Between Metal Atoms*', 3rd Edition, Cotton, F. A.; Murillo, C. Walton, R. A., Eds., Springer-Science and Business Media, Inc.: New York, **2005**, pp 465-589.

22 Christoph, G. G.; Koh, Y.-B. *J. Am. Chem. Soc.* **1979**, *101*, 1422-1434.

23 Lutterman, D. A.; Degtyareva, N. N.; Johnston, D. H.; Gallucci, J. C.; Eglin, J. L.; Turro, C. *Inorg. Chem.* **2005**, *44*, 5388-5396.

24 Bown, S. G. *Phil. Trans. Soc. A* **2013**, *371*, 20120371.

25 Dougherty, T. J.; Grindey, G. B.; Fiel, R.; Weishaupt, K. R.; Boyle, D. G. *J. Natl. Cancer I* **1975**, *55*, 115-121.

26 O'Connor, A. E.; Gallagher, W. M.; Byrne, A. T. *Photochem. Photobiol.* **2009**, *85*, 1053-1074.

27 Szaciłowski, K.; Macyk, W.; Drzewiecka-Matuszek, A.; Brindell, M.; Stochel, G. *Chem. Rev.* **2005**, *105*, 2647−2694.

28 Dunlop, R. A.; Brunk, U. T., Rodgers, K. J. *IUBMB Life* **2009**, *61*, 522–527**.**

29 Celli, J. P.; Spring, B. Q.; Rizvi, I.; Evans, C. L.; Samkoe, K. S.; Verma, S.; Pogue, B. W.; Hasan, T. *Chem. Rev.* **2010**, *110*, 2795−2838.

30 Allison, R. R.; Sibata, C. H. Photodiagn. *Photodyn. Ther* **2010**, *7*, 61−75.

31 Wolkenberg, S. E.; Boger, D. L. *Chem. Rev.* **2002**, *102*, 2477−2496.

32 Dougherty, T. J.; Gomer, C. J.; Henderson, B. W.; Jori, G.; Kessel, D.; Korbelik, M.; Moan, J.; Peng, Q. *J. Natl. Cancer Inst.* **1998**, *90*, 889−905.

33 Dolmans, D. E.; Fukumura, D.; Jain, R. K. *Nat. Rev. Cancer* **2003**, *3*, 380-387.

34 Darwent, J. R.; Douglas, P.; Harriman, A.; Porter, G.; Richoux, M. *Coord. Chem. Rev.* **1982**, *44*, 83-126.

35 Liu,Y.; Hammitt, R.; Lutterman, D. A.; Joyce,L. E.; Thummel,R. P.; Turro, C. *Inorg. Chem.* **2009**, *48*, 375-385.

36 Sun, Y.; Joyce, L. E.; Dickson, N. M.; Turro, T. *Chem. Commun.* **2010**, *46*, 2426-2428.

37 Sun, Y.; Joyce, L. E.; Dickson, N. M.; Turro, T. *Chem. Commun.* **2010**, *46*, 6759-6761.

38 Demas, J. N.; Harris, E. W.; McBride, R. P. *J. Am. Chem. Soc.* **1977**, *99*, 3547–3551.

39 Gao, R.; Ho, D. G.; Hernandez, B.;Selke, M.; Murphy, D.; Djurovich, P. I.; Thompson, M. E. *J. Am. Chem. Soc.* **2002**, *124*, 14828-14829.

40 Ragone, F.; Saavedra, H. H. M.; Gara, P. M. D.; Ruiz, G. T.; Wolcan, E. *J. Phys. Chem. A* **2013**, *117*, 4428–4435.

41 Abdel-Shafi, A. A.; Bourdelande, J. L.; Ali, S. S. *Dalton Trans.* **2007**, 2510−2516.

42 Garcia-Fresnadillo, D.; Georgiadou, Y.; Orellana, G.; Braun, A.M.; Oliveros, E. *Helv. Chem. Acta* **1996**, *79* 1222-1238.

43 Bonnett, R. *Chem. Soc. Rev.* **1995**, *24*, 19-33

44 Bradley, P. M.; Bursten, B. E.; Turro, C. *Inorg. Chem.* **2001**, *40*, 1376-1379.

45 Angeles-Boza, A. M.; Bradley, P. M.; Fu, P. K.-L.; Shatruk, M.; Hilfiger, M. G.; Dunbar, K. R.; Turro, C. *Inorg. Chem.* **2005**, *44*, 7262-7264.

46 Angeles-Boza, A. M.; Bradley, P. M.; Fu, P. K.-L.; Wicke, S. E.; Bacsa, J.; Dunbar, K. R.; Turro, C. *Inorg. Chem.* **2004**, *43*, 8510-8519.

47 Bradley, P. M.; Angeles-Boza, A. M.; Dunbar, K. R.; Turro, C. *Inorg. Chem.* **2004**, *43*, 2450-2452.

48 Joyce, L. E.; Aguirre, J. D.; Angeles-Boza, A. M.; Chouai, A.; Fu, P. K.-L.; Dunbar, K. R.; Turro, C. *Inorg. Chem.* **2010**, *49*, 5371–5376.

49 Lewis, N. S.; Nocera, D. G. *Proc. Natl. Acad. Sci. USA* **2006**, *103*, 15729-15735.

50 Sun, L.; Hammarström, L.; Åkermark, B.; Styring, S. *Chem. Soc. Rev.* **2001**, *30*, 36-49.

51 Cook, T. R.; Dogutan, D. K.; Reece, S. Y.; Surendranath, Y.; Teets, T. S.; Nocera, D. G. *Chem. Rev.* **2010**, *110*, 6474–6502.

52 Evans D. J.; Pickett, C. J. *Chem. Soc. Rev.* **2003**, *32*, 268–275.

53 Thomas, C. M.; Ru¨diger, O.; Liu, T.; Carson, C. E.; Hall, M. B.; Darensbourg, M. Y. *Organometallics* **2007**, *26*, 3976–3984.

54 Woolerton, T. W.; Sheard, S.; Chaudhary, Y. S.; Armstrong, F. A. *Energy Environ. Sci.* **2012**, *5*, 7470-7490.

55 Teets, T. S.; Nocera, D. G. *Chem. Commun.* **2011**, *47*, 9268-9274.

56 Dempsey, J. L.; Brunschwig, Winkler, J. R.; Gray, H. B. *Acc. Chem. Res.* **2009**, *42*, 1995-2004.

57 Du, P.; Knowles, K.; Eisenberg, R. *J. Am. Chem. Soc.* **2008**, *130*, 12576-12577.

58 Du, P.; Schneider, J.; Luo, G.; Brennessel, W. W.; Eisenberg, R. *Inorg. Chem.* **2009**, *48*, 4952-4962.

59 Fihri, A.; Artero, V.; Pereira, A.; Fontecave, M. *Dalton Trans.* **2008**, 5567-5569.

60 Probst, B.; Rodenberg, A.; Guttentag, M.; Hamm, P.; Alberto, R. *Inorg. Chem.* **2010**, *49*, 6453-6460.

61 Jasimuddin, S.; Yamada, T.; Fukuju, K.; Otsuki, J.; Sakai, K. *Chem. Commun.* **2010**, *46*, 8466-8468.

62 Luo, S. -P.; Mejia, E.; Friedrich, A.; Pazidis, A.; Junge, H.; Surkus, A.-E.; Jackstell, R.; Denurra, S.; Gladiali, S.; Lochbrunner, S.; Beller, M. *Angew. Chem. Int. Ed.* **2013**, *52*, 419 –423.

63 Marinescu, S. C.; Wrinkler, J. R.; Gray, H. B. *Proc. Natl. Acad. Sci. USA* **2012**, *109*, 15127-15131.

64 Helm, M. L.; Stewart, M. P.; Bullock, R. M.; DuBois, M. R.; DuBois, D. L. *Science* **2011**,*333*, 863-866

65 Karunadasa, H. I.; Chang, C. J.; Long, J. R. *Nature* **2010**, *464*, 1329-1333.

66 Darensbourg, M. Y.; Lyon, E. J.; Zhao X.; Georgakaki, I. P. *Proc. Natl. Acad. Sci. U. S. A.* **2003**, *100*,3683–3688.

67 Fihri, A.; Artero, V.; Pereira, A.; Fontecave, M. *Dalton Trans.* **2008**, 5567-5569.

68 Esswein, A. J.; Veige, A. S.; Nocera, D. G. *J. Am. Chem. Soc.* **2005**, *127*, 16641-16651.

69 Lee, C. H.; Cook, T. R.; Nocera, D. G. *Inorg. Chem.* **2011**, *50*, 714-716.

70 Elgrishi, N.; Teets, T. S.; Chambers, M. B.; Nocera, D. G. *Chem. Commun.* **2012**, *48*, 9474-9476.

71 Cook, T. R.; Surendranath, Y.; Nocera, D. G. *J. Am. Chem. Soc.* **2009**, *131*, 28-29.

72 Fimiani, V.; Ainis, T.; Cavallaro, A.; Piraino, P. *J. Chemother.* **1990**, *2*, 319-326.

73 Kornecki, K. P.; Briones, J. F.; Boyarskikh, V.; Fullilove, F.; Autschbach, J.; Schrote, K. E.; Lancaster, K. M.; Davies, Huw M. L.; Berry, J. F. *Science* **2013**, *342*, 351-354.

74 Chavan, M. Y.; Zhu, T. P.; Lin, X. Q.; Ahsan, M. Q.; Bear, J. L.; Kadish, K. M. *Inorg. Chem.* **1984**, *23*, 4538-4545.

75 Chavan, M. Y.; Ahsan, M. Q.; Lifsey, R. S.; Bear, J. L.; Kadish, K. M. *Inorg. Chem.* **1986**, *25*, 3218-3223.

76 He, L.-P.; Yao, C.-L.; Naris; Lee, M. J. C.; Korp, J. D.; Bear, J. L. *Inorg. Chem.*, **1992**, *31*, 620-625.

77 Piraino, P.; Bruno, G.; Lo Schiavo, S.; Laschi, F.; Zanello, P. *Inorg. Chem.* **1987**, *26*, 2205-2211.

78 Braunschweig, H.; Damme, A.; Dewhurst, R. D.; Vargas, A. *Nat. Chem*. **2013**, *5*, 115-121.

79 Drago, R. S.; Tanner, S. P.; Richman, R. M.; Long, J. R. *J. Am. Chem. Soc.* **1979**, *101*, 2897-2903.

80 Pirrung, M. C.; Morehead, A. T. Jr. *J. Am. Chem. Soc.* **1994**, *116*, 8991-9000.

81 Evans, M. E.; Jones, W. D. *Organometallics*, **2011**, *30*, 3371-3377.

82 Bear, J. L.; Han, B.; Wu, Z.; Van Caemelbecke, E.; Kadish, K. M. *Inorg. Chem.* **2001**, *40*, 2275-2281.

83 Handa, M.; Yasuda, M.; Muraki, Y.; Yoshioka, D.; Mikuriya, M.; Kasuga, K. *Chem. Lett.* **2003**, *32*, 946-947.

84 Girolami, G. S.; Andersen, R. A. *Inorg. Chem.* **1981**, *20*, 2040-2044.

85 Klendworth, D. D.; Welters III, W. W.; Walton, R. A. *Organometallics* **1982**, *1*, 336-343.

86 Cameron, C. J.; Tetrick, S. M.; Walton, R. A. *Organometallics* **1984**, *3*, 240-247.

87 Allison, J. D.; Wood, T. E.; Wild, R. E.; Walton, R. A. *Inorg. Chem.* **1982**, *21*, 3540-3548.

88 Mann, K. R.; Cimolino, M.; Geoffroy, G. L.; Hammond, G. S.; Orio, A. A.; Albertin, G.; Gray, H. B. *Inorg. Chim. Acta* **1976**, *16*, 97-101.

89 Mann, K. R.; Lewis, N. S.; Miskowski, V. M.; Erwin, D. K.; Hammond, G. S.; Gray, H. B. *J. Am. Chem. Soc*. **1977**, *99*, 5525-5526.

90 Miskowski, V. M.; Sigal, I. S.; Mann, K. R.; Gray, H. B.; Milder, S. J.; Hammond, G. S.; Ryason, P. R. *J. Am. Chem. Soc.* **1979**, *101*, 4383-4385.

91 Maverick, A. W.; Smith, T. P.; Maverick, E. F.; Gray, H. B. *Inorg. Chem.* **1987**, *26*, 4336-4341.

92 Balch, A. L.; Olmstead, M. M. *J. Am. Chem. Soc.* **1976**, *98*, 2354-2358.

93 Balch, A. L.; Labadie, J. W.; Delker, G. *Inorg. Chem.* **1979**, *18*, 1224-1227.

94 Balch, A. L. *J. Am. Chem. Soc.* **1976**, *98*, 8049-8054.

95 Olmstead, M. M.; Balch, A. L. *J. Organomet. Chem.* **1978**, *148*, C15-C18.

96 Tran, N. T.; Stork, J. R.; Pham, D.; Chancellor, C. J.; Olmstead, M. M.; Fettinger, J. C.; Balch, A. L. *Inorg. Chem.* **2007**, *46*, 7998-8007.

97 Tejel, C.; Ciriano, M. A.; Lopez, J. A.; Lahoz, F. J.; Oro, L. A. *Organometallics* **1997**, *16*, 4718-4727.

98 Carmona, D.; Oro, L. A.; Pérez, P. L.; Tiripicchio, A.; Tiripicchio-Camellini, M. *J. Chem. Soc., Dalton Trans.* **1989**, 1427-1433.

99 Tortorelli, L. J.; Woods, C.; McPhail, A. T. *Inorg. Chem.* **1990**, *29*, 2726-2733.

100 Stace, J. J.; Lambert, K. D.; Krause, J. A.; Connick, W. B. *Inorg. Chem.* **2006**, *45*, 9123-9131.

101 Ugi, I.; Fetzer, U.; Eholzer, U.; Knupfer, H.; Offerman. K. *Angew. Chem., Int. Ed.* **1965**, *4*, 472-484.

102 Piraino, P.; Tresoldi, G.; Faraone, F. *J. Organomet. Chem.* **1982**, *224*, 305-312.

103 Hartman, W. W.; Dickey, J. B. *Org. Synth*. **1934**, *14*, 24.

104 Catalan, K. V.; Hess, J. S.; Maloney, M. M.; Mindiola, D. J.; Ward, D. L.; Dunbar, K. R. *Inorg. Chem.* **1999**, *38*, 3904-3913.

105 Cotton, F. A.; Murillo, C. A.; Wang, X. P.; Yu, R. M. *Inorg. Chem.* **2004**, *43*, 8394-8403.

106 Gaussian 09, Revision B.01, Frisch, M. J.; Trucks, G. W.; Schlegel, H. B.; Scuseria, G. E.; Robb, M. A.; Cheeseman, J. R.; Scalmani, G.; Barone, V.; Mennucci, B.; Petersson, G. A.; Nakatsuji, H.; Caricato, M.; Li, X.; Hratchian, H. P.; Izmaylov, A. F.; Bloino, J.; Zheng, G.; Sonnenberg, J. L.; Hada, M.; Ehara, M.; Toyota, K.; Fukuda, R.; Hasegawa, J.; Ishida, M.; Nakajima, T.; Honda, Y.; Kitao, O.; Nakai, H.; Vreven, T.; Montgomery, J. A., Jr.; Peralta, J. E.; Ogliaro, F.; Bearpark, M.; Heyd, J. J.; Brothers, E.; Kudin, K. N.; Staroverov, V. N.; Kobayashi, R.; Normand, J.; Raghavachari, K.; Rendell, A.; Burant, J. C.; Iyengar, S. S.; Tomasi, J.; Cossi, M.; Rega, N.; Millam, N. J.; Klene, M.; Knox, J. E.; Cross, J. B.; Bakken, V.; Adamo, C.; Jaramillo, J.; Gomperts, R.; Stratmann, R. E.; Yazyev, O.; Austin, A. J.; Cammi, R.; Pomelli, C.; Ochterski, J. W.;

Martin, R. L.; Morokuma, K.; Zakrzewski, V. G.; Voth, G. A.; Salvador, P.; Dannenberg, J. J.; Dapprich, S.; Daniels, A. D.; Farkas, Ö.; Foresman, J. B.; Ortiz, J. V.; Cioslowski, J.; Fox, D. J. Gaussian, Inc., Wallingford CT, **2009**.

107 Adamo, C.; Barone, V. *J. Chem. Phys.* **1998,** *108*, 664-675.

108 Perdew J. P.; Chevary, J. A.; Vosko S. H.; Jackson K. A.; Pederson M. R.; Singh D. J.; Fiolhais C. *Phys. Rev. B* **1992**, *46*, 6671-6687.

109 Perdew, J. P.; Burke, K.; Wang, Y. *Phys. Rev. B* **1996**, *54*, 16533-16539.

110 Dolg, M.; Stoll, H.; Preuss, H.; Pitzer, R. M. *J. Phys. Chem.* **1993**, *97*, 5852-5859.

111 Petersson, G. A.; Bennett, A.; Tensfeldt, T. G.; Allaham, M. A.; Shirley, W. A.; Mantzaris, J. *J. Chem.l Phys.* **1988,** *89*, 2193-2218.

112 Petersson, G. A.; Allaham, M. A. *J. Chem. Phys.* **1991,** *94*, 6081-6090.

113 Bauernschmitt, R.; Ahlrichs, R. *Chem. Phys. Lett.* **1996,** *256*, 454-464.

114 Casida, M. E.; Jamorski, C.; Casida, K. C.; Salahub, D. R. *J. Chem. Phy.* **1998,** *108*, 4439-4449.

115 Stratmann, R. E.; Scuseria, G. E.; Frisch, M. J. *J. Chem. Phys.* **1998,** *109*, 8218-8224.

116 Van Caillie, C.; Amos, R. D. *Chem. Phys. Lett.* **1999,** *308*, 249-255.

117 Van Caillie, C.; Amos, R. D. *Chem. Phys. Lett.* **2000,** *317*, 159-164.

118 Furche, F.; Ahlrichs, R. *J. Chem. Phys.* **2002,** *117*, 7433-7447.

119 Scalmani, G.; Frisch, M. J.; Mennucci, B.; Tomasi, J.; Cammi, R.; Barone, V. *J. Chem. Phy.* **2006,** *124*, 1-15.

120 Tomasi, J.; Mennucci, B.; Cammi, R. *Chem. Rev.* **2005,** *105*, 2999-3093.

121 Tomasi, J. *Structure and Reactivity in Aqueous Solution* **1994,** *568*, 10-23.

122 Agui 9.2.1, Dennington, R. D., II; Keith, T. A.; Millam, J. M. Semichem, Inc., Shawnee Mission KS, **2008**.

123 SAINT, Program for area detector absorption correction, Siemens Analytical X-Ray Instruments Inc., Madison, WI 53719, USA, 1994-1996.

124 Sheldrick, G. M.; SADABS, Program for Siemens area detector absorption correction, University of Göttingen, Göttingen, Germany, 1996.

125 Barbour, L. J. X-Seed, Graphical interface to SHELX-97 and POV-Ray, 1999 (http://www.x-seed.net).

126 Barbour, L. J. J. *Supramol. Chem*. **2001**, *1*, 189-191.

127 Atwood, J. L.; Barbour, L. J. *Cryst. Growth Des*. **2003**, *3*, 3-8.

128 Sheldrick, G. M. *Acta Crystallogr. Sect. A* **2008**, *A64*, 112-122.

129 Chifotides, H. T.; Catalan, K. V.; Dunbar, K. R. *Inorg. Chem.* **2003**, *42*, 8739-8747.

130 Pimblett, G.; Garner, C. D.; Clegg, W. *J. Chem. Soc., Dalton Trans.* **1986**, 1257-1263.

131 Dunbar, K. R.; Majors, S. O.; Sun, J. S. *Inorg. Chim. Acta* **1995**, *229*, 373-382.

132 Connelly, N. G.; Einig, T.; Herbosa, G. G.; Hopkins, P. M.; Mealli, C.; Orpen, A. G.; Rosair, G. M.; Viguri, F. *J. Chem. Soc., Dalton Trans.* **1994**, 2025-2039.

133 Eagle, C. T.; Farrar, D. G.; Pfaff, C. U.; Davies, J. A.; Kluwe, C.; Miller, L. *Organometallics* **1998**, *17*, 4523-4526.

134 Chakravarty, A. R.; Cotton, F. A.; Tocher, D. A.; Tocher, J. H. *Organometallics* **1985**, *4*, 8-13.

135 Hyde, E. M.; Kennedy, J. D.; Shaw, B. L. *J. Chem. Soc., Dalton Trans.* **1977**, *16*, 1571-1576.

136 Cotton, F. A.; Feng, X. J. *Inorg. Chem.* **1989**, *28*, 1180-1183.

137 Lutterman, D. A.; Degtyareva, N. N.; Johnston, D. H.; Gallucci, J. C.; Eglin, J. L.; Turro, C. *Inorg. Chem.* **2005**, *44*, 5388-5396.

138 Bonati, F.; Minghett, G. *Inorg. Chim. Acta* **1974**, *9*, 95-112.

139 Thomas, R. K.; Leisegang, E. C.; Thompson, H. F. R. S. *Proc. R. Soc. Lond. A* **1972**, *330*, 15-28.

140 Ugi, I.; Meyr, R. *Chem. Ber*. **1960**, *93*, 239-248.

141 Buschmann, W. E.; Miller, J. S. *Chem. Eur. J.* **1998**, *4*, 1731-1737.

142 Prater, M. E.; Pence, L. E.; Clerac, R.; Finniss, G. M.; Campana, C.; Auban-Senzier, P.; Jerome, D.; Canadell, E.; Dunbar, K. R. *J. Am. Chem. Soc.* **1999**, *121*, 8005-8016.

143 Ren, T.; Lin, C.; Valente, E. J.; Zubkowski, J. D. *Inorg. Chim. Acta* **2000**, *297*, 283-290.

144 Kessler, M.; Ring, H.; Trambarulo, R.; Gordy, W. *Phys. Rev*. **1950**, *79*, 54-56.

145 Rogachev, A. U.; Hoffman, R. *J. Am. Chem. Soc.* **2013**, *135*, 3262-3275.

146 Cotton, F. A.; Falvello, L. R.; Gerards, M.; Snatzke, G. *J. Am. Chem. Soc.* **1990**, *112*, 8979-8980.

147 Norman, J. G.; Kolari, H. J. *J. Am. Chem. Soc.* **1978**, *100*, 791-799.

148 Cotton, F. A.; Hillard, E. A.; Liu, C. Y.; Murillo, C. A.; Wang, W.; Wang, X. *Inorg. Chim. Acta* **2002**, *337*, 233-246.

149 Bursten, B. E.; Cotton, F. A. *Inorg. Chem*. **1981**, *20*, 3042-3048.

150 Kawamura, T.; Maeda, M.; Miyamoto, M.; Usami, H.; Imaeda, K.; Ebihara, M. *J. Am. Chem. Soc*. **1998**, *120*, 8136-8142.

151 Kawamura, T.; Fukamachi, K.; Sowa, T.; Hayashida, S.; Yonezawa, T. *J. Am. Chem. Soc*. **1981**, *103*, 364-369.

152 King, A. E.; Surendranath, Y.; Piro, N. A.; Bigi, J. P.; Long, J. R.; Chang, C. J. *Chem. Sci*. **2013**, *4*, 1578-1587.

153 Tinker, L. L.; McDaniel, N. D.; Curtin, P. N.; Smith, C. K.; Ireland, M. J.; Bernhard, S. *Chem. Eur. J.* **2007**, *13*, 8726 – 8732.

154 Rau, S.; Schafer, B.; Gleich, D.; Anders, E.; Rudolph, M.; Friedrich, M.; Gorls, H.; Henry, W.; Vos, J. G. *Angew. Chem., Int. Ed.* **2006**, *45*, 6215-6218.

155 Stoll, T.; Gennari, M.; Serrano, I.; Fortage, J.; Chauvin, J.; Odobel, F.; Rebarz, M.; Poizat, O.; Sliwa, M.; Deronzier, A.; Collomb, M.-N. *Chem. Eur. J.* **2013**, *19*, 782 – 792.

156 Sutin, N.; Creutz, C.; Fujita, E. *Comments Inorg. Chem.* **1997**, *19*, 67-92.

157 Cline, E.; Adamson, S.; Bernhard, S. *Inorg. Chem.* **2008**, *47*, 10378-10388.

158 Che , G.; Li, W; Kong , Z; Su, Z; Chu, B; Li, B.; Zhang, Z; Hu, Z; Chi, H. *Syn. Comm.* **2006**, *36*, 2519-2524.

159 Mann, K. R.; Bell, R. A.; Gray, H. B. *Inorg. Chem.* **1979**, *18*, 2671-2673.

160 Liu, Y.; Hammitt, R.; Lutterman, D. A.; Joyce, L. E.; Thummel, R. P.; Turro, C. *Inorg. Chem.* **2009**, *48*, 375-385.

161 Sun, Y.; Lutterman, D. A.; Turro, C. *Inorg. Chem.* **2008**, *47*, 6427-6434.

162 Joshi, T.; Barbante, G. J.; Francis, P. S.; Hogan, C. F.; Bond, A. M.; Spiccia, L. *Inorg. Chem.* **2011**, *50*, 12172-12183.

163 Liu, X. W.; Li, J.; Deng, H.; Zheng, K. C.; Mao, Z. W.; Ji, L. N. *Inorg. Chim. Acta* **2005**, *358*, 3311-3319.

164 Connelly, N. G.; Geiger, W. E. *Chem. Rev.* **1996**, *96*, 877-910.

165 Inoue, M; Inoue, M. B. *Faraday Trans. 2* **1985**, *81*, 539-547.

166 Delaney, S.; Pascaly, M.; Battacharya, P. K.; Han, K.; Barton, J. K. *Inorg. Chem.* **2002**, *41*, 1966-1974.

167 Rosenberg, B.; Van Camp, L.; Krigas, T. *Nature* **1965**, *205*, 698-699.

168 Rosenberg, B.; Van Camp, L.; Trosko, J. E.; Mansour, V. H. *Nature* **1969**, *222*, 385-386.

169 Dhar, S.; Lippard, S. J. Current Status and Mechanism of Action of Platinum-Based Anticancer Drugs. In Bioinorganic Medicinal Chemistry; Alessio, E., Ed.; Wiley-VCH: Weinheim, **2010**; pp 79−86.

170 Ang, W. H.; Myint, M. N. Z.; Lippard, S. J. *J. Am. Chem. Soc.* **2010**, *132*, 7429−7435.

171 Todd, R. C.; Lippard, S. J. *J. Inorg. Biochem.* **2010**, *104*, 902−908.

172 Kelland, L. *Nat. Rev. Cancer* **2007**, *7*, 573−584.

173 Jung, Y.; Lippard, S. J. *Chem. Rev.* **2007**, *107*, 1387−1407.

174 Mantri, Y.; Lippard, S. J.; Baik, M. H. *J. Am. Chem. Soc.* **2007**, *129*, 5023−5030.

175 Wang, D.; Lippard, S. J. *Nat. Rev. Drug Discov.* **2005**, *4*, 307−320.

176 Jamieson, E. R.; Lippard, S. J. *Chem. Rev.* **1999**, *99*, 2467−2498.

177 Zamble, D. B.; Lippard, S. J. *Trends Biochem. Sci.* **1995**, *20*, 435−439.

178 Cisplatin: Chemistry and Biochemistry of a Leading Anticancer Drug; Lippert, B., Ed.; Wiley-VCH: Wurzburg, Germany, **1999**.

179 Platinum-Based Drugs in Cancer Therapy; Kelland, L. R., Farell, N., Eds.; Humana: Totowa, NJ, **2000**.

180 Rajski, S. R.; Williams, R. M. *Chem. Rev.* **1998**, *98*, 2723−2795.

181 Cohen, S. M.; Lippard, S. J. *Prog. Nucleic Acid Res. Mol. Biol.* **2001**, *67*, 93-130.

182 Zhang, C. X.; Lippard, S. J. *Curr. Opin. Chem. Biol.* **2003**, *7*, 481-489.

183 Fuertes, M. A.; Alonso, C.; Perez, J. M. *Chem. Rev*. **2003**, *103*, 645-662.

184 Fuertes, M. A.; Castilla, J.; Alonso, C.; Perez, J. M. *Curr. Med. Chem.: Anti-Cancer Agents* **2002**, *2*, 539-551.

185 Siddik, Z. H. *Cancer Treat. Res.* **2002**, *112*, 263 - 284.

186 Siddik, Z. H. *Oncogene* **2003**, *22*, 7265-7279.

187 Calvert, A. H., Harland, S. J., Newell, D. R., Siddik, Z. H., Jones, A. C., McElwain, T. J., Raju, S., Wiltshaw, E., Smith, I. E., Baker, J. M., Peckham, M. J., Harrap, K. R. *Cancer Chemother. Pharmacol.* **1982**, *9*, 140-147.

188 Evans, B. D., Raju, K. S., Calvert, A. H., Harland, S. J., Wiltshaw, E. *Cancer Treat. Rep.* **1983**, *67*, 997-1000.

189 Raymond, E.; Faivre, S.; Chaney, S.; Woynarowski, J.; Cvitkovic, E. *Mol. Cancer Ther.* **2002**, *1*, 227-235.

190 Di Francesco, A. M.; Ruggiero, A.; Riccardi, A. *Cell. Mol. Life Sci.* **2002**, *59*, 1914–1927.

191 Wheate, N. J.; Walker, S.; Craig, G. E.; Oun, R. *J. Chem. Soc. Dalton Trans* **2010**, *39*, 8113-8127.

192 Hope, J. M.; Wilson, J. J.; Lippard, S. J. *J. Chem. Soc. Dalton Trans.* **2013**, *42*, 3176-3180.

193 Wilson, J. J.; Lippard, S. J. *Inorg. Chem.**2012**, 51*, 9852-9864.

194 Park, G. Y.; Wilson, J. J.; Song, Y.; Lippard, S. J. *Proc. Natl. Acad. Sci. USA* **2012**, *109*, 11987-11992.

195 Wilson, J. J.; Lippard, S. J. *J. Med. Chem. **2012**, 55*, 5326-5336.

196 Zhu, G.; Myint, M.; Ang, W. H.; Song, L.; Lippard, S. J. *Cancer Research **2012**, 72*, 790-800.

197 Lovejoy, K.; Serova, M.; Bieche, I.; Emami, S.; D'Incalci, M.; Broggini, M.; Erba, E.; Gespach, C.; Cvitkovic, E.; Faivre, S.; Raymond, E.; Lippard, S. J. *Mol. Cancer Ther. **2011**, 10*, 1709-1719.

198 Wilson, J. J.; Lippard, S. J. *Inorg. Chem.* **2011**, *50*, 3103−3115.

199 Varbanov, H.; Valiahdi, S. M.; Legin, A. A.; Jakupec, M. A.; Roller, A.; Galanski, M.; Keppler, B. K. Eur. *J. Med. Chem.* **2011**, *46*, 5456−5464.

200 Reithofer, M. R.; Bytzek, A. K.; Valiahdi, S. M.; Kowol, C. R.; Groessl, M.; Hartinger, C. G.; Jakupec, M. A.; Galanski, M.; Keppler, B. K. *J. Inorg. Biochem.* **2011**, *105*, 46−51.

201 Scaffidi-Domianello, Y. Y.; Meelich, K.; Jakupec, M. A.; Arion, V. B.; Kukushkin, V. Y.; Galanski, M.; Keppler, B. K. *Inorg. Chem.* **2010**, *49*, 5669−5678.

202 Mangrum, J. B.; Farrell, N. P. *Chem. Commun.* **2010**, *46*, 6640−6650.

203 Gwak, H.-S.; Shingu, T.; Chumbalkar, V.; Hwang, Y.-H.; DeJournett, R.; Latha, K.; Koul, D.; Yung, W. K.; Powis, G.; Farrell, N. P.; Bögler, O. *Int. J. Cancer* **2010**, *128*, 787−796.

204 Ma, G.; Min, Y; Huang, F; Jiang, T.; Liu, Y. *Chem.* Commun. **2010**, *46*, 6938-6940.

205 Li, C.; Li, Z; Sletten, E.; Arnesano, F.; Losacco, M; Natile, G.; Liu, Y. *Angew. Chem. Int. Ed.*, **2009**, *48*(*45*), 8497 – 8500.

206 DeRosa, M. C.; Crutchley, R. J. *Coord. Chem. Rev.* **2002**, *233-234*, 351-371.

207 Harris, A. L. *Nat. Rev. Cancer* **2002**, *2*, 38−47.

208 Shannon, A. M.; Bouchier-Hayes, D. J.; Condron, C. M.; Toomey, D. *Cancer Treat. Rev.* **2003**, *29*, 297−307.

209 Guppy, M. *Biochem. Biophys. Res. Commun.* **2002**, *299*, 676 - 680.

210 Westendorf, A. F.; Zerzankova, L.; Salassa, L.; Sadler, P. J.; Brabec, V.; Bednarski, P. J. *J. Inorg. Biochem.* **2011**, *105*, 652−662.

211 Ronconi, L.; Sadler, P. J. *J. Chem. Soc. Dalton Trans.* **2011**, *40*, 262−268.

212 Liu, H.-K.; Sadler, P. J. *Acc. Chem. Res.* **2011**, *44*, 348−359.

213 Farrer, N. J.; Woods, J. A.; Salassa, L.; Zhao, Y.; Robinson, K. S.; Clarkson, G.; Mackay, F. S.; Sadler, P. J. *Angew. Chem. Int. Ed.* **2010**, *49*, 8905−8908.

214 Salassa, L.; Ruiu, T.; Garino, C.; Pizarro, A. M.; Bardelli, F.; Gianolio, D.; Westendorf, A.; Bednarski, P. J.; Lamberti, C.; Gobetto, R.; Sadler, P. J. *Organometallics* **2010**, *29*, 6703−6710.

215 Farrer, N. J.; Woods, J. A.; Munk, V. P.; Mackay, F. S.; Sadler, P. J. *Chem. Res. Toxicol.* **2010**, *23*, 413−421.

216 Farrer, N. J.; Salassa, L.; Sadler, P. J. *J. Chem. Soc. Dalton Trans.* **2009**, *48*, 10690−10701.

217 Betanzos-Lara, S.; Salassa, L; Habtemariam, A.; Novakova, O.; Pizarro, A. M.; Clarkson, G. J.; Liskova, B.; Brabec, V.; Sadler, P. J. *Organometallics* **2012**, *31*, 3466−3479.

218 Zhao, Y.; Roberts, G. M.; Greenough, S. E.; Farrer, N. J.; Paterson, M. J.; Powell, W. H.; Stavros, V. G.; Sadler, P. J. *Angew. Chem. Int. Ed.* **2012**, *51*, 11263 –11266.

219 Butler, J. S.; Woods, J. A.; Farrer, N. J.; Newton, M .E.; Sadler, P. J. *J. Am. Chem. Soc.* **2012**, *134*, 16508−16511.

220 Respondek, T.; Garner, R. N.; Herroon, M. K.; Podgorski, I.; Turro, C.; Kodanko, J. J. *J. Am. Chem. Soc.* **2011**, *133*, 17164−17167.

221 Garner, R. N.; Joyce, L. E.; Turro, C. *Inorg. Chem.* **2011**, *50*, 4384−4391.

222 Sgambellone, M. A.; David, A.; Garner, R. N.; Dunbar, K. R.; Turro, C. *J. Am. Chem. Soc.*, **2013**, *135*, 11274–11282.

223 Burya S. J.; Palmer, A. M.; Galucci, J. C.; Turro, C. *Inorg. Chem.* **2012**, *51*, 11882-11890.

224 Li, Z.; Burya, S. J.;Turro, C.; Dunbar, K. R. *Phil. Trans. R. Soc. A.* **2013**, *371*, 20120128.

225 Rempel, G. A.; Legzdins, P.; Smith, H.; Wilkinson, G. *Inorg. Syn.* **1971**, *13*, 90−91.

226 Cotton, F. A.; Felthouse, T. R. *Inorg*. *Chem*. **1981**, *20*, 584-600.

227 Cotton, F. A.; Han, S.; Wang, W. *Inorg, Chem.* **1984**, *23*, 4762-4765.

228 Pruchnik, F. P.; Starosta, R.; Lis, T.; Lahuerta, P. *J. Organomet. Chem.* **1998**, *568*, 177.

229 Li, Z.; Chifotides, H. T.; Dunbar, K. R. *Chem. Sci.* **2013**, *4*, 4470-4485.

230 Li, Z.; Leed, N. A.; Dickson-Karn, N. M.; Dunbar, K. R.; Turro, C. *Chem. Sci.* **2014**, 5 (2), 727-737.

231 Wang, H.; Lu, Z.; Lord, S. J.; Moerner, W. E.; Twieg, R. J. *Tetrahedron Lett.* **2007**, *48*, 3471.

232 Singleton, M. L.; Crouthers, D. J.; Duttweiler, R. P.; Reibenspies, J. H.; Darensbourg, M. Y. *Inorg. Chem.* **2011**, *50*, 5015.

233 Kolmakov, K.; Belov, V. N.; Bierwagen, J.; Ringemann, C.; Muller, V.; Eggeling, C.; Hell, S. W. *Chem. Eur. J.* **2010**, *16*, 158.

234 Peneva, K.; Mihov, G.; Nolde, F.; Rocha, S.; Hotta, J.; Braeckmans, K.; Hofkens, J.; Uji-I, H.; Herrmann, A.; Mullen, K. *Angew. Chem. Int. Ed.* **2008**, *47*, 3372.

235 Liu, W. Q.; Liu, X. J.; Knaebel, D.; Luck, L.; Li, Y. Z. *Antimicrob. Agents Chemother.* **1998**, *42*, 911.

236 Giessler, K.; Griesser, H.; Gohringer, D.; Sabirov, T.; Richert, C. *Eur. J. Org. Chem.* **2010**, 3611.

237 Niu, S. L.; Ulrich, G.; Ziessel, R.; Kiss, A.; Renard, P. Y.; Romieu, A. *Org. Lett.* **2009**, *11*, 2049.

238 Guha, S.; Chakraborty, T.; Banerjee, A. *Green Chem.* **2009**, *11*, 1139.

239 Meltola, N. J.; Wahlroos, R.; Soini, A. E. *J. Fluoresc.* **2004**, *14*, 635.

240 Collins, T.; D'Amico, S.; Georlette, D.; Marx, J. C.; Huston, A. L.; Feller, G. *Anal. Biochem.* **2006**, *352*, 299.

241 D'Amico, S.; Feller, G. *Anal. Biochem.* **2009**, *385*, 389.

242 Niu, S.; Ulrich, G.; Ziessel, R.; Kiss, A.; Renard P.-Y. and Romieu, A. *Org. Lett.* **2009**, *11*, 2049-2052.

243 Sonogashira, K. *J. Organomet. Chem.* **2002**, *653*, 46–49.

244 Garner, R. N.; Gallucci, J. C.; Dunbar, K. R.; Turro, C. *Inorg. Chem.* **2011**, *50*, 9213–9215.